Analysis of Nuclear Fuel Cycle Materials by X-ray Absorption Spectroscopy

A thesis submitted to the College of Graduate and Studies and Research

in partial fulfillment of the requirements for the degree of

Doctor of Philosophy of Science

in the Department of Chemistry

University of Saskatchewan

Saskatoon

By

John R. Hayes

PERMISSION TO USE

In presenting this thesis/dissertation in partial fulfillment of the requirements for a Postgraduate degree from the University of Saskatchewan, I agree that the Libraries of this University may make it freely available for inspection. I further agree that permission for copying of this thesis/dissertation in any manner, in whole or in part, for scholarly purposes may be granted by the professor or professors who supervised my thesis/dissertation work or, in their absence, by the Head of the Department or the Dean of the College in which my thesis work was done. It is understood that any copying or publication or use of this thesis/dissertation or parts thereof for financial gain shall not be allowed without my written permission. It is also understood that due recognition shall be given to me and to the University of Saskatchewan in any scholarly use which may be made of any material in my thesis/dissertation.

Requests for permission to copy or to make other uses of materials in this thesis/dissertation in whole or part should be addressed to:

Head of the Department of Chemistry
University of Saskatchewan
Saskatoon, Saskatchewan
S7N 5C9, Canada

OR

Dean
College of Graduate Studies and Research
University of Saskatchewan
107 Administration Place
Saskatoon, Saskatchewan S7N 5A2
Canada

It is not a myth, there is no debate, facts are in
Fact is, there's never been any question.
We are facing crisis.
We dismiss the truth not because we can't accept it,
But because having to commit ourselves to change is a scary prospect for anybody.
The most alarming part of the statement 'we are facing crisis'
Isn't the word 'crisis',
It's the word 'we'.
Because those two letters take the responsibility away from one
And rest it squarely on the shoulders of everybody.
We are Atlas now.

– Shane Koyczan, from the poem *Shoulders*

ACKNOWLEDGEMENTS

While there are many people who I would like to thank for their help in completing this thesis, I would be remiss if I did not mention my family first. To my parents: thank you for pushing me to achieve when I thought it wasn't possible, and thank you for all your love and support throughout my entire academic career. You have supported me when things looked grim and helped me celebrate the good times as well, and I want you to know I appreciate you and everything you have done to help me. I would also like to thank my brother Jeff, who has challenged me to look beyond the narrow field of science and see some of the bigger picture of life. Jeff - you have challenged me to explore more of life, and for that I am thankful. My extended family has also been instrumental in helping me write this thesis, and I extent my heartfelt thanks to them as well.

I would like to thank my fellow Grosvenor Group members, both past and present. In our group, beamtime, and all the fatigue associated with it, is a shared experience, regardless of whose samples are being run. While I initially thought that this was common amongst all groups, I have come to realize our group is unique in its sharing of beamtime experiences, and my heartfelt gratitude goes to my group, who make such sacrifices seem so commonplace. Without my groupmates' support, I am sure this thesis would not have been possible. I would especially like to thank Mr. Mohamed Ruwaid Rufiuaddin and Dr. Esther Rani Aluri, who helped collect the XAS spectra presented in Chapter 4. Over the course of my graduate studies, I have been blessesd to meet and be taught my a number of wonderful individuals. In the case of this thesis, my supervisor, Dr. Andrew Grosvenor, has provided immeasurable amounts of support and guidance. Andrew, thank you very much for the challenge and drive you provided. I would also like to thank Dr. Mouna Saoudi, who supervised me when I worked at Canadian Nuclear Labortories Limited (CNL) and provided invaluable feedback and input when preparing Chapters 3 and 5, in addition to a number of other publications and documents not included in this thesis. Mouna, you provided invalubale support and tutaledge during my attachment at CNL. You also taugt me the value of "following up", which has proven invaluble throughout my academic career. I also thank Dr. Kebbi Hughes for help and supervision, as she supervised some of the work done in Chapter 2 and kindly escorted me on a

trip to see the McClean Lake facility. I also would like to thank Dr. John Rowson and Mr. Ryan Frey, who contributed their knowledge, expertise, and editorial support during the preparation of Chapter 2. Dr. Joel Reid is also thanked for teaching me how to analyze the Laue diffraction patterns presented in Chapter 2.

The work in this thesis has also been greatly enhanced by the advice and wisdom of a large number of other scientists as well. Dr. Rosura Ham-Su and Dr. Lawrence Dickson (CNL) are thanked for their support and intellectual contributions to this thesis. Mr. Tom Bonli and Mr. Blaine Novakovski are thanked for their help in carrying out the SEM experiments presented in Chapter 4. Mr. Clinton Mayhew and Mr. Jozef Mouris (CNL) are thanked for their help in carrying out the SEM experiments presented in Chapter 3 and Chapter 5. Dr. Weifeng Chen and Dr. Ning Chen are thanked for their help in carrying out experiments on the HXMA beamline at the CLS. I would like to thank Dr. Yongfeng Hu and Ms. Aimee Maclennan for their help in completing the experiments presented in Chapter 3 and Chapter 5 using the SXRMB beamline at the CLS. Finally, I would like to thank Dr. Robert Gordon (Moyie Institute) and Dr. Zou Finfrock for their help in completing the experiments performed using the 20-BM beamline at the CLS@APS. I would also like to thank Ms. Maclennan for agreeing to marry me.

In my life, and especially over the portion of my life it took to complete this thesis, I have had the fortune and honour to to meet and befriend a large number of wonderful and supportive people, and no Acknowledgments section could ever do these friends justice. (It would end up being longer than the thesis itself!) To all my friends: please know that you have my gratitude, and that you have added the much-needed spice to life, turning my journey into an adventure! I would also like to take this opportunity to specifically thank my partner, Aimee. You have kept me sane, reminded me to sit back and enjoy life, and I am so happy to have met you! And, as it turns out, we have chemistry together! I would also like to thank my cats, Eugene and Kevin, who helped me write this komklb hn lj;lkj; thesis.

Finally, I have to thank the organizations that have provided the funding for the work done in this thesis. I thank the National Science and Engineering Research Council (NSERC) for financial

support through the Canada Graduate Scholarship program and the University of Saskatchewan for support through the Herzberg Memorial Scholarship program. The Canadian Foundation for Innovation (CFI) is thanked for providing funds to purchase the PANalytical Empyrean powder X-ray diffractometer used in this work. This work was supported by in-kind contributions from CNL under agreement No. CRA-110812. Access to Sector 20 was obtained through the CLS-APS Partnership Agreement. Sector 20 facilities at the Advanced Photon Source, and research at these facilities, are supported by the US Department of Energy - Basic Energy Sciences, the Canadian Light Source and its funding partners, the University of Washington, and the Advanced Photon Source. Use of the Advanced Photon Source, an Office of Science User Facility operated for the U.S. Department of Energy (DOE) Office of Science by Argonne National Laboratory, was supported by the U.S. DOE under Contract No. DE-AC02-06CH11357. The CLS is supported by NSERC, the National Research Council of Canada, the Canadian Institutes of Health Research, the Province of Saskatchewan, Western Economic Diversification Canada, and the University of Saskatchewan.

ABSTRACT

Nuclear energy can be used to reliably generate large quantities of electricity while providing minimal lifetime CO_2 emissions. Given the extreme importance of safety in the nuclear industry, it is necessary to have a fundamental understanding of the materials used throughout the nuclear fuel cycle. It is of particular importance to develop an understanding of these materials at an atomic level. In this thesis, X-ray absorption spectroscopy (XAS), along with several other X-ray based techniques, has been used to study materials that are produced or proposed for use in the nuclear fuel cycle.

Uranium mining and milling operations generate large quantities of waste, known as mine and mill tailings. AREVA Resources Canada disposes of the tailings waste produced at their McClean milling facility in Northern Saskatchewan using the JEB Tailings Management Facility (TMF). AREVA monitors the mineralization of elements of concern (i.e., Ni, As, Fe, Mo, Ra, and U) within the TMF as part of its on-going commitment towards managing the facility's environmental impact. Molybdenum (Mo) is predicted to mineralize as insoluble powellite ($CaMoO_4$) within the TMF. However, no experimental evidence confirmed the presence of powellite in the TMF. In Chapter 2, the presence of powellite, and other Mo-bearing minerals, was determined using powder X-ray diffraction (XRD), X-ray fluorescence imaging, and Mo K-edge XAS. The results of this study confirmed that powellite was present in the TMF and showed that Mo K-edge XAS was the only effective way to detect the Mo minerals within the TMF.

New materials for use as nuclear fuels were also investigated in this thesis. Spent nuclear fuel must be securely stored for long periods of time due to the presence transuranic elements (TRU; i.e., Pu, Am, Np, Cm). Inert matrix fuels (IMF), which consist of actinides embedded in a neutron transparent (inert) material, can be used to "burn-up" or transmute these TRU species in currently available reactors. Stabilized ZrO_2 materials have been proposed for use in IMF applications, and in Chapter 3 the thermal stability of a series of $Nd_xY_yZr_{1-x-y}O_{2-\delta}$ materials made by a ceramic synthetic route have been studied using powder XRD, scanning electron microscopy (SEM), and X-ray absorption spectroscopy. (Nd was used as a surrogate for Am.) The results of this study showed

that the fluorite structure of the $Nd_xY_yZr_{1-x-y}O_{2-\delta}$ materials was stabilized when $y \geq 0.05$, and that the local environment around Zr was independent of composition or annealing temperature.

The effect of synthetic method on the thermal stability of the $Nd_xY_yZr_{1-x-y}O_{2-\delta}$ materials was also determined, and this is the subject of Chapter 4. In this study a series of $Nd_xY_{0.25-x}Zr_{0.75}O_{1.88}$ materials were synthesized using a low-temperature co-precipitation synthesis and then annealed at 1400 °C and 1500 °C. The as-synthesized and annealed materials were characterized by powder XRD, SEM, and XAS. This study confirmed that the thermal stability of the materials was dependent on synthetic method, and that materials made using a solid-state method were superior to those produced by a solution-based approach.

Y-stabilized zirconia has a low thermal conductivity, which is not ideal for a nuclear fuel. The thermal conductivity could be increased if a lighter cation, such as Sc, was used to stabilize the fluorite structure. In Chapter 5, the thermal stability of a series of $Nd_xSc_yZr_{1-x-y}O_{2-\delta}$ materials was investigated. The as-synthesized and annealed materials were studied by powder XRD, SEM, and XAS. These results showed that the fluorite structure was only stable in the annealed materials when $x+y \geq 0.15$ and $y \geq 0.10$. The results of this study provided insight into the possible use of scandia-stabilized zirconia for use as an inert matrix fuel.

The studies presented in this thesis have used X-ray absorption spectroscopy and a number of other techniques to characterize materials important to the nuclear fuel cycle. The studies presented here were only possible because of the unique information that can be obtained using XAS. This thesis serves to highlight the importance of XAS as a technique and how it can be applied to solve problems related to the material science of the nuclear fuel cycle.

Contents

List of Tables

List of Figures

List of Abbreviations

ADU	Ammonium diuranate
APS	Advanced Photon Source
AUC	Ammonium uranyl carbonate
BSE	Backscatter Electron
CANDU Reactor	Canada Deuterium Uranium Reactor
CLS	Canadian Light Source
CN	Coordination Number
EDS	Energy Dispersive Spectroscopy
EXAFS	Extended X-ray Absorption Fine Structure
FBR	Fast Breeder Reactor
HLW	High Level Waste
HWR	Heavy Water Reactor
ILW	Intermediate Level Waste
IMF	Inert Matrix Fuel
LCF	Linear Combination Fitting

LLW	Low Level Waste
LWR	Light Water Reactor
MOX	Mixed Metal Oxide Fuel
NNN	Next Nearest Neighbour
PCA	Principle Component Analysis
PFY	Partial Fluoresence Yield
PUREX	Plutonium and Uranium Redox EXtraction
RE	Rare-earth
ScSZ	Scandia-stabilized zirconia
SDD	Silicon Drift Detector
SE	Secondary Electron
SEM	Scanning Electron Microscopy
SNF	Spent Nuclear Fuel
SOFC	Solid Oxide Fuel Cell
TBP	Tri-butyl phosphate
TEY	Total Electron Yield
TMF	Tailings Management Facility
TRU	Transuranic Element; i.e., Np, Pu, Am, Cm
WDS	Wavelength Dispersive Spectroscopy
XANES	X-ray Absorption Near-Edge Spectroscopy

XAS	X-ray Absorption Spectroscopy
XRD	X-ray Diffraction
XRF	X-ray fluorescence
YSZ	Yttria-stabilized zirconia

Chapter 1

INTRODUCTION

1.1 Introduction

The harnessing of energy is central to all human activities, and energy can be viewed as the ultimate base currency of any economy. The need to produce more useful energy has expanded exponentially as economies have expanded over the past several centuries. This demand has been sufficiently met by the increased burning of fossil fuels, though the consequences of using these energy sources are now coming to bear. The negative effects of air pollution and CO_2 release from the burning of fossil fuels are readily apparent, and it is therefore up to the science and technology sectors to develop alternative, emissions-free sources of energy.

Ultimately, it is desirable to use renewable resources, such as wind and solar energy, to power the future world as these resources can be harnessed to produce energy with minimal environmental impacts. However, there is still a considerable energy gap that must be met, and solar and wind energies are currently not capable of sustaining the always-on baseload required to power a modern electric grid. Nuclear power, which extracts energy from the fission of atomic nuclei, can be used to meet these baseload requirements and provide the energy necessary to meet the ever-growing energy demand of an increasingly industrialized world. Nuclear energy has been successfully used to generate electricity since 1951, when the experimental, 100 kW EBR-I reactor in Arco,

Idaho, USA started producing power [1]. Since then, nuclear energy has proven to be a safe way to generate electricity while producing minimal air pollution and carbon emissions. However, nuclear energy does produce radioactive spent nuclear fuel, which must be stored for many thousands of years, and this waste must be dealt with appropriately. Additionally, uranium mining activities also can produce negative environmental consequences. Given these concerns, it is therefore necessary to continue to develop science and technology that will reduce these impacts and enable increased use of nuclear energy to power the future. This thesis aims to do so by furthering the fundamental understanding of materials associated with different steps in the nuclear fuel cycle through the use of X-ray absorption spectroscopy (XAS). Materials associated with nuclear energy must be well understood and modelled given the high safety standards of the nuclear industry. Given this high standard for safety, it is necessary to develop a complete understanding of a material and its properties in order to ensure that it will behave in a predictable manner. To this end, this thesis presents research investigating several materials related to the nuclear fuel cycle. XAS was used to develop a fundamental understanding of these materials on an atomic scale. The XAS studies were then complemented with powder X-ray diffraction (XRD) and scanning electron microscopy (SEM) characterization, which allowed for an understanding of the structures and behaviour of the structures of these materials at different length scales. This comprehensive approach is necessary, as it allows for better prediction of the behaviour of the materials studied during irradiation in a nuclear reactor and over very long time scales under ambient conditions.

It is necessary to understand how nuclear energy is produced in order to provide the context for the science presented in this work. A full discussion of nuclear fuel cycles is beyond the scope of this thesis, as the nuclear fuel cycles are relatively complicated and diverse. However, this chapter will give a general overview of some of the steps found in a nuclear fuel cycle, with a focus on the steps relevant to the research presented in this thesis. At the end of this chapter, the reader should have a better understanding of why nuclear energy is necessary in a modern industrialized world and how nuclear fuel is produced. The chapter will then conclude by explicitly stating the objectives of this thesis.

1.2 Climate Change and Meeting Energy Demands of an Industrialized World

Over the past century, the western world has experienced an incredible increase in industrial output and energy use, and primary power consumption was 16 times greater at the end of the 20^{th} century than it was at the beginning [2]. This increased demand has largely been met by utilizing fossil fuels, and over the 20th century burning fossil fuels led to an increase in the atmospheric concentration CO_2 from 275 ppm to 370 ppm [2]. CO_2 levels have continued to increase, and the average atmospheric CO_2concentration measured at the Mauna Loa Observatory was 401.85 ppm in December 2015 [3]. It is now widely accepted that CO_2 and other greenhouse gas emissions are resulting in anthropogenic climate change [4]. The effects of anthropogenic climate change are wide-ranging, and the full extent of the consequences of are still not understood [5–7]. However, given the possible consequences of anthropogenic climate change, it is prudent to make reducing CO_2 emissions a top priority in order to stabilize atmospheric CO_2 concentrations [2, 4, 5, 8–11].

It has been previously estimated that atmospheric CO_2 concentration must be stabilized at $\sim$450 ppm by 2050 in order to prevent coral reef bleaching, thermohaline circulation shutdown, and sea level rise [2, 12]. An estimated 25 TW of emissions free power generation will be required in order to meet this goal [2, 13]. The world had an energy production capacity of 12 TW as of 2002, of which approximately 85% was generated via fossil fuels [2]. This figure indicates that meteoric efforts will be required in order to stabilize atmospheric CO_2 emissions, and that both changes in policy and changes in technology will be required to meet this goal.

The difficulties associated with meeting this goal are better understood by examining the current sources of electricity generation. The sources of electricity production in 2014 versus the projected demand in 2040 are presented in Figure 1.1 [14]. Based on current demand trends, the global electricity production will need to nearly double in the next 25 years, with most of this demand increase localized in China, India, and the Latin American nations [14]. This future energy demand cannot be obtained by only expanding the use of other renewables, such as solar and wind

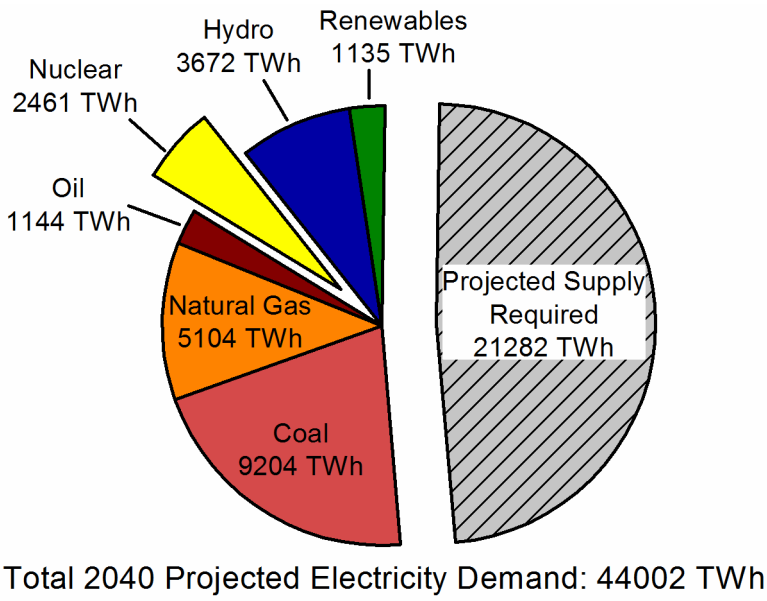

Figure 1.1: The 2014 sources of global electricity supply are given in TWh, along with the expected increase in demand for electricity by 2040. The total projected global demand in 2040 is 44002 TWh, while the current total global electricity supply is 22720 TWh. Data is taken from [14].

power. For example, a 3.3 TW capacity from solar power would require 220,000 km^2 of solar cells at current operating efficiencies, while only 3 km^2 have been produced from 1982-1998 [2]. Further, solar power, like wind power, is not an "always-on" source, requiring an alternative source of power to provide the required baseload supply [2, 9, 14, 15]. It is therefore germane to look to non-carbon emission sources other than solar and wind energy to meet the required energy demands of the future.

Nuclear energy is a proven means to produce vast quantities of always-on energy while producing minimal carbon emissions. The exact amount of carbon emitted by nuclear energy is difficult to accurately estimate as it is highly dependent on the fuel cycle and grade of uranium ore mined. Most of the carbon emissions produced by nuclear power generation is attributable to the uranium mining and fuel fabrication processes, which account for $\sim$38% of carbon emissions. The carbon emissions increase as the grade of the ore (i.e., the uranium content) decreases. Average uranium ore grades can vary from as little as 0.0004% U to greater than 20% U, as found in the Cigar Lake uranium deposit in Northern Saskatchewan [11, 16–19]. Further, the degree of U-235 enrichment required varies based on the reactor used, which also affects the carbon emissions significantly.

For example, typical light water reactors (LWR) require enrichment to 3-10% U-235 while heavy water reactors (HWR), such as the CANDU reactors, can utilize natural U (0.73% U-235) [20]. It is therefore unsurprising that estimates of CO_2 emissions vary widely, with published estimates ranging from 10 g CO_2/kWh_{el} – 130 g CO_2/kWh_{el}, where g/kWh_{el} is mass of CO_2 released by the production of 1 kWh of electrical energy (kWh_{el}) [10, 11]. The average reported value is 65 g CO_2/kWh_{el}, and compares favorably with solar energy carbon emissions, which has been estimated to produce 90 g CO_2/kWh_{el}. Nuclear energy CO_2 emissions are much less than electricity produced from fossil fuel technologies which can produce 600 g CO_2/kWh_{el} (natural gas) to 1200 g CO_2/kWh_{el} (coal) [10]. Therefore, there is a strong impetus to utilize nuclear energy to produce electricity from a climate change perspective.

However, despite the merits of nuclear energy, no discussion of its use is complete without mention of the inherent nuclear waste problem. This radioactive waste can be divided into several different levels, and is dealt with according to its hazard. A full discussion and description of the waste produced in the nuclear fuel cycle and how this waste is being handled is presented in Section 1.6 on page 31. Here, it is worth discussing the scale of the problem in the context of environmental impact. The most problematic waste produced by nuclear energy is spent nuclear fuel, which is highly radiotoxic and must be stored for thousands of years [21–24]. However, the actual volume of spent nuclear fuel that must be stored is comparatively low when considering industrial scale processes. The world's total spent fuel inventory was estimated to have a volume of 2 x 10^5 m^3 as of 2007, and the total radioactive waste inventory, which includes a variety of non-active materials, is estimated have a volume of 2.4 x 10^6 m^3 [25]. In comparison, approximately 3 x 10^5 m^3 of coal fly ash, which is a toxic by-product from the burning of coal, is produced annually [26]. The environmental impact of storing nuclear fuel is relatively minimal compared to the environmental impact of other energy sources because of this small volume. This serves to further show that using nuclear energy to produce electricity is a viable option, and plans to meet the growing energy demands must include an expansion of nuclear energy power capacity in order to meet sustainable carbon emission goals.

1.3 An Overview of the Nuclear Fuel Cycle

The nuclear fuel cycle is one of the most important aspects of nuclear energy generation even though it only accounts for ∼20% of the cost of electricity generation by nuclear energy [20]. A nuclear fuel cycle consists of a chain of value-adding steps in which uranium is extracted from the Earth's crust, used to produce electricity, and then subsequently stored back into the Earth's crust. The specifics of the steps involved can vary between different implementations of the fuel cycle, and these specifics can affect a number of factors, including the volume and radiotoxicity of waste to be stored, the type of reactor used, and amount of fuel required. However, the various cycles can be broadly broken into one of two categories: open and closed fuel cycles [20]. In open fuel cycles, also known as once-through fuel cycles, the uranium oxide fuel is disposed after irradiation in a reactor. In a closed fuel cycle, remaining U-235 and Pu-239 are extracted from the irradiated nuclear fuel, and reprocessed into new fuel, though ultimately the high level waste will be stored in a deep geological repository. Both open and closed fuel cycles have merits and limitations, and countries and utility companies must perform concise cost-to-benefit analyses when choosing which cycle to pursue.

1.3.1 How a Nuclear Reactor Works

Nuclear reactors utilize the heat generated by the fission of atoms to produce electricity. There are a number of ways in which to harness this energy, which is reflected by the large number of nuclear reactor designs that are currently available or proposed for future deployment. However, these reactors do share several common operating principles, which will be discussed in this section.

Most modern reactors utilize the energy released by the neutron-induced fission of U-235 and Pu-239 atoms. These fission reactions can be written as follows:

$$^{235}\mathrm{U} + \mathrm{n} \rightarrow \mathrm{F.P.} + 2\mathrm{n} + 215\,\mathrm{MeV} \tag{1.1}$$

$$^{239}\mathrm{Pu} + \mathrm{n} \rightarrow \mathrm{F.P.} + 2\mathrm{n} + 207\,\mathrm{MeV} \tag{1.2}$$

where F.P. denotes the two daughter fission products released by the fission process (note that the fission products are widely varied). The fission process also releases two neutrons, which can be used to trigger further fission processes, resulting in a chain reaction [27]. A nuclear reactor controls the rate of that chain reaction in order to safely harness the heat produced by these reactions in order to produce electricity [27,28]. This provides the basis for most commercial power generation by nuclear energy.

There are two major types of nuclear reactors: light water reactors (LWR), in which the primary coolant and neutron moderator is normal, light water (i.e., H_2O) and heavy water reactors (HWR), in which the primary coolant and neutron moderator is deuterated, heavy water (i.e., D_2O). LWRs are advantageous because they do not use heavy water, which is expensive and difficult to manufacture [29]. HWRs are advantageous because they can use on-line refueling schedules and have a better neutron economy compared to LWRs [29]. However, HWRs utilize heavy water, which is expensive [29]. While the choice of coolant/moderator dictates many of the details of power generation, the basic operating principles are relatively similar regardless of moderator choice, and a schematic of a basic reactor design is shown in Figure 1.2.

The heart of the reactor is the pressure vessel, which contains the nuclear fuel. The fuel typically consists of highly dense UO_2 oxide pellets [31]. These pellets are stacked and encapsulated in a zirconaloy sheath, forming a fuel rod or fuel element [31]. The fuel rods are then bundled together, and this assembly is often referred to as a fuel bundle [31]. These fuel bundles are then loaded into the reactor core, where the fission reactions occur [27, 28]. Control rods, which consist of a neutron absorbing material such as carbon or boron, are then raised or lowered into the reactor core in order to control the rate of the fission reactions (and subsequently, the rate of heat released) [27, 28]. Primary coolant circuit, which is usually water, is flowed through the reactor core [27, 28]. This primary coolant serves two purposes. First, it cools the reactor core, preventing melting of the fuel materials, and, second, the coolant often operates as a neutron moderator, reducing the energy of the neutrons emitted by the fission reactions [27, 28]. It is necessary to reduce the energy of the neutrons in order to sustain the chain reaction, as only low-energy neu-

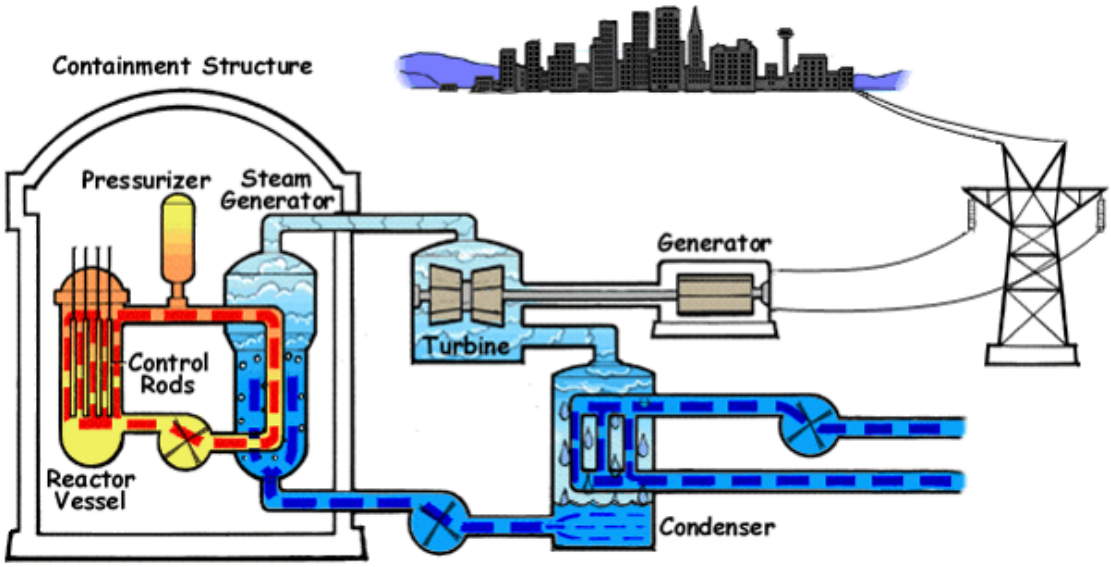

Figure 1.2: A schematic of a basic nuclear reactor is shown. Heat is generated in the nuclear reactor core by the fission of U-235 and Pu-239, and this heat is absorbed by the primary cooling circuit. The heat from the primary coolant is used to generate steam in a a secondary cooling circuit. This steam is then used to power a steam turbine, generating electricity. Figure was reproduced from the public domain; original author was the United States Nuclear Regulatory Commission. [30]

trons have a significant probability of initiating a fission reaction [27]. After the primary coolant is passed through the reactor core, it is then circulated through a serious of heat exchangers, which transfer the heat from the primary coolant into a secondary cooling circuit. Steam is generated in this secondary cooling circuit, and this steam is then used to power a steam turbine, producing electricity.

1.3.2 Open Fuel Cycles

The open fuel cycle is the most common type of fuel cycle used today, and a flow diagram summarizing the steps is presented in Figure 1.3. The distinguishing feature of open fuel cycles is that the fuel is only used once, and is considered waste after irradiation [10, 32, 33]. After reactor service, the fuel can be reprocessed into alternate waste forms, however it is most common for the used fuel assembly to be directly disposed [32, 34]. The up-front costs of an open fuel cycle are less than those of a closed fuel cycle because it omits expensive fuel reprocessing steps [20,35,36].

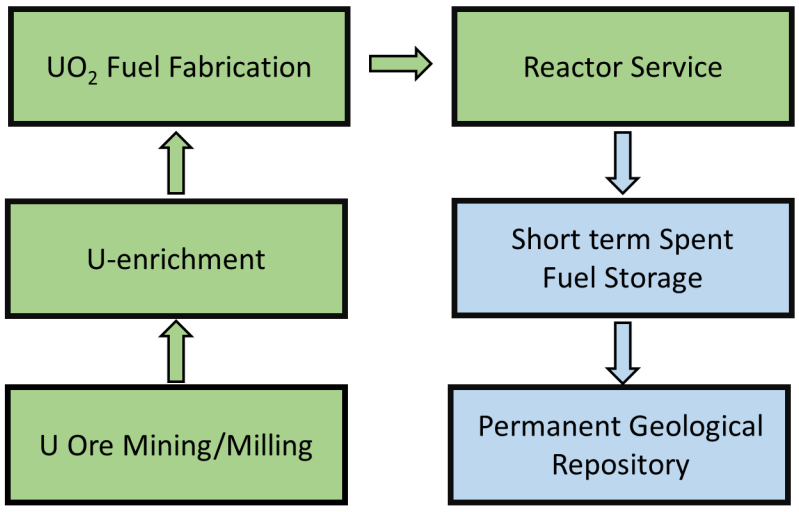

Figure 1.3: A schematic flow chart showing steps in an open nuclear fuel cycle. Steps which involve the use of un-irradiated are shown in green while gray boxes show steps which involve the disposal of spent fuel materials.

Additionally, open fuel cycles have the added benefit of being more resistant to nuclear arms proliferation as Pu and other weapons-grade fissile materials produced during irradiation in the nuclear reactor are not separated from the spent nuclear fuel [32, 36]. However, the once-through fuel cycle results in the disposal of usable fissile materials, and results in a significant strain on natural uranium resources [36]. Further, the amount of high-level waste that must be stored is larger in an open fuel cycle than in closed fuel cycles, and the time scales for which this waste must be securely stored are an order of magnitude larger than other closed cycle options [32, 37, 38].

The open fuel cycle starts with the extraction of uranium from the Earth's crust via mining activities [36, 38, 39]. Here, there are several options for how the uranium ore is extracted. The grade of the ore, i.e., the amount of uranium contained per mass of material mined, varies significantly and largely drives the selection of mining process. Additionally, uranium co-mineralizes with other mined resources such as rare-earth elements, and can be extracted simultaneously [10, 11, 39]. The prime example of this is uranium mining at the Olympic Mine in Australia, which is primarily a copper mine [39]. In Saskatchewan, the methods for the extraction of uranium ore are mainly open pit or underground (shaft) mining [18, 19, 39, 40]. Regardless of method, once the uranium ore is collected, it must be refined and purified to economic grade uranium ore through a milling process,

and a full discussion of these processes is presented in Section 1.4.2. The end result of these milling operations is the production of reduced yellow cake, which largely consists of U_3O_8 [11, 20].

The isotopic distribution of the U in the yellow cake is 0.73% U-235, which is the fissile isotope used to produce power [10, 11, 38]. Here, the fuel cycle diverges into two branches: one for LWRs and one for HWRs. In the latter case, no enrichment is required and the fuel is directly reduced to UO_2 [41]. For light water reactors, the U must be enriched to 3-10% U-235 before it can be used [38, 42]. Once the U is enriched, the U-238 fraction (also known as depleted uranium) is collected and sold for use in non-nuclear applications [43].

After enrichment, the UO_2 is formed into dense pellets, which are then encapsulated in a zircaloy sheath. Multiple fuel pellets are contained in the zircaloy sheath, which is referred to as the fuel cladding, and the encapsulated fuel pellet assemblies are called fuel rods or fuel elements [20, 42, 44, 45]. Multiple fuel rods are then assembled together, forming a fuel bundle, and these are loaded into the reactor chamber [45]. The reactor is then turned on and electricity is produced. In the case of LWRs, the reactor must be turned off when refuelling, while HWRs are designed for online refuelling. These limitations largely drive the amount of burn-up, or fission processes, the fuel undergoes before refuelling occurs.

The spent fuel assemblies are initially stored onsite in a storage pool after irradiation. The high heat load generated by the spent fuel requires active cooling which is provided by the storage pool, and the water also acts as an effective radiation shield [20, 46]. After a cooling period of at least one year, the spent fuel assemblies may be either reprocessed into separate waste forms or transferred for dry storage in concrete casks [11, 23, 41, 47]. In the former case, the fission products and actinide species are partitioned and incorporated into new waste forms for storage in a permanent geological repository [20, 37, 42]. For example, the actinides may be incorporated into a zirconia-based pyrochlore ceramic waste form capable of withstanding irradiation damage over a geological time scale [32, 34, 48, 49]. In the latter case, the concrete casks are meant for intermediate term storage (i.e., up to 50 years), and are usually stored on concrete pads in above ground facilities. The dry cask storage facilities are meant to be temporary storage while countries

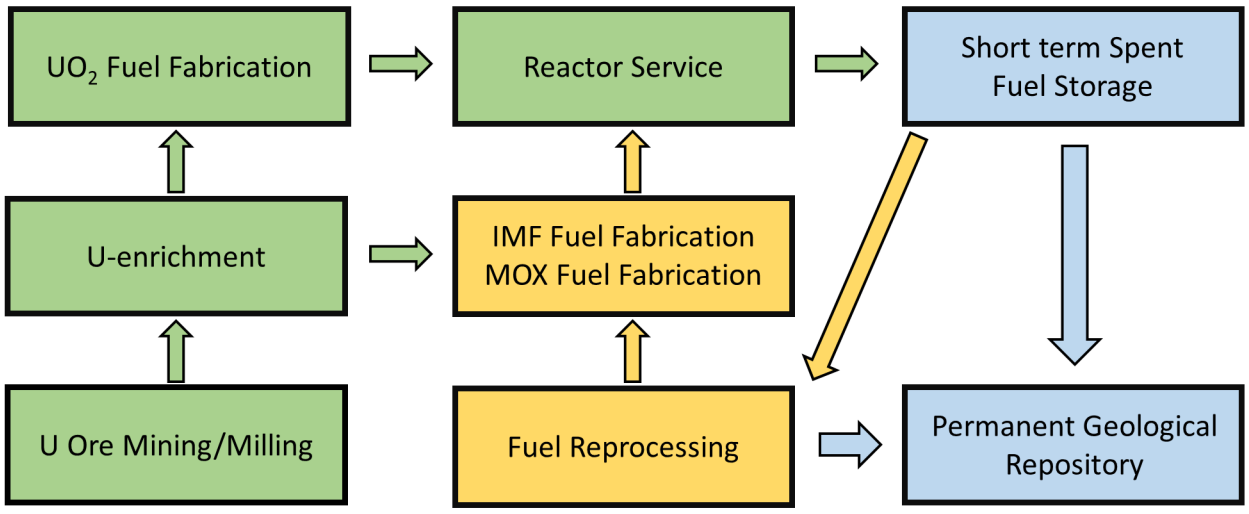

Figure 1.4: A schematic flow chart showing steps in a closed nuclear fuel cycle. Steps which involve the use of un-irradiated are shown in green, reprocessing steps are shown and yellow, and gray boxes show steps which involve the disposal of spent fuel materials.

begin to implement permanent geological repositories [11, 23, 41, 47]. A full discussion of these permanent geological repositories is presented in Section 1.6.2.

1.3.3 Closed Fuel Cycles

Contrary to the name, spent fuel still contains a large fraction of fissile isotopes, as refuelling schedules are largely driven by degradation of the fuel material properties rather than the depletion of fissile isotopes [50, 51]. In closed fuel cycles, such as the one presented in Figure 1.4, the spent fuel is reprocessed to collect the fissile isotopes still present in the fuel [20, 37, 38, 42]. Closed fuel cycles have the advantage of requiring less uranium mining and can reduce the amount of waste that must be stored in deep geologic repositories [20, 37, 38, 42]. However, closed fuel cycles also introduce a reprocessing step which could lead to the proliferation of nuclear weapons, and the spent fuel from closed fuel cycles also have more stringent storage requirements [45, 52].

Closed nuclear fuel cycles begin in the exact same fashion as open fuel cycles, with the extraction of uranium from the Earth's crust, followed by enrichment and fuel fabrication. The fuel is then irradiated in a reactor, and during irradiation in the reactor, U-238, which is a fertile isotope, can be transformed into Pu-239 as well as a number of other transuranic elements (TRUs; i.e., Np,

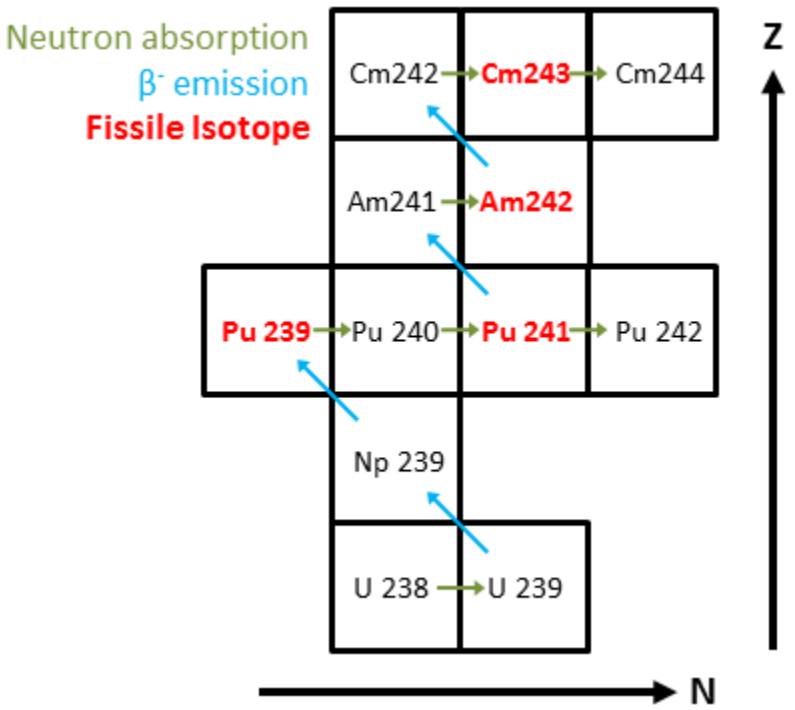

Figure 1.5: Pathways for the transformation of U-238 to various TRU isotopes are shown. Fissile isotopes are shown in red, while neutron capture is shown in gold and β-decay is shown in blue. Adapted from [53].

Pu, Am, Cm) via neutron capture followed by β-decay [53]. The pathways for the formation of these TRU species is outlined in Figure 1.5. (Note that these TRU species are produced in open fuel cycles as well.) After in-reactor service, the spent fuel must be stored in a fuel storage pool for several years to allow the fuel to cool and radioactivity to decay to safer levels before reprocessing. Despite this cooling off period, significant shielding measures must be used to safely work with the spent fuel. After this cooling period the fuel is then reprocessed, though the method of reprocessing, number of reprocessing steps, and the fissile elements extracted vary between proposed fuel cycles.

Closed fuel cycles are industrially mature, and France currently employs a plutonium mono-recycling scheme [38, 42]. In this scheme, the Pu generated in reactor is harvested from the spent UO_2 fuel using the solution-based Plutonium and Uranium Redox EXtraction (PUREX) process [38]. The PUREX process is described in Section 1.5.3 on page 26, along with another reprocessing technique known as pyroprocessing. In a Pu mono-recycling scheme, only the Pu

is collected, and the amount of Pu collected is highly controlled to sustain a constant Pu inventory in order to reduce proliferation risks [38, 42]. In France, the remaining fission products and minor actinide species are then incorporated into a borosilicate glass waste through a vitrification process [38]. In other proposed fuel cycles, these waste products could be partitioned and incorporated into separate ceramic waste forms [32, 34, 38, 54]. Regardless, the encapsulated waste is packaged and will eventually be stored in deep geologic repository facilities [38].

The harvested Pu is oxidized and mixed with U to form a solid-oxide solution, (Pu,U)O_2, which is also known as a mixed oxide (MOX) fuel [20,38]. The ratio of Pu to U can vary substantially, and is dependent on the reactor. Reactors are then refuelled with a mixture of MOX fuel assemblies and UO_2 fuel assemblies (the fuel rods only contain MOX or UO_2). After reactor service, the MOX fuel assemblies will eventually be sent for deep geologic disposal after an interim cooling period [38,42]. Further reprocessing of the MOX fuel rods present special challenges compared to UO_2 fuel rods, as they generate nearly four times as much heat as their UO_2 counterparts. Further, storage of the MOX fuel rods is also challenging, as there is also an increase in the amount of fission gases present inside the fuel rod, and internal fuel rod pressures can reach up to 40-60 bars at room temperature, with typical fuel rod temperatures being up to 400 °C [20, 38]. The increased fuel rod temperatures and internal pressures lead to increased embrittlement of the fuel rod cladding, which is undesirable as fuel rod cladding failures can lead to the release of radioactive elements [20, 38, 45]. This increases the difficulty of dry cask storage, and hampers further reprocessing of the fuel [20, 38].

Despite these challenges, fuel cycles in which the MOX fuels are recycled several times have been proposed [37, 55–58]. These strategies are greatly aided by the proposed use of so-called fast-reactors, in which fast neutrons are used to induce fission, as these reactors reduce the amount of Pu and other minor actinide species in the spent fuel [37,55,59–62]. Further, multiple recycling cycles can benefit from the partitioning and transmutation of TRU species in the spent fuel, which eliminates some of the hazards posed by the presence of TRU species. The TRUs can be used as fuel in both currently available LWRs as well as in fast-reactors, though the latter case is more

feasible and desirable as it leads to more efficient burn-up of these species [37, 55]. In the case of partitioning and transmutation, the TRU species can either be incorporated into MOX fuels or can be incorporated into a neutron transparent matrix, known as an inert matrix fuel (IMF). The material properties and developments of IMFs are further discussed in Section 1.5.4 on page 27. Though partitioning and transmutation of IMFs leads to higher upfront costs, it also reduces the volume of waste that must be stored [36]. Additionally, the time period for which it must be stored is reduced, as after about 265 years, the majority of the activity produced by spent fuel is due to the presence of TRU species (see Section 1.5.4) [63].

Ultimately, adoption of closed nuclear fuel cycles requires substantial investements by both utilities and governments. Significant technical and economic challenges must be overcome to implement efficient closed cycles. These include both the development of fast reactors and the development of materials for nuclear reactor components and fuels. Further, proliferation concerns continue to plague proposed closed fuel cycles, and this challenge must also be addressed. Significant research must be done to further the viability of these fuel cycles if they are to be widely implemented in the future.

1.4 The Origins of Nuclear Fuel: Mining and Milling Operations

The beginning of both the open and closed nuclear fuel cycles begins with the extraction of uranium from the Earth's crust. Originally, uranium was considered as an unwanted by-product during the mining of other minerals, and had minimal economic value. The main uses of uranium before the Second World War were as colorants in ceramic glazes and glasses. In Canada, the first uranium mine was Port Radium, which was initially opened as a radium mine. (Radium was used for glow-in-the-dark pigment applications, such as the markings on watch dial faces. [64]) Starting in 1942, the Port Radium site was extensively mined for its uranium resources, and played a large role in supplying the American and British defense forces as they developed the atomic bomb [39, 65].

Today, though the world's largest recoverable uranium reserves reside in Australia, Canada is the world's second leading uranium producer until 2009, and produced ∼10,771 tU in in 2014 (tU = tonnes U_3O_8) [10, 43, 66]. (The world's largest uranium ore producer is Kazakhstan [66].) Canada is host to the highest-grade uranium deposits in the world, specifically at the Cigar Lake site in Northern Saskatchewan [16, 67]. The extraction and refinement of uranium ore from this deposit, as well as other deposits found in Northern Saskatchewan will be the focus of this section, given their economic importance.

1.4.1 Uranium Minerals and their Occurence in Nature

Uranium is widely distributed throughout the Earth's crust, and is relatively abundant at an average concentration of 2.4 ppm [43]. This is more abundant than several more familiar elements such as silver, gold, mercury, and tin [43]. During the formation of igneous rock layers, uranium is initially present in magmas as U^{4+}. The low concentration of uranium and the large size of U^{4+} prevents it from being incorporated into silicates and other species formed as the magmas cool [43]. Therefore, the uranium is concentrated into the remaining hydrothermal solutions and pegmatites as the magmas solidify. The uranium then tends to crystallize as uraninite (UO_2), though the formation of coffinite, $U(SiO_4)_{1-x}(OH)_{4x}$, which is a tetragonal distortion of the zircon structure, is also possible [43, 68]. In both cases, uranium is predominately present as U^{4+} upon initial formation, though higher U valence states are also present to a small degree. However, U^{4+} is not stable under normal oxidizing conditions (i.e., when exposed to air or oxygenated groundwater), and readily oxidizes to U^{6+}. In the case of UO_2, a number of UO_{2+x} compounds can be formed, with x varying from 0 – 1, and this mixture of UO_{2+x} compounds is commonly referred as pitchblende or uraninite [16, 43, 68]. The oxidation of U^{4+} to U^{6+} in water can also result in the formation of uranyl ions, $(UO_2)^{2+}$. U^{4+} is sparingly soluble in aqueous solution under most conditions, while U^{6+} readily dissolves in aqueous solutions [43]. This coupled with the unique shape of the uranyl ions, which act as distinct units in crystal structures, leads to the formation of a number of secondary uranium-bearing minerals [43]. The large number of uranium-bearing minerals complicates the

discussion of secondary uranium minerals, as over 185 uranium-bearing minerals with over 300 names have been catalogued to date [39]. The complexity of the secondary mineralization prevents rigid categorization of uranium deposits, though some defining characteristics can be used to classify the various types of deposits that have been found.

The deposits found in the Athabasca Basin of Northern Saskatchewan, such as the Cigar Lake deposit, generally belong to a class of deposits known as the unconformity type [16, 43]. An unconformity is a region between two distinct rock layers in where a gap in the geologic record exists [69]. The Cigar Lake deposit is found between an upper metasediment layer (i.e., sandstone) and a lower unmetamorphized group, and the deposit appears to be the result of hydrothermal deposition processes [16]. This paragenesis[1] is similar to the paragensis of the uranium deposits at the Key Lake and McClean Lake sites [16]. The average depth of the Cigar Lake deposit is between 410 – 450 m underground, with very little surface expression, which necessitates underground mining operations [16]. This contrasts with the ore deposits found near the McClean Lake site in Northern Saskatchewan, in which the uranium was found near to the surface, allowing for open-pit mining. At an average grade of $>$20% U, the Cigar Lake deposit is the richest uranium deposit in the world, and it contains upwards of $\sim$150,000 tU [16].

At the Cigar Lake site, as well as many of the other Northern Saskatchewan sites, the uranium ore is hosted in sandstone. The ore is generally found in the form of uraninite, though coffinite is also found [16]. The coffinite is generally found on the outer edge of the deposit veins, and is younger than the uraninite minerals [16, 17]. In the Cigar Lake deposit, the main mineralization at the unconformity was formed during three major mineralization stages [16]. The first stage was associated with the formation of uraninite and Ni-Co and Fe-Co arsenides and sulpharsenides. During the second distinct mineralization stage, uraninite associated with Fe-Cu sulfides was formed, in addition to Ni-Co arsenides and sulpharsenides. Finally, in the third stage, Fe-oxides and hydroxides were mineralized, and coffinite was formed in the Fe-rich clays and minerals, replacing the outer layer of the uraninite deposit. In addition to these mineral phases, a number of clay

[1] Paragenesis, n.: the formation of minerals in contact in such a manner as to affect one another's development [70]

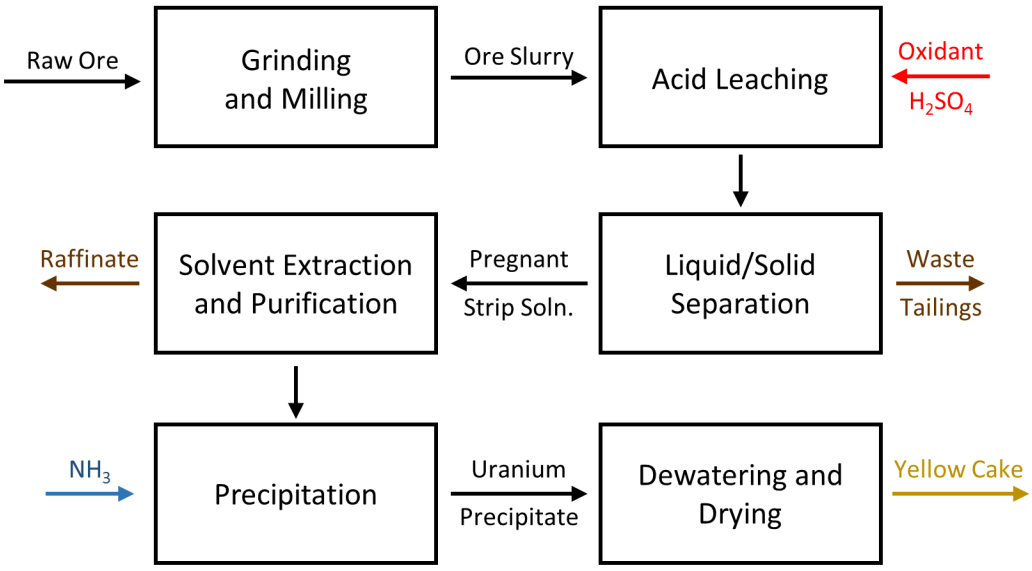

Figure 1.6: A flow diagram depicting the uranium ore milling process is shown. Adapted from [39].

phases, including illite, Fe-chlorite and Mg-chlorite are also found within the ore deposit [16]. The presence of these gangue minerals, along with the form of the uranium ore minerals, drives the decisions of which milling processes to use when refining the ore [39].

1.4.2 Mining, Milling, and Processing of Uranium Ore

Once the uranium ore is extracted from the ground, it must be milled and refined to produce a usable material. The exact milling processes vary between sites, but all milling processes include the comminution[2] of the ore, followed by leaching, purification, and precipitation of the uranium product [39]. The basic steps for an acid-leach method are outlined in Figure 1.6. An alkaline leaching process can also be used as an alternative to the acid leach process, but these are less common and the choice between methods is largely dependent on the nature of the ore body and its related gangue mineralogy. Currently, the acid leach process is the preferred process used at the Northern Saskatchewan milling sites [39].

The first step of the milling process is the comminution of the ore body to reduce the ore particles to a usable size. This crushing and grinding process serves two purposes: it liberates the

[2]Comminute, tran. v.: to reduce to minute particles [70]

uranium, increasing the surface area of the U-bearing phases, and allows for the formation of a slurry which allows for easier processing [39]. Originally, the ore was crushed using rod-mill/ball-mill set-ups. However, the high clay content of Northern Saskatchewan ores prevents the use of crushing mills as it readily clogs conventional mills [39]. In these cases, comminution is achieved by autonomous grinding or semi-autonomous grinding. After the initial grinding, a finishing grind is performed using either ball or pebble mills [39].

The ground ore is then processed into a slurry, and the uranium is solubilized using a leaching process. The leaching tanks can either be mechanically agitated or air-agitated Pachuca tanks. As was mentioned previously, the predominate U^{4+} minerals are not readily soluble, and the uranium must be oxidized to U^{6+}. This is done by adding Fe^{3+} to the slurry, which results in the following reaction:

$$U^{4+} + 2Fe^{3+} \rightarrow U^{6+} + 2Fe^{2+} \tag{1.3}$$

The Fe^{2+} must be re-oxidized, and this is done by adding an oxidant to the reaction mixture [39]. In Northern Saskatchewan, hydrodgen peroxide or Caro's Acid (H_2O_2/H_2SO_4) is typically used, as the ores have relatively high oxidation requirements due to the presence of Ni and As in the ore [39]. After leaching, the depleted solids must be removed from the pregnant strip solution. Counter-current decantation is often used to provide an initial separation, though horizontal vacuum belt filters can also be used. The final clarification of the solution is proved by either reactor clarifiers or pressure sand filters.

The resulting clarified solution is referred to as the pregnant strip solution, and the U^{6+} must be selectively extracted from this solution. This can be done using either solvent exchange or ionic exchange methods. Ionic exchange is more common at mills where the grade of the ore processed is low while solvent exchange extractions are more common when processing high-grade ores [39]. As such, mills in Northern Saskatchewan typically use a solvent exchange method. In this method, primary long-chain amines dissolved in an organic solvent are used to complex the U^{6+} ions in pregnant strip solution, resulting in the transfer of U^{6+} into the organic solvent [39]. The organic

solution is then separated from the waste aqueous solution, and the U^{6+} is then stripped back into an aqueous phase, resulting in a purified solution.

After purification, the uranium is then precipitated from solution. Several precipitating agents, such as H_2O_2, caustic soda, and magnesia can be used to precipitate the U, though the most common precipitant is NH_3 [39]. Once precipitated, the solid uranium material is then washed with water to remove soluble impurities, and then dried. The drying method also depends on the mill, and can either be performed in direct fire furnaces at 700 °C or it in can dried in indirectly heated dryers [39]. This drying process can also double as a calcination step, removing volatile counter ions resulting the formation of a uranium oxide [39]. This final product is usually U_3O_8, which is commonly referred to as yellow cake. The yellow cake is the final product that is shipped to enrichment facilities for processing into nuclear fuel.

1.4.3 The JEB Tailings Management Facility

The uranium mining process inherently produces large quantities of waste given the generally low grades of the ore. For example, producing 1 t of uranium from a 5% grade ore would produce 19 t of waste. This waste contains toxic elements which must be isolated from the biosphere. These elements of concern are co-mineralized in the uranium ore, and include Ni, As, Mo, U, Fe, Se, and Ra [40]. The elements of concern are liberated into mobile phases during the milling process. It is therefore imperative that the waste streams are dealt with appropriately in order to minimize the environmental impact of the mining activities.

At AREVA Resources Canada's McClean Lake milling facility, located in Northern Saskatchewan, the mine tailings are disposed of in the JEB Tailings Management Facility (TMF). However, before being placed in the TMF the tailings and raffinate (i.e., aqueous waste) produced during the milling process are subjected to additional treatment before being placed in the TMF. An outline of the treatment process is presented in Figure 1.7. The treatment consists of a stepped neutralization of the tailings slurry up to a slightly basic pH of 7.5 through the addition of lime (CaO) [40]. The main objective of these treatments is to neutralize and immobilize the As that

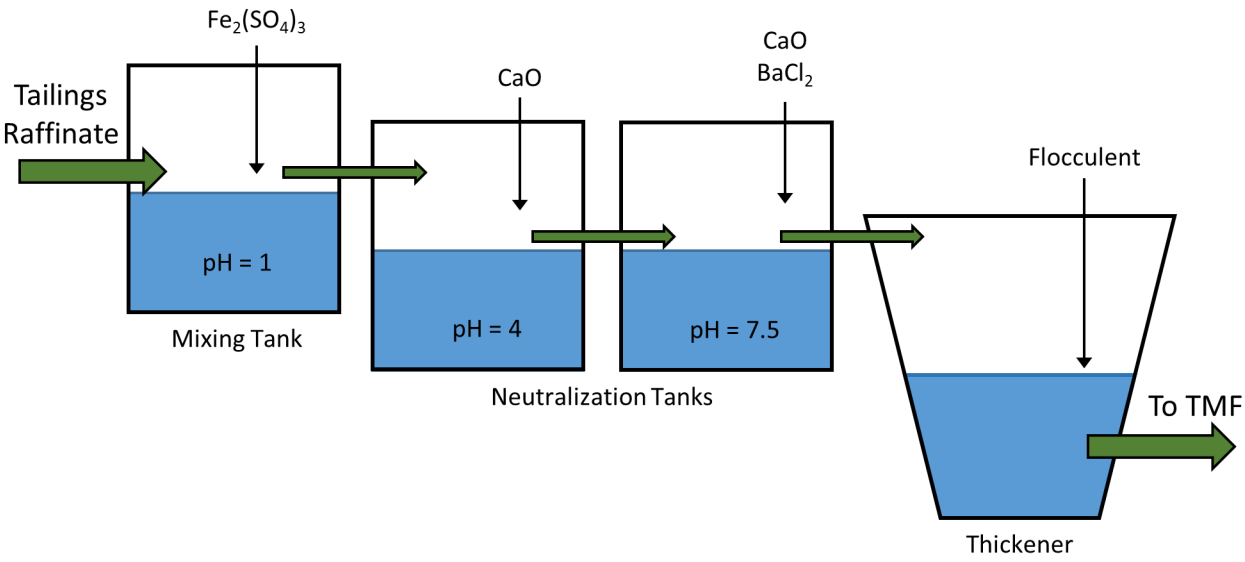

Figure 1.7: The tailings and raffinate treatment process used at the McClean Lake facility operated by AREVA Resources Canada is depicted. In this process, the pH of the waste is gradually increased to 7.5, and $Fe_2(SO_4)_3$ is added, which forms Fe-complexes with free arsenic present in the waste. Mo is also complexed by the $Fe_2(SO_4)_3$, resulting in the formation of ferrimolybdite and molybdate absorbed on ferrihydrite. Figure adapted from [40].

is present in the waste stream through the formation of insoluble, As-bearing secondary minerals in the TMF. This process is also effective in controlling the release of several other elements of concern, such as Ni, Mo, and U [71–74]. However, the chemistry that occurs within the treatment tanks is not necessarily the final chemistry that will be present in the TMF over long periods of time, as the conditions in the TMF are subject to change and the equilibrium reactions that take place are slow relative to typical laboratory time scales (on the order of decades or more).

Controlling this chemistry is one of the central means by which the JEB TMF is able to contain these elements of concern for up to 10,000 a. The JEB TMF, which is schematically depicted in Figure 1.8, is constructed from a depleted open pit mine, and uses both active and passive geochemical and geotechnical engineering controls. The main active control used at the JEB TMF is a ring of dewatering wells, which lowers the level of the water table around the TMF to ensure that all surrounding ground water will flow into the TMF, preventing the release of contaminates into nearby water bodies [40]. Additionally, tailings are deposited using a placement barge which is located at the center of the TMF. This ensures that the tailings become settled, which reduces

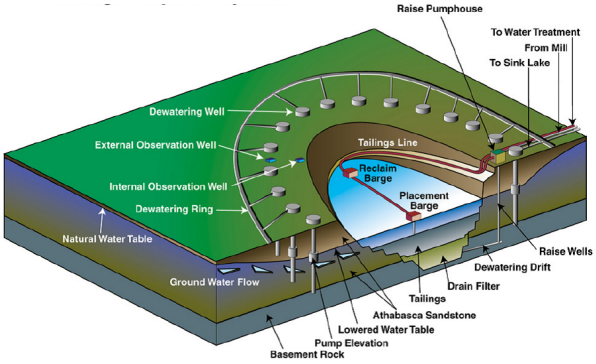

Figure 1.8: A schematic of the JEB TMF is presented. A ring of dewatering wells lowers the water table around the TMF so that all groundwater flows into the TMF resevoir. The placement barge is used to deposit the tailings waste at the center of the TMF, which results in a settled tailings bed. Figure is provided courtesy of AREVA Resources Canada [40].

the water flow through the tailings body. Because of the high clay mineral content of the tailings, water flow is reduced relative to the surrounding sandstone by up to two orders of magnitude [40]. This passive control serves to trap the pore water within the tailings, which retards the migration of elements of concern into the surrounding environment. The settled nature of the tailings samples also serves to act as convenient dating mechanism, as materials found closer to the bottom of the TMF will be older than the materials found near the surface [40].

The chemistry of the tailings also serves to immobilize elements of concern by trapping them in insoluble phases. However, the chemistry that occurs is complicated, given the complex nature of the tailings, and it is therefore necessary to experimentally confirm that the projected chemistry is actually taking place. While a significant body of work has already been generated to understand the chemistry of As and Ni in the JEB TMF, very little work has been done to determine the speciation of Mo in the JEB TMF [71–74]. Ferrimolybdite ($Fe_2(MoO_4)_3$) and molybdate adsorbed on ferrihydrite ($Fe(OH)_3$-MoO_4) are the primary phases initially present in the treated tailings samples [75]. However, these species are not expected to be stable under the TMF conditions, and instead, given the high Ca^{2+} content of the treated tailings, it is expected that powellite ($CaMoO_4$) will be formed in the TMF [75]. Since powellite is insoluble in water, this will be the primary Mo sink, and it is expected that the formation of powellite will ultimately control the Mo pore water concentrations within the TMF [75]. However, until recently, an experimental confirmation of the

presence of powellite within the TMF had not been achieved. This is the subject of Chapter 2, which presents work done to develop a method to detect powellite, and other Mo-bearing species, in the JEB TMF using X-ray absorption spectroscopy.

1.5 Nuclear Fuel Fabrication and Chemistry

After the uranium is extracted and refined it must be converted into a nuclear fuel material. Nuclear fuels are unique from other fuels in that the energy comes from atomic nuclei, rather than chemical bonds. In this regard, the fuel material is not totally destroyed when the energy is extracted, and the material properties of the fuel both before and after irradiation must be considered. Additionally, nuclear fuel is considered the first layer of containment to prevent the release of radioactive nuclides. Therefore, nuclear fuels must have unique material properties that allow them to withstand exposure to extremely high radiation fields, large temperature gradients, and large variations in composition without changing structure significantly. These requirements, in addition to the challenges associated with safely manufacturing fuel pellets and possible reprocessing considerations, make the design and manufacture of nuclear fuel particularly challenging.

1.5.1 Fuel Material Requirements

The single most important characteristic of a nuclear fuel material is its thermal conductivity. The thermal conductivity determines how well the fuel will be able to transfer the heat generated by the fission processes into the cooling systems [76–78]. This heat transfer is used to generate the steam, which is ultimately used to produce electricity. The thermal conductivity of the fuel also affects the fuel pellet temperature, and temperatures above the fuel melting point could arise if the material does not have a sufficiently high thermal conductivity. In general, the fuel pellets are subjected to a thermal gradient along the radial direction of the pellet, with centerline temperatures reaching upwards of 1300 °C and pellet surfaces reaching temperatures of $\sim$300 °C [76–79]. (A small axial temperature gradient is also present, but this is limited by the stacking of the pellets within the fuel

rod [79].)

In addition to having a high thermal conductivity, the nuclear fuel material must be resistant to radiation damage and must be able to incorporate a large number of fission products. Today's nuclear fuels are generally crystalline, solid-state materials, and it is imperative that the crystal structure be maintained during irradiation [51]. Changes in the crystal structure of the fuel material are detrimental for several reasons, most crucial of which is that changes in crystal structure are accompanied by changes in thermal conductivity. These changes can lead to increased fuel temperatures, which can result in centerline fuel melting [76–79]. Secondly, changes in the material crystal structure are often accompanied by changes in the volume of the material [45, 80]. In most LWRs and HWRs, the fuel is enclosed in a zircaloy sheath, and the gap between the sheath and the fuel pellet is very small [45,80]. Expansions in the volume of the fuel pellet result in added pressure against this fuel cladding, which can result in fuel cladding failures (i.e., breaches in the fuel cladding). To a certain extent, these negative effects due to crystal structure changes during irradiation are unavoidable. However, by engineering the nuclear fuel materials to be resistant to these changes, the in-reactor lifetime of the fuel can be extended, reducing the amount of downtime required to refuel the reactor.

Finally, the fuel materials must be resistant to corrosion, especially in the event of a fuel cladding failure event. During a fuel cladding failure, the fuel is exposed to the primary coolant, and the U^{4+} in the fuel can be oxidized to U^{6+} [44, 81]. This is undesirable because, unlike U^{4+}, U^{6+} is soluble in aqueous solution and dissolution of the fuel material will lead to release of fission products into the primary coolant system [45]. Fuel cladding failures are generally uncommon, and are not as much of a safety concern as they are an economic concern [45]. The release of fission products into the primary cooling system necessitates the need for expensive decontamination and replacement of the failed fuel assembly [45]. To prevent these economic losses, it is therefore of value to engineer the fuel material to be resistant to oxidation upon exposure to steam. Further, engineering the materials to be resistant to corrosion upon exposure to water can also have the added benefit of making the fuels appropriate for disposal in deep geological repositories without

further processing (see Section 1.6.2). The material requirements for nuclear fuels are extensive, and the properties outlined here are not complete, but serve to paint a general picture of the material challenges faced when producing new nuclear fuel materials.

1.5.2 Current UO_2 Fuel Fabrication Process

Currently, most reactors in operation use UO_2 as the primary nuclear fuel material. The UO_2 fuel fabrication processes are well known, and the fuel production capacity exceeds demand [20]. These conditions have forced vendors to optimize their fuel production processes, which has resulted in lower production costs [20]. For fuels used in LWRs, the fuel process begins with the enrichment of U-235 in yellow cake uranium [31]. This is done by converting the yellow cake (U_3O_8) into UF_6. UF_6 is highly volatile, which allows for the partial separation of $^{235}UF_6$ and $^{238}UF_6$. This is usually done by either gas diffusion or by gas centrifugation [10, 31, 39]. Gas diffusion operations are usually more antiquated and expensive to operate, and new enrichment facilities generally opt for gas centrifuge methods [10]. HWRs do not require U-enrichment, and can run using naturally abundant uranium [41].

Once the uranium is enriched, the UF_6 must be converted into UO_2 and processed into a fuel pellet. (In the case of fuel for HWR, this step is not necessary.) The general fuel pellet production process is outlined in Figure 1.9. The first step of the fuel production process is the conversion of the UF_6 into UO_2 powder. This is usually done using one of three methods, two of which are solvent based while the third is a dry process. The solvent methods are named based on the intermediate uranium precipitate that is formed, either ammonium diuraniate (ADU) or ammonium uranyl carbonate (AUC) [31]. The AUC method is the more widely implemented method, and is predominately used in Europe [31]. The AUC method is advantageous because the UO_2 particles made using this method are free-flowing and do not require further processing [31]. The dry method, which uses a rotating kiln furnace to transform the UF_6 into UO_2, is more popular in North America [31]. The dry method is advantageous because it is relatively simple and does not generate any liquid waste. However, the UO_2 particles produced are very fine, and the material

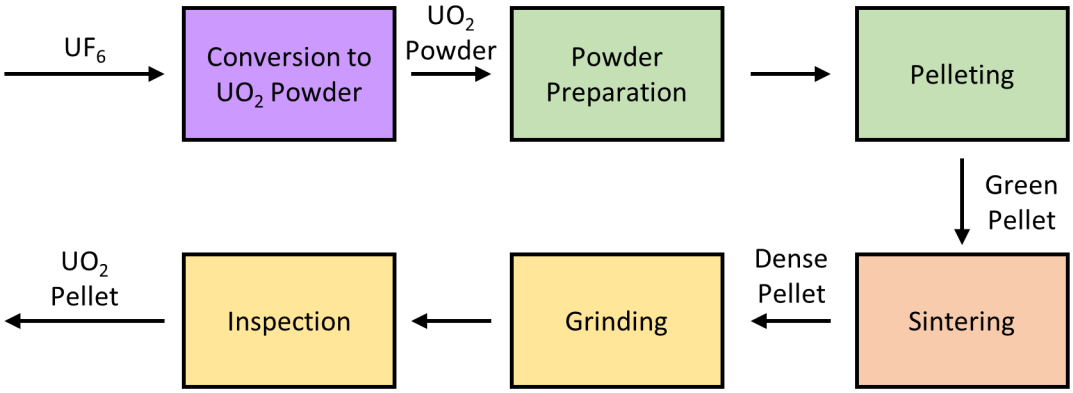

Figure 1.9: Steps in the UO_2 fuel pellet production are shown. UF_6 is converted to UO_2, and the UO_2 is formed into a free flowing powder. The powder is pressed into a pellet, and the pellet is sintered at high temperature, followed by grinding and inspection. Adapted from [31].

must be pre-pressed into bricks, crushed, and sieved to produce a free-flowing powder.

After the UO_2 powder has been synthesized, it must be prepared for the pelletization process. Binding agents, lubricants, and small amounts of $MgCl_2$, Al_2O_3, Cr_2O_3, Nb_2O_5, SiO_2, and/or TiO_2 may be added to the UO_2 mixture to enhance the quality of the pellet and control the UO_2 grain size [31]. Once the final powder has been prepared, it is then pressed into pellets. These "green" pellets are usually pressed using dies which result in the pellets having either chamfered edges or dished ends [31]. This shaping is added to accommodate for the thermal expansion of the pellets during in-reactor service [31,45]. The green pellets are then sintered under a hydrogen atmosphere, and the sintering process may also include an initial dewaxing step to remove the binding agents and lubricants that were added to the UO_2 powder. After sintering, the pellets have a density that is 95-97% of the theoretical density [31]. The sintered pellets have a slight hour-glass shape, due to the uneven distribution of pressure during the pellet pressing process. This deformity is corrected after sintering by grinding the pellets to a uniform cylindrical shape. After grinding, the pellets are inspected, and are then ready for assembly into nuclear fuel elements.

1.5.3 Fuel Reprocessing

Nuclear reactor re-fuelling schedules are largely driven by the fuel material properties, and not by a lack of fissile elements. In addition, some of the U-238 initially present in the reactor will be transmuted to Pu-239, which is a fissile element [53]. Therefore, the spent nuclear fuel represents a vast inventory of fissile nuclides, and in closed fuel cycles these nuclides are harvested from the fuel. While there are several reasons to incorporate this reprocessing step into the fuel cycle, the most interesting advantage, with regards to the research presented in this thesis, is that reprocessing and transmuting the transuranic elements in the fuel can reduce the heat load and decay period of spent nuclear fuel, making it easier to dispose of spent fuel materials [37, 55, 62]. To date, there are two main routes by which fuels can be reprocessed: the PUREX process and electrochemical pyroprocessing [20, 31, 38, 45].

The PUREX process is a solvent-based method which is used to separate the U and Pu from the fission products and minor actinide species in the spent nuclear fuel (SNF). Over time, PUREX has come to denote a series of different separation processes, though the general basis of these processes is similar [82–84]. Several factors, such as the chelating agent, loadings, and oxidation and reduction agents can vary depending on the reprocessing facility [82] . The PUREX process involves the collection of Pu and proliferation concerns are somewhat inherent to the process, though PUREX processes can be modified to limit the risk of proliferation [82]. In all cases, the process starts by decladding the fuel and dissolving it in a 6 M HNO_3 solution, followed by oxidation of Pu^{3+} to Pu^{4+}. The U^{6+} and Pu^{4+} in solution are then selectively extracted into an organic solution using tri-butyl phosphate (TBP) [82–84]. The TBP selectively binds to Pu^{4+} and U^{6+}, but does not bind to Pu^{3+} [84]. This provides the basis for the separation of the U and Pu, and the Pu^{4+} is reduced to Pu^{3+} to separate the Pu from the U [84]. After the U and Pu are separated, the Pu is then precipitated from solution and calcined to form PuO_2, which can be used to make MOX fuels. Transuranic species can also be collected from the initially stripped aqueous solution using several other solution stripping steps, and these processes are collectively known as the TRUEX process [82]. However, a full discussion of TRUEX is beyond the scope of this thesis.

In contrast to the PUREX process, the pyroprocessing option is based on the use of electrochemical methods to separate the actinides and fission products in the SNF. The process again starts by decladding the fuel, and the fuel is then placed in a cathode basket in a LiCl melt with added Li_2O [85–87]. The metal oxide fuel is reduced to metals, and the fission products are released and incorporated into the LiCl melt as metal chloride salts [85–87]. The mixed metal products, which contain both the U, Pu, and other TRU species are then transferred to a second electrorefining cell, which consists of a anode basket containing the metallic U and TRU species, and two separate cathodes, one being liquid Cd and the other being a solid cathode [85–87]. Metallic U is formed at the solid cathode while the TRU products are collected at the liquid Cd cathode. Pyroprocessing has the advantage of having relatively few reactants which will not degrade upon exposure to radiation, and this consideration is especially beneficial when considering the reprocessing of spent MOX fuels, which are hotter and more active than spent UO_2 fuels. Further, because the TRU species are not explicitly separated from the Pu, the proliferation risk is reduced. However, pyroprocessing is generally most advantageous when considering fuel cycles which use metallic fuel, and has relatively limited value when considering metal-oxide fuels as the Pu is not directly separated from the other TRU species [85–87]. Additionally, pyroprocessing systems are bulky, which is undesirable as fuel reprocessing activities must occur in hot cells. In general, both reprocessing options have merits and drawbacks, and the adoption of either method is largely dependent on the fuel cycle to be adopted.

1.5.4 Inert Matrix Fuels

The major advantage of a closed fuel cycle is that it reduces or eliminates the inventory of TRUs that must be stored in deep geological repositories. Reducing the amount of TRU species that must be stored has two major advantages: first, it reduces the heat load of SNF, which increases the capacity of deep geological repositories; and second, it significantly reduces the period of time for which the SNF must be stored [37, 52, 57, 63]. The second point is illustrated by Figure 1.10, which depicts the relative radiotoxicity of the SNF individual components as a function of time.

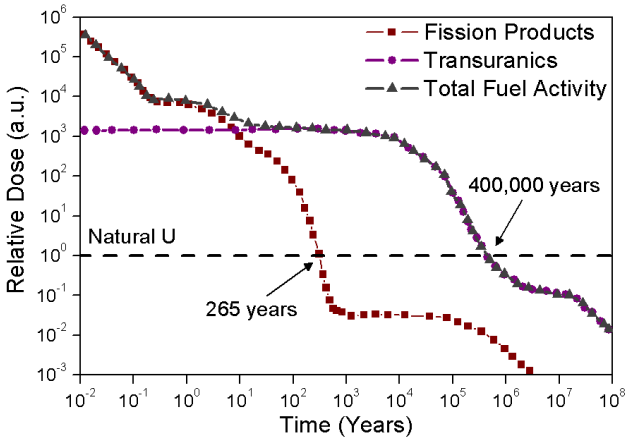

Figure 1.10: The radiotoxicity of the various components in used CANDU fuel are plotted as a function of time. The activity of the fission products rapidly decays after 100 a, and the activity from the fission products is equivalent to the activity of natural uranium after about 265 years. After 265 years, the TRU species are largely responsible for the remaining activity of the spent nuclear fuel. Adapted from [63].

The activity of the fission products diminishes significantly after 265 years, and the remaining radiotoxicity of the SNF is attributable to the slowly decaying TRU elements [37,63]. It is therefore the presence of TRUs that drives the length of the SNF storage time required, and having a means to eliminate TRU species would strengthen the case for increased implantation of nuclear energy.

The use of inert matrix fuels (IMF) has been proposed to "burn-up" (transmute) TRU species using both currently available commercial pressurized-water reactors (PWR) and future Generation IV fast breeder reactors (FBRs) [60, 61, 88–90]. IMFs consist of actinides embedded in a neutron transparent (inert) matrix, and unlike MOX fuels which contain U-238, IMFs allow for TRU burn-up without breeding Pu in the process [60]. The higher burn-up efficiency of IMF materials means that a smaller IMF loading is required in the reactor core, and makes IMFs economically comparable to MOX fuels. In addition, IMFs may be designed to act as a geological storage matrix (see Section 1.6.2), which eliminates expensive post-service reprocessing [59–61, 89, 91, 92].

In order for a material to be considered for use in IMF applications, the material should exhibit favourable neutronic properties, compatibility with the reactor coolant, the ability to withstand high radiation doses, high thermal conductivity, and the ability to incorporate burnable poisons such as Gd and Er [60]. Cubic zirconia (ZrO_2), adopting the fluorite-type structure, shown in Figure 1.11,

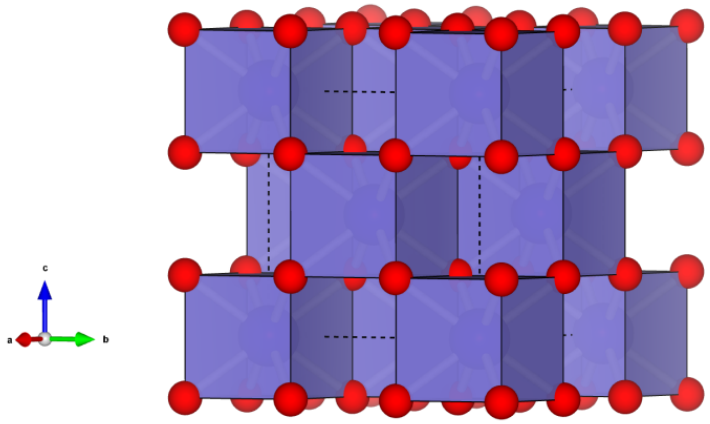

Figure 1.11: The fluorite structure of cubic zirconia is shown. Zr, Y, and Nd are randomly distributed in one 8-fold coordination site (blue cubes), and the O (red-spheres) adopts a 4-fold coordination environment in this structure. All atoms occupy special positions. [93, 94]

is a material that has been shown to retain its mechanical and chemical stability under extreme temperature and irradiation conditions. As such, this material has been studied extensively for use in IMF applications [54, 89, 93–101]. However, pure cubic zirconia is only stable at temperatures above 2370 °C, adopting a tetragonal structure at temperatures between 1170 °C-2370 °C and a monoclinic structure at temperatures below 1170 °C [54, 102, 103]. These structures are highly related, and the tetragonal and monoclinic structures may be considered as distortions of the parent cubic structure [103]. It is well known that the cubic structure can be stabilized by doping the material with aliovalent cations such as Ca^{2+}, Y^{3+}, or Sc^{3+} [60, 104–108]. The size difference between Zr and the doped cation in addition to O-vacancies generated due to charge-balancing requirements act to stabilize the cubic structure across a range of temperatures [109, 110]. Yttria-stabilized zirconia (YSZ) has been extensively studied for use in IMF applications, likely due to the extensive knowledge base generated on YSZ from its use and study as a structural ceramic in the nuclear industry [111, 112]. Additionally, YSZ has been widely studied as a solid-oxide fuel cell material and a thermal barrier coating [113–115]. However, relatively little research has been performed to understand how the addition of actinide elements to the YSZ system will affect the thermal stability of these materials.

The extremely complex reactions and changes in composition that occur within a nuclear fuel

during service make it necessary to understand how the structure of actinide-doped YSZ materials will change when they are subjected to a wide range of temperatures over a range of actinide doping levels. A phase change from a cubic structure to a lower symmetry structure will result in a decrease in the thermal conductivity, and the transition to a monoclinic structure is accompanied by a 3-5% increase in volume [102, 116–119]. Additionally, it has been previously shown that the properties of tetragonal ZrO_2 such as its mechanical stability deteriorate drastically when exposed to water at 300 °C - 400 °C [102]. These changes could lead to unsafe reactor operation, and given the need to control and reduce the risks associated with nuclear power, it is necessary to thoroughly characterize these materials to obtain an understanding of the fundamental properties of actinide-doped YSZ materials before it can be used in commercial service. This is the focus of Chapters 3 and 4, which present investigations of changes in the local and long-range structures of Nd-doped YSZ materials when they are exposed to varying temperatures. (Nd was used as a surrogate for Am^{3+} [104, 120–122].)

While Y-doped ZrO_2 materials have been extensively studied for use as an IMF material, the materials have a low thermal conductivity which leads to undesirably high fuel pellet temperatures [88, 96, 98, 116, 123]. The thermal conductivity of the doped ZrO_2 materials could be increased if a lighter dopant element was used, as thermal conductivity increases as the molar mass of the material decreases [124]. To this end, it is worth exploring a number of other stabilized zirconia materials, which use elements such as Sc to stabilize the fluorite structure. Sc-doped ZrO_2 materials have been studied for use in solid-oxide fuel cells (SOFC) due to their high oxygen conductivity. However, these materials have been shown to not be stable at SOFC operating temperatures, as the fluorite structure degrades. Studies have shown that the addition of a small amount ($\sim$1 wt%) of rare-earth element can enhance the stability of the fluorite structure at SOFC operating temperatures [107, 125–127]. Despite the interest in Sc-doped ZrO_2 materials as SOFC materials, very little research has been done to understand how the addition of significant amounts ($>$ 1 wt%) of an actinide will affect the structure of these materials, and the characterization of a series of Nd-doped Sc-stabilized ZrO_2 materials are the subject of Chapter 5. The local and long-

range structures of $Nd_xSc_yZr_{1-x-y}O_{2-\delta}$ materials and the changes in these structures upon exposure to various temperatures are explored in this chapter.

1.6 Disposal and Storage of Spent Nuclear Fuel

The final disposal of the radioactive waste produced from the production of power by nuclear energy is perhaps the most vexing and difficult challenge that prevents further deployment of this technology. The spent nuclear fuel will be radioactive for tens of thousands of years, a time scale which goes beyond the total age of civilized humanity. Many technological advances made to store these materials for these time scales, and strong strategies which involve deep geological storage for the control of these waste materials have been developed. However, it is also important to acknowledge that a number of social challenges have also arisen, and that these social issues are just as, if not more, important than the technological challenges.

1.6.1 Classification of Nuclear Waste

Many different types of waste are produced during the nuclear fuel cycle. In general, waste can be divided into three major categories: high level waste (HLW), intermediate level waste (ILW), and low level waste (LLW) [58]. Each waste stream presents a different level of hazard, and these wastes must be dealt with as appropriate for their hazard level. HLW is usually considered to entail the radioactive nuclides produced during irradiation in a reactor, and largely consists of SNF [35,52,58,128]. HLW also entails the waste products from the reprocessing of SNF to recover usable U and Pu (see Section 1.5.3) [58]. Additionally, HLW can also include the actinide species generated during the production and dismantlement of nuclear weapons [58, 129]. While it only represents a small portion of the total volume of nuclear waste produced, HLW represents >95% of the radioactivity of the nuclear waste streams [58]. Additionally, the radioactivity from HLW is usually long-lived due to the presence of significant amounts of transuranic species in the SNF (Figure 1.10). Therefore HLW requires special storage and disposal, and the disposal of HLW is

discussed in detail in Section 1.6.2.

In contrast to HLW, ILW is more nebulously defined, but can be characterized as having activities high enough that workers must be shielded from the waste. ILW represents $\sim$7% of the total waste nuclear waste stream and accounts for $\sim$4% of the total radioactivity of nuclear waste [58]. Examples of ILW include irradiated reactor components, reactor cooling circuit sludge, and medical isotopes [58]. ILW can be further divided into two sub-categories: short-lived ILW and long-lived ILW. Short-lived ILW decays quickly, and can usually be handled using the "delay to decay" principle, in which permanent disposal of the waste only occurs after a pre-determined cooling period [58]. For long-lived ILW, a "concentrate and contain" strategy is used, in which the waste is compacted and stored in sub-surface repositories, which consist of caverns excavated at depths in the tens of meters [58]. Long-lived ILW can also be disposed of in deep geological repositories used for the containment of HLW. Ultimately, the means of ILW disposal is dependent on each country's individual disposal strategy and the nature of the waste.

LLW consists of materials that may have been contaminated by contact with radioactive material or exposure to radiation [58]. Examples of LLW are personal protective equipment and clothing, paper, rags, and tools used in a contaminated zone [58]. Given the large volume of LLW, there are several subcategories of LLW, with each subcategory having different disposal requirements. In general, most LLW waste can be stored at surface sites in trenches that have been lined to prevent ground-water leakage. The waste is usually compacted to reduce its volume, and can also be sealed in secondary containers. Additionally, some LLWs can also be incinerated if the activity levels are low enough. Even though LLW represents the largest volume of the nuclear waste streams (90%), it only accounts for $\sim$1% of the total nuclear waste radioactivity and the disposal of this waste is generally similar to the disposal of other industrial waste streams [58].

1.6.2 Storage of Spent Nuclear Fuel

The disposal of HLW and SNF is probably the biggest challenge facing the nuclear industry. Disposal facilities must be able to contain the SNF materials and ensure that they are not released into

the environment for tens of thousands of years . There is a strong global consensus that geological sequestration of the SNF in deep geological repositories is the only means to ensure that SNF will remain separated from the biosphere over these periods of time [21]. Deep geological repositories operate on the principle that the geology of the facility is relatively stable, with little groundwater creep [21, 23, 24, 69]. In addition, the deep depths of these facilities (often greater than 700 m below ground) ensure that the groundwater surrounding these repositories is separated from aquifers and other clear water sources [21, 23, 24, 69]. In general, deep geological repositories have been slow to open, largely due to the social issues and stigma associated with these facilities.

The main strategy used in the geological sequestration is a depth of defense approach [57, 130]. In this approach the SNF materials are contained via multiple layers of defense. The first, and most important means of containment, is the SNF material itself [131–133]. Depending on the fuel cycle and disposal strategy, the form of the SNF can vary widely. In Canada, where an open fuel cycle is preferred, direct disposal of the SNF fuel material is the method currently being considered, given that CANDU reactors use naturally abundant uranium for fuel [134]. In this case, the fuel assemblies are stored in a copper-plated steel casks, and these casks are then directly stored in the repository [134]. For countries that choose to adopt a closed fuel cycle, such as France, HLW comes in several forms. In France, spent MOX fuels, along with waste generated from the reprocessing of fuels must be stored [38]. The HLW from fuel reprocessing is encapsulated in borosilicate glass in a process known as vitrification [33, 38, 135]. Vitrified waste forms have been shown to be relatively resistant to radiation damage, though low loadings of the glass and the precipitation of Mo from the glass matrix remain challenging issues [136, 137]. The vitrified HLW and spent MOX fuel are deposited in the repository for final disposal.

Partitioning of HLW has been proposed as an alternative to vitrification, with the fission products and minor actinide species being incorporated into separate ceramic materials specifically designed to contain different groups of elements [32, 34, 38, 58]. A number of materials have been proposed, but the most common are zirconia-based pyrochlore and defect fluorite ceramics, similar to the IMF materials discussed in Section 1.5.4 [32, 34, 48, 49, 54, 138–141]. These ce-

ramic materials can incorporate higher TRU loadings, reducing the volume of waste that must be stored [32, 34, 48, 49, 54, 138–141]. Further, these ceramics can better contain certain fission products such as I and Mo, which are relatively unstable in the vitrified waste form [38]. Partitioning strategies are particularly effective in fuel cycles which include multiple fuel reprocessing steps, as the expensive partitioning processes are already included in the fuel cycle. The research regarding new ceramic materials as nuclear waste forms is prolific, and this field of study continues to grow [32, 34, 48, 49, 54, 138–141]. In addition to research regarding the waste form materials, further materials research into the waste containers and their interactions with the environment are also on-going. Given the challenge of modelling waste behaviour over tens of thousands of years, an extremely precise knowledge of the materials involved is required, and this is a very active field of research.

1.7 Thesis Objectives

The research presented in the thesis is aimed at meeting the need to further develop technologies and materials for the nuclear fuel cycle. The licensing process for materials related to the nuclear fuel cycle is intense, and requires a detailed understanding of the all of the materials relevant properties, both through modelling and experiment. It is therefore imperative to understand how the materials behave at an atomic scale, in addition to intermediate- and long-range scales. The main goal of the research in this thesis is to provide a fundamental understanding of materials related to the nuclear fuel cycle at both atomic level and at long-range ordering levels. Here, X-ray absorption spectroscopy (XAS), along with a number of other techniques, has been used to investigate a number of materials associated with the nuclear fuel cycle. The use of XAS techniques was necessary because they provide an understanding of the material properties on an atomic level. XAS provides a means to understand the local chemical and structural environments around individual metal centres [142]. Further, XAS techniques are chemically sensitive, and they can be used to speciate metals in chemically complex matrices [142]. The combination of XAS tech-

niques at various metal absorption edges, along with techniques which probe long-range structures and ordering, such as powder XRD and SEM, allowed for a comprehensive understanding of the structural properties of a material. This comprehensive approach is important, as it is required for modelling the behaviour of materials over very long periods of time.

Materials associated with the beginning of the nuclear fuel cycle are investigated in Chapter 2, which presents a study of the Mo-speciation of uranium mill tailings at the McClean Lake milling facility in Northern Saskatchewan. This study used multiple techniques to show that powellite is present in the JEB TMF. Chapter 2 shows that only Mo K-edge X-ray Absorption Near-Edge Spectroscopy (XANES) was effective in speciating Mo in the tailings samples, and outlines a definitive procedure for further Mo-speciation studies. The objective of this study was to provide definitive experimental evidence that powellite was present in the JEB TMF. The work presented in this thesis was the first to confirm the presence of powellite within the JEB TMF.

The structural properties of $Nd_xY_yZr_{1-x-y}O_{2-\delta}$ inert matrix fuel materials are explored in Chapters 3 and 4. Chapter 3 characterizes the thermal stability of a series of $Nd_xY_yZr_{1-x-y}O_{2-\delta}$ materials made by a ceramic synthetic route (Nd was used as a surrogate for Am). The materials have been studied using powder XRD, SEM, and X-ray absorption spectroscopy. The objective of this study was to determine and understand how the local and long-range structures of $Nd_xY_yZr_{1-x-y}O_{2-\delta}$ materials behaved at various temperatures. It is necessary to understand how these materials will behave at different temperatures for these materials to be licensed as nuclear fuels, and this study provided a comprehensive description of the behaviour of the long-range and local structures of these materials when annealed at a number of high temperatures.

Chapter 4 continues this work, by exploring the properties of $Nd_xY_yZr_{1-x-y}O_{2-\delta}$ materials made by a solution-based, low-temperature co-precipitation synthetic route. A co-precipitation route could be more easily automated than a standard ceramic method, and solution-based synthetic approaches avoid the production of hazardous radioactive dust particles. This ultimately makes a co-precipitation synthetic method safer and easier to implement than standard ceramic methods. In this chapter, the long-range and local structures of the $Nd_xY_yZr_{1-x-y}O_{2-\delta}$ materials made

by the co-precipitation method were characterized using powder XRD, SEM, and XAS, and the effects of exposure to high temperature were also studied. The objective of this study was to determine if the synthetic method used affected the behaviour of long-range and local structures in $Nd_xY_yZr_{1-x-y}O_{2-\delta}$ materials at various temperatures. This study showed that the materials made by the co-precipitation method were more disordered and had a reduced range of compositions in which the fluorite phase was stable at 1400 °C.

The low thermal conductivity of YSZ materials limits their performance in IMF applications, and it is therefore desirable to explore other properties of materials with higher thermal conductivity. To this end, Chapter 5 presents an exploration of the applicability of Scandium-stabilized zirconia (ScSZ) as IMF materials. ScSZ was studied because it theoretically has a higher thermal conductivity than YSZ materials [124]. This was the first study to explore to use of ScSZ materials for IMF applications. In this chapter, the long-range and local structures of a number of $Nd_xSc_yZr_{1-x-y}O_{2-\delta}$ materials made by a co-precipitation method were characterized by powder XRD, SEM, and XAS. The thermal stability of these materials was also characterized by annealing them at high temperatures. The objective of this study was to determine and understand how the local and long-range structures of $Nd_xSc_yZr_{1-x-y}O_{2-\delta}$ materials behaved at various temperatures. The results in this chapter show that both Nd and Sc are required to stabilize the fluorite structure at high temperature, and these results show that changes in the composition of the material during in-reactor service must be considered when assessing the applicability of ScSZ for IMF applications.

This thesis presents research that enhances the understanding of materials related to the nuclear fuel cycle. The studies presented in the following chapters have advanced the understanding of the fundamental properties of several nuclear fuel materials. Further, the studies outline a general strategy that can be used to study materials by XAS, and show how complementary techniques can be used to fully describe material properties.

Chapter 2

ANALYSIS OF THE Mo SPECIATION IN THE JEB TAILINGS MANAGEMENT FACILITY AT MCCLEAN LAKE, SASKATCHEWAN[1]

2.1 Introduction

The JEB Tailings Management Facility (TMF) is central to reducing the environmental impact of AREVA Resources Canada's (AREVA) uranium ore processing operations at the McClean Lake facility in Northern Saskatchewan. Ultimately, geochemical control of solute concentrations in the JEB TMF, like many other TMFs around the world, will be provided over the long term through equilibrium with the supporting mineral phases present in the TMF. The placed tailings are generally heterogeneous, and at the time of deposition into the TMF, the initial solute concentrations are generally out of equilibrium with their respective solids. Once the tailings are placed in the TMF, the solutes and mineralogy will gradually evolve towards a stable mineralogical end point. This evolution is slow (i.e., years, decades, or centuries), and is generally limited by low hydraulic conductivity, low temperature ($\sim$6 °C), and low liquid/solid ratios that limit mass transport [40]. As part of its operating license issued by the Canadian Nuclear Safety Commission, it is incumbent upon AREVA to determine the minerals controlling the long-term pore water concentration of

[1]Reproduced in part with permission from J.R. Hayes, A.P Grosvenor, J. Rowson, K. Hughes, R.A. Frey, J. Reid *Environmental Society and Technology* (2014) 48, 4460-4467. DOI: 10.1021/es404980x. Copyright 2014 American Chemical Society. The candidate performed all data collection and analysis, and was responsible for drafting the original manuscript. Editorial contributions were provided by the co-authors.

several elements of concern. These elements of concern are often co-mineralized with U in the ore-body and include As, Ni, Mo, and Se in addition to U and ^{226}Ra. Mineralogical investigations by AREVA concerning several of these elements have been in progress for over a decade [71–74,143]. However, little work has been done to determine the Mo-bearing minerals present [40]. In concordance with AREVA's operating requirements, it is prudent to ascertain what Mo bearing phases are currently present in the TMF and how these phases evolve over time.

During the tailings preparation process, Mo is precipitated out of the solution component of the tailings slurry at a pH of 4 as ferrimolybdite ($Fe_2(MoO_4)_3 \cdot 8H_2O$) and molybdate adsorbed on ferrihydrite ($Fe(OH)_3$-MoO_4). But under the near-neutral TMF conditions unique to the JEB TMF (pH = 7.3), these species are not stable and should dissolve, resulting in the formation of a new, relatively insoluble Mo-bearing phase. The geochemical models of the JEB TMF, which were based on thermodynamic calculations, predict that powellite ($CaMoO_4$) should precipitate in the TMF and control the Mo pore water concentration [75]. This is in contrast to another Northern Saskatchewan TMF, which is operated at a higher pH, where $NiMoO_4$ or molybdate adsorbed on ferrihydrite have been identified as the prominent Mo species currently present [144]. It is necessary to experimentally determine if powellite is currently present in the JEB TMF to help verify the geochemical model. Further, it is also necessary establish what other Mo-bearing phases are in the TMF, and to understand how the Mo mineralogy in the TMF evolves over time. Such a study will help establish how the solubility of Mo will change over the very long term in a TMF with near-neutral pH.

To this end, the Mo speciation in several tailings samples from the 2008 sampling campaign was analyzed. AREVA conducts a sampling campaign of the TMF once every five years and each campaign acts as a snap shot in time. The collective results will allow for an understanding of how these various equilibria processes evolve over time [40]. The Mo concentrations in the samples studied here range from 20 ppm – 409 ppm (Table A.1 in Appendix A). Powder XRD, μ-XRF mapping, and XANES were used to analyze the Mo species present in the tailings. Based on this study, it can be concluded that powellite is present in the TMF, and that it currently accounts

for 10-40% of the Mo species in the JEB TMF. This result will aid future modelling of the JEB TMF and other TMFs over time. This study also found that the balance of the Mo was present as ferrimolybdite ($Fe_2(MoO_4)_3 \cdot 8H_2O$) and molybdate adsorbed on ferrihydrite ($Fe(OH)_3$-MoO_4). Additionally, the effectiveness of several common techniques used in identifiying the speciation of low-concentration elements is also discussed. This investigation showed that only XANES was effective in determining the Mo species present due to the low Mo concentration and highly complex nature of the tailings samples.

2.2 Experimental

2.2.1 Mine Tailings Sample Selection

The samples used in this study were collected during the 2008 sampling of the JEB TMF. In these studies, drilling was conducted at four different locations around the TMF, and samples were collected at 3 m vertical intervals. The samples studied here were collected from two drilling positions, TMF08-01 (N 112.00°, E 52.89°), which is in the center of the TMF, and TMF08-03 (N 112.22°, E 52.39°), which is located at the periphery of the TMF. Three samples from each position were analyzed, and these are labelled as TMF08-01 SA04, TMF08-01 SA09, TMF08-01 SA19, TMF08-03 SA02, TMF08-03 SA08, and TMF08-03 SA16, where increasing SA numbers indicate deeper sampling depths. The depths of the samples used in this study are reported in Table A.1 on page 164. In general, due to the deposition process of tailings within the TMF, coarser particles were expected to be found near the center of the TMF and finer particles were expected to be found at the periphery. Because of the settled nature of the TMF, the depth of the core sample can be correlated to the sample age, allowing for an analysis of the aging process of the tailings.

2.2.2 Preparation of Standard Materials

A series of Mo-bearing standards were either prepared or purchased to allow for analysis of the Mo speciation via Mo K-edge XANES experiments. These standards were chosen based on a previous study of the Mo content of the DTMF operated by the Cameco Corporation [144]. The purchased standards were MoO_3 (Acrôs Organics, 99+%), MoS_2 (Aldrich), MoO_2 (Alpha Aesar, 99%), and H_2MoO_4 (Sigma Aldrich, >85%). The synthesized standards were powellite ($CaMoO_4$), α-$NiMoO_4$, α-$FeMoO_4$, ferrimolybdite ($Fe_2(MoO_4)_3$), and MoO_4^{2-} adsorbed on ferrihydrite ($Fe(OH)_3$-MoO_4) [144–149]. Powellite was prepared by mixing stoichiometric amounts of $CaCO_3$ and MoO_3 [145]. This mixture was heated at 700 °C for 1.5 days to decompose $CaCO_3$ to CaO. The powder was air quenched, reground, and then heated at 1200 °C for 3 days. α-$NiMoO_4$ and α-$FeMoO_4$ were also prepared via a solid-state synthesis reaction [146]. Stoichiometric amounts of NiO and MoO_3 or Fe, Fe_2O_3 and MoO_3 were mixed and sealed in evacuated fused silica ampules. The samples were then heated at 950 °C for 1.5 d. The α-$FeMoO_4$ sample was quenched in liquid nitrogen to prevent the formation of β-phase impurities, and the α-$NiMoO_4$ sample was also quenched in air [146].

An anhydrous ferrimolybdite standard ($Fe_2(MoO_4)_3$) was prepared using a co-precipitation synthesis route [147]. Stoichiometric amounts of H_2MoO_4 and $Fe(NO_3)_3{\cdot}9H_2O$ were dissolved separately in ∼50 mL of distilled water. A small amount of concentrated ammonia was added to the H_2MoO_4 solution to aid the dissolution of H_2MoO_4. The two solutions were then mixed and stirred, resulting in the formation of a bright yellow precipitate. After stirring, the solution was placed in an oven at 110 °C and left to dry overnight. The resulting light-brown powder was then collected, ground, and calcined at 400 °C for 4 h.

Fresh ferrihydrite ($Fe(OH)_3$) was prepared within 2 weeks of beamtime using a previously reported procedure [144, 148]. Briefly, 8.0769 g of $Fe(NO_3)_3{\cdot}_9H_2O$ was dissolved in 100 mL of distilled water, and the pH of the solution was then raised from 1.38 to 7.43 through the addition of 14.81 mL of 4M NaOH solution. A dark brown precipitate was formed during this process. This precipitate was collected via vacuum filtration, washed six times, and dried in air for 24 h. MoO_4^{2-}

was adsorbed to the ferrihydrite by mixing a 0.3 M solution of H_2MoO_4 with a slurry containing 0.3000 g of ferrihydrite [144, 149]. The pH was then adjusted to 8.89 by adding 4 M NaOH and this mixture was covered and stirred for 24 h. The solid product was then collected via vacuum filtration and left to dry in air overnight.

The phase purity of all the synthesized standards was checked by XRD using the instrument described in Section 2.2.3.

2.2.3 Powder XRD

Powder X-ray diffraction patterns from the tailings samples were collected to make an initial assessment of the phases present in these materials. Measurements were collected using a PANalytical Empyrean X-ray diffractometer equipped with a Cu K$\alpha_{1,2}$ X-ray source. The μ-XRD diffraction patterns were collected using a 200 μm diameter spot size. Bulk powder diffraction patterns were collected by grinding the tailings samples and mounting the resulting powder on glass slides using ethanol. A spinning sample stage was employed during these measurements to minimize preferred orientation effects. Following these measurements, the Cu X-ray tube was mounted in the "Point Focus" position and the diffractometer was equipped with a mono-capillary attachment that reduced the X-ray spot size to a 200 μm diameter to collect micro powder X-ray diffraction (μ-XRD) patterns. Samples were prepared by mounting unground sample on a glass slide using ethanol, and 10 slides per tailings sample were prepared. The samples were mounted on the diffractometer using a stationary sample holder during the μ-XRD measurements. All powder XRD patterns were analyzed using the X'Pert HighScore Plus and PowderCell software packages [150].

2.2.4 X-ray Fluorescence Imaging and Laue Diffraction

XRF maps and Laue X-ray diffraction patterns from three of the tailings samples were collected using the VESPERS beamline at the Canadian Light Source (CLS). (μ-XRD experiments were also attempted using multiple incident energies, but the collected signal was not high enough to pro-

duce a usable diffraction pattern.) Samples were prepared by sealing a thin layer of the unground tailings sample between two layers of Kapton tape. The samples were mounted perpendicular to the beamline and at an angle of 45° from the horizontal axis. X-ray fluorescence emissions were collected using a single element Vortex silicon drift detector (SDD) and the diffraction patterns were imaged using a Pilatus CCD located directly above the sample. All fluorescence spectra and diffraction patterns were collected using the "Pink Beam" mode, which includes all X-ray energies from 5-30 keV. Note that a significant drop off in flux occurs for energies above 20 keV. For all measurements, a 5 μm spot size was used. Fluorescence spectra were collected by rastering over a 1000 μm x 1000 μm area using 10 μm steps and a 1 s dwell time per step. Fluorescence (elemental) maps were created and analyzed using the SMAK program and the Laue diffraction patterns were analyzed using the XMAS program [151, 152].

2.2.5 XANES

Bulk Mo K-edge XANES measurements were carried out using the HXMA beamline at the CLS [153, 154]. The flux was on the order of 10^{12} photons/s, and the maximum achievable resolution was better than 2 eV at 20 keV using the Si (220) monochromator [153]. Tailings samples were prepared by packing the as-provided material in 2.38 mm thick Teflon sample holders which were then sealed between two layers of Kapton tape. Spectra were collected using a 0.3 eV step through the absorption edge, and the spectra were measured in partial fluorescence yield mode using a 32-element Canberra Ge detector. To prepare the Mo-bearing standards, the materials were finely ground and mounted on a strip of Kapton tape which was then folded multiple times. The Mo K-edge spectra from the standards were collected in transmission mode using ionization chambers filled with $N_{2(g)}$. All spectra were calibrated using the Mo K-edge spectra from a Mo metal reference foil collected in-line with the sample, which has a known absorption-edge energy of 20,000 eV [154]. In all cases, multiple scans of each sample were collected at a single spot. These scans did not change in any systematic way, indicating that no beam damage occurred during the measurements. The spectra were fitted from 25 eV below the absorption edge to 55 eV above the

absorption edge when performing the principal component analysis (PCA) and linear combination fittings (LCF). The absorption edge of a spectrum was defined as the most intense, lowest-energy peak in the first-derivative of the spectrum. The Athena software program was used to normalize the spectra and perform all of the PCA and LCF analysis [155].

2.3 Results

2.3.1 Powder XRD

Powder XRD patterns from the bulk tailings samples were collected to provide an initial characterization of the tailings materials (Figure 2.1). The dominant crystalline phases observed in these samples were quartz and gypsum. In general, the patterns from the central bore-hole samples (TMF08-01 SA04, TMF08-01 SA09, TMF08-01 SA19; Figure 2.1a) have a flatter background than the patterns from the periphery bore-hole samples (TMF08-03 SA02, TMF08-03 SA08, TMF08-03 SA16; Figure 2.1b), which contain a broad peak spanning $\sim$15°-30°. This is consistent with the design of the TMF, as coarser particles are expected to congregate near the center of the TMF while finer particles are expected to be found towards the edge of the TMF. These results indicate that the samples from the central bore-hole are more crystalline than the samples from the periphery bore-hole [156]. Finally, the powder patterns show that none of the expected crystalline Mo-bearing phases (i.e., α-$FeMoO_4$, α-$NiMoO_4$, powellite) could be detected using bulk powder XRD. This result was expected given the low concentrations of Mo in these samples (see Table A.1 Appendix A) but does not preclude the presence of these phases in the tailings samples.

Given the limitations of a standard powder XRD experiment, these studies were followed by performing μ-XRD experiments. The X-ray beam was focused to a 200 μm spot size in these studies and diffraction patterns were gathered from multiple aliquots of each sample. The results from sample TMF08-03 SA08 are presented in Figure 2.2. (The μ-XRD patterns from the other

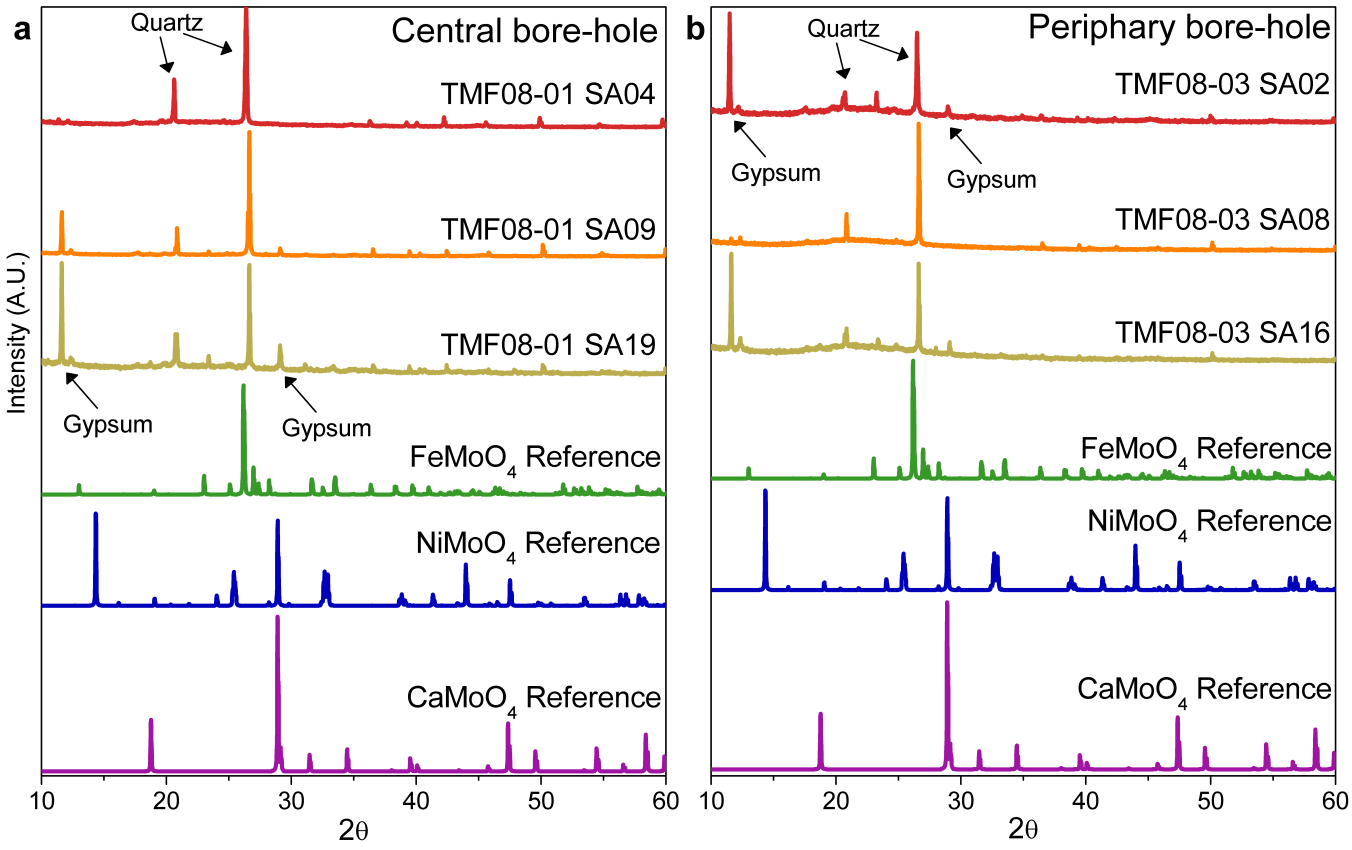

Figure 2.1: Bulk powder XRD patterns from the (a) central bore-hole and (b) periphery bore-hole tailings samples are compared to reference patterns from Mo-bearing standards. The predominant crystalline phases in the tailings samples are gypsum and quartz. No evidence of Mo-bearing species was observed.

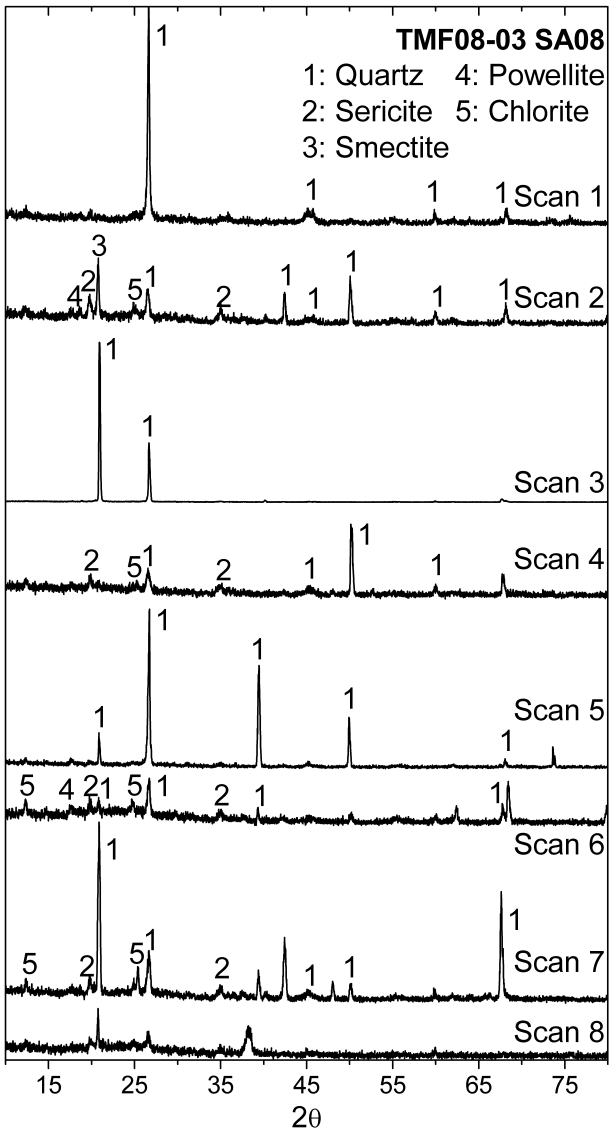

Figure 2.2: μXRD patterns collected from aliquots of the TMF08-03 SA08 tailings sample. The diameter of the beam spot was 200 μm. In some scans, the intensity of the identified peaks do not match the calculated intensity from the reference pattern. This is most notably seen for the quartz peaks in Scans 3 and 7, and is likely caused by graininess of the crystallites. A peak consistent with the presence of powellite is found in Scans 2 and 6.

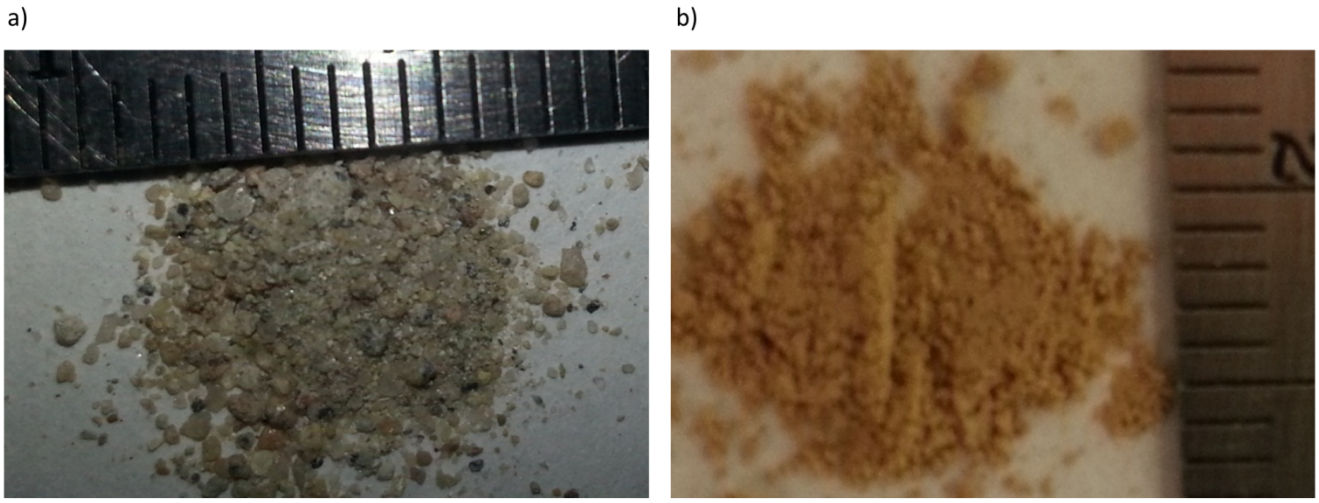

Figure 2.3: Photographs of the tailings samples from a) TMF08-01 SA09 and b) TMF08-03 SA16. The ruler markings indicate 1 mm intervals. These pictures provide a visual confirmation that the tailings samples are heterogeneous. The photographs also show that the heterogeneity of the samples varied widely. In general, the μ-XRD patterns from the highly heterogeneous samples (i.e. TMF08-01 SA09, cf. Figure S3) varied more than the less heterogeneous samples (i.e., TMF08-03 SA16, cf. Figure S6).

tailings samples are presented in Figures A.1-A.5 in Appendix A.) The significant variations in the diffraction patterns observed indicate that the tailings samples are heterogeneous, which was also confirmed by visual inspection. Photographs of two of the tailings samples are presented in Figure 2.3. Additionally, the peak widths of the μ-XRD patterns vary, indicating that the crystallinity of the tailings is not uniform. Here, diffraction patterns with sharper peaks indicate a more crystalline sample. In general, the peaks can be assigned to phases previously reported to be found in the samples [40]. Interestingly, the intensities of peaks from highly crystalline phases varied significantly between samples (cf. scans 3 and 5 in Figure 2.2). These intensities also deviated significantly from the reported standard diffraction pattern. It is likely that these variations occur due to poor crystallite statistics ('graininess'), in which the crystallites are sufficiently large that too few grains are illuminated to obtain a statistically representative distribution of grain orientations, resulting in a random distortion of the diffraction peak intensities [157]. This seems likely given the large grain sizes (the samples were not ground) and the small X-ray spot size. These patterns provide some possible evidence for the presence of β-$FeMoO_4$ and powellite phases. However,

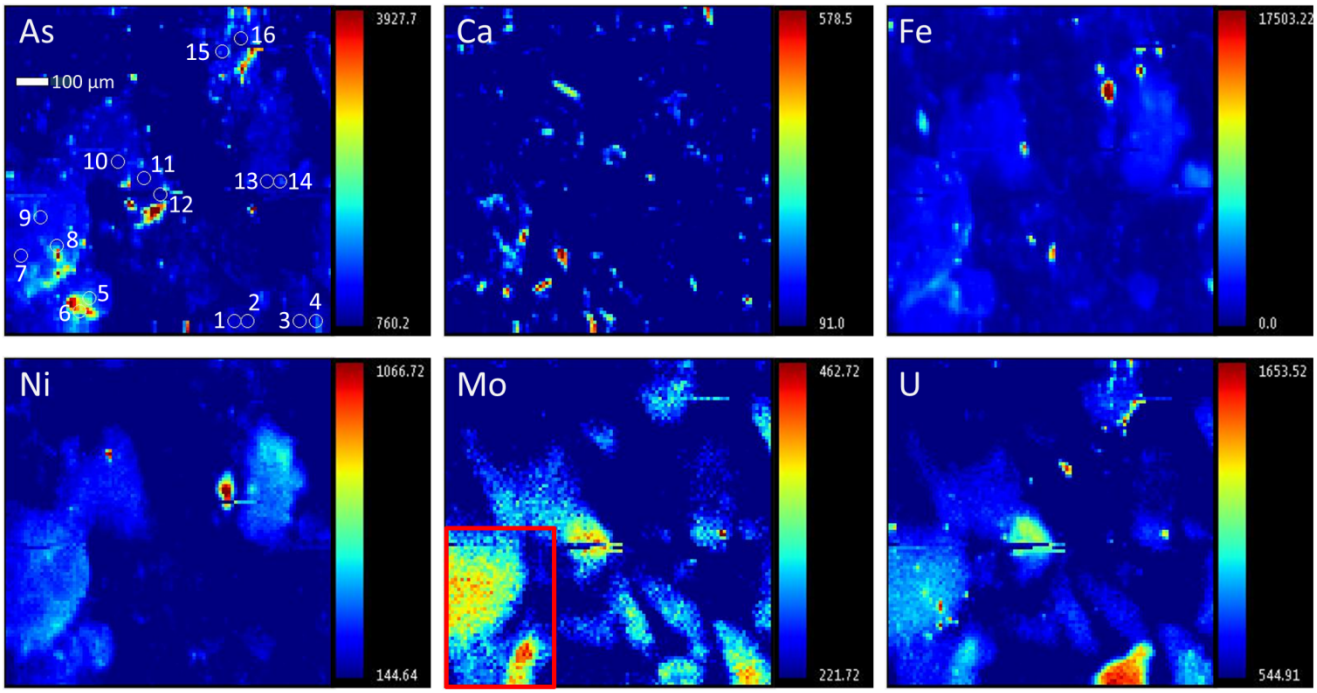

Figure 2.4: Fluorescence maps collected from the TMF08-03 SA08 sample. The spot size of the beam was 5 μm x 5 μm and the map was collected using 10 μm steps. The spots where Laue diffraction patterns were collected are labelled according to their Scan number in the As map. A large Mo concentration hotspot was found in the lower left-hand corner of the Mo map, as outlined by the red rectangle. Fe, Ni, As, and U fluorescence signals were also observed in this region, indicating that these elements were likely intimately mixed. A scale bar is presented in the As map.

for powellite, the predominant peak observed is not the most intense peak in the reported reference pattern, suggesting graininess is likely an issue here as well. Overall, these results show that a more sophisticated approach is required to determine the Mo speciation in these tailings samples.

2.3.2 XRF Imaging and Laue Diffraction

2.3.2.1 XRF Imaging

XRF experiments were performed to map the elemental distribution within the tailings samples. In these experiments, the samples were illuminated with a highly-focused X-ray pink beam which had a spot size of 5 μm. The samples were then rastered using 10 μm steps, and the resulting fluorescence at each spot was measured allowing for a map to be generated. The results of this experiment for the TMF08-03 SA08 sample are shown in Figure 2.4. Two other tailings samples

were also mapped (Figures A.6, A.7), but Mo could not be detected in the regions studied.

A Mo-rich region was observed near the bottom left-hand corner of the map, as outlined by the red rectangle in Figure 2.4. Relatively intense fluorescence signals from U, As, Ni, and Fe were also observed in this region. The size and shape of these hotspots were similar, suggesting that these elements are intimately mixed with Mo. There was little overlap between the Ca- and Mo-rich regions, though some small, isolated Ca hotspots were observed to overlap with the main Mo hotspot. A strong correlation between the U and Mo signals was observed, which may indicate that U and Mo are present in a single phase. However, it is more likely that this result is an artifact of the relatively poor resolution of the fluorescence detector. The Mo K_α emission line has an energy of 17480 eV and the U L_β emission line has an energy of 17220 eV, and it is possible that overlap between signal channels resulted in this correlation [154]. In general, these results may indicate that Ni and Mo are intimately mixed, consistent with the presence of a $NiMoO_4$ phase, but it is more likely that this observation was a result of the co-mineralization of Ni-bearing and Mo-bearing phases from the original ore. Overall, no conclusive results about the Mo speciation could be drawn from this experiment.

2.3.2.2 Laue Diffraction

Laue diffraction patterns were collected at different sample positions based on the results of the XRF mapping experiments. The positions at which patterns were collected are labelled in Figure 2.4, and Figures A.6 and A.7 in Appendix A, on the As fluorescence maps. The samples were illuminated using an X-ray pink beam, which includes all energies from 5 keV-30 keV, with a spot size of 5 μm in these experiments. Representative examples of the patterns collected are presented in Figure 2.5.

The spot size used (5 μm x 5 μm) was on the order of the size of the crystallites, and the resulting diffraction patterns collected generally resemble single-crystal diffraction patterns. This is observed best in the pattern presented in Figure 2.5b, in which small, well-defined diffraction spots are observed. However, the significant penetration depth of the X-rays can also result in

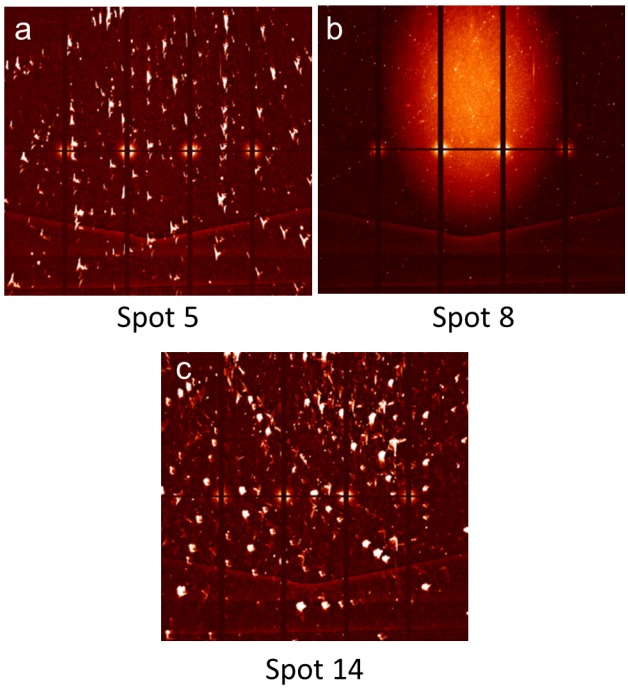

Figure 2.5: Laue diffraction patterns collected at (a) Spot 5, (b) Spot 8, and (c) Spot 13 from the TMF08-03 SA08 tailings sample. The spot size of the beam was 5 μm x 5 μm. The "V-shape" present in the bottom half of the patterns is the result of shadowing from the sample holder. The diffraction patterns collected at Spot 5 and Spot 14 are broad and non-circular, indicating that multiple crystallites were illuminated. The diffraction pattern collected at Spot 8 is small and circular, indicating that only one crystallite was illuminated.

Table 2.1: Summary of Laue fitting results, TMF08-03 SA08

Image[a]	Number of Peaks Indexed[b]						
	Powellite	**Quartz**	**Illite-Smectite**	**Chlorite**	**Gypsum**	**Kamiokite**	**β-$FeMoO_4$**
1	34	43	42	49	46	29	126
2	47	49	36	43	46	45	147
6	19	12	15	15	29	18	48
8	56	56	48	54	58	54	175
11	55	43	43	27	39	43	147
13	43	31	28	27	41	27	97
14	35	40	31	42	45	40	131
15	35	42	41	60	40	41	156
16	43	67	42	49	52	40	162

[a]Numbering refers to where on the sample the diffraction pattern was collected. Please refer to Figure 2.4 for image locations.
[b]A larger numbers of peaks indexed usually indicates a higher quality fit.

several crystallites being illuminated simultaneously, resulting in large, non-circular diffraction spots (see Figure 2.5a and 2.5c).

These patterns were analyzed using the crystal structure of known standards to index the diffraction spots. If the number of diffraction spots indexed was close to the number of diffraction spots observed, it is likely that the phase indexed is present [158]. Here, the phases indexed were those reported by AREVA to be in the tailings. The results of these fitting attempts are summarized in Table 2.1, and in Tables A.2 and A.3. (Note that some spots did not produce usable diffraction patterns.) In general, none of the phases indexed resulted in a definitive fit. However, for TMF08-03 SA08, spot 8 may have been indexed by powellite, and the diffraction pattern of spot 6 was modeled fairly well by gypsum. Ultimately, the complexity of the tailings samples did not allow for any conclusions to be drawn.

2.3.3 XANES

Mo K-edge XANES spectra from the tailings samples and a series of Mo-bearing standards were collected and are presented in Figure 2.6. The spectra were analyzed to determine the speciation of Mo in the tailings samples. The results of this analysis are discussed below.

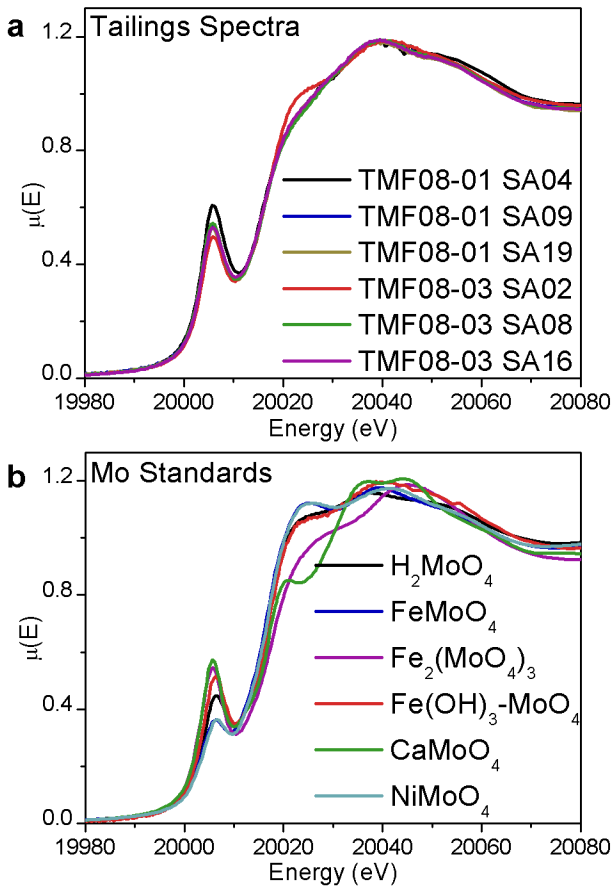

Figure 2.6: (a) The Mo K-edge XANES spectra from the tailings samples. All spectra were fairly similar with the exception of the spectrum collected from the TMF08-03 SA02 sample. (b) The Mo K-edge XANES spectra from the Mo standards used for the linear combination fitting.

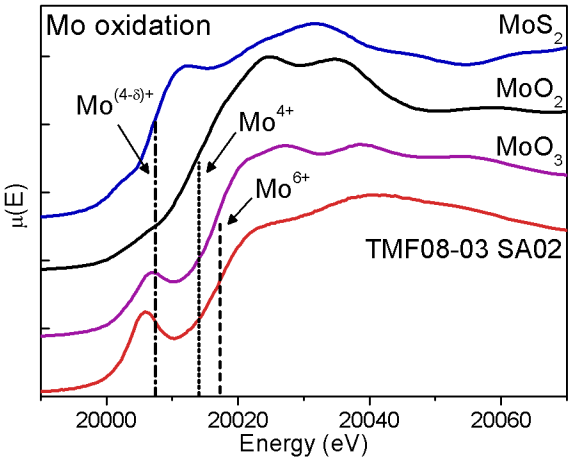

Figure 2.7: The absorption-edge energy of the TMF08-03 SA02 sample is compared to Mo standards with different oxidation states. The absorption edge energy is similar to that from MoO_3, which has a 6+ oxidation state, indicating that Mo likely adopts a 6+ oxidation state and is surrounded by O^{2-} anions in the tailings samples.

2.3.3.1 Analysis of the Mo Oxidation State in the Tailings

The Mo K-edge XANES spectra were first analyzed to determine the oxidation state of Mo in the tailings species. This analysis was performed by comparing the absorption edge-energies of spectra from the tailings samples to spectra from samples with known Mo-oxidation states (Figure 2.7). The absorption edge energy is sensitive to the oxidation state of the metal centre, as the absorption edge shifts to higher energy with increasing oxidation state. Increasing the oxidation state decreases the amount of screening of the nuclear charge that the core-electron experiences, leading to a more tightly bound ground state [159, 160]. The edge energy is also sensitive to the chemical environment around the metal center, as changes in the electronegativity of the surrounding anions can change the bond covalency. In general, as the surrounding ions become less electronegative (i.e., the bonds become more covalent), the charge of the Mo-center decreases, and the absorption edge energy shifts to lower energy [159, 160]. This is best observed by comparing the edge energies of MoO_3 (Mo^{6+}), MoO_2 (Mo^{4+}), and MoS_2 ($Mo^{4-\delta+}$) in Figure 2.7: as the Mo oxidation state decreases, the edge energy also decreases. The absorption edge energies from the tailings samples are similar to the absorption edge energy from MoO_3 (Figure 2.7). It can be concluded that Mo adopts a 6+ oxidation state in the tailings samples and is likely surrounded by O anions.

This is consistent with the processing of the tailings, in which a large amount of Fe^{3+} is added to the mixture, as it is well known that the $Fe^{3+}/Mo^{4/5+}$ redox couple strongly favors the formation of Fe^{2+} and Mo^{6+} under a wide variety of conditions [161, 162].

2.3.3.2 Prinicipal Component Analysis

Beyond information on the oxidation state and the local coordination environment around the metal center, XANES can also provide information about the number of species present in a mixture and the identity of those species. Such information is achieved through the use of advanced data processing techniques, such as PCA. In this context, the term "component" and the term "factor" are interchangeable. To avoid the confusion of trying to refer to both chemical and mathematical components, the term "factor" will be used when describing PCA components. The basic principal of PCA (in the context of XANES) is grounded in the fact that a XANES spectrum from a mixture can be constructed from a linear combination of the spectra from each of the individual components in that mixture [163]. Because of this property, the spectra from a series of mixtures bearing similar individual components can be decomposed into q principal factors which can be used to reconstruct the original data [164]. PCA has been performed on the set of tailings spectra investigated here, and the results of this analysis are plotted in Figure 2.8. It is important to note that despite their appearance, the principal factors derived from the data are mathematical constructs and do not have physical meaning. The analysis of the spectra reported here is similar to the analysis used to determine the Mo species present in the DTMF, which is a U-milling TMF also located in Northern Saskatchewan [144].

Given a perfect data set with no experimental error, the number of principal factors would be equal to the number of components within the set of mixtures. However, the number of principal factors derived is always greater than the number of components in the set of mixtures due to experimental error [164]. In this case, the excess principal factors describe the contributions of experimental error to the data. The principal factors attributable to the components within the set of mixtures are referred to as primary factors while principal factors attributable to experimental

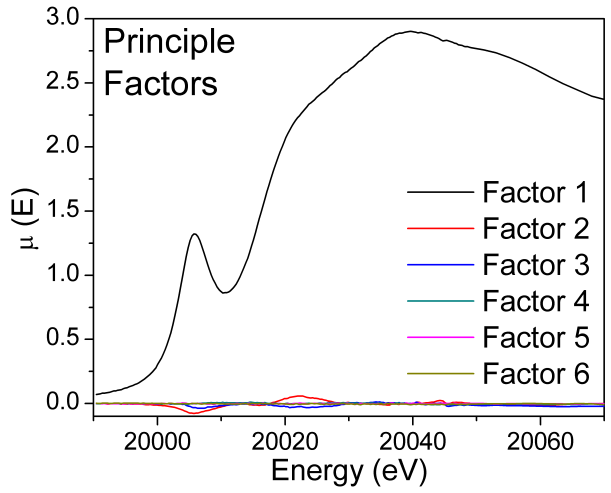

Figure 2.8: The principal factors calculated from the set of Mo K-edge XANES spectra from the tailings samples are presented. Only factors 1-3 appear to have significant amplitudes. It should be noted that, despite their appearance, the principal factors are only mathematical constructs and do not have physical meaning.

error are referred to as secondary factors. Malinowski has developed the empirical IND function to differentiate between the primary and secondary factors, and the number of primary factors is given when the IND function output is minimized [164, 165]. The values of the IND function have been evaluated and are plotted in Figure 2.9. The IND function reached a minimum value when the number of principal factors was 3. It was concluded from this analysis that there are three Mo-bearing species in the tailings. This conclusion is confirmed by the reconstructions of the tailings spectra (Figure 2.10). It can be clearly seen in Figure 2.10 that no significant improvements are observed when reproducing the spectra with four components versus three components, indicating that only three factors are necessary to describe the data.

2.3.3.3 Quantitative Analysis of Mo Speciation

The Mo K-edge spectra collected from the tailings samples can be compared to the Mo K-edge spectra from Mo-bearing standards to determine the speciation of Mo in the tailings samples. The standards used to fit the Mo K-edge spectra were H_2MoO_4, α-$FeMoO_4$, α-$NiMoO_4$, molybdate adsorbed on ferrhydrite ($Fe(OH)_3$-MoO_4), ferrimolybdite, and powellite. The Mo K-edge spectra from these standards are presented in Figure 2.6b. (The anhydrous ferrimolybite standard used

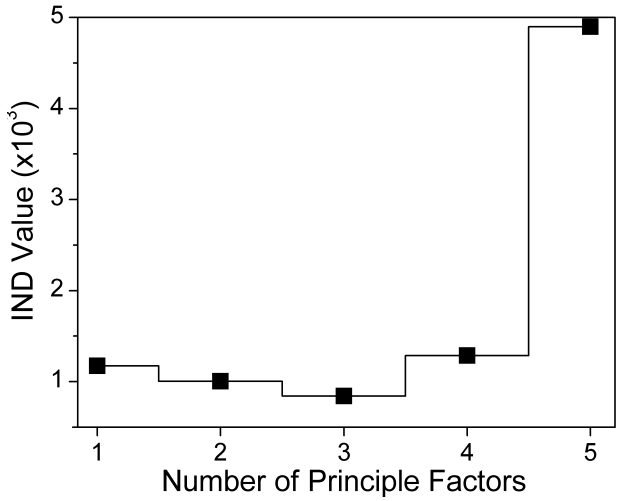

Figure 2.9: A plot of the calculated IND values as a function of the number of primary factors. The connecting lines are meant as a guide to the eye only. The IND value is minimized when the number of primary factors is 3, indicating that there are at most 3 Mo-bearing species in the tailings samples.

Table 2.2: Summary of LCA Fits

Sample	Powellite		Ferrimolybdite		$Fe(OH)_3$-MoO_4		R-factor	χ^2
	Conc.	Error	Conc.	Error	Conc.	Error		
TMF08-01 SA04	0.40	0.040	0.24	0.071	0.37	0.029	0.00466	0.16064
TMF08-01 SA09	0.38	0.022	0.26	0.038	0.36	0.017	0.00155	0.05318
TMF08-01 SA19	0.37	0.042	0.30	0.027	0.38	0.018	0.00178	0.06292
TMF08-03 SA02	0.10	0.033	0.29	0.014	0.60	0.0097	0.00052	0.01788
TMF08-03 SA08	0.42	0.038	0.26	0.027	0.31	0.018	0.00175	0.06185
TMF08-03 SA16	0.36	0.037	0.22	0.028	0.42	0.019	0.00191	0.06674

was an appropriate model system for hydrated ferrimolybdite given the local structural similarities around the Mo center in the two systems.)

The tailings spectra were fitted by linear combinations of the XANES spectra from the standards using the linear combination fit function in the Athena software program [155]. Each tailings spectrum was fitted by all combinations of three or fewer standards, and the best fit was determined by the χ^2 value from these fittings. The coefficients of the linear combination fit were normalized and represent the concentrations of each species present as a function of total percent Mo. The best fits to the spectra are summarized in Table 2.2 and the fitted spectra are plotted in Figure 2.11.

In all cases, the spectra were fitted best using ferrimolybdite, powellite, and either H_2MoO_4 or $Fe(OH)_3$-MoO_4. The linear combination fits using either H_2MoO_4 or $Fe(OH)_3$-MoO_4 were gen-

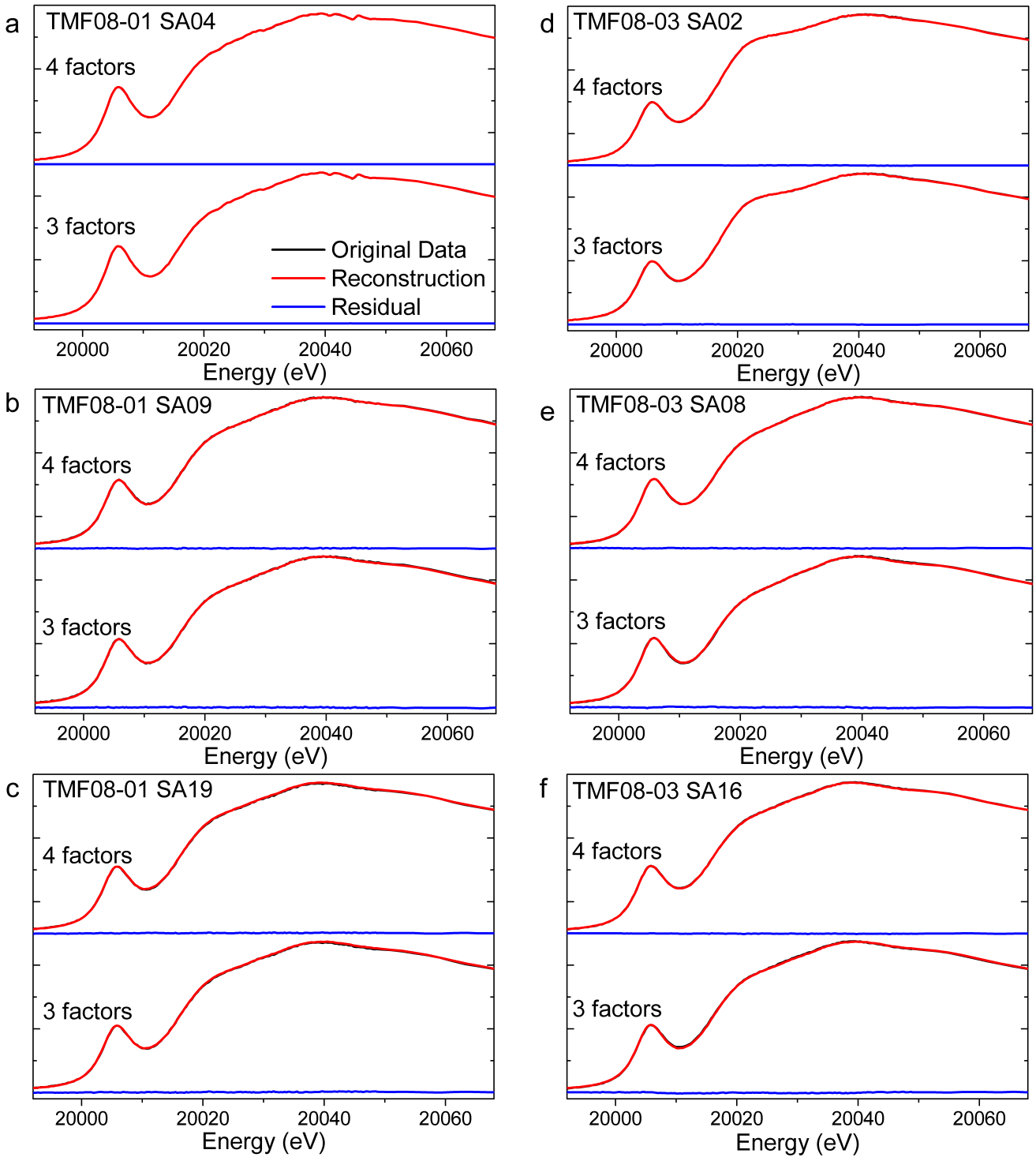

Figure 2.10: Reconstructions of the Mo K-edge spectra from (a) TMF08-01 SA04, (b) TMF08-01 SA09, (c) TMF08-01 SA19, (d) TMF08 03 SA02, (e) TMF08 03 SA02, and (f) TMF08-03 SA16 using either 3 or 4 factors. In all cases, no significant improvements were observed in the quality of the reconstructions when using more than 3 factors.

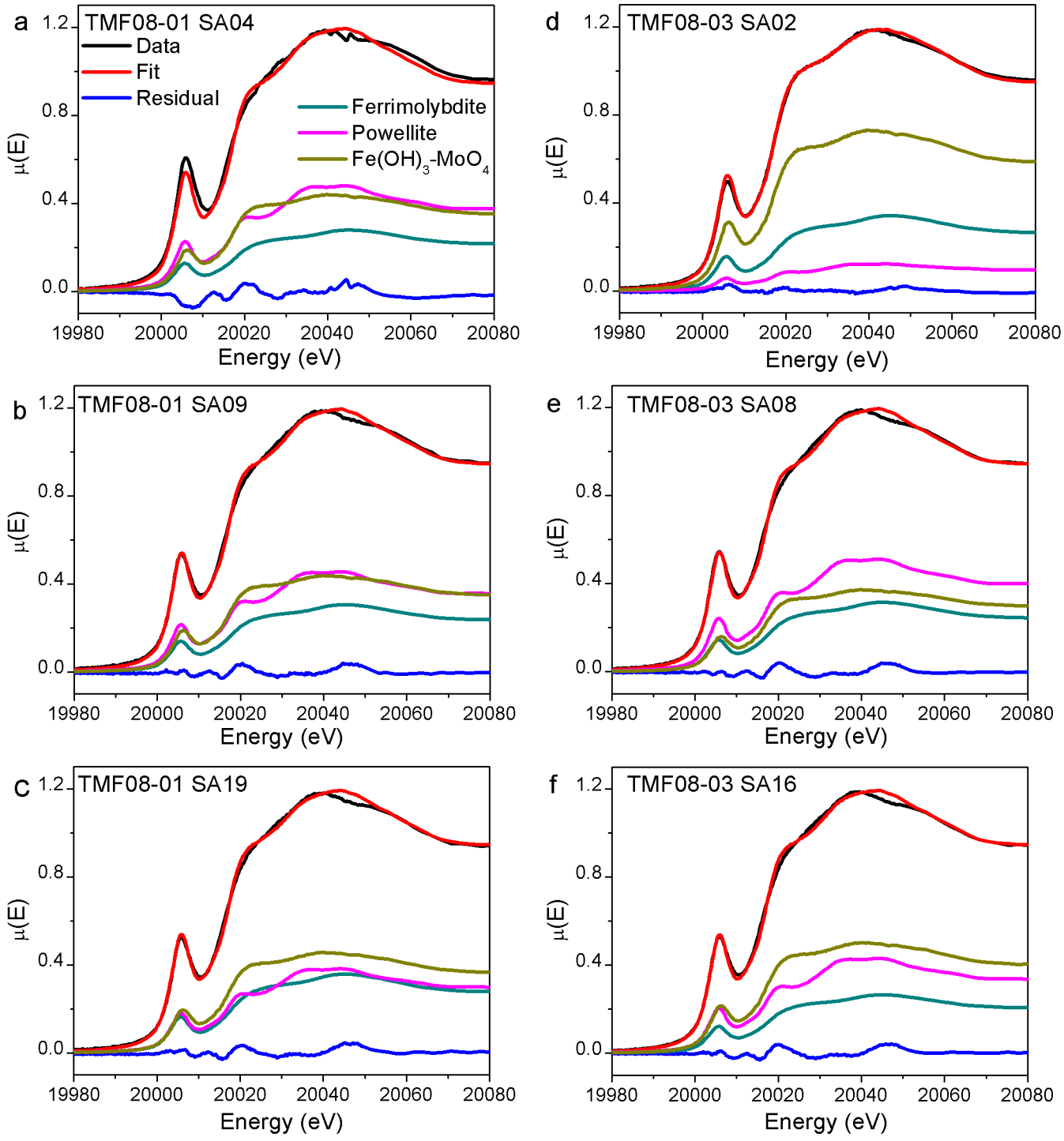

Figure 2.11: The Mo K-edge XANES spectra from (a) TMF08 01 SA04, (b) TMF08 01 SA09, (c) TMF08 01 SA19, (d) TMF08-03 SA02, (e) TMF08-03 SA08, and (f) TMF08-03 SA16 are presented along with results of the linear combination fit. The weighted spectra from the fitted standards are also plotted.

erally of equal quality; likely because of the strong similarities between the spectra from H_2MoO_4 and $Fe(OH)_3$-MoO_4 (Figure 2.6b). Therefore, it is not possible to determine which of these species (H_2MoO_4 or $Fe(OH)_3$-MoO_4) is present by analysis of the XANES spectra alone. However, H_2MoO_4 is known to be highly soluble at the pH of the pore water present in the TMF (pH = 7.3), and it therefore does not seem likely that this phase would be found as a solid in the JEB TMF [166]. This leads to the conclusion that the third component in these samples is $Fe(OH)_3$-MoO_4.

In general, the resulting fits accurately reproduce the collected spectra from the tailings samples, with the exception of the region between 20040-20050 eV, where the fitted spectra are consistently more intense than the experimental data. It is likely that multi-scattering resonances (MSR) contribute significantly to the intensity of the features found in this region of the spectra [167]. In an MSR process, the core-electron is excited to a continuum state and scatters multiple times off neighboring atoms, resulting in constructive and destructive interference of the photoelectron wave [168]. As such, these structures are highly dependent on the crystal structure of the materials, and the intensity of MSR features will decrease as the crystallinity of the material decreases [169]. The XRD patterns show that the crystallinity of the phases present in the tailings samples vary widely, and exhibit a high degree of disorder (cf. Figure 2.2 and Figure 2.1). Therefore, it is highly likely that the Mo-phases have only a low degree of crystallinity in the tailings samples which would result in a muted MSR feature compared to the MSR feature observed in the Mo K-edge XANES spectra from the crystalline standards.

The interpretation reported here relies heavily on the assumption that the standards used in this analysis account for all the Mo-bearing species in the sample. For example, the β-$NiMoO_4$ phase, which could not be successfully synthesized, represents a possible Mo-species that was not included in the standards measured. In this species, Mo occupies a tetrahedral site, which would increase the intensity of the XANES spectrum in the pre-edge region (i.e., the $\sim$20000-20010 eV energy range) compared to the pre-edge region from α-$NiMoO_4$, in which Mo occupies a six-coordinate site [170]. When fitting the spectra using α-$NiMoO_4$ as a component, the pre-edge

was consistently under fitted while the main-edge was accurately reproduced. The statistics of these fits were poor compared to the ones reported in Table 2.2, which lead to the conclusion that α-$NiMoO_4$ was not a component in the tailings samples. However, based on the XRF results, which showed some correlation between the Ni and Mo signals, and the conditions under which the tailings are treated, which are similar to the reported β-$NiMoO_4$ synthetic conditions, it seems possible that β-$NiMoO_4$ could be present [40, 171, 172]. Notwithstanding, all fits which included α-$NiMoO_4$ also required a significant contribution from the powellite spectrum to reproduce the data. Therefore, based on these fits, the conclusions regarding the presence of powellite remain valid.

2.4 Conclusions

The results presented in this chapter show that powellite is present as a major component in the JEB TMF. They also show that ferrimolybdite and $Fe(OH)_3$-MoO_4 likely account for significant amounts of the Mo species present in the TMF. The conclusions of this study are consistent with the long-term geochemical models of the TMF, which predict powellite will be the predominant Mo-bearing phase when the TMF reaches equilibrium [75].

Chapter 3

AN INVESTIGATION OF THE THERMAL STABILITY OF $Nd_xY_yZr_{1-x-y}O_{2-\delta}$ INERT MATRIX FUEL MATERIALS[1]

3.1 Introduction

Inert matrix fuels (IMFs) are used to "burn-up" or transmute transuranic elements (TRUs; i.e., Np, Pu, Am, Cm) found in spent nuclear fuel. A full discussion of IMFs is presented in Section 1.5.4 on page 27. In this chapter, the thermal stability of a series of Nd-doped YSZ materials ($Nd_xY_yZr_{1-x-y}O_{2-\delta}$; $0 \leq x \leq 0.30$, $0 \leq y \leq 0.30$) has been studied. (Due to the similarity of their ionic radii and oxidation state, Nd^{3+} was used as a surrogate for Am^{3+} [104, 120–122].) It has been shown that changes in the structure of fuel materials during or after irradiation in a reactor can lead to poor fuel perfomance and can cause pontential safety issues. It is therefore of interest to understand how these materials will behave when exposed to a variety of different temperatures. The thermal stability of thse materials was studied by annealing them at multiple temperatures ranging from 600 °C – 1400 °C. The as-synthesized and annealed materials were characterized using powder XRD, SEM, and XAS. While powder XRD allowed for characterization of the long-range structure with annealing, XAS allowed for characterization of the local structures around the individual metal centres at a scale not easily observable by XRD. This study has proved that the

[1]Reprinted in part from *Journal of Alloys and Compounds,* 635, J.R. Hayes, A.P. Grosvenor, M. Saoudi "An Investigation of the Thermal Stability of $Nd_xY_yZr_{1-x-y}O_{2-\delta}$ Inert Matrix Fuel Materials," 245-255, 2015, DOI: 10.1016/j.jallcom.2015.02.022 with permission from Elsevier. The candidate performed all data collection and analysis, and was responsible for drafting the original manuscript. Editorial contributions were provided by the co-authors.

structure of cubic $Nd_xY_yZr_{1-x-y}O_{2-\delta}$ materials is stable across a wide range of temperatures and compositions when $y \geq 0.05$.

3.2 Experimental

3.2.1 Synthesis

The $Nd_xY_yZr_{1-x-y}O_{2-\delta}$ ($0 \leq x \leq 0.30$, $0 \leq y \leq 0.30$) compounds were synthesized via a standard solid-state synthesis. Briefly, stoichiometric amounts of Nd_2O_3 (Alfa Aesar, 99.9%), Y_2O_3 (Alfa Aesar, 99.99%), and ZrO_2 (Alfa Aesar, 99.978%) powders were ground and mixed together under acetone using an agate mortar and pestle. The mixture was then pressed into a pellet at 8 MPa and heated in an alumina crucible at 1500 °C for six days with intermittent grinding and quenched in air. (8 MPa was the pellet gauge pressure, and the actual pressure exerted on the pellet is much greater.) The thermal stability of the $Nd_xY_yZr_{1-x-y}O_{2-\delta}$ compounds was studied by annealing the as-synthesized materials at 600 °C, 900 °C, 1200 °C, and 1400 °C. The annealed samples studied by XAS and powder XRD were prepared by annealing ∼0.07 g aliquots of the as-synthesized material for five days as free powders.

The phase analysis of the materials was performed using powder X-ray diffraction. The powder X-ray diffraction patterns were collected using a PANalytical Empyrean diffractometer set-up in a Bragg-Brentano geometry using either Cu $K_{\alpha 1,2}$ (λ=1.5406 Å) or Co $K_{\alpha 1,2}$ (λ=1.7890Å) radiation. Patterns were collected from 10-90° 2θ using a 0.017° step-size and a dwell time of 31.1 s/step. The unit cell parameters and the weight amounts of the crystallized phases of the synthesized materials were quantified by Rietveld refinement using the PANalytical HighScore Plus software [173]. Rietveld refinements were performed by fitting cubic ZrO_2, tetragonal ZrO_2, and monoclinic ZrO_2 phases to the data [174–176]. The phases used to model the diffraction data were adapted from the pure ZrO_2 patterns by artificially adding Nd and Y to the crystallographic site occupied by Zr. The site occupancies were set to be consistent with the ideal stoichiometry of each material. As an example, the cubic ZrO_2 pattern for the $Nd_{0.10}Y_{0.10}Zr_{0.80}O_{1.90}$ pattern was generated by

adding Y and Nd to the Zr 4a site. The Zr site occupancy was set to 0.80 while the Y and Nd site occupancies were each set to 0.10. The addition of Y and Nd impacted the intensity of the modelled peaks and significantly improved the quality of the fit. The background was fitted using a 3rd order polynomial function which also included a $1/2\theta$ term [173].

3.2.2 Scanning Electron Microscopy

SEM samples were prepared by pressing ∼0.17 g of the as-synthesized material into a ¼" (0.635 cm) pellet at 8 MPa, and then then sintering the pellets at 1500 °C for 12 h. The pellets for SEM analysis were annealed at the given temperature for five days and air quenched. Several of the pellets were cut using a diamond saw and mounted to allow for imaging of the pellet cross-section. The pellets were embedded in a resin matrix and ground manually to a flat surface using SiC paper. The pellet surfaces were then polished using 0.25 μm diamond paste. The samples were coated with a thin carbon layer to reduce sample charging effects. A Zeiss Supra-55 WDS-VP SEM coupled with an Energy Dispersive X-ray Spectrometer (EDS) was used to collect SEM images and to carry out EDS mapping. Secondary electron (SE) images were collected to study the surface topography and backscatter electron (BSE) images were collected to study the Nd-distribution in the zirconia matrix. Samples were mapped by EDS for Zr and Nd at 500x magnification, and the EDS maps were collected using an ∼8 μm step size at an accelerating voltage of 20 kV.

3.2.3 X-ray Absorption Spectroscopy Measurements

3.2.3.1 Zr K-, Nd L_3-, and Y K-edge XANES

Zr K-, Nd L_3-, and Y K-edge XAS spectra from the as-synthesized and annealed samples were collected using the Pacific Northwest Consortium/X-ray Sciences Division Collaborative Access Team (PNC/XSD-CAT, Sector 20) bending magnet beamline (20BM) located at the Advanced Photon Source (APS) at Argonne National Laboratory. A silicon (111) double crystal monochromator with a Rh harmonic rejection mirror was used, which has a resolution of 2.4 eV and a photon flux

of $\sim 10^{11}$ photons/s at 17 keV [177]. The samples were finely ground and sealed between layers of Kapton tape and the number of layers was adjusted to maximize the absorption signal. Samples were mounted at an angle of $\sim 45°$ to the incident beam.

The Zr K-edge and Y K-edge XAS spectra were collected in transmission mode. The incident beam intensity (I_o) was measured with a N_2-filled ion chamber and the transmission spectra were measured with ion chambers filled with an 80% N_2-20% Ar gas mixture. Both the Zr K- and Y K-edge spectra were calibrated using Zr metal foil, having a known Zr K-edge absorption energy of 17998 eV [154]. The Zr metal foil spectrum was measured concurrently with the Zr K-edge spectra from the samples. During collection of the Y K-edge spectra, Zr metal foil XAS spectra were measured separately for calibration. The X-ray absorption near-edge (XANES) region of the Zr K- and Y K-edge spectra were measured using a 0.3 eV step through the edge. The extended X-ray absorption fine structure (EXAFS) region of the Zr K-edge spectra was measured to k = 15 and the EXAFS of the Y K-edge was measured to k = 14.

The Nd L_3-edge spectra were collected in transmission mode and the incident beam intensity was measured with an ion chamber filled with an 80% He-20% N_2 gas mixture. The transmission spectra were collected using N_2 filled ion chambers. The spectra were calibrated using a Mn foil, which was measured separately and has a known absorption-edge energy of 6539 eV [154]. The Nd L_3-edge XANES region was measured using a 0.15 eV step through the edge and measured to k = 10.5. (The Nd L_3-edge is limited by the presence of the Nd L_2-edge at 6722 eV.) All XAS spectra discussed in this article were normalized and analyzed using the Demeter software suite (i.e., Artemis and Athena) [155].

3.2.3.2 Analysis of Zr K- and Y K-edge EXAFS Spectra

The EXAFS spectra were analyzed by fitting the parameters of the standard EXAFS equation 3.1:

$$\chi(k) = \sum_j \frac{N_j S_o^2}{kR_j^2} F_j(k) e^{-2\sigma_j^2 k^2} e^{-2R_j/\lambda} \sin(2kR_j + \phi_j(k)) \tag{3.1}$$

where N_j is number of j^{th} atoms at a distance Rj from the absorbing atomic centre, $F_j(k)$ is the backscattering function, $\sigma_j{}^2$ is the Debye-Waller Factor, and ϕj(k) is the phase-shift function of the jth atom. $F_j(k)$ describes how strongly the photoelectron scatters off the neighboring atom and $\phi_j(k)$ describes how the phase of the photoelectron shifts upon scattering. Both functions are dependent on the neighbouring atom atomic number (Z), which makes the EXAFS phenomenon chemically sensitive [178]. $S_o{}^2$ is the amplitude factor and λ is the inelastic mean-free path of the photoelectron [178]. N_j is equivalent to the coordination number for single-scattering paths, and will be referred to here as CN (i.e., coordination number). The EXAFS spectra were analyzed by calculating $F_j(k)$, $\phi_j(k)$ and λ for each set of scattering pairs in a given cluster using the FEFF6 code [179]. The other parameters were fit using a least-squares refinement as described below using the program Artemis, which is included in the Demeter software suite [155].

A scattering cluster was generated using the cubic zirconium structure with lattice constants determined from the powder XRD patterns (*vide infra*). An appropriate amount of Zr in the second coordination shell was replaced by Nd before conducting the FEFF calculation. Multiple calculations with Nd located at different sites were performed, and it was determined that the results of the FEFF calculations were independent of the locations of the Nd substitutions. Zr and Y were treated as equivalent atoms in this model, as the atomic numbers of Y and Zr (39 and 40, respectively) were similar and no significant changes in the scattering amplitude and phase shift functions were observed [180]. The model was constructed using four single scattering paths. The single scattering paths were the nearest neighbor Zr–O path, the next-nearest neighbor Zr–Zr/Y and Zr–Nd paths, and the third shell Zr–O scattering path (labelled here as Zr–O2). The CN of each scattering path was set manually. The amplitude factor, $S_o{}^2$, and energy shift, ΔE_o, were fitted across all scattering paths. The changes in the scattering path lengths, ΔR, and the Debye-Waller factor, σ^2, of each single-scattering path were individually fitted. In addition to the single-scattering paths, two multi-scattering paths corresponding to the three-legged Zr–O–Zr/Y and Zr–O–Nd scattering paths were also fitted. The changes in multi-scattering path lengths were modelled as $2\Delta R_{Zr–O}$+ $\Delta R_{Zr–Zr/Y/Nd}$, and the Debye-Waller factors were modelled as $2\sigma^2{}_{Zr–O} + \sigma^2{}_{Zr–Zr/Y/Nd}$.

The central Zr atom in the scattering cluster was replaced by Y in the model used to fit the Y K-edge spectra. The Y K-edge EXAFS spectra were fitted using a model similar to the one used to fit the Zr K-edge spectra. The Y K-edge spectra were fitted using Y–O, Y–Zr/Y, Y–Nd single scattering paths, and the third shell Y–O single scattering paths (labelled as Y–O2). The Y–O–Y/Zr and Y–O–Nd multi-scattering paths were also included in the fit. The CN was set manually in all cases. The restraints used for the multi-scattering paths were analogous to those used to fit the Zr K-edge.

3.2.3.3 Zr L_3-edge XANES

Zr L_3-edge XANES spectra were collected using the Soft X-ray Microcharacterization Beamline (SXRMB, 06B1-01) located at the Canadian Light Source (CLS). The beamline has a photon flux of >1 x 10^{11} photons/s and provides a resolution of $\sim$0.25 eV when using a Si (111) crystal monochromator at X-ray energies less than 2500 eV [181]. Samples were prepared by applying the finely ground powder to Kapton tape and adhering the Kapton tape onto the sample holder using double-sided C tape. Spectra were measured in total electron yield (TEY) mode using a 0.10 eV step through the absorption edge. Spectra were calibrated using Zr foil, which has a known Zr L_3-edge absorption energy of 2223 eV [154].

3.3 Results

3.3.1 Powder X-ray Diffraction

Powder XRD patterns from the as-synthesized and annealed compounds are presented in Figure 3.1, and Figures B.1 and B.2 in Appendix B. The unit-cell parameters and phase quantification of these materials was determined by Rietveld refinement, and the results of this analysis are summarized in Table 3.1 and Table B.1 in Appendix B. The size of the unit cell decreased linearly as the Y content increased at constant Zr concentrations in $Nd_xY_yZr_{1-x-y}O_{2-\delta}$, consistent with Vegard's Law [182]. No significant changes in the unit cell parameters were observed when any of the

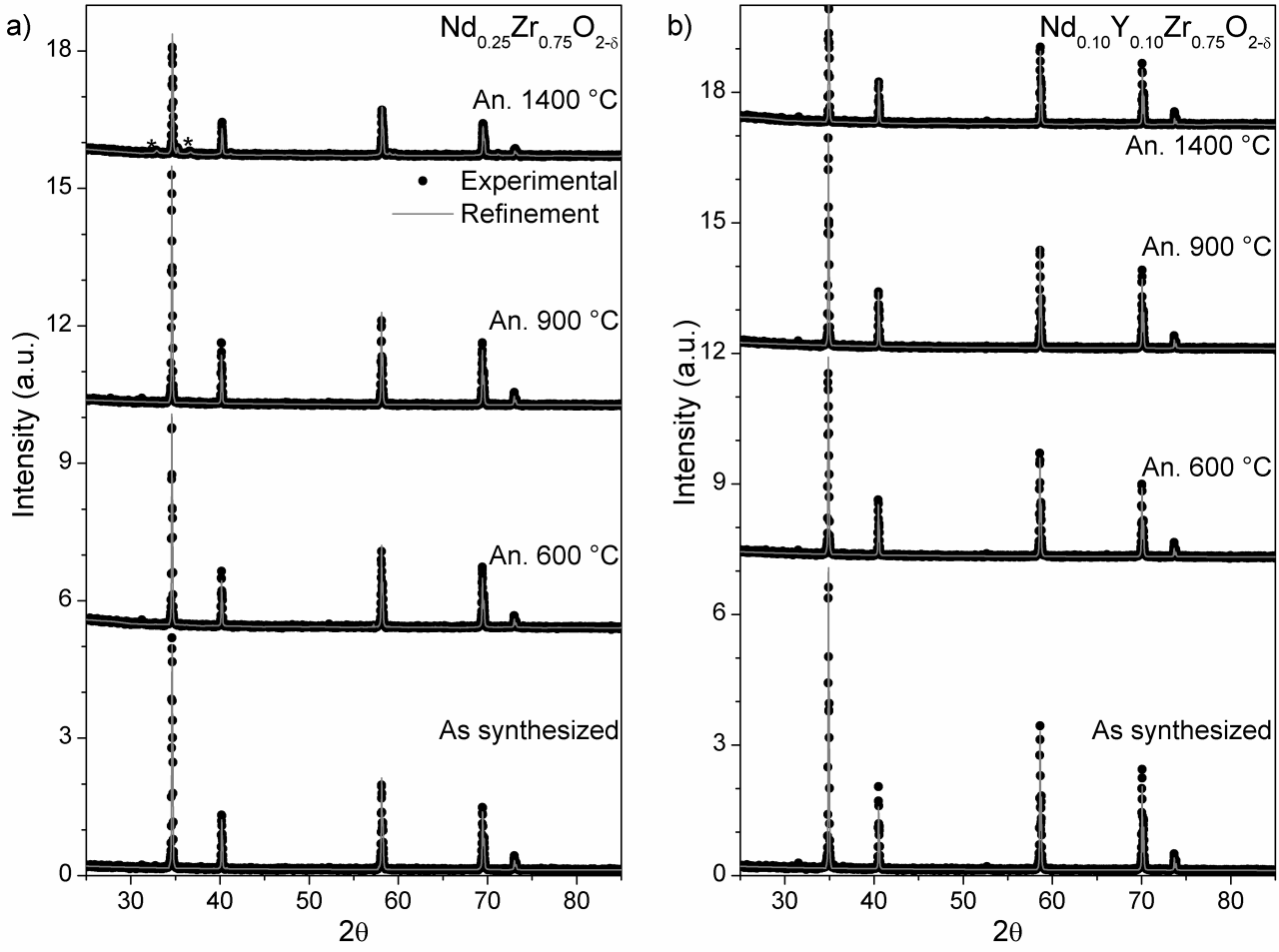

Figure 3.1: The powder X-ray diffraction patterns of the as-synthesized and annealed materials from (a) $Nd_{0.25}Zr_{0.75}O_{2-\delta}$ and (b) $Nd_{0.10}Y_{0.10}Zr_{0.80}O_{2-\delta}$ are plotted along with patterns generated by Rietveld refinement of the data. (Annealed materials are labelled as An.) The intensities of the (220) reflections found at ∼58° and the (311) reflections found at ∼69.6° were generally underfit by the simulated pattern, which may indicate there was a deviation from the ideal stoichiometry in these materials. The XRD patterns from $Nd_{0.25}Zr_{0.75}O_{2-\delta}$ indicate that a small amount of monoclinic ZrO_2 phase was formed when the material was annealed at 1400 °C as shown by the peaks marked with asterisks. No changes in the diffraction patterns were observed when the $Nd_{0.10}Y_{0.10}Zr_{0.80}O_{2-\delta}$ material was annealed.

Table 3.1: Summary of powder XRD Rietveld Refinement Results

	As-synthesized	Annealed 1400 °C
$Nd_{0.25}Zr_{0.75}O_{1.88}$		
R_{wp}[a]	7.14	9.00
Unit Cell[b]	5.2089(7)	5.2060(1)
Wt. Fraction	100% Cubic	84.5 % Cubic
		11.3% Monoclinic
		4.2% Tetragonal
$Nd_{0.20}Y_{0.05}Zr_{0.75}O_{1.88}$		
R_{wp}[a]	7.05	12.29
Unit Cell[b]	5.1977(6)	5.1932(1)
Wt. Fraction	100% Cubic	100 % Cubic
$Nd_{0.05}Y_{0.20}Zr_{0.75}O_{1.88}$		
R_{wp}[a]	8.66	12.74
Unit Cell[b]	5.1658(6)	5.1639(1)
Wt. Fraction	100% Cubic	100 % Cubic
$Y_{0.25}Zr_{0.75}O_{1.88}$		
R_{wp}[a]	7.41	9.38
Unit Cell[b]	5.1555(7)	5.1494(1)
Wt. Fraction	100% Cubic	100 % Cubic

[a] $R_{wp} = \sum w_i(y_{io} - y_{ic})^2 / \sum w_i y_{io}$; w_i= i^{th} comp. wt. fraction; y_{ic}=calculated intensity; y_{io} = diffraction pattern intensity
[b] Cubic unit cell parameter

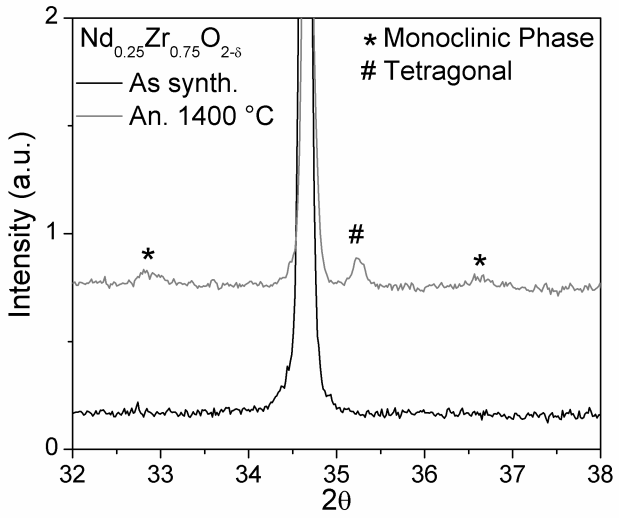

Figure 3.2: The diffraction patterns from as-synthesized $Nd_{0.25}Zr_{0.75}O_{2-\delta}$ and $Nd_{0.25}Zr_{0.75}O_{2-\delta}$ annealed at 1400 °C are presented. The diffraction patterns show that small amounts of tetragonal and monoclinic ZrO_2 are formed when $Nd_{0.25}Zr_{0.75}O_{2-\delta}$ is annealed at 1400 °C.

materials synthesized at 1500 °C were subsequently annealed at temperatures up to 1400 °C.

The calculated pattern obtained by Rietveld refinement consistently underfitted the intensities of the (311) and (222) peaks found at ∼69.6° and ∼73.2°, respectively. Changes from the ideal site occupancies based on the ideal stoichiometry of each material could affect the intensities of these reflections, accounting for the mismatch in peak intensities. Additionally, a slight preferential orientation away from the (100) direction was observed in several compounds. (The preferred orientation factor varied from 0.93 to 1.02.)

In general, all of the ternary $Nd_xZr_{1-x}O_{2-\delta}$ materials studied that were synthesized at 1500 °C were stable up to and including a post-annealing temperature of 900 °C. However, two peaks at ∼32.8° and 36.7° associated with monoclinic ZrO_2 and one at ∼34.3° associated with tetragonal ZrO_2 were observed when $Nd_{0.25}Zr_{0.75}O_{1.88}$ was annealed at 1400 °C (Figure 3.2). The concentrations of each phase in this system were determined to be 11.3% the monoclinic phase, 4.2% the tetragonal phase, and 84.5% the cubic phase (see Table B.1). This result indicated that the cubic structure of the ternary Nd-stabilized zirconia sample was not stable when annealed at this temperature. No peaks associated with lower-symmetry zirconia phases were observed when the quaternary Nd-YSZ materials were annealed at 1400 °C (cf. Figure 3.1b, Figures B.1 and B.2).

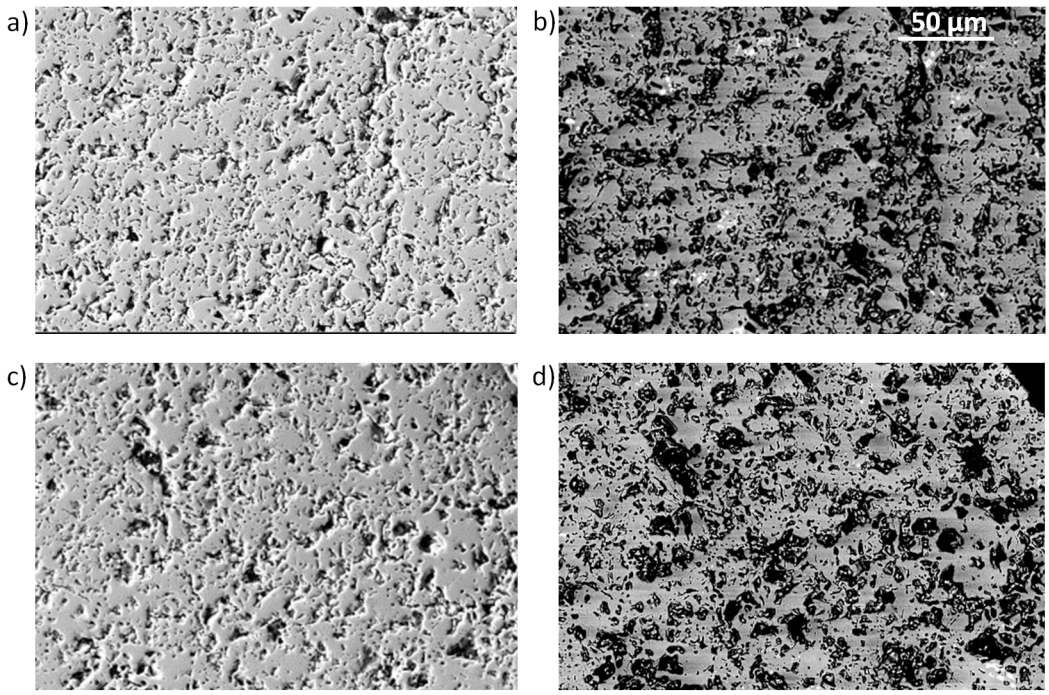

Figure 3.3: Secondary electron micrographs from (a) as-synthesized $Nd_{0.25}Zr_{0.75}O_{1.88}$ and (c) $Nd_{0.25}Zr_{0.75}O_{1.88}$ annealed at 1400 °C are presented. The backscattering electron micrographs from (b) as-synthesized $Nd_{0.25}Zr_{0.75}O_{1.88}$ and (d) $Nd_{0.25}Zr_{0.75}O_{1.88}$ annealed at 1400 °C are also presented. The secondary electron images show that there were no significant changes in the pellet surface when the materials were annealed. Bright spots in the backscattered election images indicate that Nd-rich inclusions were present in these materials. A 50 μm scale bar is included in (b) and the scale for all the images is the same.

The powder XRD results showed that the long-range cubic fluorite structure can be stabilized by the addition of a small amount of Y^{3+} to the $Nd_xZr_{1-x}O_{2-\delta}$ system.

3.3.2 SEM and EDS

SEM micrographs were collected from several of the pellets and these are presented in Figure 3.3 and Figures B.3-B.7 in Appendix B. The micrographs were collected in secondary electron (SE; Figure 3.3a,c) and backscattering electron (BSE; Figure 3.3b,d) modes, which allowed for an examination of both the surface topography and the distribution of Nd in the sample. No significant changes in the porosity or topography of any of the pellet surfaces were observed when the $Nd_xY_yZr_{1-x-y}O_{2-\delta}$ materials were annealed at 1400 °C (Figure 3.3a,c, Figures B.3-B.7). This observation indicates that the pellets did not crack or degrade during the annealing process.

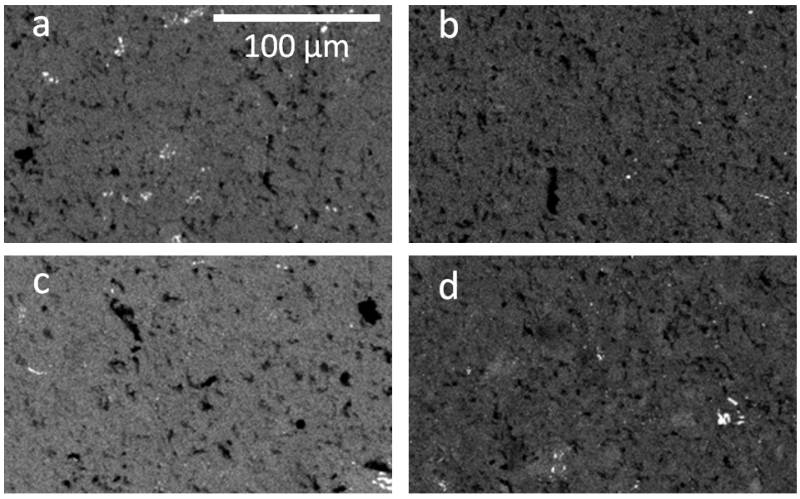

Figure 3.4: Nd L_α EDS maps from (a) as-synthesized $Nd_{0.25}Zr_{0.75}O_{1.88}$, (b) as-synthesized $Nd_{0.10}Y_{0.10}Zr_{0.80}O_{1.90}$, (c) $Nd_{0.25}Zr_{0.75}O_{1.88}$ annealed at 1400 °C, and (d) $Nd_{0.10}Y_{0.10}Zr_{0.80}O_{1.90}$ annealed at 1400 °C are presented. The maps were collected in the same region and at the same magnification as the micrographs presented in Figure 3.3. These maps confirm that Nd was not homogenously distributed in these materials. A 100 μm scale bar is included in (a) and the scale for all the images is the same.

Several bright spots were observed in the BSE images from both the as-synthesized and annealed $Nd_xY_yZr_{1-x-y}O_{2-\delta}$ materials (Figure 3.3b,d, Figures B.3-B.7). The bright spots are indicative of regions of high Nd concentration because Nd scatters electrons much more efficiently than Zr or Y due to the higher atomic number of Nd. The heterogeneous distribution of Nd within the materials was confirmed by the Nd L_α EDS maps, as shown in Figure 3.4 and Figures B.3-B.7. The EDS maps show that no significant change in the Nd distribution occurred upon annealing.

The Zr L_α EDS maps presented in Figure 3.5 showed that there was a significant segregation of Zr in the ternary $Nd_xZr_{1-x}O_{2-\delta}$ materials, and the number of Zr inclusions increased when the materials were annealed at 1400 °C. The presence of Zr inclusions in $Nd_xZr_{1-x}O_{2-\delta}$ could be indicative of the formation of small islands of monoclinic ZrO_2, which is consistent with the powder XRD results that showed monoclinic and tetragonal ZrO_2 phases were formed when $Nd_{0.25}Zr_{0.75}O_{1.88}$ was annealed at 1400 °C (*vide supra*). In contrast, no obvious Zr inclusions were observed in the Zr EDS maps from any of the quaternary $Nd_xY_yZr_{1-x-y}O_{2-\delta}$ materials. These results indicate that

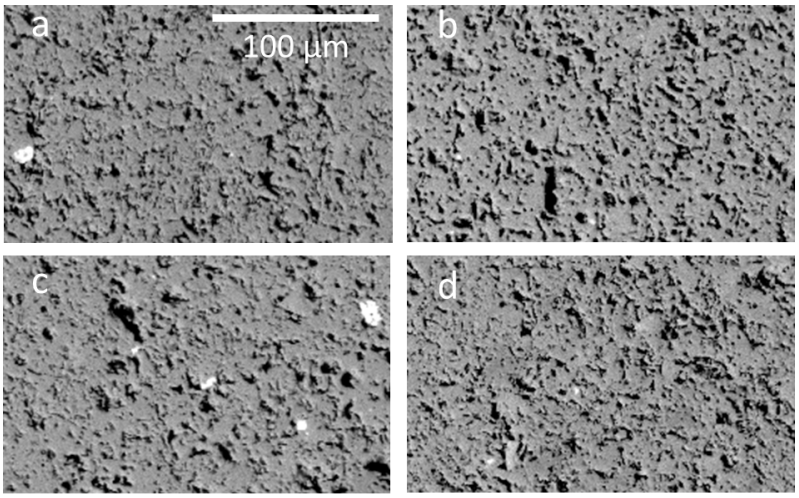

Figure 3.5: Zr L_α EDS maps from (a) as-synthesized $Nd_{0.25}Zr_{0.75}O_{1.88}$, (b) as-synthesized $Nd_{0.10}Y_{0.10}Zr_{0.80}O_{1.90}$, (c) $Nd_{0.25}Zr_{0.75}O_{1.88}$ annealed at 1400 °C, and (d) $Nd_{0.10}Y_{0.10}Zr_{0.80}O_{1.90}$ annealed at 1400 °C are presented. The maps were collected in the same region and at the same magnification as the micrographs presented in Figure 3.3. The maps show that Zr was not homogenously distributed in the $Nd_{0.25}Zr_{0.75}O_{1.88}$ materials. A 100 μm scale bar is included in (a) and the scale for all the images is the same.

the addition of a small amount of Y will increase the thermal stability of $Nd_xZr_{1-x-y}O_{2-\delta}$ materials.

3.3.3 Zr K-edge XAS

3.3.3.1 XANES

The Zr K-edge XANES spectra collected from the as-synthesized and annealed $Nd_xY_yZr_{1-x-y}O_{2-\delta}$ compounds are presented in Figure 3.6 and Figure B.8 in Appendix B. Three features were observed in these spectra, which are labelled as A, B, and B' in Figure 3.6a. Feature A is attributed to dipole-forbidden (quadrapolar) Zr 1s $\rightarrow$ Zr 3d transitions, and features B and B' are attributed to the dipole-allowed Zr 1s $\rightarrow$ Zr 4p transitions [183, 184]. The Zr K-edge spectra did not change when the composition was changed (Figure 3.6a). However, a small increase in the intensity of the feature located at $\sim$18020 eV was observed when $Nd_{0.25}Zr_{0.75}O_{2-\delta}$ was annealed at 1400 °C (Figure 3.6b). This change can be understood by comparing these spectra to the spectra collected from tetragonal ZrO_2 ($Y_{0.09}Zr_{0.91}O_{1.96}$) and monoclinic ZrO_2 (Figure 3.6c). The energy difference

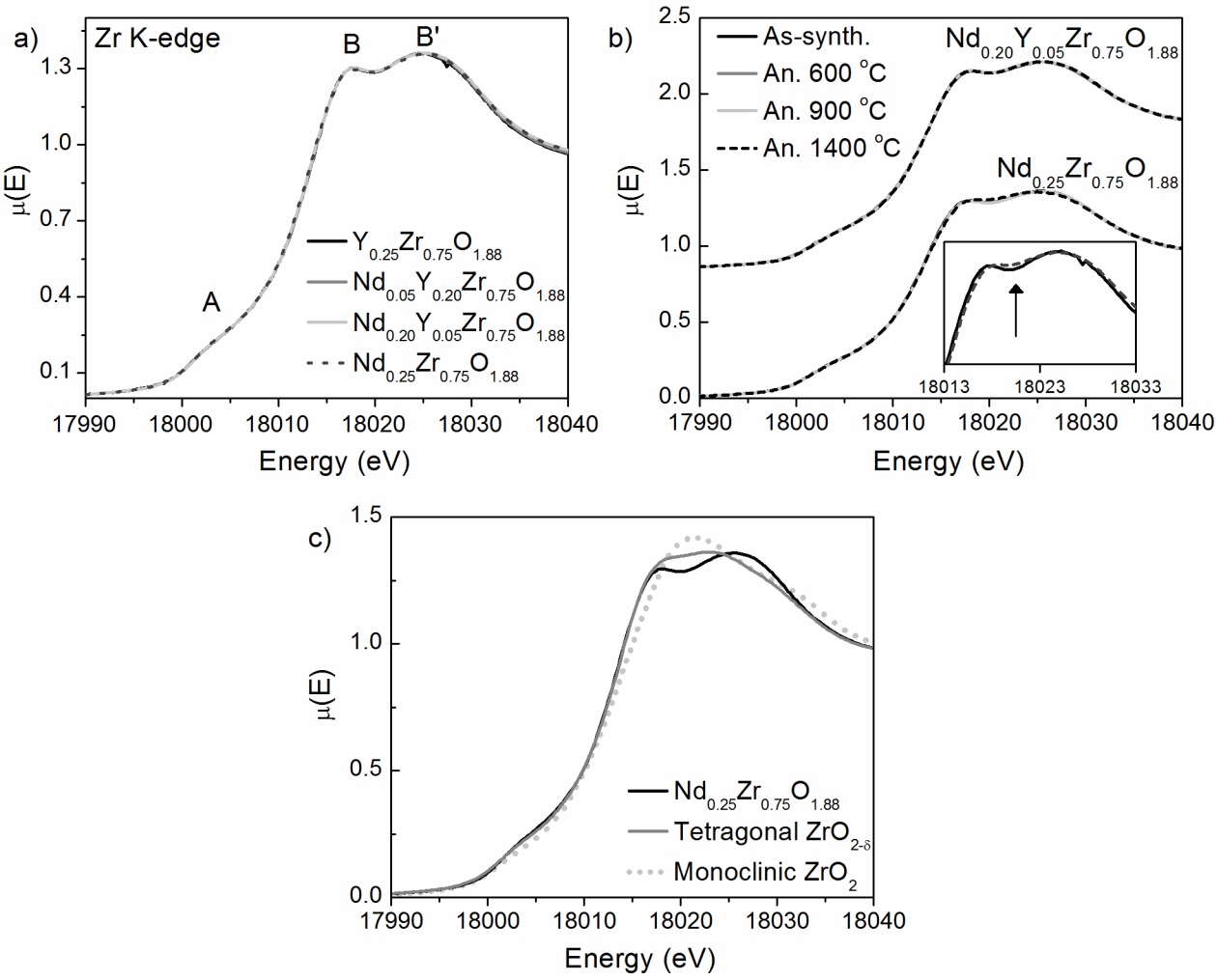

Figure 3.6: (a) Zr K-edge XANES spectra from the as-synthesized $Nd_xY_yZr_{1-x-y}O_{2-\delta}$ materials are presented. Three features, A, B, and B' were observed and correspond to quadrapolar (A) and dipolar (B, B') transitions. The Zr K-edge spectra did not change with changes in composition. (b) The Zr K-edge XANES spectra from the as-synthesized and annealed $Nd_{0.25}Zr_{0.75}O_{1.88}$ and $Nd_{0.20}Y_{0.05}Zr_{0.80}O_{1.90}$ materials are compared. A slight increase in intensity was observed at around 18025 eV when the $Nd_{0.25}Zr_{0.75}O_{1.88}$ material was annealed at 1400 °C and peak B' shifted to slightly lower energy. Inset: A close-up view of the change observed upon annealing in the main-edge region of the spectra from as-synthesized $Nd_{0.25}Zr_{0.75}O_{1.88}$ and $Nd_{0.25}Zr_{0.75}O_{1.88}$ annealed at 1400 °C. (c) The Zr K-edge XANES spectra from $Nd_{0.25}Zr_{0.75}O_{1.88}$, tetragonal ZrO_2 ($Y_{0.09}Zr_{0.81}O_{1.96}$), and monoclinic ZrO_2 are compared. The separation of the features B and B' decreased with decreasing symmetry of the unit cell.

between features B and B' decreases as the symmetry of the structure decreases, resulting in an increase in the intensity at ~18020 eV. Based on this comparison to the spectra from the Zr standards, the change in the spectra from $Nd_{0.25}Zr_{0.75}O_{1.88}$ upon annealing is attributed to the formation of tetragonal and/or monoclinic ZrO_2. This result is consistent with the powder XRD results which showed that monoclinic and tetragonal ZrO_2 was formed when the $Nd_{0.25}Zr_{0.75}O_{1.88}$ material was annealed at 1400 °C (*vide supra*). No changes were observed when the other $Nd_xY_yZr_{1-x-y}O_{2-\delta}$ materials were annealed at temperatures up to 1400 °C (cf. Figure 3.6b, Figure B.8), which is also consistent with the powder XRD results. These results show that the addition of Y^{3+} stabilized the cubic structure of $Nd_xY_yZr_{1-x-y}O_{2-\delta}$.

3.3.3.2 EXAFS

The Zr K-edge EXAFS spectra were collected from the as-synthesized and annealed $Nd_xY_yZr_{1-x-y}O_{2-\delta}$ materials to better understand how the local structure around Zr changed with composition and annealing temperature. The Fourier transformed EXAFS spectra from the as-synthesized samples are presented in Figure 3.7a. These spectra have two prominent peaks, which are labelled as C and D. Peak C is attributed to scattering in the first shell between Zr and the nearest-neighbour O atoms, and peak D is attributed to the second shell scattering path between Zr and the next-nearest-neighbour (NNN) Zr, Y, and Nd atoms. The intensity of Peak C did not change with Nd content while the intensity of peak D decreased with increasing Nd content.

It has been previously suggested that the decrease in the intensity of feature D is due to an increase in the disorder of the second shell cations [185]. However, an examination of the real portion of the Fourier transformed EXAFS spectra, shown in Figure 3.7b, indicates that this decrease may in fact be due to changes in the backscattering amplitude function ($F_j(k)$) and phase-shift function ($\phi_j(k)$) of the NNN atoms. It can clearly be seen from the plots in Figure 3.7b and 3.7c that the amplitude of the Zr–Zr/Y/Nd scattering path decreases with increasing Nd content, and that the decrease in feature D is due to changes in the phase-shift function ($\phi_j(k)$) and backscattering amplitude function ($F_j(k)$) between the Zr–Nd and Zr–Zr/Y scattering paths. (The Zr-Zr and Zr-Y

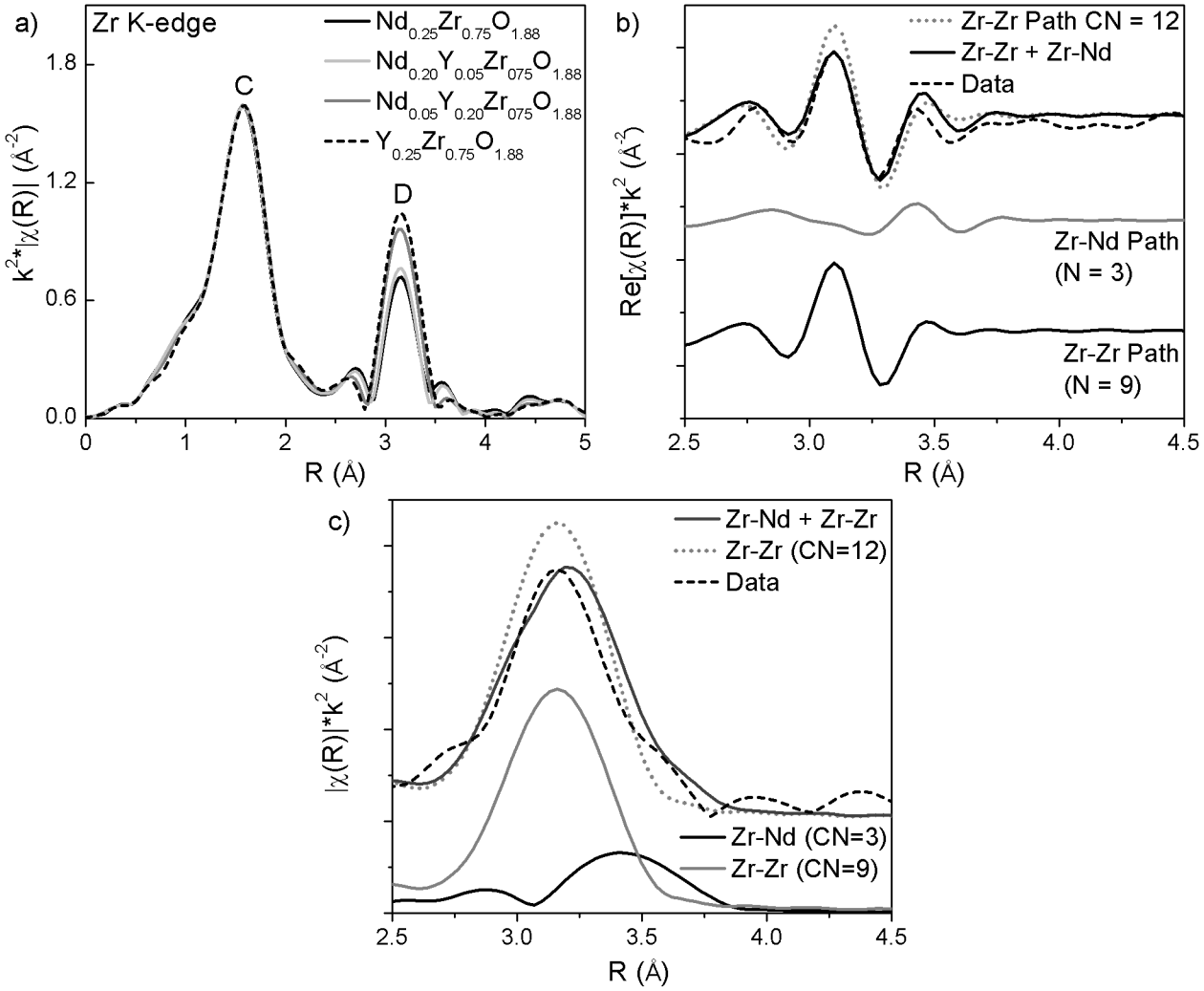

Figure 3.7: (a) The magnitudes of the Fourier-transformed Zr K-edge EXAFS spectra from the as-synthesized materials are compared. Two features were observed in these spectra, labelled as C and D. Feature C was due to Zr–O single scattering paths and feature D was due to Zr-Zr/Y/Nd single scattering paths. Feature C was independent of composition while feature D increased with decreasing Nd content. (b) The real part of the Fourier transformed Zr K-edge EXAFS spectrum from $Nd_{0.25}Zr_{0.75}O_{1.88}$ along with the real portions of the contributions from the Zr–Zr (CN=9) and Zr –Nd (CN=3) scattering paths are shown. The sum of these scattering path contributions is compared to the contribution from a Zr–Zr path with CN = 12. The oscillations in the summed scattering path are reduced compared to the Zr–Zr scattering path with CN = 12 and better match the data. (c) The magnitudes of the scattering path contributions from the Zr–Zr and Zr–Nd single scattering paths (i.e., Feature D) are compared with the Zr K-edge EXAFS spectrum from $Nd_{0.25}Zr_{0.75}O_{1.88}$.

Table 3.2: Zr K-edge EXAFS Results

$Nd_{0.25}Zr_{0.75}O_{1.88}$						
	As-synthesized			Annealed 1400 °C		
	S_o^2 = 0.8(1), ΔE = -4(1) eV			S_o^2 = 0.9(1), ΔE = -4(1) eV		
	R_{fit} = 0.030			R_{fit} = 0.028		
	CN	R(Å)	σ^2	CN	R(Å)	σ^2
Zr - O	7	2.15(1)	0.007(1)	7	2.16(1)	0.007(1)
Zr - Zr	9	3.55(1)	0.010(1)	9	3.54(1)	0.011(1)
Zr - Nd	3	3.72(4)	0.010(5)	3	3.8(1)	0.02(2)
Zr - O2	22	4.38(5)	0.04(2)	33	4.43(5)	0.04(2)
$Nd_{0.20}Y_{0.05}Zr_{0.75}O_{1.88}$						
	As-synthesized			Annealed 1400 °C		
	S_o^2 = 0.87(9), ΔE = -4(1) eV			S_o^2 = 0.93(9), ΔE = -2(1) eV		
	R_{fit} = 0.028			R_{fit} = 0.020		
	CN	R(Å)	σ^2	CN	R(Å)	σ^2
Zr - O	7	2.16(1)	0.006(1)	7	2.15(1)	0.008(2)
Zr - Zr	9.6	3.56(2)	0.011(2)	9.6	3.56(1)	0.012(2)
Zr - Nd	2.4	3.8(1)	0.013(9)	2.4	3.71(3)	0.009(4)
Zr - O2	22	4.40(6)	0.04(2)	22	4.34(7)	0.04(2)

scattering paths were treated as being identical during this analysis given the similar atomic numbers of Zr and Y.) Therefore, the change in the intensity of peak D is attributed to the differences between the Zr–Zr and Zr–Nd phase-shift and amplitude functions, and is not due to structural changes.

The changes observed in the EXAFS spectra from $Nd_{0.25}Zr_{0.75}O_{1.88}$ when it was annealed at different temperatures are presented in Figure 3.8a. Only minimal changes in the intensity of feature C were observed; however, the intensity and peak width of feature D decreased when the material was annealed at 1400 °C. This change likely occurred due to increased disordering in the second shell (*vide infra*). In contrast, only small changes in feature C and almost no changes in feature D were observed when the quaternary $Nd_xY_yZr_{1-x-y}O_{2-\delta}$ materials were annealed (Figure B.9).

The results of the fits of the EXAFS data are presented in Table 3.2 and Table B.2, and are plotted in Figure 3.8 and Figures B.10-B.16in Appendix B. The Zr–O bond length was determined to be 2.16 ± 0.01 Å in all the materials studied, which is in good agreement with previously reported

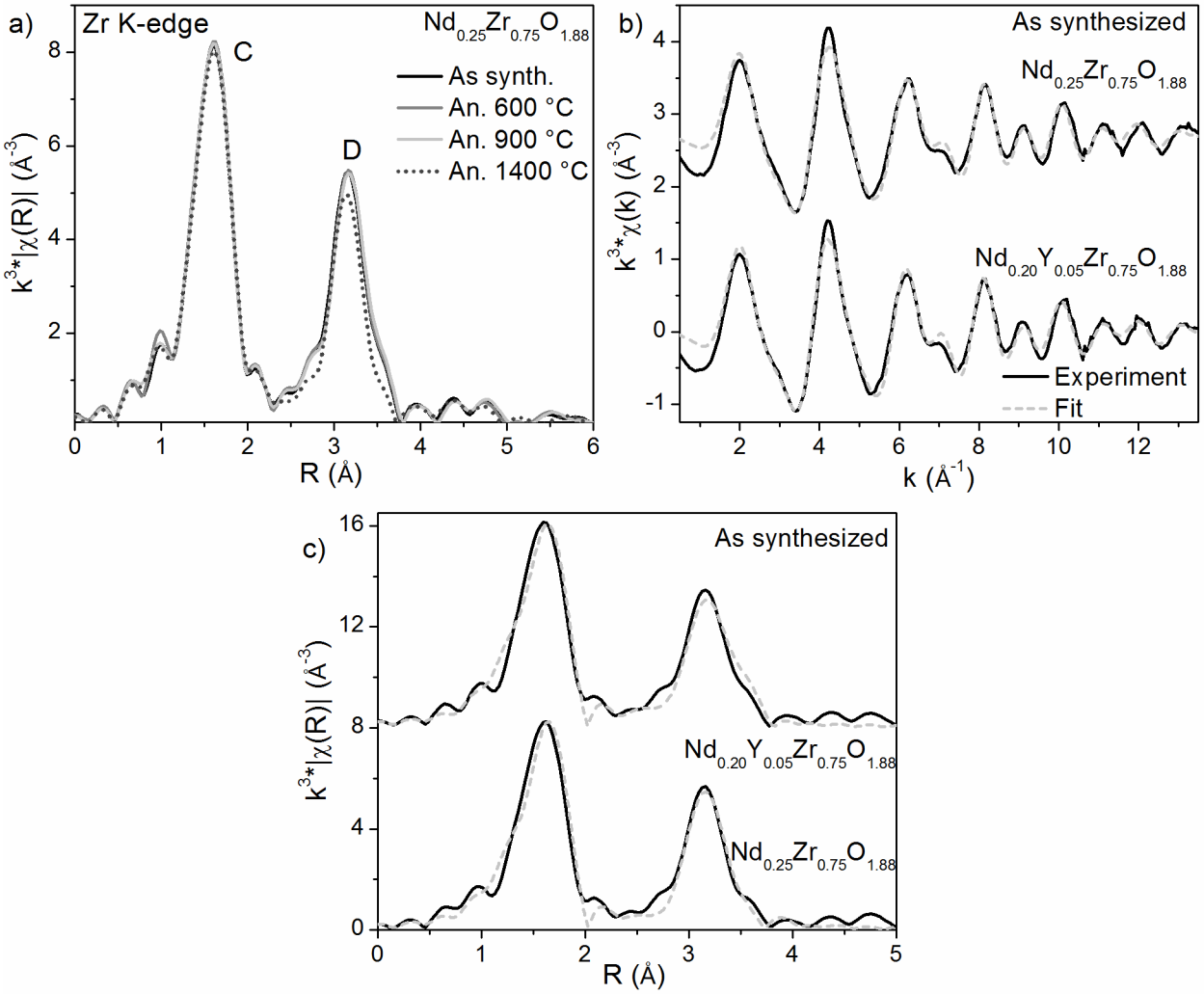

Figure 3.8: (a) The magnitudes of the Fourier-transfromed Zr K-edge EXAFS spectra from the as-synthesized and annealed $Nd_{0.25}Zr_{0.75}O_{1.88}$ materials are compared. Feature C was relatively independent of annealing temperature while there was a decrease in the intensity of peak D when $Nd_{0.25}Zr_{0.75}O_{1.88}$ was annealed at 1400 °C. The EXAFS spectrum from the as-synthesized $Nd_{0.25}Zr_{0.75}O_{1.88}$ is compared with its fit in (b) k-space and (c) real space. Overall there is good agreement between the data and the fit.

results from cubic zirconia materials [101,180,186,187]. The Zr–O bond length and Debye Waller factor (σ^2) were independent of composition and annealing temperature, indicating that the local Zr–O coordination environment remained unchanged upon annealing. The Zr–Zr/Y bond lengths were determined to be 3.55 $\pm$ 0.01 Å, which is again in good agreement with previously reported results [180, 186]. The Zr–Nd bond length was found to vary between 3.7–3.8 Å. The Zr–Zr and Zr–Nd bond lengths are only slightly less than the bond length predicted using the ionic radii of Zr^{4+} and Nd^{3+} [121]. The Zr–O2 bond distance was found to be 4.34-4.43 Å, though the error for this value was found to be large ($\pm$0.07 Å). In general, the Zr–O2 scattering path did not contribute significantly to the fitted model of the EXAFS spectra.

The Debye-Waller factor of the Zr–Zr/Y scattering paths did not vary significantly with changes in composition or annealing temperature in all the materials studied. However, the Debye-Waller factor of the Zr–Nd path nearly doubled when the $Nd_{0.25}Zr_{0.75}O_{1.88}$ material was annealed at 1400 °C. The Debye-Waller factor contains contributions from both static disorder and thermal disorder, and an increased value indicates more disorder in the system [178]. The thermal disorder is expected to remain nearly constant as all spectra were collected at room temperature [188]. Therefore, the observed changes in the Debye-Waller factor are likely attributable to changes in the static disorder of the system. The EXAFS results indicate that while the local coordination environment around Zr remains relatively constant, the extended system becomes disordered when $Nd_{0.25}Zr_{0.75}O_{1.88}$ is heated at 1400 °C. The Zr K-edge EXAFS results also show that this disordering does not occur in the quaternary $Nd_xY_yZr_{1-x-y}O_{2-\delta}$ materials (see Table B.2 and Table B.2).

3.3.4 Zr L_3-edge XANES

Zr L_3-edge XANES spectra collected from several of the as-synthesized and annealed $Nd_xY_yZr_{1-x-y}O_{2-\delta}$ compounds, as well as monoclinic ZrO_2 are presented in Figure 3.9. The Zr L_3-edge is attributable to Zr 2p $\rightarrow$ Zr 4d transitions, and the two observed features (E and F in Figure 3.9) are due to the crystal field splitting of the Zr 4d states. Feature E is attributed to Zr 2p $\rightarrow$ Zr 4d e_g transitions while feature F is attributed to Zr 2p $\rightarrow$ Zr 4d $t_{2g}{}^*$ transitions [189, 190].

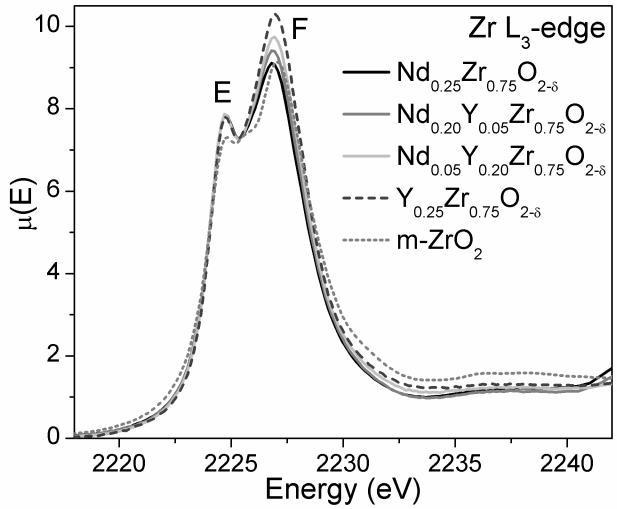

Figure 3.9: The Zr L_3-edge XANES spectra from the as-synthesized materials are plotted along with the spectrum from monoclinic ZrO_2. Features E and F arise from transitions to e_g and t_{2g}^* states, respectively. Feature F decreased as the Nd content decreased.

The features in the spectra from the $Nd_xY_yZr_{1-x-y}O_{2-\delta}$ materials were more intense and sharper than the features observed in the spectrum from monoclinic ZrO_2. Additionally, a feature observed at ~2225 eV in the monoclinic ZrO_2 spectrum is not present in the spectra from $Nd_xY_yZr_{1-x-y}O_{2-\delta}$. The intensity of Feature F was observed to increase as the amount of Nd in the $Nd_xY_yZr_{1-x-y}O_{2-\delta}$ materials decreased. The origin of these changes may be caused by a shift to a more symmetric coordination environment around the Zr centres. This increase in symmetry results in more degenerate 3d states, leading to narrower, more intense peaks [189]. These results indicate that the symmetry of the Zr coordination environment increased as Y replaced Nd in the $Nd_xY_yZr_{1-x-y}O_{2-\delta}$ system. The Zr L_3-edge is more sensitive to changes in the geometry of the Zr coordination environment than the Zr K-edge, which is why the Zr K-edge XANES and EXAFS spectra did not indicate there were changes in the local coordination environment. These results indicate that changes in the coordination geometry of Zr occurred when Y replaced Nd in the quaternary $Nd_xY_yZr_{1-x-y}O_{2-\delta}$ system.

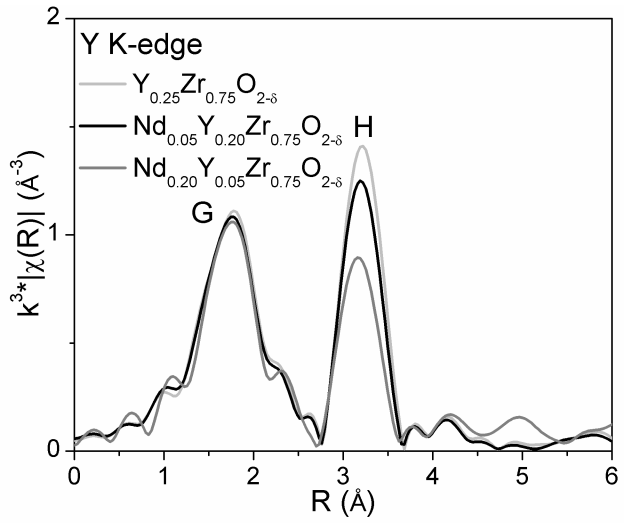

Figure 3.10: The magnitudes of the Fourier transformed Y K-edge EXAFS spectra from the as-synthesized materials are presented. Feature G arises due to Y-O single-scattering paths and feature H is attributed to Y Y/Zr/Nd single scattering paths. The intensity of both features increased with decreasing Nd content.

3.3.5 Y K-edge EXAFS

The EXAFS region of the Y K-edge spectra allows for an understanding of how the local structure around Y in the $Nd_xY_yZr_{1-x-y}O_{2-\delta}$ materials changed with both composition and annealing temperature. The Fourier transformed EXAFS spectra from several of the as-synthesized materials are presented in Figure 3.10. These spectra strongly resembled the Zr K-edge EXAFS spectra, and exhibited two main peaks, labelled as G and H. Similar to the Zr K-edge, peak G is attributed to first shell Y–O scattering paths and feature H is attributed to scattering between Y and the second-shell cation ions (i.e., Y, Zr, and Nd). The intensity of peak H decreased as the Nd content increased, and the intensity of peak G did not change with changing Nd content. The change in the intensity of peak H can be attributed to the difference in the scattering amplitude and phase shift functions of Nd compared to Y, similar to the Zr K-edge EXAFS spectra discussed in 3.3.3.2. The Fourier transform of the Y K-edge EXAFS spectra from the as-synthesized and annealed materials are compared in Figure 3.11a and Figure B.17. These comparisons show that no significant changes in the EXAFS spectra are observed when the materials were annealed. Therefore, it can be concluded that the Y coordination environment did not change with annealing temperature.

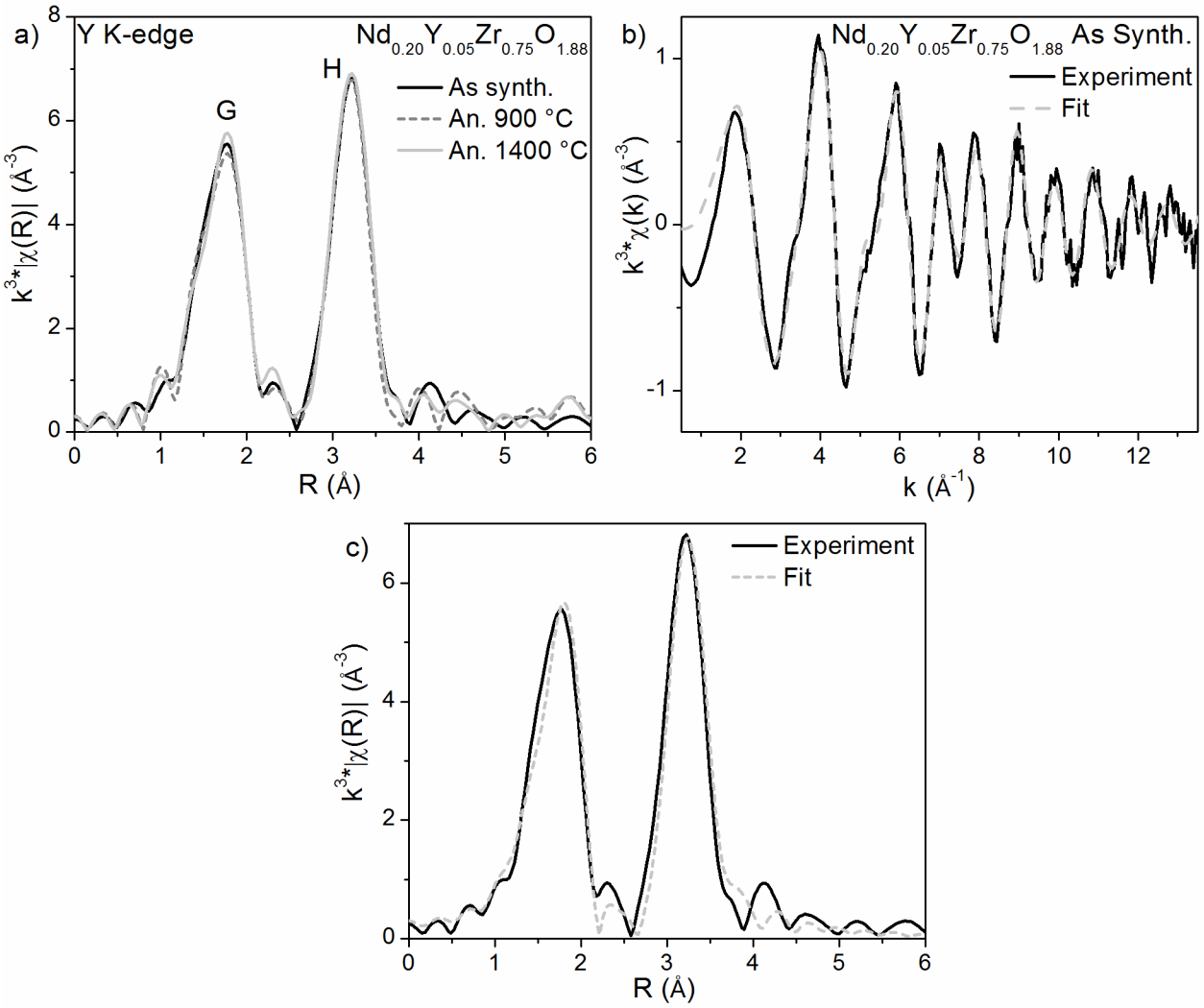

Figure 3.11: (a) The magnitudes of the Fourier transformed Y K-edge EXAFS spectra from the as-synthesized and annealed $Nd_{0.20}Y_{0.05}Zr_{0.75}O_{2-\delta}$ materials are plotted. Feature G changes slightly with annealing temperature while feature H was independent of annealing temperature. The EXAFS spectrum from the as-synthesized $Nd_{0.20}Y_{0.05}Zr_{0.75}O_{2-\delta}$ is compared with its fit in (b) k-space and (c) real space. Overall, there is good agreement between the data and the fit.

Table 3.3: Y K-edge EXAFS Fitting Results

$Y_{0.25}Zr_{0.75}O_{1.88}$									
	As-synthesized			Annealed 900 °C			Annealed 1400 °C		
	S_o^2 = 0.9(1), ΔE = -3(1) eV			S_o^2 = 1.2(2), ΔE = -6(1) eV			S_o^2 = 0.9(1), ΔE = -3(1) eV		
	R_{fit} = 0.033			R_{fit} = 0.011			R_{fit} = 0.033		
	CN	R(Å)	σ^2	CN	R(Å)	σ^2	CN	R(Å)	σ^2
Y - O	8	2.32(1)	0.009(2)	8	2.32(1)	0.012(2)	8	2.32(1)	0.008(2)
Y - Zr/Y	12	3.626(8)	0.008(1)	12	3.616(9)	0.009(1)	12	3.626(8)	0.007(1)
Y - O2	22	4.39(9)	0.03(2)	22	4.29(7)	0.027(8)	22	4.36(6)	0.02(1)
$Nd_{0.20}Y_{0.05}Zr_{0.75}O_{1.88}$									
	As-synthesized			Annealed 900 °C			Annealed 1400 °C		
	S_o^2 = 1.1(1), ΔE = -3(1) eV			S_o^2 = 0.77(8), ΔE = -4(1) eV			S_o^2 = 0.86(9), ΔE = -4(1) eV		
	R_{fit} = 0.022			R_{fit} = 0.018			R_{fit} = 0.010		
	CN	R(Å)	σ^2	CN	R(Å)	σ^2	CN	R(Å)	σ^2
Y - O	8	2.32(1)	0.009(2)	8	2.33(1)	0.009(2)	8	2.33(1)	0.009(1)
Y - Zr/Y	9.6	3.639(8)	0.008(1)	9.6	3.66(1)	0.008(2)	9.6	3.632(8)	0.0092(7)
Y - Nd	2.4	3.52(9)	0.02(2)	2.4	3.41(3)	0.005(2)	2.4	3.4(1)	0.03(2)
Y - O2	22	4.40(6)	0.03(1)	22	4.1(2)	0.1(1)	22	4.42(6)	0.03(1)

The EXAFS spectra were fitted using models similar to the ones constructed to analyze the Zr K-edge EXAFS spectra, and are plotted in Figure 3.11 and Figure B.18. The parameters determined from this fit are given in Table 3.3 and Table B.3 in Appendix B. The first shell Y–O bond distance was determined to be 2.33 Å, consistent with previous literature reports [100, 180, 185, 186]. This value is smaller than expected from the sum of the Y^{3+} and O^{2-} ionic radii when Y is in an eight-fold coordination environment, and, instead, this bond distance is more consistent with Y occupying a 7-fold coordination environment [100, 121, 180]. It has been previously suggested that the reduced Y–O bond distance is caused by compression of the Y–O polyhedra, and is not indicative of a reduced coordination number [100, 180]. The Debye-Waller factor (σ^2) was only slightly elevated (0.009 $Å^2$) when the CN was set to 8. However, σ^2 and CN are correlated, and an overly large CN would result in a large σ^2 value. Therefore, it is concluded here that the Y CN was 8. In all cases, the Y–O bond distance and σ^2 were independent of composition and annealing temperature, indicating that the Y-coordination environment was not sensitive to these variables.

The second shell Y–Zr/Y bond distance was determined to be 3.63±0.01 Å, and the bond length

was independent of both composition and annealing temperature. This value is within error of the 3.64 Å metal–metal bond distance determined from XRD and is only slightly contracted from the value calculated using the Zr–O and Y–O bond lengths determined from the EXAFS fits. In contrast, the Y–Nd bond distance in $Nd_{0.20}Y_{0.05}Zr_{0.75}O_{2-\delta}$ determined from the fit of the EXAFS data was found to be between 3.4-3.5 Å, which is significantly less than the expected value of 3.94 Å based on the Y^{3+} and Nd^{3+} ionic radii. The Debye-Waller factor (σ^2) of the Y–Nd shell was determined to be 0.02-0.03 $Å^2$, which is unreasonably large. The large σ^2 value shows that there is significant disorder in the second shell Y-Nd scattering paths. The large σ^2 value could also indicate that too large a CN was used, given that the CN and σ^2 are highly correlated. This likely indicates that Nd and Y were not homogeneously distributed, and that Nd preferentially occupied sites that were not adjacent to Y atoms.

The fitted Y–Nd bond distance is unreasonable within the fluorite structure, and likely represents a failure in the fitting model. However, a 3.4 Å Nd–Y bond distance is found in the structure of B-phase mixed RE_2O_3 sesquioxides (RE = Rare-earth, Y, Sc), and the fitted result could possibly indicate that such a phase is present here [191]. Calculated Y_2O_3-Nd_2O_3 phase diagrams also support the possible presence of a B-phase $Nd_{2-x}Y_xO_3$ type material as the B-phase is stabilized at Y_2O_3 mole fractions as low as 0.16 [192]. The presence of such a phase is also supported by a previous study of Y-doped CeO_2 by XRD [191]. If a B-phase $Nd_{2-x}Y_xO_3$ was formed in the materials studied here, it is likely that it would not be observable by conventional powder XRD given the low concentration and low symmetry of this phase, and further investigation is necessary to confirm if B-phase $Nd_{2-x}Y_xO_3$ is present in this system.

3.3.6 Nd L_3-edge XANES

The Nd L_3-edge XANES spectra were collected from several of the $Y_yNd_xZr_{1-x-y}O_{2-\delta}$ materials and these spectra are presented in Figure 3.12. A single, intense feature is observed in these spectra, which corresponds to excitation of the Nd 2p electrons to Nd 5d valence states [193]. There were no changes in the Nd L_3-edge XANES spectra when any of the as-synthesized $Nd_xY_yZr_{1-x-y}O_{2-\delta}$

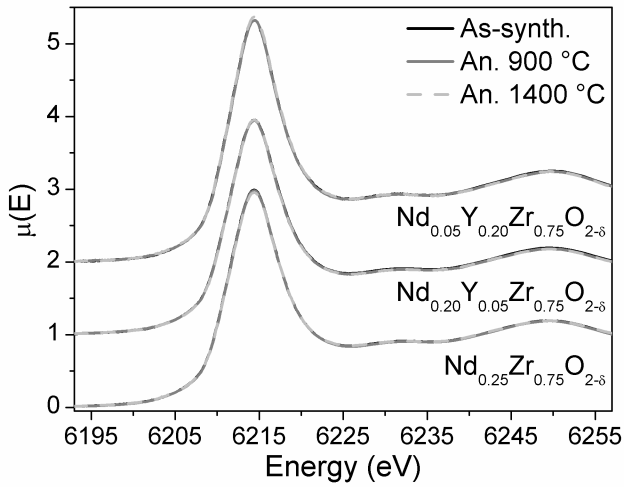

Figure 3.12: The Nd L_3-edge XANES spectra from as-synthesized and annealed $Nd_xY_yZr_{1-x-y}O_{2-\delta}$ materials are presented. The strong white-line feature at 6014 eV is due to Nd 2p→Nd 5d transitions. No changes in the spectra were observed between the as-synthesized and annealed materials.

materials were annealed (Figure 3.12b). This likely indicates that the local coordination environment around Nd was stable for all of the materials studied.

3.4 Discussion

The results presented above show that the $Nd_xZr_{1-x}O_{2-\delta}$ materials synthesized at 1500 °C undergoes a partial phase-transition to a lower-symmetry state when they are annealed at 1400 °C. This result is consistent with previously reported ternary Y_2O_3-Nd_2O_3-ZrO_2 phase diagrams calculated at 1400 °C and 1600 °C, which are presented in Figure 3.13 [194]. These phase diagrams showed that the range of Nd_2O_3-ZrO_2 mixtures that stabilized the fluorite phase decreased with decreasing temperature, and help explain how the materials synthesized at 1500 °C were not stable when annealed at 1400 °C.

The energy dispersive spectroscopy (EDS) maps (cf. Figure 3.4 and 3.5) showed that Nd inclusions were present in both the $Nd_xZr_{1-x}O_{2-\delta}$ and $Nd_xY_yZr_{1-x-y}O_{2-\delta}$ materials, and that Zr inclusions were present in the $Nd_xZr_{1-x}O_{2-\delta}$ materials. It is possible that the Nd and Zr inclusions were observed due to the intrinsic shortcomings of the synthetic process. Given that the materials

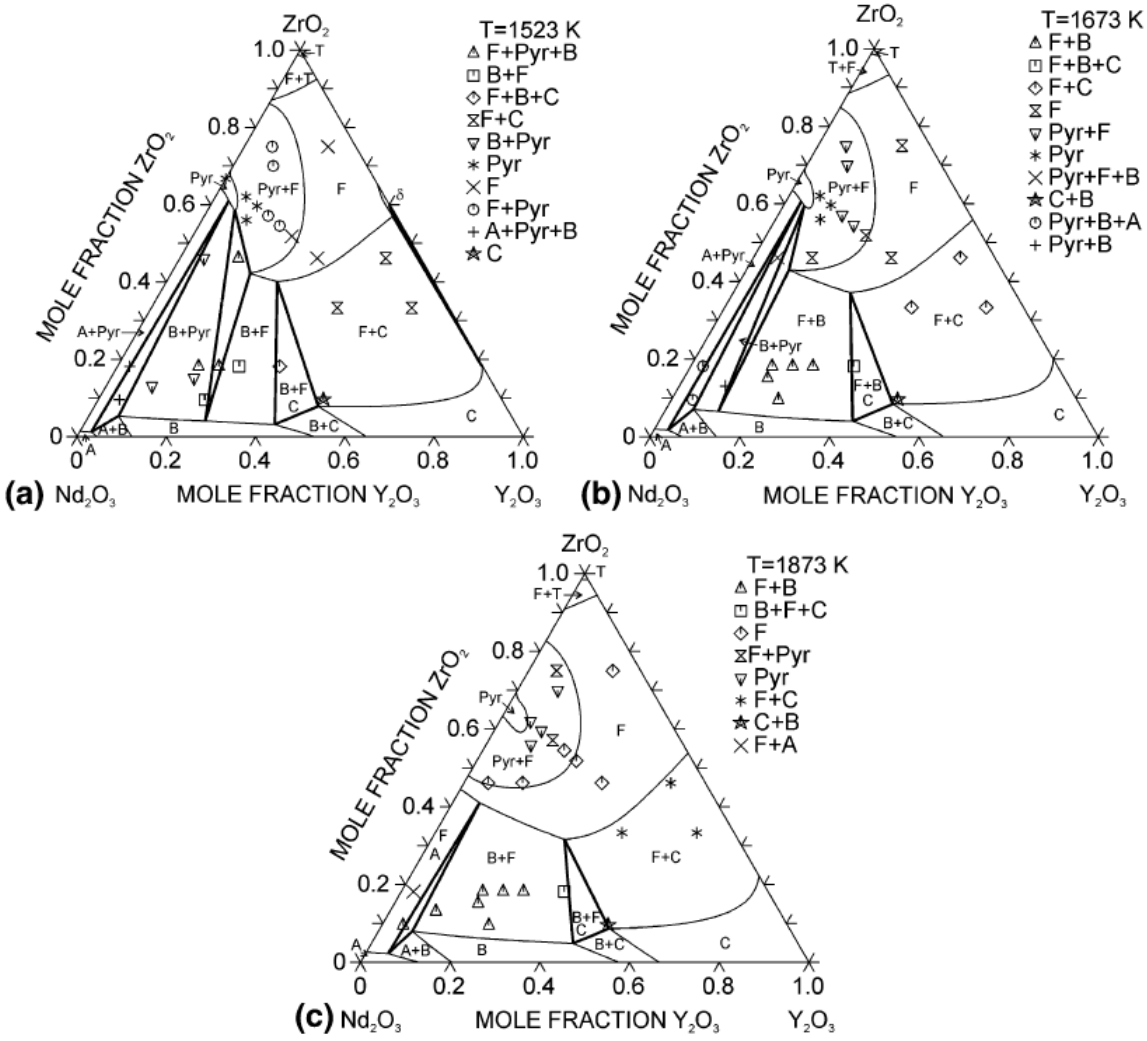

Figure 3.13: The isothermal sections of the ZrO_2-Nd_2O_3-Y_2O_3 system calculated based on thermodynamic parameters assessed in present study along with experimental data from present work: (a) 1523 K (1250 °C), (b) 1673 K (1400 °C), (c) 1873 K (1600 °C). Reproduced from the Journal of Phase Equilibria and Diffusion, 32, O. Fabrichnaya, G. Savinykh, G. Schreiber, H.J. Seifert "Phase Relations in the ZrO_2-Nd_2O_3-Y_2O_3 System: Experimental Study and Advanced Thermodynamic Modeling" 284-297, 2011, with permission from Springer.

were made via a high-temperature solid-state reaction using the binary oxides powders as starting materials, it is likely that the reaction kinetics were limited by the rate of solid-state diffusion. If the initial starting powders were not thoroughly mixed to a homogenous state, small heterogeneous regions would be expected as the Nd, Y, and Zr atoms will not be able to diffuse to a homogenous state within a reasonable time period. The SEM and EDS results highlight the difficulty of generating a true $Nd_xY_yZr_{1-x-y}O_{2-\delta}$ solid-solution, and the importance of the synthetic procedure when making these materials.

The fits of the Zr K-edge EXAFS spectra indicated that the σ^2 paramter of Zr–Nd scattering paths in the $Nd_{0.25}Zr_{0.75}O_{1.88}$ increased upon annealing at 1400 °C. These results indicate that the disorder between the metal centred polyhedra increased upon annealing, and suggest that Nd and Zr became further segregated upon annealing. Segregation of Zr and Nd upon annealing was also observed by EDS, and both Zr-rich and Nd-rich inclusions were observed in the annealed $Nd_{0.25}Zr_{0.75}O_{1.88}$ material. The powder XRD results showed that monoclinic and tetragonal zirconia phases were formed when $Nd_xZr_{1-x}O_{2-\delta}$ was annealed at 1400 °C, and these phases likely account for the Zr-rich inclusions. No Nd-rich phase was observed by powder XRD in any of the materials. This likely indicates that Nd-rich phase(s) were either present at concentrations below the XRD detection limit or adopted a low-symmetry crystal structure. The former seems more likely given that powder XRD is relatively insensitive to very low concentration phases [195]. The formation of Nd and Zr rich phases provides an explanation for the formation of monoclinic and tetragonal ZrO_2 that was observed upon annealing. Nd and Zr became further segregated upon annealing, and Zr-rich inclusions were formed. These inclusions contained an insufficient amount of Nd to allow for stabilization of the fluorite structure, resulting in the formation of lower-symmetry tetragonal and monoclinic phases. No tetragonal or monoclinic zirconia phases were observed in the $Nd_xY_yZr_{1-x-y}O_{2-\delta}$ materials and Zr inclusions were not observed when these materials were annealed at temperatures up and including to 1400 °C. This was likely observed because Y stabilized the cubic structure, which prevented Zr migration in these materials.

3.5 Conclusions

The thermal stability of the long-range and local structures in the $Nd_xY_yZr_{1-x-y}O_{2-\delta}$ series was characterized in order to assess the applicability of these materials as IMFs. The results showed that both monoclinic and tetragonal zirconia phases were formed when the $Nd_xZr_{1-x}O_{2-\delta}$ materials were annealed at 1400 °C. Therefore, the ternary materials are not suitable candidates for IMF applications. The addition of a small amount of Y ($y \geq 0.05$) stabilized these materials at temperatures up to and including 1400 °C, and the quaternary materials should still be considered as IMF materials. The EXAFS results showed that Y and Zr occupy different coordination environments, and these differences in coordination are not visible by XRD. The SEM and EDS images indicated the presence of Nd inclusions randomly distributed in the materials studied here, and Nd inclusions were observed regardless of composition and annealing temperature. Based on these results, it appears that the synthetic method used to produce these materials must be improved if these materials are to be used in IMF applications. This study also indicated the importance of understanding changes in the structure on both long-range and local scales and showed the utility of using XAS techniques in studying cubic stabilized zirconia materials for IMF applications.

Chapter 4

INVESTIGATION OF $Nd_xY_{0.25-x}Zr_{0.75}O_{1.88}$ INERT MATRIX FUEL MATERIALS MADE BY A CO-PRECIPITATION SYNTHETIC ROUTE[1]

4.1 Introduction

In the previous chapter, the thermal stability of a number of $Nd_xY_yZr_{1-x-y}O_{2-\delta}$ materials made by the ceramic method was explored. However, Nd was not evenly distributed in these materials, and it is therefore of interest to investigate if the Nd distribution can be improved using alternate synthetic techniques. Further, ceramic synthesis is generally costly, and the presence of powdered radioactive material would make large scale syntheses envisioned for safe nuclear fuel production difficult [196]. A low-temperature, liquid-based approach could be more easily automated as well, reducing the costs of safely producing nuclear fuels bearing TRU species [196]. This chapter presents research on a series of $Nd_xY_{0.25-x}Zr_{0.75}O_{1.88}$ materials which have been produced using a co-precipitation method, followed by calcining at 800 °C. These "as-synthesized" materials were then annealed at 1400 °C and 1500 °C to explore the effect of high temperature annealing on the thermal stability of Nd-doped yttria-stabilized zirconia made by the co-precipitation method. The local and long-range structures of these materials have been investigated using XRD, SEM, and XAS. These results were compared to similar results from Nd-YSZ materials made via a ceramic

[1] A version of this paper has been accepted by the *Canadian Journal of Chemistry* for publication as an article by J.R. Hayes and A.P. Grosvenor. The candidate performed all data collection and analysis, and was responsible for drafting the original manuscript. Editorial contributions were provided by the co-authors.

method presented in Chapter 3. This study has shown that the local bonding structures around the metal centres in the materials made by the co-precipitation synthesis method or the ceramic synthesis method are similar. However, the intermediate and long-range structures of the materials made by the co-precipitation method were more disordered compared to the structures of the materials made by the ceramic method. Finally, this study has also shown that cubic $Nd_xY_{0.25-x}Zr_{0.75}O_{1.88}$ materials made by a co-precipitation method are less stable compared to Nd-YSZ materials made by the ceramic method. This study highlights the importance of synthetic method and the impacts it can have on the properties of zirconia-based inert matrix fuels.

4.2 Experimental

4.2.1 Preparation of $Nd_xY_{0.25}Zr_{0.75}O_{1.88}$ materials

$Nd_xY_{0.25-x}Zr_{0.75}O_{1.88}$ materials were prepared via co-precipitation using an adaptation of a previously reported synthetic method [197]. Nd_2O_3 (Alfa Aesar, 99.9%) and Y_2O_3 (Alfa Aesar, 99.99%) were dissolved in boiling nitric acid while $ZrOCl_2{\cdot}8H_2O$ (Alfa Aesar, 99.9%) was dissolved in deionized water at room temperature. The boiling Nd^{3+}/Y^{3+} solution was added to the room temperature Zr^{4+} solution and room temperature concentrated ammonia was added which resulted in the formation of a precipitate. The solid was collected via vacuum filtration, washed with deionized water to remove counter-ions and excess ammonia, and dried in air at 110 °C for 24 h. The dried precipitate was then calcined as a free powder at 800 °C for 24 h, resulting in the final product. These materials are referred to as the "as-synthesized" samples in this article. Aliquots of the as-synthesized materials were then annealed at 1400 °C and 1500 °C as free powders for 24 h. The synthesis of the $Nd_xY_{0.25-x}Zr_{0.75}O_{1.88}$ materials prepared by the ceramic method is given in Section 3.2.1 on page 61.

The phase identification of the as-synthesized and annealed materials was performed using powder XRD. The powder XRD patterns were collected using a PANalytical Empyrean diffractometer using either Cu $K_{\alpha1,2}$ (λ=1.5406 Å) or Co $K_{\alpha1,2}$ (λ=1.7890 Å) radiation. Phase quantifi-

cation was obtained by Rietveld refinement using the PANalytical X'pert HighScore Plus software program [173]. Rietveld refinements were performed by fitting cubic ZrO_2, tetragonal ZrO_2, and monoclinic ZrO_2 phases to the data [174–176] [174–176]. The method used to analyze the data was identical to the one described in Section 3.2.1 on page 61.

4.2.2 SEM and WDS Analysis

Scanning electron micrographs were collected from several of the as-synthesized and annealed samples using a JEOL 8600 electron microprobe. Samples were prepared by pressing $\sim$0.125 g of the as-synthesized material into a pellet at 8 MPa, and sintering the pellet at 800 °C for 24 h; these are referred to as the "as-synthesized" pellets. (8 MPa was the pellet gauge pressure, and the actual pressure exerted on the pellet is much greater.) After sintering, several of the "as-synthesized" pellets were further annealed at 1400 °C for 24 h; these pellets are referred to as the annealed pellets. The pellets were mounted in a plastic disk using a polymer resin, and the surface of the sample disk was polished to a smooth surface using diamond paste. The surface was coated with a thin C film to reduce charging effects before being inserted into the microprobe sample chamber. All electron micrographs were collected in backscattered electron mode, and the electron beam accelerating voltage was 20 kV.

Wavelength dispersive spectroscopy (WDS) was also performed to collect elemental distribution maps. The electron beam accelerating voltage was 20 kV and the probe current was 50 nA. The peak counting times were 60 s on peak and 30 s each on high and low background. The X-ray maps were collected using the Nd L_α and Y L_α signals measured simultaneously using two different WDS spectrometers. The WDS spectrometers were tuned to the correct fluorescence energy using the fluorescence signals from (Nd,Ce)PO_4 (Nd $L_{\alpha 1}$) and Y_2O_3 (Y $L_{\alpha 1}$) standards. All X-ray maps were collected at the same magnification and from the same region as the electron micrographs.

4.2.3 Zr K- and Y K-edge X-ray Absorption Spectroscopy

Zr K- and Y K-edge X-ray absorption spectra were collected using the CLS@APS Sector 20 Bending Magnet beamline at the Advanced Photon Source (APS) located at Argonne National Laboratories. The specifications of this beamline and the sample preparation have been previously described in Section 3.2.3.1 on page 62. The samples were mounted at 45° to the incident beam and spectra were collected in both transmission and partial fluorescence yield (PFY) mode. The incident beam ion chamber (I_o) was filled with $N_{2(g)}$ while the transmitted beam ion chamber, I_T, and reference ion chamber, I_{REF}, were filled with an 80% $Ar_{(g)}$:20% $N_{2(g)}$ mixture. A Canberra 13 element Ge fluorescence detector was used to record the PFY signal. The parameters used to collect the Zr K- and Y K-edge spectra are described in Section 3.2.3.1. The EXAFS spectra were analyzed by modelling the data using the same methods and paramters described in Section 3.2.3.2 on page 63.

4.3 Results and Discussion

4.3.1 Powder XRD

The powder X-ray diffraction patterns from the as-synthesized and annealed $Nd_xY_{0.25-x}Zr_{0.75}O_{1.88}$ materials synthesized via a co-precipitation method are presented in Figures 4.1 and 4.2 and Figure C.1 in Appendix C. Only peaks associated with the cubic fluorite phase were observed in the as-synthesized materials. The diffraction peaks were sharper in the materials annealed at high temperature compared to the diffraction peaks from the materials calcined at 800 °C, indicating that the crystallinity of the materials improved upon annealing. The difference in the peak widths could also indicate that the as-synthesized materials had a significantly smaller particle size than the materials annealed at high temperature. Several of the compositions annealed at high temperature were not phase pure, and lower symmetry monoclinic and tetragonal ZrO_2, in addition to an unidentified phase, were observed (Figure 4.1a, Figure 4.2).

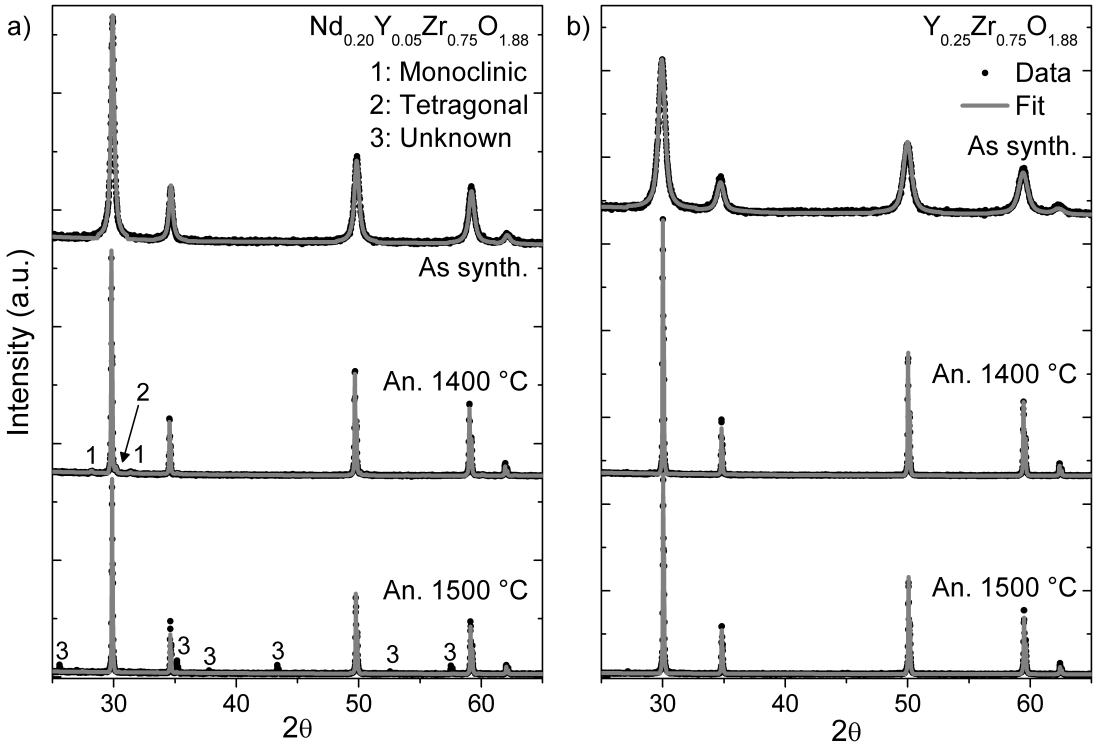

Figure 4.1: Powder X-ray diffraction patterns from the as-synthesized and annealed (a) $Nd_{0.20}Y_{0.05}Zr_{0.75}O_{1.88}$ and (b) $Y_{0.25}Zr_{0.75}O_{1.88}$ materials made by the co-precipitation method. The as synthesized samples are denoted as "As synth." and the annealed samples are denoted as "An." in all figures. A small amount of monoclinic and tetragonal ZrO_2 phase was formed when the $Nd_{0.20}Y_{0.05}Zr_{0.75}O_{1.88}$ material was annealed at 1400 °C and an unidentified phase was produced when the material was annealed at 1500 °C, which is not included in the fit. The $Y_{0.25}Zr_{0.75}O_{1.88}$ material maintained a single fluorite phase when annealed at 1400 °C and 1500 °C.

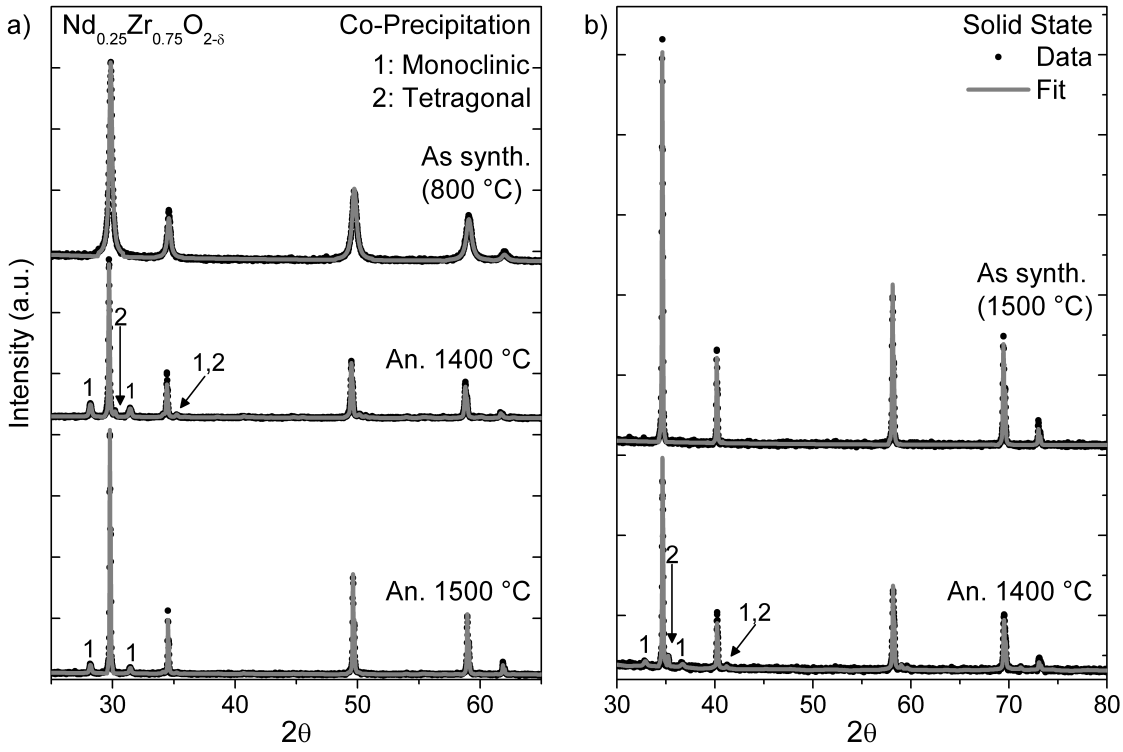

Figure 4.2: Powder X-ray diffraction patterns of $Nd_{0.25}Zr_{0.75}O_{1.88}$ prepared by (a) co-precipitation and (b) ceramic synthetic routes (Chapter 3). Monoclinic and tetragonal zirconia phases were formed when the materials prepared by both synthetic routes were annealed at 1400 °C. A monoclinic zirconia phase was observed when the material prepared by the co-precipitation method was annealed at 1500 °C. No monoclinic zirconia phase was observed in the as-synthesized material made by the ceramic synthetic route (which was fired at 1500 °C).

Phase analysis was performed using Rietveld refinement and the results of these fits are given in Table 4.1. The $Nd_xY_{0.25-x}Zr_{0.75}O_{1.88}$ materials prepared by the co-precipitation method with $x \leq 0.15$ that were annealed at high temperatures were phase pure, and only peaks associated with the fluorite structure were observed (Figure 4.1b, Figure C.1). When $Nd_{0.20}Y_{0.05}Zr_{0.75}O_{1.88}$ made by the co-precipitation method was annealed at 1400 °C, minor contributions from monoclinic (4.0 %) and tetragonal (3.4%) ZrO_2 phases were observed. Peaks associated with an unidentified phase were also observed when the $Nd_{0.20}Y_{0.05}Zr_{0.75}O_{1.88}$ material made by co-precipitation was annealed at 1500 °C (Figure 4.1a). Monoclinic (24.7%) and tetragonal (3.6 %) ZrO_2 phases were observed when the $Nd_{0.25}Zr_{0.75}O_{1.88}$ sample synthesized via the co-precipitation method was annealed at 1400 °C (Figure 4.2a). When this material was annealed at 1500 °C the amount of monoclinic and tetragonal ZrO_2 present decreased, and the Rietveld analysis indicated that the material contained 14.5% monoclinic ZrO_2. This result is expected, as ternary phase diagrams of the Nd_2O_3-Y_2O_3-ZrO_2 systems have shown that the cubic fluorite structure is stable across a wider range of compositions at higher temperatures (1600 °C) than at lower temperatures (1400 °C) [194].

These results differ from the results of the powder XRD analysis for $Nd_xY_{0.25-x}Zr_{0.75}O_{1.88}$ materials prepared by the ceramic method. $Nd_{0.20}Y_{0.05}Zr_{0.75}O_{1.88}$ made via the ceramic route at 1500 °C was phase pure, and no unidentified peaks were observed in the powder XRD pattern, and no impurity phases were observed when $Nd_{0.20}Y_{0.05}Zr_{0.75}O_{1.88}$ made by the ceramic method was annealed at 1400 °C (see Section 3.3.1 on page 65). Only the fluorite phase was observed in the $Nd_{0.25}Zr_{0.75}O_{1.88}$ material made via the ceramic method at 1500 °C. Similar to $Nd_{0.25}Zr_{0.75}O_{1.88}$ made by the co-precipitation method, the material made by the ceramic synthesis was also observed to decompose to lower symmetry phases upon annealing at 1400 °C, though the degree of decomposition was much less when compared to the material made by a co-precipitation route (Figure 4.2b). Again, decomposition to a lower symmetry phase upon annealing is expected based on the calculated Nd_2O_3-Y_2O_3-ZrO_2 ternary phase diagrams; however, it was not expected that the degree of decomposition the materials would be dependent on synthetic method [194]. In all

Table 4.1: Summary of Rietveld Refinement Results

	As synth.	An. 1400 °C	An. 1500 °C
$Y_{0.25}Zr_{0.75}O_{1.88}$			
R_{wp}[a]	7.32	8.62	8.54
Unit Cell (Å)[b]	5.1489(5)	5.15163(5)	5.15113(6)
Wt. Fraction	100% Cubic	100% Cubic	100% Cubic
$Nd_{0.05}Y_{0.20}Zr_{0.75}O_{1.88}$			
R_{wp}[a]	7.28	9.61	9.03
Unit Cell (Å)[b]	5.1534(4)	5.1553(5)	5.15675(5)
Wt. Fraction	100% Cubic	100% Cubic	100% Cubic
$Nd_{0.10}Y_{0.15}Zr_{0.75}O_{1.88}$			
R_{wp}[a]	7.12	8.74	8.01
Unit Cell (Å)[b]	5.1596(4)	5.16052(6)	5.16101(6)
Wt. Fraction	100% Cubic	100% Cubic	100% Cubic
$Nd_{0.15}Y_{0.10}Zr_{0.75}O_{1.88}$			
R_{wp}[a]	7.50	8.85	8.94
Unit Cell[b]	5.1715(4)	5.17165(6)	5.17329(6)
Wt. Fraction	100% Cubic	100% Cubic	100% Cubic
$Nd_{0.20}Y_{0.05}Zr_{0.75}O_{1.88}$			
R_{wp}[a]	9.27	9.03	N/A
Unit Cell[b]	5.1763(4)	5.18281(7)	5.17924(6)
Wt. Fraction	100% Cubic	92.6% Cubic	Unknown Phases
		4.0% Tetragonal	Present
		3.4% Monoclinc	
$Nd_{0.25}Zr_{0.75}O_{1.88}$			
R_{wp}[a]	7.90	7.29	7.10
Unit Cell[b]	5.1852(3)	5.2065(1)	5.19341(6)
Wt. Fraction	100% Cubic	71.7% Cubic	85.5% Cubic
		3.6% Tetragonal	14.5% Monoclinic

[a] $R_{wp} = \sum w_i(y_{io} - y_{ic})^2 / \sum w_i y_{io}$; w_i= i^{th} comp. wt. fraction; y_{ic}=calculated intensity; y_{io} = diffraction pattern intensity
[b] Cubic unit cell parameter

cases, no superstructural peaks associated with a pyrochlore phase were observed, indicating that the oxygen vacancies were not significantly ordered on a long-range scale within the material.

The results presented above indicate that the fluorite structure is more stable for the materials made by the ceramic synthetic route than by the co-precipitation route. This stability is likely driven by the kinetics of the cubic to tetragonal ZrO_2 and cubic to monoclinic ZrO_2 phase transitions, which are controlled by the diffusion of cations within the matrix [198–201]. In the case of the co-precipitation synthesis, the cations are already intimately mixed at an atomic level, facilitating a faster reaction. Additionally, the materials made by the co-precipitation method likely had a smaller crystallite size compared to the materials prepared by the ceramic synthetic method, as evidenced by the difference in the width of the diffraction peaks. This change in particle size could also be responsible for accelerating the transition from cubic ZrO_2 to lower symmetry ZrO_2 phases. This is evident by the difference in the annealing times required to induce phase changes, which were much shorter in the case of the co-precipitation route (24 h) as compared to the materials made by the ceramic route (5 d). These results suggest that the kinetically labile materials made by the co-precipitation method may have reached a thermodynamically favorable endpoint upon annealing. These results also suggest that there is a possibility that while the fluorite structure of the $Nd_{0.20}Y_{0.05}Zr_{0.75}O_{1.88}$ material made by the ceramic route was stable when annealed at 1400 °C for 5 d, it may not be stable when annealed at 1400 °C for extended periods of time. Further annealing studies, using much longer heating times, should be performed to explore this possibility fully.

The lattice constants of the as-synthesized and annealed $Nd_xY_{0.25-x}Zr_{0.75}O_{1.88}$ materials made by the co-precipitation and ceramic syntheses were determined by Rietveld refinement (Table 4.1), and the lattice constants are plotted as a function of Nd content in Figure 4.3. The lattice constants of the as-synthesized materials synthesized by both the co-precipitation and ceramic methods varied linearly with Nd content (x), consistent with Vegard's law [182]. The lattice constants of all the as-synthesized and annealed materials synthesized via co-precipitation were less than the lattice constants of the materials synthesized by the ceramic method. The lattice constants of the mate-

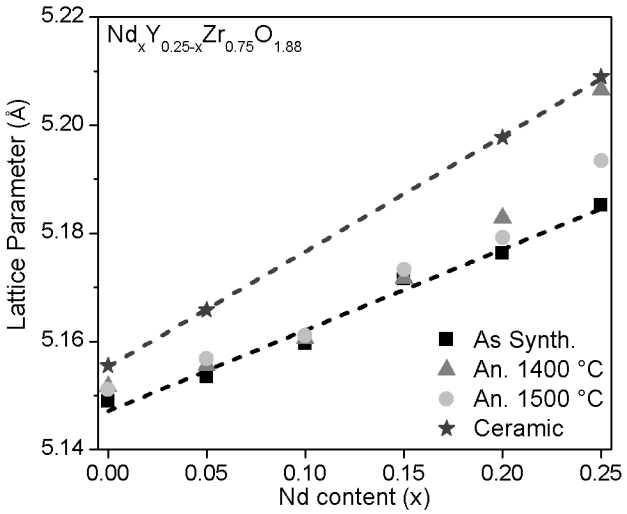

Figure 4.3: The lattice parameters of the as-synthesized and annealed $Nd_xY_{0.25-x}Zr_{0.75}O_{1.88}$ materials made via the co-precipitation route are plotted as function of Nd content. The lattice parameters of the $Nd_xY_{0.25-x}Zr_{0.75}O_{1.88}$ materials made by the ceramic synthetic route at 1500 °C are also included. The black dashed lines are the linear best fit line of the as-synthesized materials made by the co-precipitation and ceramic route, and indicate that Vegard's law is followed in both cases.

rials synthesized by the co-precipitation method increased when they were annealed at 1400 °C and 1500 °C, which resulted in deviations from Vegard's law. The magnitude of the change in the lattice constants induced by annealing at high temperature decreased with increased Nd content when "x" in the chemical formula was less than 0.10. Conversely, the magnitude of the change in the lattice constant caused by annealing increased as the Nd content increased when x was greater than 0.10. The lattice constant of the materials annealed at 1500 °C were lower than the lattice constants of the materials annealed at 1400 °C when x = 0.20 and x = 0.25. It should also be noted that at higher Nd concentrations, the changes in the phase composition, which are driven by Nd segregation within the material (see 4.3.2), likely affect the lattice constant of the fluorite structure.

It has been previously suggested that the fluorite lattice constant is affected by ordering of the metal-oxygen polyhedral units [180]. Put another way, this means that the unit cell is affected by how the metal-oxygen polyhedra are arranged, rather than by variations in the local metal-oxygen bond lengths and angles [180]. The lattice constant is expected to increase as arrangement of the metal-oxygen polyhedra becomes more ordered, resulting in less efficient packing of the metal-oxygen polyhedral units [180]. The changes in the lattice constants observed here suggest that

there was more long-range disorder in the as-synthesized materials made by the co-precipitation route compared to the materials synthesized by the ceramic method and the materials synthesized by co-precipitation method that were annealed at high temperature. In the case of the ceramic synthetic route, this ordering may derive from both the high temperature at which the materials were annealed and also the inherent crystallinity of the starting materials. The starting binary oxides used in the ceramic route had defined crystal structures, which likely acted as a template, increasing the ordering between the metal-oxygen polyhedra [202]. In contrast, the starting precipitate materials that were formed in the co-precipitation method lacked this inherent structure. This explains why the lattice constants of the materials made via the ceramic method were greater than the materials made via the co-precipitation route.

4.3.2 SEM and WDS

The SEM micrographs and Nd and Y X-ray maps collected from the as-synthesized and annealed $Nd_{0.20}Y_{0.05}Zr_{0.75}O_{1.88}$ and $Y_{0.25}Zr_{0.75}O_{1.88}$ materials prepared by the co-precipitation route are presented in Figures 4.4 and 4.5. The micrographs from the as-synthesized samples (Figures 4.4a, 4.5a) show that the surfaces of the pellets contained large, faceted grains, and that the surfaces were similar to the previously reported surfaces of $Nd_xSc_yZr_{1-x-y}O_{2-\delta}$ pellets that were also synthesized using a co-precipitation method and annealed at 800 °C (see Section 5.3.2 on page 124). The surfaces became less faceted and more porous upon annealing at 1400 °C (Figures 4.4b, 4.4c). The topography of the surfaces of the pellets annealed at 1400 °C were similar to the surfaces of $Nd_xY_yZr_{1-x-y}O_{2-\delta}$ pellets prepared by the ceramic method. An identical change in topography was also observed by SEM when $Nd_xSc_yZr_{1-x-y}O_{2-\delta}$ materials made via co-precipitation were annealed at 1400 °C. This indicates that the surface topography depends significantly on annealing temperature, with material composition and synthetic method playing little to no role.

The Y K_α X-ray maps (Figures 4.4b,d and Figures 4.5c,f) show that Y was evenly distributed throughout the material in both the as-synthesized and annealed $Nd_{0.20}Y_{0.05}Zr_{0.75}O_{1.88}$ and $Y_{0.25}Zr_{0.75}O_{1.88}$ materials made using the co-precipitation route. A similar result was ob-

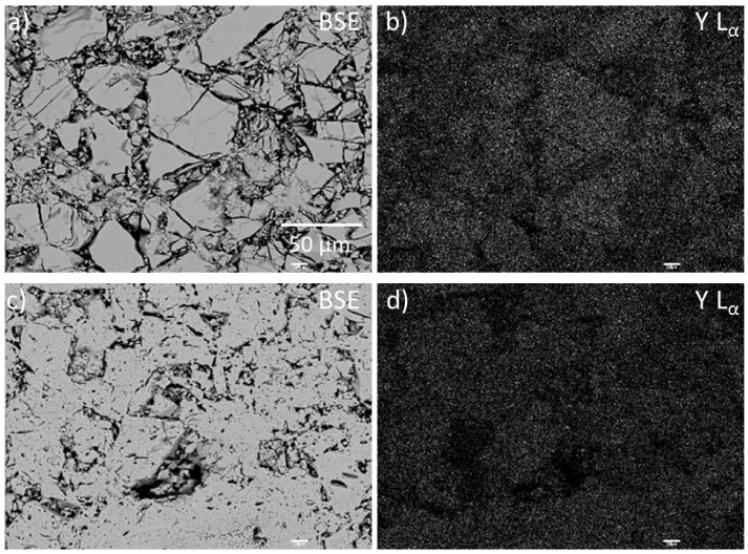

Figure 4.4: Micrographs collected from as-synthesized $Y_{0.25}Zr_{0.75}O_{1.88}$ and $Y_{0.25}Zr_{0.75}O_{1.88}$ annealed at 1400 °C prepared by a co-precipitation method are presented. (a) A BSE image from the as-synthesized $Y_{0.25}Zr_{0.75}O_{1.88}$ and (b) the Y L_α WDS map from the same spot. (c) A BSE image from the $Y_{0.25}Zr_{0.75}O_{1.88}$ annealed at 1400 °C and (d) the Y L_α WDS map from the same spot. All images were collected at the same magnification and a scale bar is shown in (a).

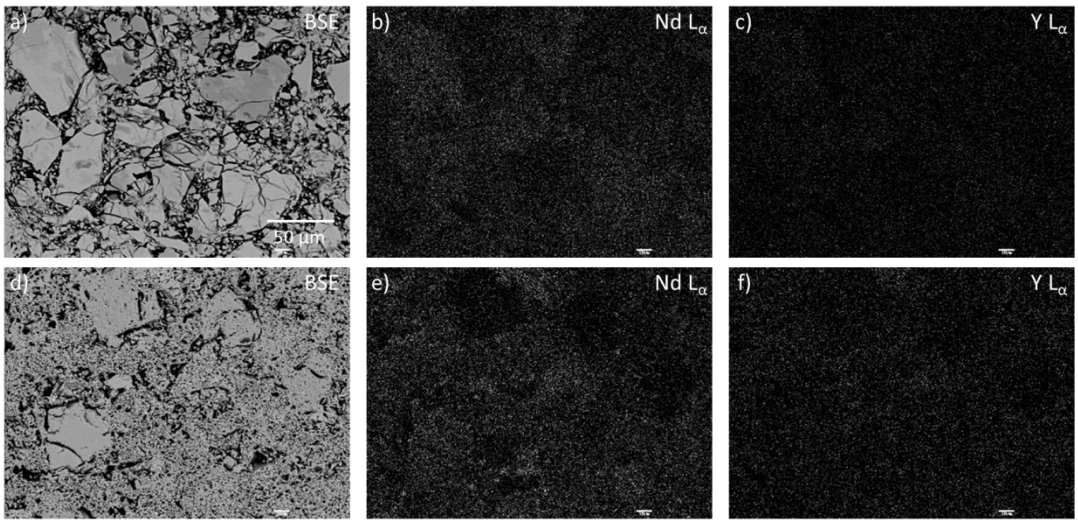

Figure 4.5: Micrographs collected from as-synthesized $Nd_{0.20}Y_{0.05}Zr_{0.75}O_{1.88}$ and $Nd_{0.20}Y_{0.05}Zr_{0.75}O_{1.88}$ annealed at 1400 °C prepared by a co-precipitation method are presented. (a) A BSE image from the as-synthesized $Nd_{0.20}Y_{0.05}Zr_{0.75}O_{1.88}$, (b) the Nd L_α WDS map, (c) the Y L_α WDS map from the same spot. (d) A BSE image from the $Nd_{0.20}Y_{0.05}Zr_{0.75}O_{1.88}$ annealed at 1400 °C and (e) the Nd L_α WDS map, and (f) the Y L_α WDS map from the same spot. All images were collected at the same magnification and a scale bar is shown in (a).

served in materials made via the ceramic method (see Section 3.3.2 on page 69). The Nd L_α X-ray maps (Figures 4.5b,e) indicated that Nd was evenly distributed in the as-synthesized $Nd_{0.20}Y_{0.05}Y_{0.75}O_{1.88}$ material made by the co-precipitation method. However, small Nd bright spots were detected when this material was annealed at 1400 °C. Nd bright spots were also observed when the $Nd_xY_{0.25-x}Zr_{0.75}O_{1.88}$ materials made by the ceramic method were annealed at 1400 °C as well. The X-ray maps indicated that Y and Nd were evenly distributed in the as-synthesized $Nd_xY_{0.25-x}Zr_{0.75}O_{1.88}$ materials made by the co-precipitation method, and that Nd became segregated while Y remained homogenously distributed within the materials upon annealing at high temperature (Figures 4.4 and 4.5).

4.3.3 Zr K-edge

4.3.3.1 XANES

Zr K-edge XANES spectra were collected from the as-synthesized and annealed samples prepared by the co-precipitation method, and the spectra are presented in Figure 4.6 and Figure C.2. Three features were observed in the spectra, and are labelled A, B, and B' in Figure 4.6a. Feature A comprises the pre-edge and results from Zr 1s $\rightarrow$ 4d transitions while features B and B' comprise the main-edge and result from Zr 1s $\rightarrow$ 5p excitations [183, 184]. The Zr K-edge spectra do not vary significantly as Nd replaces Y in the system. This result indicates that the local Zr coordination environment does not change with composition, which is consistent with the analysis of $Nd_xY_yZr_{1-x-y}O_{2-\delta}$ materials prepared by the ceramic method (Section 3.3.3.1 on page 71).

The Zr K-edge spectra from the materials prepared by the co-precipitation method and annealed at high temperature are compared in Figure 4.6b. Changes in the spectra were only observed when the $Nd_{0.25}Zr_{0.75}O_{1.88}$ material was annealed at 1400 °C and 1500 °C (Inset, Figure 4.6b). When $Nd_{0.25}Zr_{0.75}O_{1.88}$ made by the co-precipitation method was annealed at 1400 °C, the energy separation between features B and B' decreased and there was an increase in intensity of the spectrum at $\sim$18020 eV. This change has previously been shown to correspond to a transition to lower symmetry ZrO_2, and is consistent with the powder XRD results (*vide supra*). The spectrum

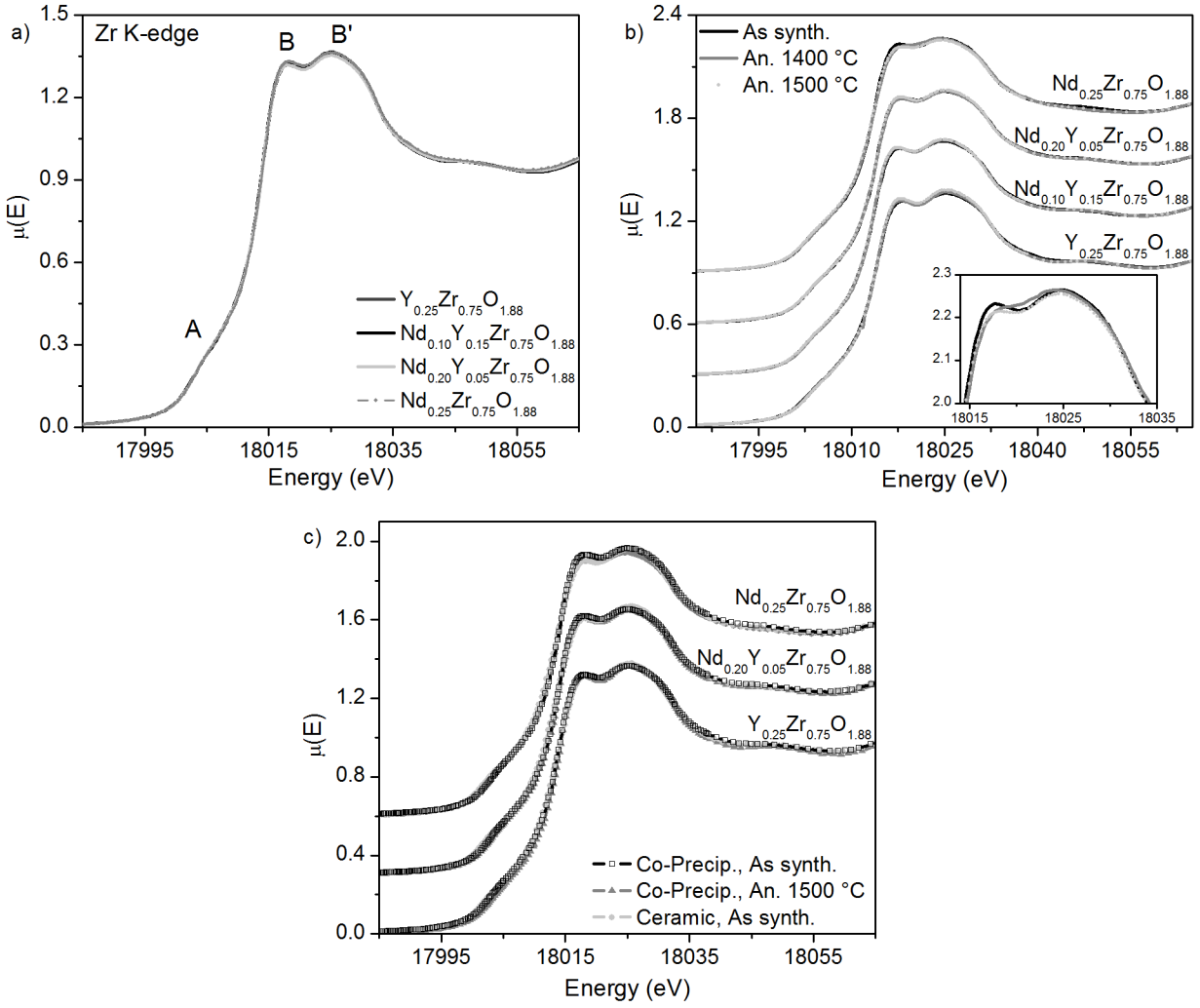

Figure 4.6: (a) The Zr K-edge XANES spectra from the as-synthesized $Nd_xY_yZr_{1-x-y}O_{2-\delta}$ materials prepared by co-precipitation are compared. Three features, labelled A, B, and B' were observed. Feature A is attributed to 1s $\rightarrow$ 4d transitions and features B and B' are attributed to 1s $\rightarrow$ 5p transitions. (b) The XANES spectra from the as-synthesized and annealed materials prepared by co-precipitation are compared. Changes in the spectra were only observed when the $Nd_{0.25}Zr_{0.75}O_{1.88}$ materials were annealed. *Inset*: An expanded view of the XANES spectra from the $Nd_{0.25}Zr_{0.75}O_{1.88}$ materials showing the changes that occurred upon annealing. (c) The spectra from the $Nd_xY_yZr_{1-x-y}O_{2-\delta}$ materials made at 800 °C via a co-precipitation method and made at 1500 °C via a ceramic method are compared. Also included are spectra from the materials made by co-precipitation annealed at 1500 °C.

from the $Nd_{0.25}Zr_{0.75}O_{1.88}$ material annealed at 1500 °C was similar to the spectrum from the as-synthesized material, though a decrease in the energy separation between features B and B' was still observed. This change indicates that lower symmetry ZrO_2 was still present in the system, but not to the degree that was observed in the $Nd_{0.25}Zr_{0.75}O_{1.88}$ material annealed at 1400 °C, which is also consistent with the powder XRD results. No changes in the Zr K-edge spectra were observed when any of the other $Nd_xY_{0.25-x}Zr_{0.75}O_{1.88}$ materials made by the co-precipitation method were annealed at high temperatures.

The Zr K-edge spectra from the as-synthesized and annealed $Nd_xY_{0.25-x}Zr_{0.75}O_{1.88}$ samples made by the co-precipitation method are compared to spectra from the as-synthesized materials made by the ceramic synthetic route in Figure 4.6c and Figure C.2. The intensity of feature A is slightly greater in the spectra collected from the materials made by the ceramic route compared to the intensity of feature A in the spectra from the materials made by the co-precipitation route. The pre-edge region is strongly affected by changes in coordination number as breaks in inversion symmetry around the metal centre result in p-d mixing, which increases the dipole character of the forbidden quadrapolar transition. Here, this likely indicates that the coordination number of Zr is lower in the materials made by the ceramic route than by the co-precipitation route. Changes in the intensities of features B and B' were observed between the spectra from the materials made by co-precipitation and the materials made by a ceramic method, and the intensity of feature B' is greater in the spectra from the materials made by the ceramic method compared to the intensity of feature B' in the spectra from the materials made by the co-precipitation method. The intensity of feature B in the spectra from the materials made by the ceramic method is greater compared to the intensity of feature B in the spectra from the materials made by the co-precipitation method. These changes are consistent with the changes in the pre-edge, and are indicative of a change in the Zr CN number [183, 184]. Overall, these results indicate the Zr coordination environment in the quaternary $Nd_xY_{1-x}Zr_{0.75}O_{1.88}$ materials was not affected by changes in composition or thermal treatment; however, the Zr coordination environment was observed to be dependent on the synthetic route used.

4.3.3.2 EXAFS

The Fourier transformed Zr K-edge EXAFS spectra were collected from the $Nd_xY_{0.25-x}Zr_{0.75}O_{1.88}$ materials made using the co-precipitation method, and these are presented in Figure 4.7 and Figure C.3. Two major features, labelled C and D in Figure 4.7a, were observed in the spectra. Feature C is attributed to the first shell Zr–O scattering path and feature D arises due to the second shell Zr–Zr, Zr–Y, and Zr–Nd scattering paths [180, 186]. The intensity of feature C changes slightly with composition, though these changes do not appear to have a general trend and are likely observed due to noise within the data. The intensity of feature D decreased as the Nd content increased. The cause for the change is related to interference between the Zr–Zr/Y scattering paths and the Zr–Nd paths; the origin of this phenomenon has been previously described in Section 3.3.3.2 on page 73.

The intensities of features C and D increased when all of the materials prepared by the co-precipitation route were annealed at high temperature (Figure 4.7b, Figure C.3 in Appendix C). The magnitude of the change in the intensity of feature C varied with composition. The change in the intensity of feature C appears to correspond with changes in the lattice parameters determined by XRD (Table 4.1, Figure 4.3). The intensity of feature C in the spectrum from the $Nd_{0.25}Zr_{0.75}O_{1.88}$ sample annealed at 1400 °C was more intense than the intensity of feature C the spectrum from the $Nd_{0.25}Zr_{0.75}O_{1.88}$ sample annealed at 1500 °C. The increase in the intensity of feature C could be attributed to increased ordering within the system, and these results likely indicate that the local ordering was slightly greater in $Nd_{0.25}Zr_{0.75}O_{1.88}$ annealed at 1400 °C than in $Nd_{0.25}Zr_{0.75}O_{1.88}$ annealed at 1500 °C. These observations could explain the origin of the changes in the lattice constants of the $Nd_xY_{0.25-x}O_{1.88}$ materials made by co-precipitation upon annealing.

The spectra were fitted to determine the scattering path lengths and ordering parameters, and these results are enumerated in Table 4.2 and Table C.1. The calculated fits and data are compared in Figure 4.7c,d and Figures C.5-C.10. In all cases, the Zr–O scattering path length was found to be 2.16 Å, which is consistent with previously reported results [101, 180, 186, 187]. The Zr–Zr/Y scattering path length was 3.56 Å, which is also in agreement with previously reported results [101,

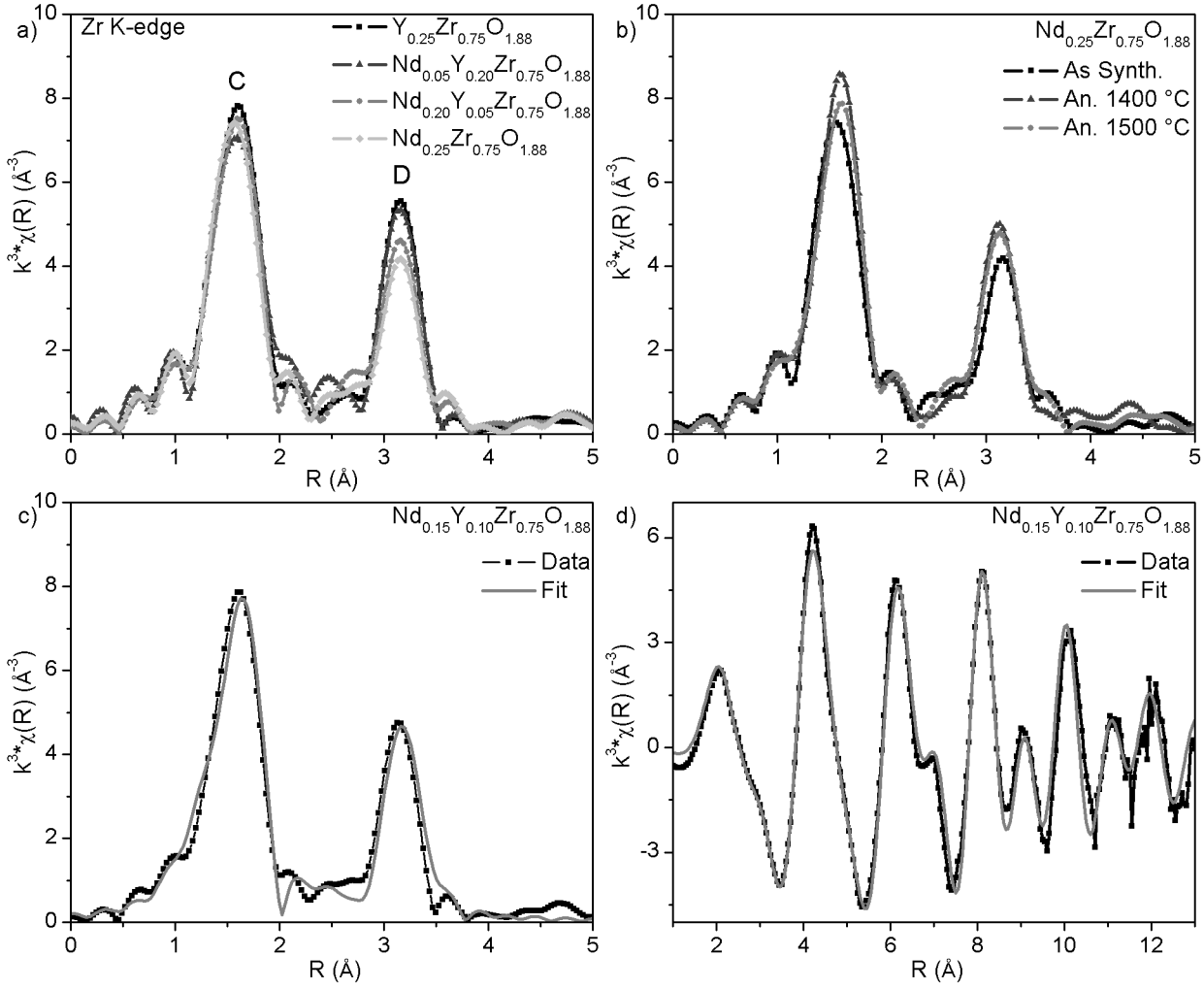

Figure 4.7: (a) The Fourier-transformed Zr K-edge EXAFS spectra from the as-synthesized $Nd_xY_yZr_{1-x-y}O_{2-\delta}$ materials prepared by co-precipitation are presented. Feature C is attributed to first shell Zr–O scattering paths and feature D is attributed to second shell Zr–Zr, Zr–Y, and Zr–Nd scattering paths. (b) The Fourier-transformed EXAFS spectra from the as-synthesized and annealed $Nd_{0.25}Zr_{0.75}O_{1.88}$ spectra are presented. The intensities of features C and D increase with increased annealing temperature. The fitted spectrum from $Nd_{0.15}Y_{0.10}Zr_{0.75}O_{1.88}$ is compared to the data in (c) R-space and (d) k-space.

Table 4.2: Zr K-edge EXAFS Fit Results

$Nd_{0.15}Y_{0.10}Zr_{0.75}O_{1.88}$									
	As synthesized			Annealed 1400 °C			Annealed 1500 °C		
	S_o^2 = 0.90(6), ΔE = -3.9(7)			S_o^2 = 0.78(6), ΔE = -4.0(7)			S_o^2 = 0.92(7), ΔE = -3.9(8)		
	R_{fit} = 0.0165			R_{fit} = 0.0165			R_{fit} = 0.0199		
	CN	R (Å)	σ^2	CN	R (Å)	σ^2	CN	R (Å)	σ^2
Zr - O	7	2.16(1)	0.008(1)	7	2.160(8)	0.007(1)	7	2.160(8)	0.008(1)
Zr - Zr/Y	10.2	3.56(1)	0.011(1)	10.2	3.56(1)	0.009(1)	10.2	3.56(1)	0.010(1)
Zr - Nd	1.8	3.21(4)	0.013(6)	1.8	3.19(4)	0.011(6)	1.8	3.19(4)	0.011(5)
Zr - O2	24	4.36(4)	0.04(1)	24	4.33(4)	0.027(8)	24	4.35(4)	0.04(1)
$Nd_{0.20}Y_{0.05}Zr_{0.75}O_{1.88}$									
	As synthesized			Annealed 1400 °C			Annealed 1500 °C		
	S_o^2 = 0.82(8), ΔE = -3.8(9)			S_o^2 = 0.82(8), ΔE = -3.6(9)			S_o^2 = 0.85(8), ΔE = -4(1)		
	R_{fit} = 0.0259			R_{fit} = 0.0314			R_{fit} = 0.0323		
	CN	R (Å)	σ^2	CN	R (Å)	σ^2	CN	R (Å)	σ^2
Zr - O	7	2.16(1)	0.007(1)	7	2.16(1)	0.007(2)	7	2.16(2)	0.007(2)
Zr - Zr/Y	9.6	3.58(1)	0.011(1)	9.6	3.57(1)	0.011(1)	9.6	3.57(1)	0.011(1)
Zr - Nd	2.4	3.36(1)	0.04(5)	2.4	3.36(1)	0.04(4)	2.4	3.36(3)	0.07(2)
Zr - O2	24	4.34(6)	0.03(1)	24	4.36(5)	0.03(1)	24	4.35(6)	0.03(1)

180, 186, 187]. The Zr–Nd path lengths determined from the EXAFS fit varied from 3.18 Å – 3.77 Å, depending on composition and annealing temperature. The most significant change occurred when the $Nd_{0.25}Zr_{0.75}O_{1.88}$ material made by co-precipitation was annealed at both 1400 °C and 1500 °C, as the Zr–Nd scattering path decreased from 3.77 Å to 3.36 Å (Table C.1). The Zr–Nd scattering path length also changed when the $Nd_{0.05}Y_{0.20}Zr_{0.75}O_{1.88}$ material synthesized via the co-precipitation route was annealed (Table C.1). Here, the path length decreased from 3.70 Å to 3.44 Å upon annealing at 1400 °C. The Zr–Nd scattering path length did not change when the other $Nd_xY_{0.25-x}Zr_{1-x-y}O_{1.88}$ materials were annealed at high temperature, and was consistently low, with values under 3.4 Å. These values are unphysical given the fluorite lattice, and it has been previously hypothesized by our group that these values possibly indicate that a Zr- and Y-doped B-Nd_2O_3 type structure, which has a 3.428 Å M–M bond length, is present in the material [203]. Failures in the fitting model must also be considered as a source of these abnormally low values as well, though these possible failures would not affect the fitted parameters of the Zr–Zr/Y and Zr–O scattering paths.

The Fourier-transformed EXAFS spectra from the as-synthesized and annealed $Nd_xY_{0.25-x}Zr_{0.75}O_{1.88}$ materials made by the co-precipitation method are compared to the EXAFS spectra from the materials made by the ceramic method in Figures 4.8 and C.4. The intensities of peaks C and D in the spectra from the as-synthesized materials made by co-precipitation are less than the intensities of peaks C and D in the spectra from the materials made by the ceramic method and the materials made by the co-precipitation method annealed at 1500 °C. The increase in the intensities of these features may be explained by increased ordering within the materials made by the ceramic method and the materials annealed at 1500 °C compared to the as-synthesized materials made by the co-precipitation method. This is consistent with the lower synthetic temperature of the co-precipitation method, and also agrees with powder XRD results. The spectra from the materials made by the ceramic method and the materials made by the co-precipitation method annealed at 1500 °C are similar. This indicates that the local structure around the Zr metal centres are similar, and that the local Zr structure is more dependent on annealing/synthetic temperature and less on the synthetic method.

4.3.4 Y K-edge

4.3.4.1 XANES

Y K-edge XANES spectra were collected from several of the as-synthesized and high-temperature annealed $Nd_xY_{1-x}Zr_{0.75}O_{1.88}$ materials made by the co-precipitation method, and these spectra are presented in Figure 4.9 and Figure C.11. Three features were observed in the Y K-edge spectra, labelled as E, F, and F' in Figure 4.9a. Similar to the Zr K-edge, feature E arises from forbidden, quadrapolar Y 1s $\rightarrow$ 4d transitions and features F and F' are due to dipolar Y 1s $\rightarrow$ 5p transitions [180]. The spectra did not change when the composition was varied. This indicates that the Y coordination environment does not depend on the composition of materials made via the co-precipitation route.

The spectra from the as-synthesized materials and materials annealed at high temperatures made via co-precipitation are presented in Figure 4.9b. As with changes in composition, no signif-

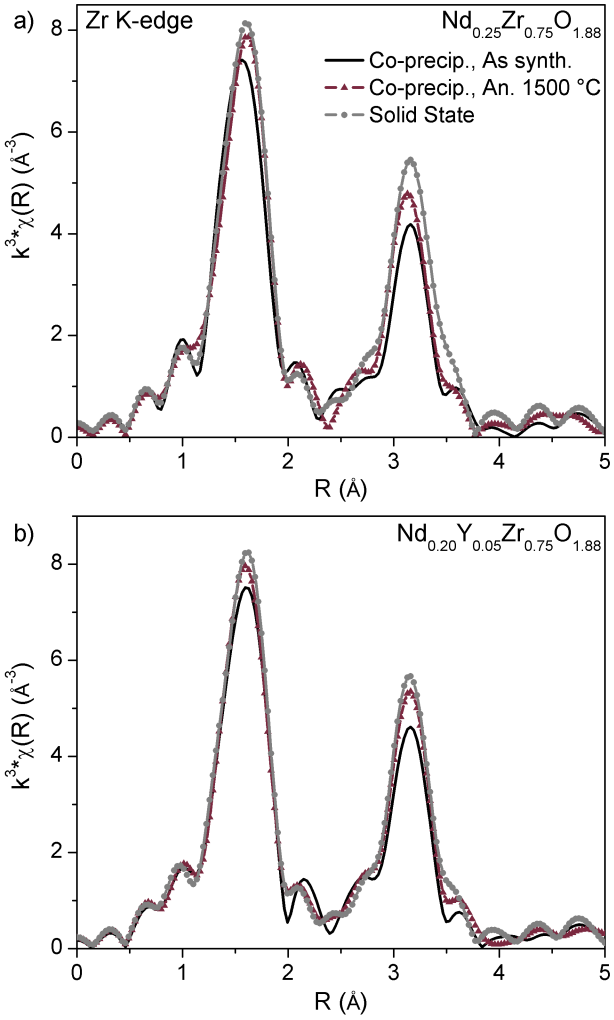

Figure 4.8: The Fourier-transformed Zr K-edge EXAFS spectra from the (a) $Nd_{0.25}Zr_{0.75}O_{1.88}$ and (b) $Nd_{0.20}Y_{0.05}Zr_{0.75}O_{1.88}$ materials prepared by co-precipitation and ceramic synthetic methods are compared. Also included is the material made via co-precipitation annealed at 1500 °C. Features C and D are more intense in the spectra from the materials made via the ceramic synthetic route as compared to both materials made via the co-precipitation route, indicating increased local ordering around the Zr metal centres.

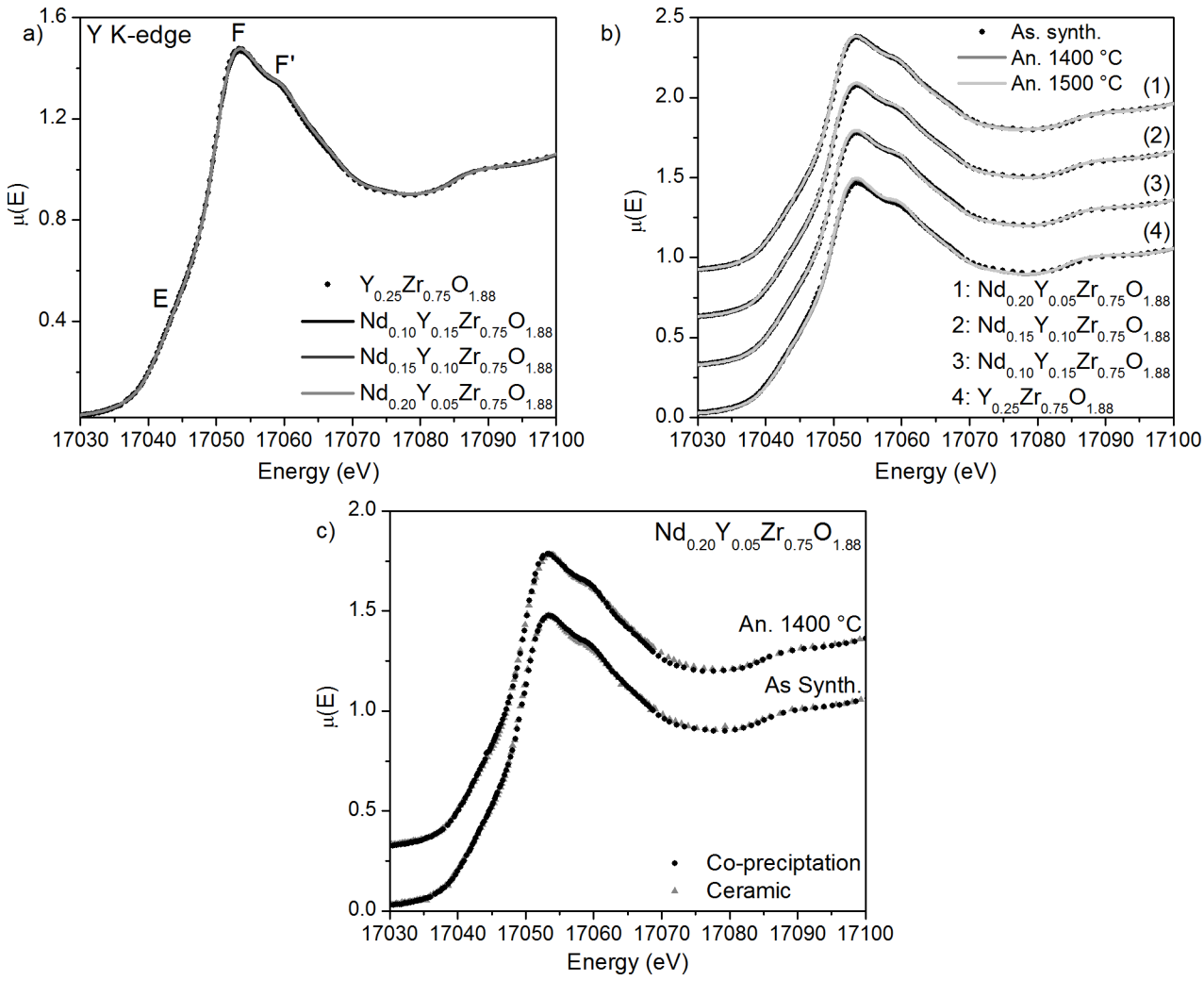

Figure 4.9: (a) Y K-edge XANES spectra from the as-synthesized $Nd_xY_yZr_{1-x-y}O2-\delta$ materials synthesized by co-precipitation are presented. Three features were observed, labelled E, F, and F'. Feature E arises due to 1s $\rightarrow$ 4d transitions and feature F and F' arise from 1s $\rightarrow$ 5p transitions. (b) The Y K-edge spectra from the as-synthesized and annealed $Nd_xY_yZr_{1-x-y}O_{2-\delta}$ materials are presented. No significant changes were observed when the materials were annealed at 1400 °C and 1500 °C. (c) The spectra from $Nd_{0.20}Y_{0.05}Zr_{0.75}O_{1.88}$ materials made via co-precipitation and ceramic synthetic routes are compared. No significant changes are observed in the spectra from the materials made using different synthetic routes.

icant changes in the spectra were observed when the $Nd_xY_{1-x}Zr_{0.75}O_{1.88}$ materials were annealed at high temperatures. This suggests that the majority of the changes that occur when the materials are annealed at high temperature are located around either the Zr or Nd metal centres. Further, only minor differences between XANES spectra from materials made by the co-precipitation and the ceramic synthetic methods were observed (Figure 4.9c, Figure C.11). This indicates that the Y coordination environment was not affected by the synthetic method used. Overall, the Y K-edge XANES results indicate that the Y coordination environment was stable when the $Nd_xY_{0.25-x}Zr_{0.75}O_{1.88}$ materials made by a co-precipitation synthesis were annealed at high temperature.

4.3.4.2 EXAFS

Y K-edge EXAFS spectra were collected from the as-synthesized $Nd_xY_{1-x}Zr_{0.75}O_{1.88}$ materials as well as materials made by co-precipitation that were annealed at high temperature. The Fourier transformed EXAFS spectra from the as-synthesized materials are presented in Figure 4.10. Two features were observed, and these features are labelled as G and H in Figure 4.10a. Feature G arises from the first shell Y–O scattering path and feature H is assigned to second shell Y–Y, Y–Zr, and Y–Nd scattering paths [180,186]. Only minor variations in the intensities of features G and H were observed as the composition of the $Nd_xY_{1-x}Zr_{0.75}O_{1.88}$ materials was varied. This is in contrast to the previous study of $Nd_xY_{1-x}Zr_{0.75}O_{1.88}$ materials made by the ceramic method, in which the intensity of feature H decreased with increased Nd content (see Section 3.3.5 on page 79). In Chapter 3, the change in the intensity of feature H was attributed to interference between the Y–Nd and Y–Y/Zr scattering paths. A similar trend was not observed in the spectra from materials made by the co-precipitation route. This could be due to non-homogenous distribution of Nd and Y in the materials made by co-precipitation, with Nd preferentially occupying sites that are separated from Y in these materials. Here, the materials were likely heterogeneous on a short-range to intermediate scale, and this heterogeneity may not be observed in the WDS results.

The intensity of feature H increased when the $Nd_xY_{1-x}Zr_{0.75}O_{1.88}$ materials made by co-

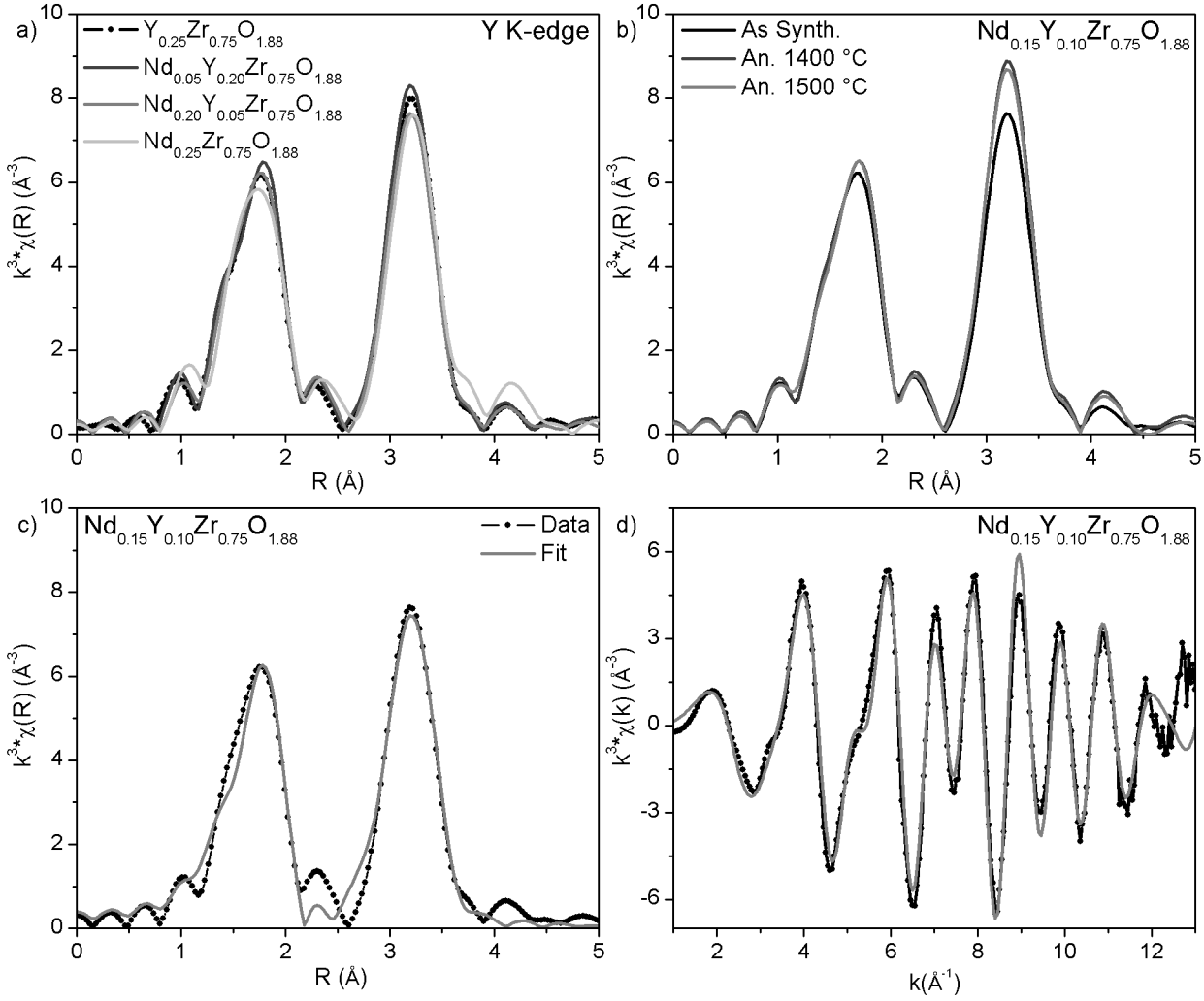

Figure 4.10: (a) The Fourier-transformed Y K-edge EXAFS spectra from the as-synthesized $Nd_xY_yZr_{1-x-y}O_{2-\delta}$ materials synthesized by co-precipitation are presented are shown. First shell Y–O scattering paths contribute to feature G while feature H arises due to second shell Y–Y, Y–Zr, and Y–Nd scattering paths. (b) The Fourier-transformed EXAFS spectra from the as-synthesized and annealed $Nd_{0.15}Y_{0.10}Zr_{0.75}O_{1.88}$ materials are shown. The intensity of feature H increases upon annealing, indicating the intermediate ordering increases occurs. The fit of the EXAFS spectra from $Nd_{0.15}Y_{0.10}Zr_{0.75}O_{1.88}$ is compared to the data in (c) R-space and (d) k-space.

Table 4.3: Y K-edge EXAFS Fit Results

$Nd_{0.15}Y_{0.10}Zr_{0.75}O_{1.88}$	As synthesized $S_o^2 = 0.8(1)$, $\Delta E = -4(1)$ $R_{fit} = 0.024$			Annealed 1400 °C $S_o^2 = 0.8(1)$, $\Delta E = -4(1)$ $R_{fit} = 0.023$			Annealed 1500 °C $S_o^2 = 0.8(1)$, $\Delta E = -3(1)$ $R_{fit} = 0.039$		
	CN	R (Å)	σ^2	CN	R (Å)	σ^2	CN	R (Å)	σ^2
Zr - O	8	2.32(1)	0.009(2)	8	2.32(1)	0.008(2)	8	2.33(2)	0.007(3)
Zr - Zr/Y	10.2	3.65(1)	0.007(2)	10	3.66(1)	0.006(2)	10.2	3.63(2)	0.004(2)
Zr - Nd	1.8	3.40(3)	0.003(3)	2	3.40(3)	0.002(3)	1.8	3.62(3)	0.000(4)
Zr - O2	24	4.7(2)	0.06(4)	24	4.7(3)	0.08(6)	24	4.50(7)	0.03(2)

$Nd_{0.20}Y_{0.05}Zr_{0.75}O_{1.88}$	As synthesized $S_o^2 = 0.8(1)$, $\Delta E = -4(1)$ $R_{fit} = 0.028$			Annealed 1400 °C $S_o^2 = 0.8(1)$, $\Delta E = -4(1)$ $R_{fit} = 0.020$			Annealed 1500 °C $S_o^2 = 0.8(1)$, $\Delta E = -4(1)$ $R_{fit} = 0.025$		
	CN	R (Å)	σ^2	CN	R (Å)	σ^2	CN	R (Å)	σ^2
Zr - O	8	2.33(2)	0.008(2)	8	2.32(1)	0.008(2)	8	2.32(1)	0.007(2)
Zr - Zr/Y	9.6	3.66(2)	0.007(2)	10	3.65(1)	0.007(2)	9.6	3.66(1)	0.006(2)
Zr - Nd	2.4	3.40(4)	0.005(4)	2	3.40(3)	0.003(3)	2.4	3.40(3)	0.003(3)
Zr - O2	24	4.7(2)	0.07(5)	24	4.7(2)	0.07(5)	24	4.8(3)	0.08(7)

precipitation were annealed at high temperature while only small changes in the intensity of feature G were observed (Figure 4.10b, Figure C.12). The increase in intensity of feature H can be explained by the increased long-range ordering in the system, as was shown by the analysis of the powder XRD patterns. In contrast, no changes in the EXAFS spectra were observed when the $Nd_xY_{1-x}Zr_{0.75}O_{1.88}$ materials made by the ceramic method were annealed at high temperature. This is because the materials made via ceramic reaction were already highly crystalline, and the long-range ordering did not increase appreciably upon annealing.

The EXAFS spectra from the as-synthesized and annealed $Nd_xY_{0.25-x}Zr_{0.75}O_{1.88}$ materials made by the co-precipitation method were modelled to determine the scattering path lengths and disorder parameters of the Y–O, Y–Y/Zr, and Y–Nd scattering paths, and the results of these fits are presented in Table 4.3 and Table C.2, and the fitted spectra are plotted in Figure 4.10c and 4.10d, and Figures C.13-C.16. The Y–O scattering path length was determined to be 2.32 Å, which is in agreement with previously reported values [100, 180, 186, 187]. The Y–O scattering path lengths and σ^2 values did not change when the composition was varied or when the materials were an-

nealed at high temperature, which is consistent with the Y K-edge XANES results. The Y–Y/Zr scattering path length and σ^2 also did not vary significantly when the composition was varied or when the materials were annealed at high temperature, and the average scattering path length was 3.65 Å. This value is in agreement with the results reported in Chapter 3. The Y–Nd scattering path value was found to be 3.39-3.40 Å in all materials except for the $Nd_{0.15}Y_{0.10}Zr_{0.75}O_{1.88}$ sample annealed at 1500 °C, where the Y–Nd scattering path was determined to be 3.62 Å (Table 4.3, Table C.2). The lower values are not physically possible in a fluorite structure, and it has been previously postulated that these results may indicate that a Zr- and Y-doped B-Nd_2O_3 type structure is present in the material in which Y is intimately mixed with Nd. The σ^2 values of the Y–Nd scattering path were also fitted to unrealistically small values in all cases. The Y–Y/Zr and Y–Nd CNs had to be varied to ensure fit a value of $\sigma^2_{\text{Y-Nd}} > 0$ in the case of the $Nd_{0.15}Y_{0.10}Zr_{0.75}O_{1.88}$ and $Nd_{0.20}Y_{0.05}Zr_{0.75}O_{1.88}$ materials prepared by co-precipitation and annealed at 1400 °C. This suggests that the model did not adequately account for the Y–Nd contributions, though the scattering path lengths and σ^2 values of the Y–Y and Y–O scattering pathways likely remain valid.

The Fourier-transformed Y K-edge EXAFS spectra from $Nd_xY_{1-x}Zr_{0.75}O_{1.88}$ materials made via the co-precipitation and ceramic synthetic method are compared in Figure 4.11 and Figure C.12. The intensities of features G and H are suppressed in the spectrum from the as-synthesized $Y_{0.25}Zr_{0.75}O_{1.88}$ material made by the co-precipitation method compared to the same material made by the ceramic route. This can be explained by a lower degree of ordering in the co-precipitated material and is consistent with the powder XRD results. However, the spectrum from the co-precipitated $Y_{0.25}Zr_{0.75}O_{1.88}$ material annealed at 1500 °C is identical to the spectrum from the $Y_{0.25}Zr_{0.75}O_{1.88}$ material made by the ceramic method at 1500 °C, which indicates that the Y coordination environment is identical in this case (Figure 4.11a). A similar result was observed for other $Nd_xY_{1-x}Zr_{0.75}O_{1.88}$ materials studied here with the exception of $Nd_{0.20}Y_{0.05}Zr_{0.75}O_{1.88}$. In this case, feature H in the spectrum from $Nd_{0.20}Y_{0.05}Zr_{0.75}O_{1.88}$ made by the ceramic method was less intense than feature H in the spectra from the as-synthesized $Nd_{0.20}Y_{0.05}Zr_{0.75}O_{1.88}$ and $Nd_{0.20}Y_{0.05}Zr_{0.75}O_{1.88}$ annealed at 1500 °C made by the co-precipitation route (Figure 4.11b).

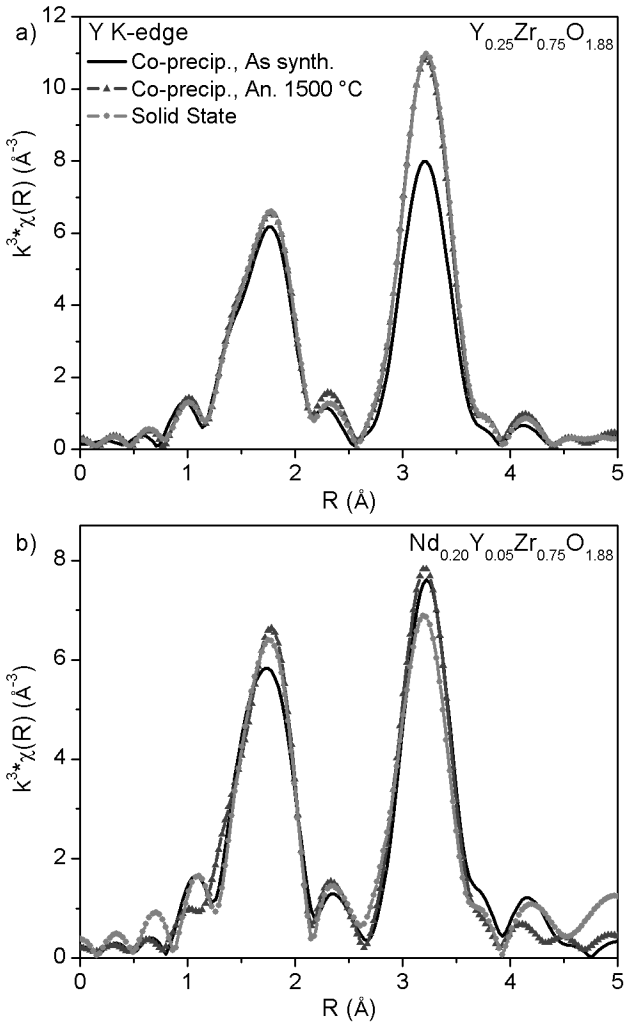

Figure 4.11: The Fourier-transformed Y K-edge EXAFS spectra from (a) $Y_{0.25}Zr_{0.75}O_{1.88}$ and (b) $Nd_{0.20}Y_{0.05}Zr_{0.75}O_{1.88}$ materials made via the co-precipitation method at 800 °C and ceramic method at 1500 °C are compared. Also included are the spectra from the materials made via the co-precipitation method annealed at 1500 °C. The spectra from the $Y_{0.25}Zr_{0.75}O_{1.88}$ made via the ceramic method and the material made via co-precipitation annealed at 1500 °C are nearly identical. Large changes in the intensities of Features G and H are observed in the spectra $Nd_{0.20}Y_{0.05}Zr_{0.75}O_{1.88}$ materials made by the different methods.

This could indicate that Nd occupied more sites further from the Y metal centres in these materials made by the co-precipitation route as destructive interference between the Y–Y/Zr and Y–Nd scattering paths would lead to a decrease in the intensity of feature H. The Y K-edge EXAFS results indicate that using a co-precipitation synthesis with a low calcining temperature (800 °C) results in increased local disorder in the $Nd_xY_{1-x}Zr_{0.75}O_{1.88}$ materials compared to the ceramic synthesis, which is performed at high temperature (1500 °C). The increased disorder in the as-synthesized materials made by the co-precipitation method is due to the lower synthetic temperature, and when these "as-synthesized" materials are annealed at high temperature (i.e., 1500 °C) the local and intermediate Y ordering becomes nearly identical to that of the materials made by the ceramic method.

4.4 Conclusions

The thermal stability, long-range structure, and local structure in a series of $Nd_xY_{0.25-x}Zr_{0.75}O_{1.88}$ materials made by a co-precipitation method have been characterized and compared to $Nd_xY_{0.25-x}Zr_{0.75}O_{1.88}$ materials made by a ceramic route. This study has shown that $Nd_xY_{0.25-x}Zr_{0.75}O_{1.88}$ materials can be successfully synthesized at low temperatures using the co-precipitation route. However, these materials are less crystalline and are more disordered than materials made by the ceramic synthetic route. Further, the compositional range at which the fluorite structure is stable at high temperatures is also diminished. The $Nd_xY_{0.25-x}Zr_{0.75}O_{1.88}$ materials made by the co-precipitation method were only stable at 1400 °C when $x \leq 0.15$, whereas the fluorite structure for materials made by the ceramic method was stable when $x \leq 0.20$. The materials made by the co-precipitation method are more kinetically labile due to the intimate mixing of the component cations on an atomic level [198–201].

The XAS results showed that the local coordination environments around the Zr and Y cations were largely similar in the materials made by the co-precipitation method and the ceramic method. The Y K-edge EXAFS and XANES spectra from the compounds made by co-precipitation and

those made by ceramic synthesis were identical when the co-precipitated materials were annealed at 1500 °C, with the exception of $Nd_{0.20}Y_{0.05}Zr_{0.75}O_{1.88}$. These results generally indicate that the main source of long-range disorder within the materials made by the co-precipitation route came from differences in the arrangements of the metal-oxygen polyhedra rather than from disorder within the metal-oxygen polyhedra. The intermediate and long-range structure is strongly dependent on annealing temperature, and the structure becomes more ordered with increased annealing temperature. Overall, this study concludes that $Nd_xY_{0.25-x}Zr_{0.75}O_{1.88}$ compounds with $x \leq 0.15$ made by a co-precipitation method could be suitable IMF candidates. The reduced annealing times required to produce these materials could lead to a significant opportunity to reduce the cost of producing IMF fuels.

Chapter 5

AN INVESTIGATION OF THE THERMAL STABILITY OF $Nd_xSc_yZr_{1-x-y}O_{2-\delta}$ MATERIALS PROPOSED FOR INERT MATRIX FUEL APPLICATIONS[1]

5.1 Introduction

The Y-doped ZrO_2 materials studied in Chapter 3 and Chapter 4 have been extensively studied for use as an IMF material, but these materials have a low thermal conductivity which leads to undesirable fuel pellet temperatures [88, 96, 98, 116, 123]. The thermal conductivity of the doped ZrO_2 materials could be increased if a lighter dopant element was used, as thermal conductivity generally increases as the molar mass of the material decreases [124]. In this chapter, a study of Sc-doped ZrO_2 materials is presented. Sc-doped ZrO_2 materials have been studied for use in solid-oxide fuel cells (SOFC) due to their high oxygen conductivity. However, these materials have been shown to not be stable at SOFC operating temperatures, as the fluorite structure degrades. Studies have shown that the addition of a small amount ($\sim$1 wt%) of rare-earth element can enhance the stability of the fluorite structure at SOFC operating temperatures. Despite the interest in Sc-doped ZrO_2 materials as SOFC materials, very little research has been done to understand how the addition of significant amounts (>1 wt%) of an actinide will affect the structure

[1]Reproduced in part with permission from J.R. Hayes, A.P. Grosvenor, M. Saoudi *Inorganic Chemistry*, (2016), 55, 1032-1043, DOI: 10.1021/acs.inorgchem.5b01886. Copyright 2106 American Chemical Society. The candidate performed all data collection and analysis, and was responsible for drafting the original manuscript. Editorial contributions were provided by the co-authors.Hayes, J.R.; Grosvenor, A.P.; Saoudi, M. Inorg. Chem. 2016, 55 (3), 1032-1043

of these materials [107, 125–127]. To this end, a series of $Nd_xSc_yZr_{1-x-y}O_{2-\delta}$ materials have been synthesized and characterized. Nd has been used here as a surrogate for Am given its similar ionic radius and chemical reactivity [104, 120–122]. The materials were made via a low-temperature co-precipitation method and the local and long-range structures of the compounds were studied by XRD, SEM, and XAS. Additionally, given the wide range of temperatures that a fuel pellet will experience in a reactor, the stability of the fluorite structure adopted by these materials at high temperatures was also studied by annealing the as-synthesized materials at 1100 °C and 1400 °C. The annealed materials were then studied by powder XRD, SEM, and XAS as well. This study shows that both Nd and Sc are required to stabilize the fluorite structure of $Nd_xSc_yZr_{1-x-y}O_{2-\delta}$ materials, and changes in composition during both in-reactor and post-reactor service must be taken into account when considering these materials for IMF applications.

5.2 Experimental

5.2.1 Synthesis

The $Nd_xSc_yZr_{1-x-y}O_{2-\delta}$ materials were synthesized via a standard co-precipitation method [197]. Stoichiometric amounts of Nd_2O_3 (Alfa Aesar, 99.9%) and Sc_2O_3 (Alfa Aesar, 99.99%) were dissolved in boiling nitric acid while $ZrOCl_2{\cdot}8H_2O$ (Alfa Aesar, 99.9%) was dissolved in deionized water. The acidic Nd-Sc solution was then added to the aqueous Zr^{4+} solution. Concentrated ammonia was added to the mixture which resulted in the formation of a precipitate. The solid was collected via vacuum filtration and dried in air for 24 h. The dried precipitate was then calcined at 800 °C for 24 h in air, resulting in the final product. The thermal stability of the materials was investigated by annealing ∼0.07 g aliquots of the as-synthesized materials in air at 1100 °C and 1400 °C for 24 h.

The phase identification of the as-synthesized and annealed materials was performed using powder XRD. The powder XRD patterns were collected using a PANalytical Empyrean diffractometer using either Cu $K_{\alpha1,2}$ (λ=1.5406 Å) or Co $K_{\alpha1,2}$ (λ=1.7890 Å) radiation. Phase quantifi-

cation was obtained by Rietveld refinement, which was performed using the PANalytical X'pert HighScore Plus software program [173]. Rietveld refinements were performed by fitting cubic ZrO_2, tetragonal ZrO_2, and monoclinic ZrO_2 phases to the data [174–176]. The phases used to model the diffraction data were adapted from the pure ZrO_2 patterns by adding Nd and Sc to the crystallographic site occupied by Zr. The site occupancies were set to be consistent with the ideal stoichiometry of each material. As an example, the cubic ZrO_2 pattern for the $Nd_{0.10}Sc_{0.10}Zr_{0.80}O_{1.90}$ pattern was generated by adding Sc and Nd to the Zr 4a site. The Zr site occupancy was set to 0.80 while the Sc and Nd site occupancies were each set to 0.10. The addition of Sc and Nd impacted the intensity of the modelled peaks and significantly improved the quality of the fit. For instance, in the example presented above when only Zr was used in the model the refinement factor R_{wp} (defined in Table D.1) was 11.82 while the R_{wp} was 9.83 when Sc and Nd were also included in the model. The background was fitted using a 3rd order polynomial function which also included a $1/2\theta$ term.

5.2.2 Scanning Electron Microscopy

SEM samples were prepared by pressing ∼0.17 g of the as-synthesized material into a ¼" (0.635 cm) pellet at 8 MPa before being sintered at 800 °C in air for 12 h. (8 MPa was the pellet gauge pressure, and the actual pressure exerted on the pellet is much greater.) Several of the pellets were subsequently annealed at 1400 °C for 24 h in air and air quenched. The pellets were embedded in a resin matrix and ground manually to a flat surface using SiC paper. The pellet surfaces were then polished using 0.25 μm diamond paste. The samples were coated with a thin carbon layer to reduce sample charging effects. A Zeiss Supra-55 WDS-VP SEM coupled with an Energy Dispersive X-ray Spectrometer (EDS) was used to collect SEM images and to carry out EDS mapping. The sample surface morphology was examined using secondary electron (SE) images. Samples were mapped by EDS for Zr, Sc, and Nd at 500x magnification, and the EDS maps were collected using an ∼8 μm step size at an accelerating voltage of 20 kV. All EDS maps from a sample were collected at the same spot.

5.2.3 X-ray Absorption Spectroscopy

5.2.3.1 Zr K-edge, Nd L_3-edge XAS

Zr K-edge and Nd L_3-edge XAS spectra from the as-synthesized and annealed samples were collected using the CLS@APS Sector 20BM bending magnet beamline located at the Advanced Photon Source (APS), Argonne National Laboratory. The beamline specifications, sample preparation procedures, and Zr K- and Nd L_3-edge spectra collection parameters have been described in Section 3.2.3.1 on page 62. All spectra were normalized and analyzed using the Demeter software suite [155].

5.2.3.2 Zr K-edge EXAFS Modelling

The EXAFS spectra were analyzed by fitting the parameters of Equation 3.1 on page 63 [178]. The Zr K-edge EXAFS spectra were analyzed by calculating $F_j(k)$, $\phi_j(k)$, and λ for each set of scattering pairs in a given cluster using the FEFF6 code [179]. The other parameters were fit using a least-squares refinement as described below using the Artemis program, which is included in the Demeter software suite [155].

A scattering cluster was generated based on a cubic zirconium structure using the parameter determined from the powder XRD patterns (*vide infra*). Two of the next-nearest-neighbor (NNN) Zr atoms were replaced by Nd and two of the NNN Zr atoms were replaced by Sc in the cluster when modelling the quaternary materials. It was necessary to add two of each dopant atoms into the system to generate the Zr–O–M scattering paths (M = Zr, Nd, Sc). (In the ternary materials only Sc or Nd was substituted into the system.) The R_j and σ^2 parameters of the first shell Zr–O, second shell Zr–Zr, and third shell Zr–O (labelled as Zr–O2) paths were fitted as separate variables for each scattering path. The CN of each scattering path was initially set to reflect the stoichiometry of each phase and was then varied manually to improve the fit. The energy shift parameter, ΔE, and S_o^2 were fitted across all scattering paths. The Zr–O–Zr, Zr–O–Sc, and Zr–O–Nd were also fitted using parameters from the single scattering paths. The changes in multi-scattering path

lengths were modelled as $\Delta R_{Zr-O} + 0.5*\Delta R_{Zr-Zr/Sc/Nd}$, and the Debye-Waller factors were modelled as $\sigma^2_{Zr-O} + 0.5*\sigma^2_{Zr-Zr/Sc/Nd}$. The CNs of the multiscattering paths were changed to reflect the CNs of the Zr–Zr, Zr–Sc, and Zr–Nd single-scattering paths.

5.2.3.3 Sc K-edge, Zr L_3-edge XAS

Zr L_3-edge and Sc K-edge XANES spectra were collected using the Soft X-ray Microcharacterization Beamline (SXRMB, 06B1-01) located at the Canadian Light Source (CLS). The beamline specifications have been previously outlined in Section 3.2.3.3 on page 65. Samples were mounted as fine powders spread on double-sided C tape. Both the Zr L_3-edge and Sc K-edge spectra were measured in total electron yield (TEY) mode using a 0.10 eV step through the absorption edge. The Zr L_3-edge spectra spectra were calibrated using Zr foil, which has a known Zr L_3-edge absorption energy of 2223 eV, and the Sc K-edge spectra were calibrated using Ti metal powder, having a known edge energy of 4966 eV [154]. Spectra were normalized and analyzed using the Demeter software suite [155].

5.3 Results and Discussion

5.3.1 Powder XRD

Powder XRD patterns were collected from the as-synthesized and annealed $Nd_xSc_yZr_{1-x-y}O_{2-x}$ materials and are presented in Figure 5.1 and 5.2, and Figures D.1 and D.2 in Appendix D. The diffraction patterns were analyzed using Rietveld refinement to determine the cubic unit cell parameter and phase composition of the materials. The results of this analysis are presented in Table 5.1 and D.1. The peaks in the patterns from the as-synthesized materials heated at 800 °C are wider than those from the annealed samples. The wide peaks indicate the poor crystallinity of the as-synthesized materials and show that the as-synthesized materials are significantly less crystalline than the materials annealed at higher temperatures [156]. This is consistent with the synthetic conditions as higher annealing temperatures should lead to a more crystalline and ordered material.

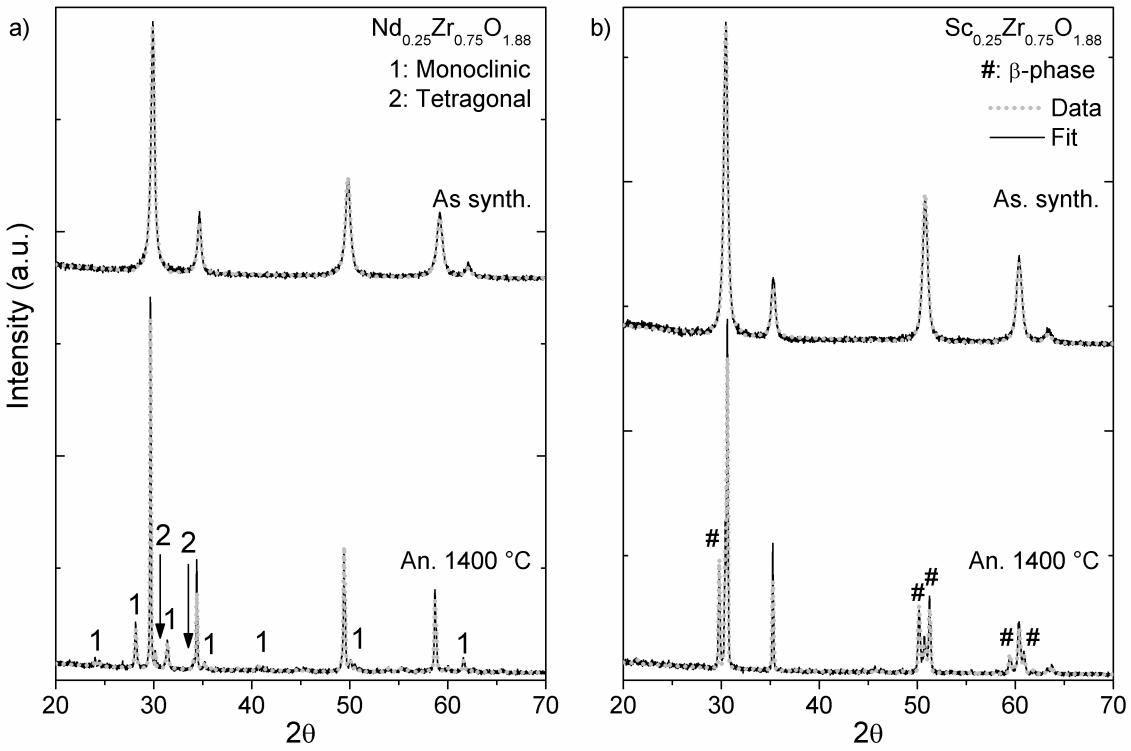

Figure 5.1: Powder XRD patterns from the as-synthesized and annealed ternary (a) $Nd_{0.25}Zr_{0.75}O_{1.88}$ and (b) $Sc_{0.25}Zr_{0.75}O_{1.88}$ materials are presented. In all figures "As-synth." indicates as-synthesized material and "An." indicates an annealed sample. Peaks from monoclinic (1) and tetragonal (2) ZrO_2 phases form when the $Nd_{0.25}Zr_{0.75}O_{1.88}$ material was annealed at 1400 °C. Peaks associated with a β-phase Sc-Zr-O material, marked with an asterisk, were observed when the $Sc_{0.25}Zr_{0.75}O_{1.88}$ material was annealed at 1400 °C. There is good agreement between the data and the fits generated by Rietveld analysis in all cases.

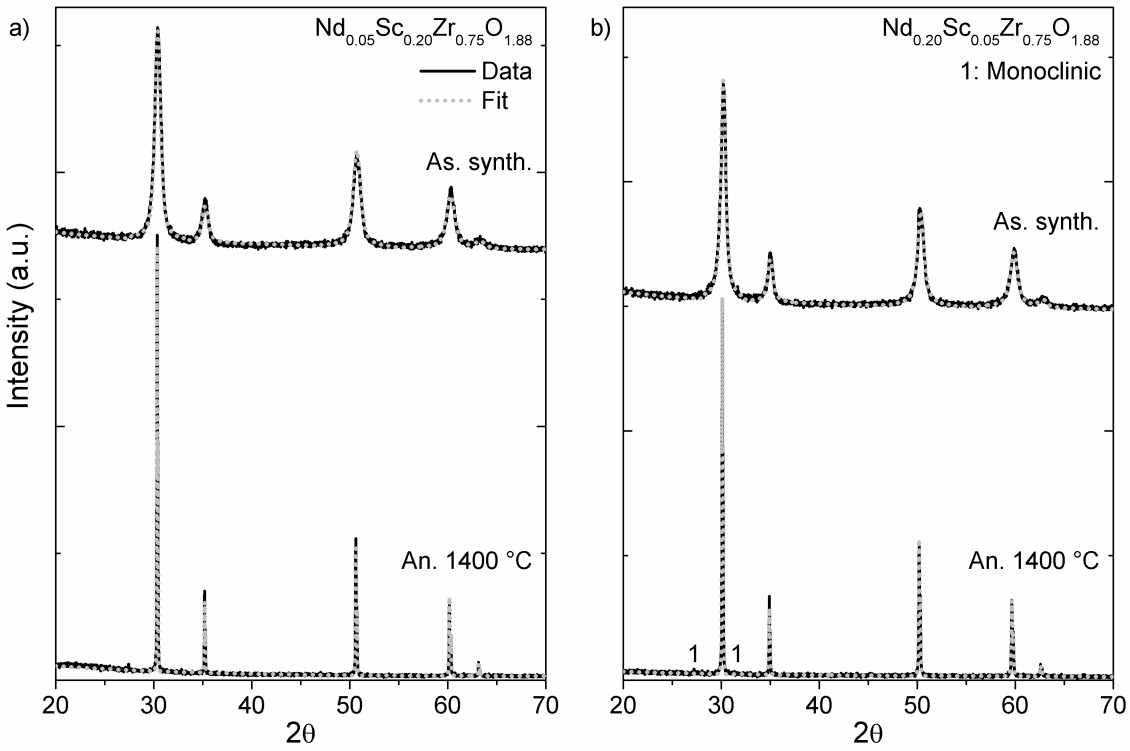

Figure 5.2: The powder X-ray diffraction patterns from the quaternary as-synthesized and annealed (a) $Nd_{0.05}Sc_{0.20}Zr_{0.75}O_{1.88}$ and (b) $Nd_{0.20}Sc_{0.05}Zr_{0.75}O_{1.88}$ materials are presented. A small monoclinic impurity phases formed when the $Nd_{0.20}Sc_{0.05}Zr_{0.75}O_{1.88}$ material was annealed at 1400 °C while the $Nd_{0.05}Sc_{0.20}Zr_{0.75}O_{1.88}$ remained a single-phase upon annealing. There is good agreement between the data and the fits generated by Rietveld analysis in all cases.

Table 5.1: Parameters of powder XRD Rietveld Refinement

	As synth.	An. 1100 °C	An. 1400 °C
$Nd_{0.25}Zr_{0.75}O_{1.88}$			
Rwp[a]	8.08	8.51	8.85
Unit Cell (Å)	5.1791(3)	5.2156(5)	5.2079(1)
Wt. Fraction	100% Cubic	64.7% Cubic	65.7% Cubic
		35.3% Tetragonal	3.5% Tetragonal
			30.9% Monoclinic
$Nd_{0.20}Sc_{0.05}Zr_{0.75}O_{1.88}$			
Rwp[a]	10.33	11.74	12.94
Unit Cell (Å)	5.1614(1)	5.1658(5)	5.1565(1)
Wt. Fraction	100% Cubic	67.4% Cubic	91.2% Cubic
		32.6% Tetragonal	8.8% Monoclinic
$Nd_{0.15}Sc_{0.10}Zr_{0.75}O_{1.88}$			
Rwp[a]	6.38	12.07	12.50
Unit Cell (Å)	5.1252(5)	5.1303(3)	5.1321(1)
Wt. Fraction	100% Cubic	100% Cubic	100% Cubic
$Nd_{0.10}Sc_{0.15}Zr_{0.75}O_{1.88}$			
	8.21	8.70	13.48
	5.1080(6)	5.1121(2)	5.1128(1)
	100% Cubic	100% Cubic	100% Cubic
$Nd_{0.05}Sc_{0.20}Zr_{0.75}O_{1.88}$			
Rwp[a]	7.89	9.41	11.24
Unit Cell (Å)	5.0885(5)	5.0921(1)	5.09130(8)
Wt. Fraction	100% Cubic	100% Cubic	100% Cubic
$Sc_{0.25}Zr_{0.75}O_{1.88}$			
Rwp[a]	7.90	N/A	10.86
Unit Cell (Å)	5.0828(3)	N/A	5.0857(3)
Wt. Fraction	100% Cubic	N/A	30.8% Cubic
			69.2% β-phase

[a] $R_{wp} = \sum w_i(y_{io} - y_{ic})^2 / \sum w_i y_{io}$; w_i= i^{th} comp. wt. fraction; y_{ic}=calculated intensity; y_{io} = diffraction pattern intensity

Only peaks associated with the cubic fluorite phase were observed in the patterns from the as-synthesized materials. However, the cubic phase was not stable when the ternary phases were annealed at high temperature. The tetragonal phase was formed in the ternary $Nd_{0.25}Zr_{0.75}O_{1.88}$ compound when it was annealed at 1100 °C and the Rietveld analysis indicated that the material was ∼33% tetragonal and 67% cubic phase (see Table 5.1). Both the tetragonal and monoclinic phases were observed when $Nd_{0.25}Zr_{0.75}O_{1.88}$ was annealed at 1400 °C, resulting in a multi-phase material containing 30.9% monoclinic phase, 3.5% tetragonal phase, and 64.7% cubic phase. An ordered Sc-Zr-O β-phase was formed when $Sc_{0.25}Zr_{0.75}O_{1.88}$ was annealed at 1400 °C. The structure of this β-phase material is complex and poorly understood, though it can be described as a superstructure of the fluorite structure in which the O-vacancies are ordered [126, 127, 200, 204–206]. The formation of a rhombahedral β-phase Sc-Zr-O observed in this study is consistent with previous studies of Sc-substituted zirconia, in which rhombahedral Sc-Zr-O phases were observed when Sc-ZrO_2 materials were heated at temperatures >600 °C [126, 127, 200, 204–206].

The stability of the cubic fluorite structure adopted by the quaternary $Nd_xSc_yZr_{1-x-y}O_{2-\delta}$ materials was found to vary with composition. A phase change was observed in the $Nd_{0.20}Sc_{0.05}Zr_{0.75}O_{1.88}$ material when it was annealed at high temperature. The cubic structure decomposed into a mix of tetragonal and cubic phase when this composition was annealed at 1100 °C. Only a small amount (8.8%) of monoclinic phase was observed when $Nd_{0.20}Sc_{0.05}Zr_{0.75}O_{1.88}$ was annealed at 1400 °C (Table 5.1). Monoclinic zirconia was also observed when $Nd_{0.15}Sc_{0.05}Zr_{0.80}O_{1.90}$ was annealed at 1400 °C (Table D.1, Figure 5.2a). These results indicate that a minimum amount of Sc ($y \geq 0.10$) must be doped into the system to stabilize the cubic phase in the quaternary materials. In addition, neither the $Nd_{0.10}Sc_{0.05}Zr_{0.85}O_{1.92}$ nor the $Nd_{0.05}Sc_{0.10}Zr_{0.85}O_{1.92}$ materials were stable upon annealing at high temperatures. These results indicate that the amount of dopant added to the material (i.e., x+y) must be greater than 0.15 to stabilize the cubic zirconia phase at a wide range of temperatures. No phase changes were observed when the $Nd_xSc_yZr_{1-x-y}O_{2-\delta}$ materials with $x+y > 0.15$ and $y \geq 0.10$ were annealed at temperatures up to 1400 °C (see Table 5.1, Table D.1).

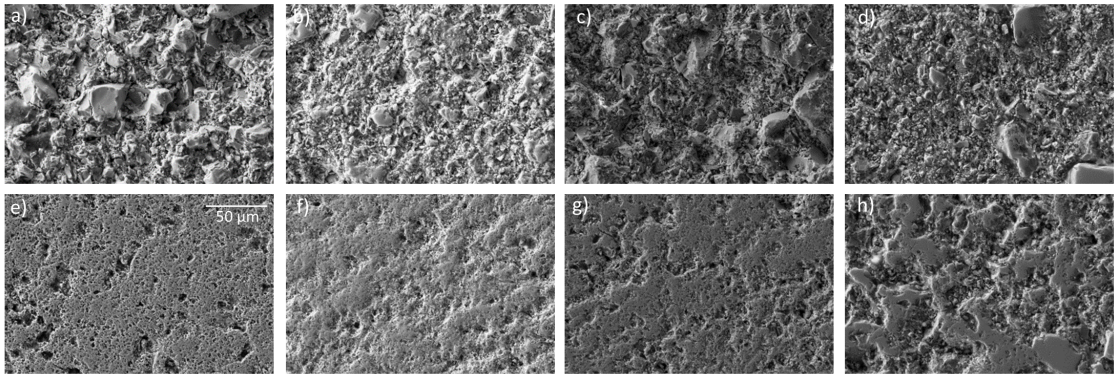

Figure 5.3: SE images from pellets of the as synthesized (a) $Nd_{0.25}Zr_{0.75}O_{1.88}$, (b) $Nd_{0.20}Sc_{0.05}Zr_{0.75}O_{1.88}$, (c) $Nd_{0.05}Sc_{0.20}Zr_{0.75}O_{1.88}$, and (d) $Sc_{0.25}Zr_{0.75}O_{1.88}$ materials and the (e) $Nd_{0.25}Zr_{0.75}O_{1.88}$, (f) $Nd_{0.20}Sc_{0.05}Zr_{0.75}O_{1.88}$, (g) $Nd_{0.05}Sc_{0.20}Zr_{0.75}O_{1.88}$, and (h) $Sc_{0.25}Zr_{0.75}O_{1.88}$ pellets annealed at 1400 °C. Upon annealing the pellet surface flattens and more surface pores are visible.

The cubic unit cell parameters are plotted in Figure D.3 in Appendix D as a function of composition. The changes in the unit cell with composition deviated from the values expected from Vegard's law (i.e., the change was not linear) and the unit cells of the end member as-synthesized $Nd_{0.25}Zr_{0.75}O_{1.88}$ and $Sc_{0.25}Zr_{0.75}O_{1.88}$ materials were much larger than expected [182]. This is in contrast to the $Nd_xY_yZr_{1-x-y}O_{2-\delta}$ system, where the lattice parameter varied according to Vegard's law (see Section 3.3.1 on page 65). This could be indicative of more disorder in these compounds when compared to the quaternary materials. The unit cell of the materials expanded slightly upon annealing with the exception of $Nd_{0.20}Sc_{0.05}Zr_{0.75}O_{1.88}$, which contracted slightly. This expansion varied between 0.0028-0.0365 Å and the magnitude of the change generally decreased as the Sc replaced Nd in the system. Again, the unit cells of the end-member $Nd_{0.25}Zr_{0.75}O_{1.88}$ and $Sc_{0.25}Zr_{0.75}O_{1.88}$ materials deviated from Vegard's Law. This deviation in the annealed materials may be explained by the large changes in phase composition that occurred upon annealing (*vide supra*).

5.3.2 SEM and EDS

The as-synthesized and annealed materials were characterized by SEM. Representative secondary electron (SE) micrographs are presented in 5.3 and Figure D.4 in Appendix D. The micrographs

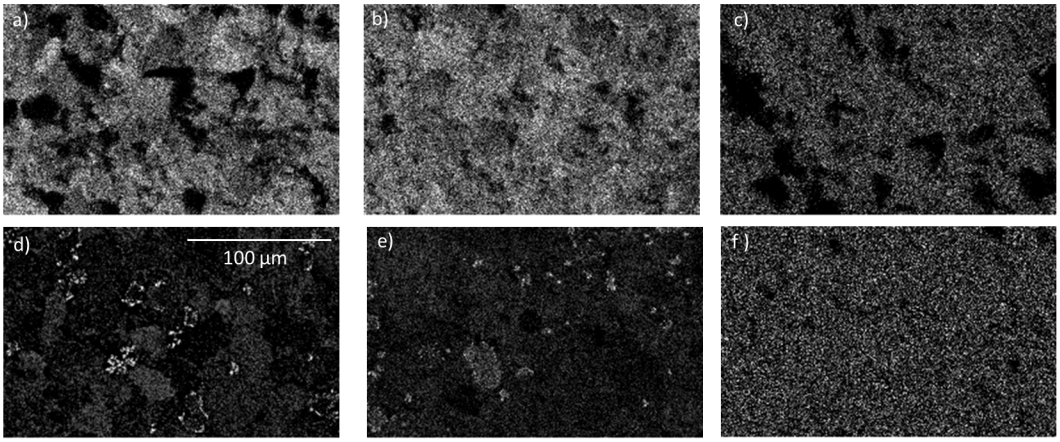

Figure 5.4: Nd L_α EDS maps from the as-synthesized (a) $Nd_{0.25}Zr_{0.75}O_{1.88}$, (b) $Nd_{0.20}Sc_{0.05}Zr_{0.75}O_{1.88}$, (c) $Nd_{0.05}Sc_{0.20}Zr_{0.75}O_{1.88}$ pellets and the (d) $Nd_{0.25}Zr_{0.75}O_{1.88}$ and (e) $Nd_{0.20}Sc_{0.05}Zr_{0.75}O_{1.88}$ and (f) $Nd_{0.05}Sc_{0.20}Zr_{0.75}O_{1.88}$ pellets annealed at 1400 °C. (Nd L_α fluorescence was not detected in the $Nd_{0.05}Sc_{0.20}Zr_{0.75}O_{1.88}$ pellet annealed at 1400 °C.) The Nd became segregated when the pellet was annealed at high temperature.

from the as-synthesized pellets (5.3a-d) showed that the surfaces contained large, faceted grains. The surface morphology did not appear to depend on composition. The surfaces became porous upon annealing at 1400 °C and no faceted surfaces were observed. The surfaces of the annealed pellets were consistent with the surfaces of the $Nd_xY_yZr_{1-x-y}O_{2-\delta}$ materials studied in Chapter 3 that were synthesized via a high temperature solid-state route. This indicates that surface morphology is strongly dependent on annealing temperature but independent of composition.

Energy dispersive spectroscopy (EDS) elemental maps were also collected from the materials and these are presented in Figures 5.4-5.6 and Figures D.5-D.7 in Appendix D. In general, lighter shaded regions indicate regions of higher elemental concentration while darker regions indicate areas of lower elemental concentration. However, some shadowing can be seen due to topography of the polished pellet surface. This shadowing is most prevalent in Figure 5.6, which shows Zr L_α maps from the $Nd_xSc_yZr_{1-x-y}O_{2-\delta}$ samples. The dark regions in these EDS maps correspond well to dark regions found in Sc and Nd EDS maps from the same composition, further confirming that the low intensity regions are due to shadowing effects, and not changes in concentration. (All of the EDS maps and SEM images were collected from a single spot and magnification for each individual sample.) Figure 5.4 shows the Nd L_α-maps of several as-synthesized materials (Figure 5.4a-c)

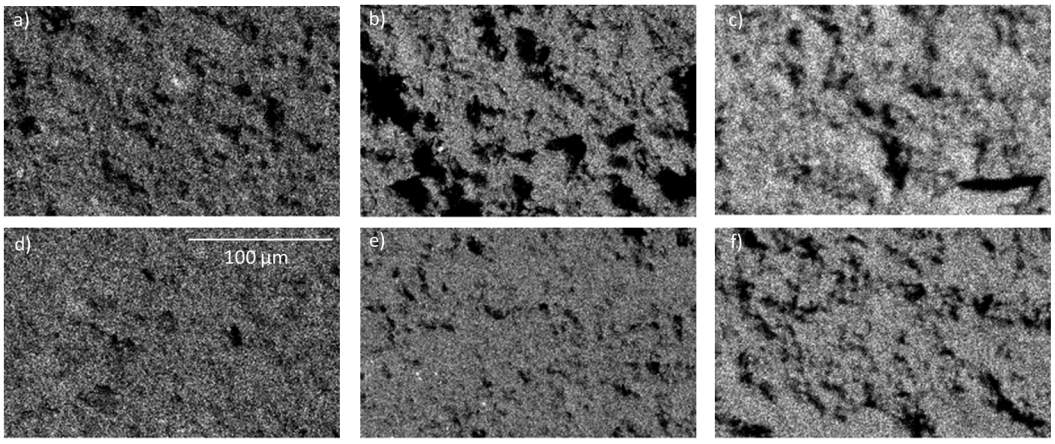

Figure 5.5: Sc K_α EDS maps from the as-synthesized (a) $Nd_{0.20}Sc_{0.05}Zr_{0.75}O_{1.88}$, (b) $Nd_{0.05}Sc_{0.20}Zr_{0.75}O_{1.88}$, and (c) $Sc_{0.25}Zr_{0.75}O_{1.88}$ materials and the (d) $Nd_{0.20}Sc_{0.05}Zr_{0.75}O_{1.88}$, (e) $Nd_{0.05}Sc_{0.20}Zr_{0.75}O_{1.88}$, and (f) $Sc_{0.25}Zr_{0.75}O_{1.88}$ materials annealed at 1400 °C.) No change in the Sc distribution was observed when the pellets were annealed at 1400 °C.

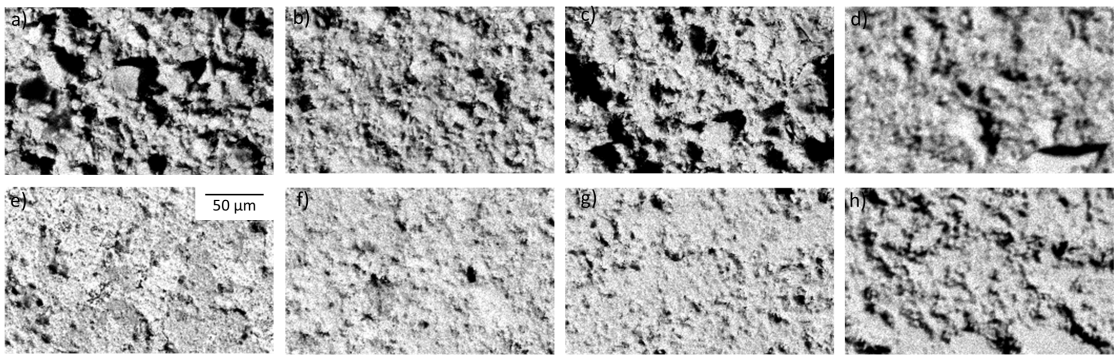

Figure 5.6: Zr K_α EDS maps from pellets of the as synthesized (a) $Nd_{0.25}Zr_{0.75}O_{1.88}$, (b) $Nd_{0.20}Sc_{0.05}Zr_{0.75}O_{1.88}$, (c) $Nd_{0.05}Sc_{0.20}Zr_{0.75}O_{1.88}$, and (d) $Sc_{0.25}Zr_{0.75}O_{1.88}$ materials and the (e) $Nd_{0.25}Zr_{0.75}O_{1.88}$, (f) $Nd_{0.20}Sc_{0.05}Zr_{0.75}O_{1.88}$, (g) $Nd_{0.05}Sc_{0.20}Zr_{0.75}O_{1.88}$, and (h) $Sc_{0.25}Zr_{0.75}O_{1.88}$ pellets annealed at 1400 °C. The Zr was homogenously distributed in all of the as-synthesized and annealed samples.

and materials annealed at 1400 °C (Figure 5.4d,e). No aggregation was observed in the Nd L_α-map from the $Nd_{0.05}Sc_{0.20}Zr_{0.75}O_{1.88}$ sample annealed at 1400 °C due to the poor signal-to-noise ratio of the map (Figure 5.4f). Nd is relatively evenly distributed in the as-synthesized materials, though some spots where higher Nd concentrations were observed (Figure 5.4a-c). In contrast, the Nd distribution becomes heterogeneous upon annealing the materials at 1400 °C, and distinct Nd aggregates were observed within the materials (Figure 5.4d,e). The observed changes in the Nd EDS maps are distinct, and the Nd distributions are qualitatively different between the as-synthesized and annealed samples. The nature of these changes indicates that the Nd distribution shifts, and that these results are not a product of changes in the surface shadowing. This change in Nd distribution upon high-temperature annealing was observed in all materials studied, and suggests that Nd segregation is a thermodynamically favorable process, rather than a kinetically driven process as was previously postulated for $Nd_xY_yZr_{1-x-y}O_{2-\delta}$ materials made via a solid-state reaction method (see Section 3.4 on page 83). The formation of Nd aggregates is not promising when considering these materials for IMF applications as the formation of areas of high actinide concentration in an IMF would lead to uneven heat distribution and activity throughout the fuel pellet [45].

The Sc K_α and Zr L_α maps are presented in Figure 5.5 and 5.6, respectively. A small number of Sc bright spots were observed in the as-synthesized materials, but these appeared to disperse upon annealing at 1400 °C. In general, it was observed that both Zr and Sc were dispersed homogenously throughout these materials. The distribution of both elements remained generally homogenous after high-temperature annealing as well. This indicates that both Zr and Sc do not segregate in the materials upon annealing.

5.3.3 Zr K-edge

5.3.3.1 XANES

Zr K-edge XANES spectra were collected from the as-synthesized and high-temperature annealed $Nd_xY_yZr_{1-x-y}O_{2-\delta}$ materials and these spectra are presented in Figure 5.7 and Figure D.8 and D.9 in Appendix D. Three features are observed in these spectra, labelled as A, B, and C in Figure 5.7a.

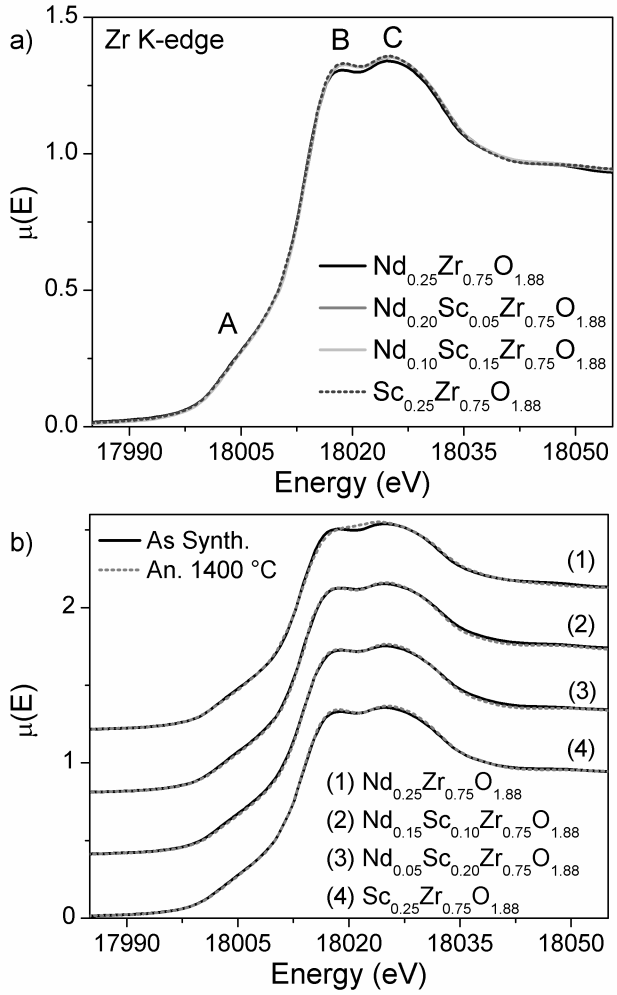

Figure 5.7: (a) Zr K-edge XANES spectra from the as-synthesized $Nd_xSc_yZr_{1-x-y}O_{2-\delta}$ materials are presented. Three features, labelled A, B and C are observed. Feature A arises from forbidden, quadrupolar Zr 1s $\rightarrow$ 4d transitions while features B and C are due to dipolar Zr 1s $\rightarrow$ 5p transitions. (b) The spectra from the as-synthesized materials are compared to the spectra from the materials annealed at 1400 °C. Only the spectrum from the $Nd_{0.25}Zr_{0.75}O_{1.88}$ materials changes upon annealing.

Feature A is known as the pre-edge and is due to forbidden, quadrupolar Zr 1s $\rightarrow$ 4d excitations [183, 184]. Features B and C constitute the main-edge, which is comprised of dipolar Zr 1s $\rightarrow$ 5p excitations [183, 184]. The intensity and shape of the pre-edge depends on the geometry of the coordination environment around the Zr metal centre [180]. The pre-edge does not change with composition, which indicates the symmetry of the Zr coordination environment likely does not vary with changing composition.

Small changes in the main-edge were observed to occur as the composition of the as-synthesized materials was varied. Feature B moved to higher energy and the intensity of features B and C increased as Sc replaced Nd in the system. A comparison to previously collected Zr K-edge spectra from tetragonal and monoclinic ZrO_2 systems indicates that these changes were due to a change in the symmetry of the Zr-bearing phases (Figure 3.5 on page 71). Therefore, it is concluded from these changes in the Zr K-edge XANES spectra that the symmetry of the local Zr coordination environment of the $Nd_xSc_yZr_{1-x-y}O_{2-\delta}$ materials decreased slightly as Sc replaces Nd in these materials.

The spectrum from the $Nd_{0.25}Zr_{0.75}O_{1.88}$ material changes upon annealing with the intensity of the main-edge at $\sim$18020 eV increasing and feature B shifting to slightly higher energy (Figure 5.7b). This change is consistent with the formation of a lower symmetry ZrO_2 phase and is consistent with the powder XRD results. The spectra from the other $Nd_xSc_yZr_{1-x-y}O_{2-\delta}$ materials do not change upon high-temperature annealing. The powder XRD results indicated that β-phase Sc-Zr-O formed when $Sc_{0.25}Zr_{0.75}O_{1.88}$ was annealed at 1400 °C. However, the β-phase Sc-Zr-O is a derivative of the fluorite supercell and the main difference between the fluorite structure and the structure of the β-phase Sc-Zr-O material is the ordering of anion vacancies within the system [126, 127, 200, 204–206]. The Zr coordination environment remains largely unchanged in these materials, and thus any changes between the spectra from the cubic phase and β-phase are too small to be observed given the relatively low energy resolution of the Zr K-edge spectra. In general, the Zr K edge XANES spectra show that the local environment around the Zr did not change significantly upon high-temperature annealing when Sc was present in the material.

5.3.3.2 EXAFS

The EXAFS region of the Zr K-edge XAS spectra were collected from the as-synthesized and annealed $Nd_xSc_yZr_{1-x-y}O_{2-\delta}$ materials and the Fourier transformed spectra are presented in Figure 5.8 and Figures D.10-D.12 in Appendix D. Three peaks were observed in these spectra, and these are labelled as D, E, and E' in Figure 5.8a. Peak D is associated with the nearest-neighbor (NN) Zr–O scattering path and peak E is associated with the next-nearest-neighbor (NNN) Zr–Zr, Zr–Sc, and Zr–Nd scattering paths. Peak E' is primarily attributed to a shoulder of the Zr–Sc single-scattering path. The intensity of Peak E was mostly independent of composition, though a small decrease in intensity was observed when Nd was added to the system. It is likely that this change was due to interference between the Zr–Zr, Zr–Sc, and Zr–Nd paths, and does not represent a physical change. The intensity of Peak E' increased with increasing Sc content. This change with increasing Sc content can be explained by the increased number of Sc NNN atoms as this peak is directly related to the Zr–Sc scattering path.

The intensity of peak D increased as Sc replaced Nd in the system. This change may indicate that the Zr coordination number increases with increasing Sc content. It has been previously shown that O-vacancies are preferentially located around Nd in Nd-ZrO_2 systems while O-vacancies are preferentially located around the Sc metal centres in Sc-ZrO_2 systems [207–209]. Here, the O-vacancies are likely pulled away from the Zr metal centres as Sc is introduced in the system resulting in an increase in the Zr CN. This phenomenon has been previously ascribed to size effects and differences in Sc-vacancy binding energy compared to the Zr-vacancy binding energy in RE_2O_3-ZrO_2 (RE = rare-earth, Y, Sc) systems, and the results here serve to further confirm these prior studies [207–209].

The Fourier transformed EXAFS spectra from the as-synthesized and annealed materials are compared in Figure 5.8b and Figures D.9-D.11 in Appendix D. The intensities of peaks D, E, and E' increased with increasing annealing temperature with the exception of the $Nd_{0.10}Sc_{0.05}Zr_{0.85}O_{1.92}$ and $Nd_{0.05}Sc_{0.10}Zr_{0.85}O_{1.92}$ samples (Figure D.9a, c). In the case of these materials, phase changes were also observed via powder XRD (Figure D.2), and, in general, these

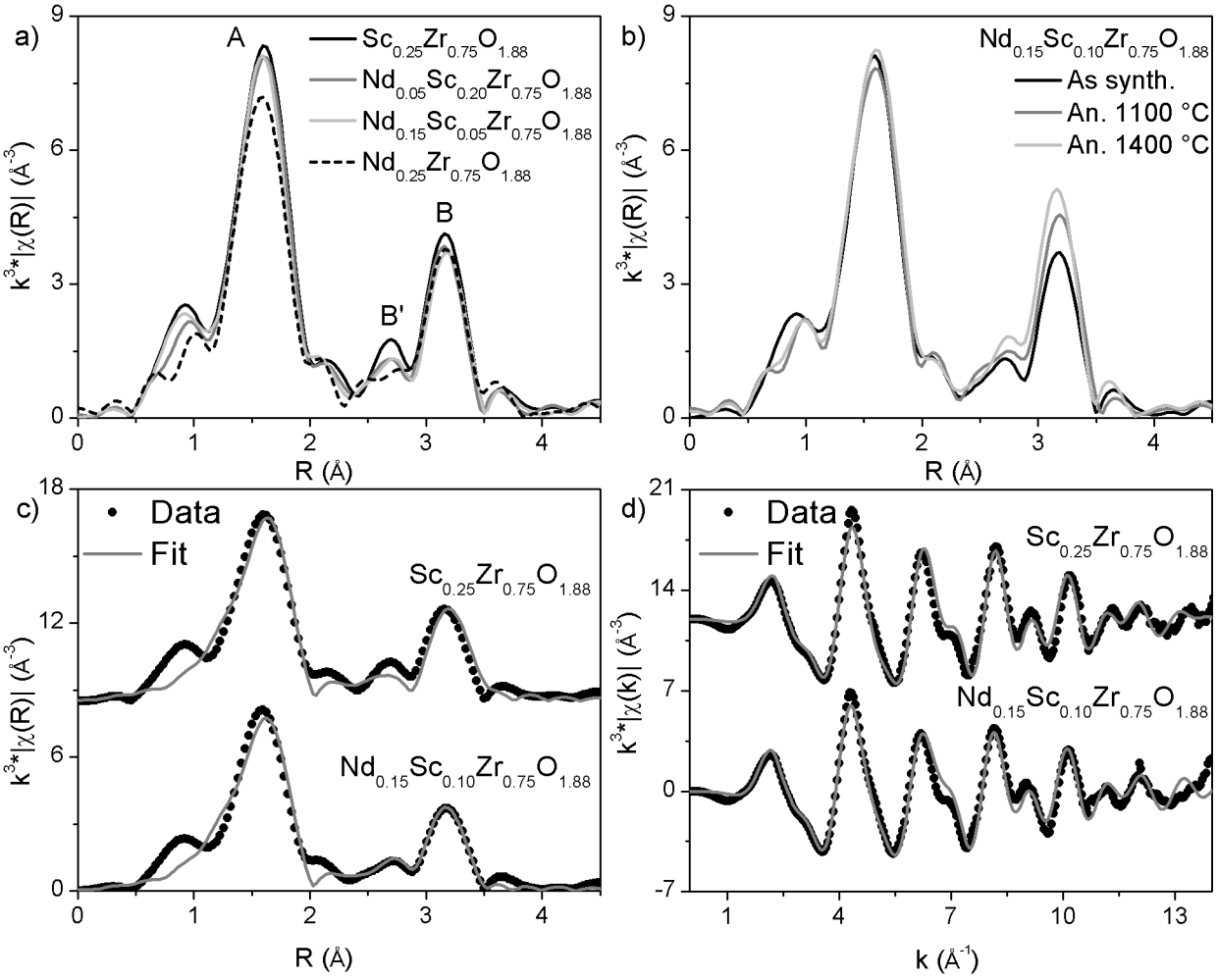

Figure 5.8: (a) Zr K-edge EXAFS spectra from several of the as-synthesized $Nd_xSc_yZr_{1-x-y}O_{2-\delta}$ materials are presented. Three features, labelled D, E, and E' are observed: feature D arises from Zr–O scattering paths and features E is attributed to the Zr–Zr, Zr–Sc, and Zr–Nd scattering paths. The contributions to feature E' are mostly attributable to the Zr–Sc scattering path. (b) The Zr EXAFS spectra from the as-synthesized and annealed $Nd_{0.15}Sc_{0.10}Zr_{0.75}O_{1.88}$ materials are compared. There is little change in the intensity of Feature D while the intensity of Features E and E' increase as the annealing temperature increases. (c) The fits of the Zr K-edge spectra are compared to the data in R-space and (d) k-space.

materials behaved differently than the other $Nd_xSc_yZr_{1-x-y}O_{2-\delta}$ materials. Here, the discussion about these materials is limited to concluding that $Nd_xSc_yZr_{1-x-y}O_{2-\delta}$ compounds with $x+y \leq 0.15$ are not stable under high-temperature annealing conditions and are therefore unsuitable for IMF applications.

With regards to the $Nd_xSc_yZr_{1-x-y}O_{2-\delta}$ compounds with $x+y > 0.15$, the increased intensity of the peaks can largely be attributed to an increase in the ordering of the local and long-range structures in these materials upon high-temperature annealing. This conclusion is consistent with the powder XRD results, as the diffraction peaks were observed to become more narrow upon annealing (*vide supra*). However, the increase in the intensity of feature D upon annealing was not consistent between material compositions, and the intensity appears to increase more when the Sc loading is high. This may indicate that the Zr CN is also increasing in these cases in addition to the increased ordering. This could be caused by a migration of O-vacancies to sites adjacent to the Sc metal centres (*vide infra*). These comparisons indicate that the $Nd_xSc_yZr_{1-x-y}O_{2-\delta}$ materials made at 800 °C become more ordered upon high-temperature annealing when $x+y > 0.15$.

The EXAFS spectra were also modelled and the resulting fits are plotted along with the Zr K-edge spectra in Figure 5.8c,d and Figures D.13-D.23 in Appendix D. The parameters of these fits are enumerated in Table 5.2 and Table D.2. Overall, there is a good agreement between the data and the modelled spectra, and the R-factors of the models are indicative of quality fits (see Table 5.2). The Zr–O bond distance was found to be $\sim$2.15 Å in all cases and the Zr–Zr bond distance was found to vary between 3.53-3.58 Å, although the differences in the Zr–Zr bond distances were not statistically significant. Both the Zr–O and Zr–Zr distances are in agreement with the values reported in Chapter 3 for $Nd_xY_yZr_{1-x-y}O_{2-\delta}$ systems. The Zr–Sc bond distances and Zr–Nd scattering distances determined from the as-synthesized and annealed $Sc_{0.25}Zr_{0.75}O_{1.88}$ and as-synthesized $Nd_{0.15}Sc_{0.10}Zr_{0.75}O_{1.88}$ were all within a statistically similar range. However, the Zr–Nd bond distance in $Nd_{0.15}Sc_{0.10}Zr_{0.75}O_{1.88}$ was observed to decrease to 3.36(3) Å when the material was annealed at 1400 °C. A similar phenomenon was observed when quaternary $Nd_xY_yZr_{1-x-y}O_{2-\delta}$ compounds were annealed at 1400 °C (see Section 3.3.3.2 on page 73). In Chapter 3, the short

Table 5.2: Zr K-edge EXAFS Fitting Results

$Sc_{0.25}Zr_{0.75}O_{1.88}$						
	S_o^2= 0.98(7), ΔE = -1.7(8)			S_o^2= 0.987, ΔE = -1.7(8)		
	R_{fit}= 0.017			R_{fit}= 0.017		
	CN	R (Å)	σ^2	CN	R (Å)	σ^2
Zr - O	7	2.149(8)	0.008(1)	7	2.152(9)	0.008(1)
Zr - Zr	9	3.55(1)	0.012(1)	9	3.53(1)	0.011(2)
Zr - Sc	3	3.57(5)	0.017(8)	3	3.56(5)	0.015(8)
Zr - O2	24	4.26(4)	0.05(1)	24	4.21(8)	0.05(1)
$Nd_{0.15}Sc_{0.10}Zr_{0.75}O_{1.88}$						
	S_o^2= 0.93(9), ΔE = -2.8(9)			S_o^2= 0.94(7), ΔE = -1.7(7)		
	R_{fit}= 0.014			R_{fit}= 0.014		
	CN	R (Å)	σ^2	CN	R (Å)	σ^2
Zr - O	7	2.160(8)	0.008(1)	7	2.158(8)	0.008(1)
Zr - Zr	9	3.57(2)	0.012(2)	9	3.58(2)	0.012(2)
Zr - Sc	2	3.58(4)	0.005(6)	1.8	3.53(4)	0.006(6)
Zr - Nd	1	3.61(3)	0.004(3)	1.2	3.36(3)	0.004(2)
Zr - O2	22	4.29(4)	0.03(1)	22	4.30(5)	0.029(8)

Zr–Nd bond lengths, which are not expected in a fluorite structure, were proposed to arise from the possible formation of a B-Nd_2O_3 structure. It also appears that a B-Nd_2O_3 type-material could be forming in the $Nd_xSc_yZr_{1-x-y}O_{2-\delta}$ compounds annealed at high temperatures, though it is also possible that this determined short bond distance was a result of an error in the model fitted to the data. In general, further research must be performed to determine if a B-Nd_2O_3 phase could be present in these materials.

The σ^2 values of each scattering path did not change with composition or annealing temperature. The σ^2 values were all physically plausible values with the exception of the σ^2 values of the Zr–Sc and Zr–Nd scattering paths from $Nd_{0.15}Sc_{0.10}Zr_{0.75}O_{1.88}$. In the case of this material, the σ^2 values of 0.005 and 0.004 were smaller than what would be expected for a NNN bond length. The Zr–Sc and Zr–Nd coordination numbers also had to be changed when fitting the spectrum from the $Nd_{0.15}Sc_{0.10}Zr_{0.75}O_{1.88}$ material annealed at 1400 °C to prevent σ^2 for these scattering paths from being negative. These low σ^2 values may indicate that some segregation of Nd, Sc, and Zr occurs in the materials after annealing at high temperature. This explanation is consistent with the SEM and EDS results as well, which showed that the Nd distribution became heterogeneous after

annealing at 1400 °C. To summarize, the Zr K-edge EXAFS results show that the Zr coordination number changes with composition and upon annealing. The results also show that the distribution of Zr, Sc, and Nd in the material also likely changes when Nd is added to the Sc-ZrO_2 system and upon annealing.

5.3.4 Zr L_3-edge

Zr L_3-edge spectra were collected from several of the as-synthesized and annealed $Nd_xSc_yZr_{1-x-y}O_{2-\delta}$ compounds, and are presented in Figure 5.9 and Figure D.24 in Appendix D. Two peaks, labelled as F and G in Figure 5.9a, were observed in these spectra due to crystal field splitting of the Zr 4d states. Peak F is attributed to Zr 2p $\rightarrow$ 4d e_g transitions while peak G arises from Zr 2p $\rightarrow$ 4d t_{2g}^* excitations. Peak G was observed to slightly increase as Sc replaced Nd in the system, which may indicate that the coordination environment around Zr became more symmetric. This is consistent with a shift to a tetragonal phase, in which the coordination environment is more symmetric and the Zr CN is 8, and these results agree with the Zr K edge XANES results (*vide supra*). However, this change is small, and only represents a minor shift in the coordination environment, which is likely why changes were not observed in the pre-edge of the Zr K-edge XANES spectra.

The Zr L_3-edge spectra did not change significantly upon high-temperature annealing of the materials (Figure 5.9b). With the exception of the spectra from the $Nd_{0.15}Sc_{0.05}Zr_{0.80}O_{1.90}$ sample, the changes were small and not significant. The spectrum from the $Nd_{0.15}Sc_{0.05}Zr_{0.80}O_{1.90}$ sample did change significantly as the intensity of feature G decreased and there was a slight increase in the intensity of the spectrum at $\sim$2226 eV when the material was annealed at 1400 °C. A comparison of the spectra from the $Nd_xSc_xZr_{1-x-y}O_{2-\delta}$ materials to the spectrum from monoclinic ZrO_2 (Figure 5.9a) indicates that this change is likely due to the formation of monoclinic zirconia upon annealing. The powder XRD results from this sample also indicated that monoclinic zirconia was formed upon annealing (see Figure D.2). Overall, these results further indicate that the coordination environment around Zr in $Nd_xSc_yZr_{1-x-y}O_{2-\delta}$ materials does not change significantly

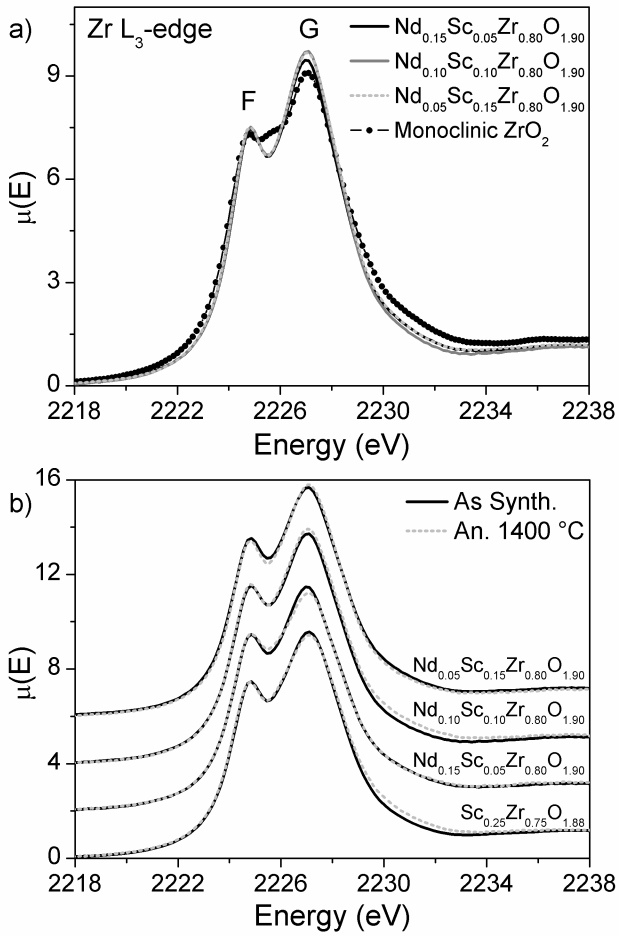

Figure 5.9: (a) The Zr L_3-edge XANES spectra from several of the as-synthesized $Nd_xSc_yZr_{1-x-y}O_{2-\delta}$ materials. Two features, F and G, were observed. Feature F is assigned to Zr 2p $\rightarrow$ 3d e_g excitations and feature G is assigned to Zr 2p $\rightarrow$ 3d t_{2g} states. The intensity of Feature G increases as the Sc content increases. (b) The Zr L_3-edge XANES spectra from several of the as-synthesized and annealed materials are compared. Changes are observed when several of the materials are annealed, but no trend is observed.

when annealed at temperatures up to 1400 °C.

5.3.5 Sc K-edge

The Sc K-edge XANES spectra from several of the as-synthesized and high temperature annealed $Nd_xSc_yZr_{1-x-y}O_{2-\delta}$ materials are presented in Figure 5.10. The spectra exhibit three pre-edge peaks, labelled as H_1, H_2, and H_3 in Figure 5.10a, which result from Sc 1s $\rightarrow$ 3d transitions. Two main-edge peaks, labelled as I_1 and I_2, were also observed, and arise from Sc 1s $\rightarrow$ 4p transitions. Beyond this, a definitive and detailed assignment of each peak is not possible as there is relatively little literature available regarding analysis of the Sc K-edge [210–213]. However, there is a similarity in shape between the Sc K-edge spectra and Ti K-edge spectra from defect fluorite and pyrochlore type systems [48,49]. Given the close proximity of Sc and Ti on the periodic table, it seems reasonable to assume that the features in the Sc K- and Ti K-edge spectra would also have similar origins. Based on this, the details of the peak origins can be tentatively assigned and further analyzed. Feature H_1 likely arises from Sc 1s $\rightarrow$ 3d e_g transitions and feature H_2 is likely due to Sc 1s $\rightarrow$ 3d t_{2g}^* excitations. Feature H_3 is likely due to a non-local excitation, known as an intersite hybrid feature, in which Sc 1s electrons are excited to 4p states interacting with next-nearest-neighbor d-states through O 2p states. Continuing the analogy to the Ti K-edge, feature I_1 is assigned to excitations of the 1s electrons to Sc 4p states interacting with O 2p states while feature I_2 can simply be assigned to transitions to empty Sc 4p states.

The line shape of the main-edge of the Sc K-edge spectra from the $Nd_xSc_yZr_{1-x-y}O_{2-\delta}$ is similar to that of the spectrum from $[Sc(OH_2)_8](CF_3SO_3)_3$, in which Sc occupies a symmetric 8-fold coordination environment [211]. The Sc K-edge spectra also bear a close resemblance to Sc-doped CeO_2 materials, which adopt a fluorite structure [212]. These similarities likely indicate that Sc occupies a cubic coordination site. The weak intensities of the pre-edge features indicate there is minimal Sc 4p-Sc 3d mixing and that the Sc coordination environment likely contains an inversion centre, which further supports the conclusion that Sc occupies a cubic coordination site. Only slight changes in the spectra from the $Nd_xSc_yZr_{1-x-y}O_{2-\delta}$ materials were observed when the

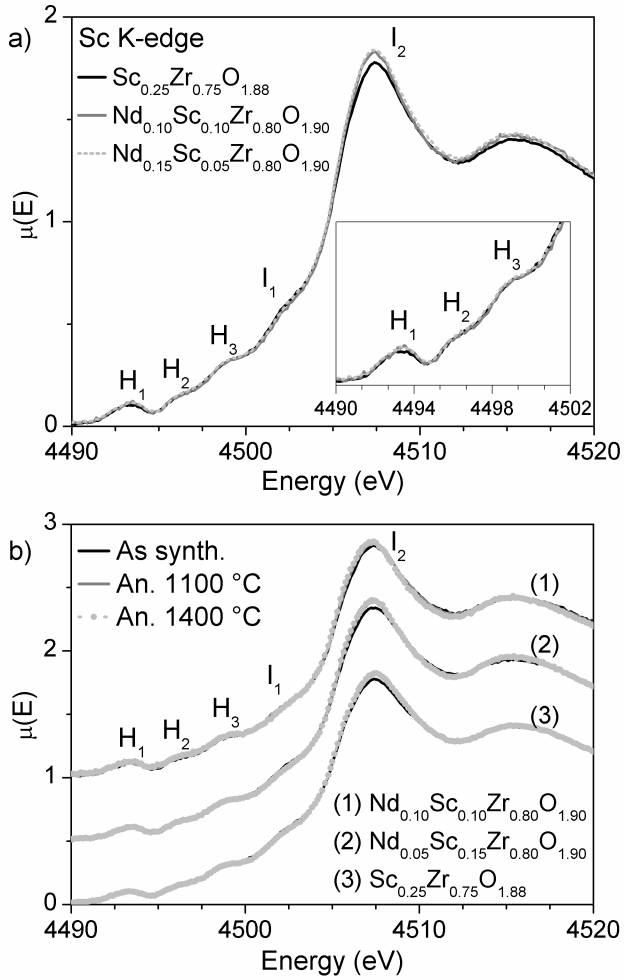

Figure 5.10: (a) Sc K-edge XANES spectra from several of the as-synthesized $Nd_xSc_yZr_{1-x-y}O_{2-\delta}$ materials. Features H_1, H_2, and H_3 arise from forbidden Sc 1s $\rightarrow$ 3d transitions and Features I_1 and I_2 are attributed to dipole-allowed Sc 1s $\rightarrow$ 4p transitions. There is a decrease in the intensity of Feature I_1 and an increase in the intensity of Feature I_2 as the Sc content decreases. (b) The Sc K-edge XANES spectra from several of the as-synthesized and annealed materials are compared. The intensity of feature I_2 increases as the annealing temperature increases. The magnitude of the change in the spectra observed upon annealing increases with increasing Sc content.

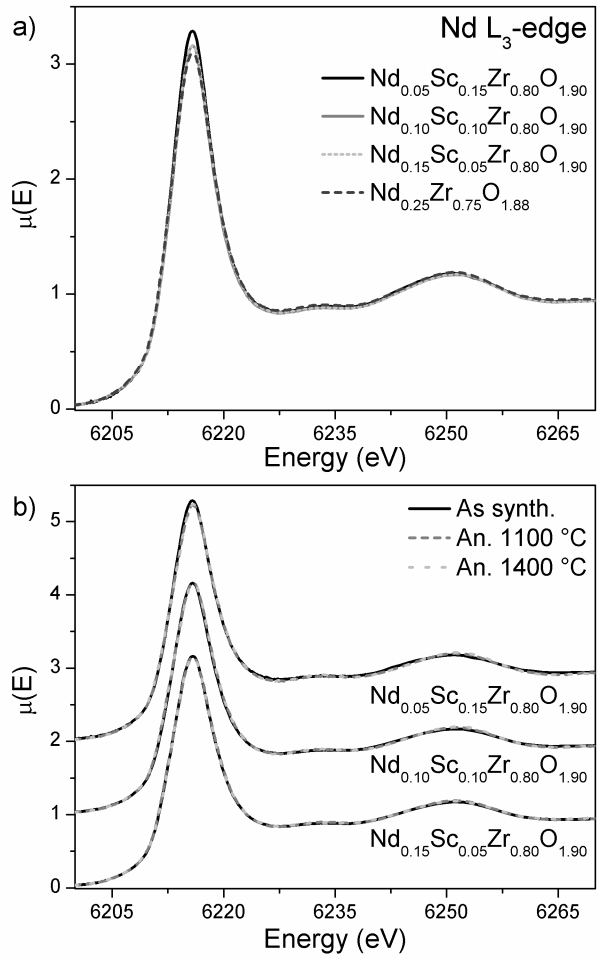

Figure 5.11: (a) Nd L_3-edge spectra from the as-synthesized $Nd_xSc_yZr_{1-x-y}O_{2-\delta}$ compounds. A strong white line is observed and the magnitude of this line increases with as the Sc content increased. (b) The Nd L_3-edge spectra from the as-synthesized and annealed materials are compared. No significant changes were observed upon annealing.

composition was varied (Figure 5.10a) and when the materials were annealed at high temperature (Figure 5.10b). These results indicate that only minor changes in the local Sc coordination environment occurred when the composition was varied and when the materials were annealed at high temperature.

5.3.6 Nd L_3-edge

Nd L_3-edge XANES spectra were collected from the as-synthesized and annealed $Nd_xSc_yZr_{1-x-y}O_{2-\delta}$ materials, and these spectra are presented in Figure 5.11. A single, intense

peak is observed in these spectra and this peak is attributed to Nd 2p $\rightarrow$ Nd 5d transitions [193]. Figure 5.11a shows that as the Nd content in the materials increased there was a small decrease in the intensity of the white line. This decrease is likely due to changes in the electronegativity of the NNN atoms. The average electronegativity of the NNN atom decreases as Nd (χ = 1.07) replaces Sc (χ = 1.20) [214]. The reduced electronegativity results in less electron density being pulled away from the absorbing Nd atom, and slightly reduces the number of unoccupied states that the core electron can be excited to. This reduction would result in the reduced peak intensity observed here.

The spectra from the as-synthesized and high-temperature annealed $Nd_xSc_yZr_{1-x-y}O_{2-\delta}$ compounds are compared in Figure 5.11b. The spectra from the as-synthesized and annealed compounds are similar, indicating that only minimal changes in the structure around Nd occur upon annealing. The broad peak at $\sim$6250 eV slightly increased with annealing temperature. This peak is attributed to multi-scattering resonances, in which the excited photoelectron scatters off multiple neighboring atoms. The increased intensity of this peak indicates that the local structures around Nd became more ordered upon annealing, which is also consistent with the powder XRD results (*vide supra*). Overall, the Nd L_3-edge spectra indicate that the Nd coordination environment in $Nd_xSc_yZr_{1-x-y}O_{2-\delta}$ does not change upon thermal treatment.

5.3.7 Mechanistic Insights

The EDS results provide insight into the mechanism of how Sc acts to stabilize the fluorite structure in the $Nd_xSc_yZr_{1-x-y}O_{2-\delta}$ materials. The EDS images showed that when all of the materials were annealed at 1400 °C the Nd became segregated within the material. This segregation led to areas where the Nd content is too low to stabilize the fluorite structure in $Nd_xZr_{1-x}O_{2-\delta}$ materials, resulting in the formation of lower symmetry monoclinic and tetragonal phases. The Zr coordination number in monoclinic ZrO_2 is reduced to 7 as the structure distorts to this lower symmetry phase. Therefore, it is not expected that this segregation would result in an increase in the Zr CN despite the increased O-content in monoclinic ZrO_2 compared to O-deficient $Nd_xZr_{1-x}O_{2-\delta}$. The effects of

the Nd segregation were mitigated by the addition of Sc into the system, which did not segregate upon annealing and kept the concentration of 3+ cations throughout the annealed material at level high enough to stabilize the fluorite structure. This stabilization mechanism was shown to occur in Chapter 3, where Y acts in a similar manner to stabilize the fluorite structure in $Nd_xY_yZr_{1-x-y}O_{2-\delta}$ systems.

The mechanism by which Nd acts to prevent the formation of the β-phase Sc-Zr-O in the $Nd_xSc_yZr_{1-x-y}O_{2-\delta}$ is more complex, though the XAS results provide insights into this phenomenon. The β-phase Sc-Zr-O forms when the anion vacancies become ordered, forming a fluorite superstructure. The fluorite structure of the as-synthesized $Sc_yZr_{1-y}O_{2-\delta}$ materials was a metastable state formed via the low-temperature co-precipitation method. In this case, high disorder within the system prevents the formation of the highly ordered β-phase. The Zr K-edge EXAFS spectra showed that the Zr CN increased upon annealing, which is consistent with a shift in O-vacancies away from Zr. The Zr K-edge XAS results also showed that the change in CN upon annealing decreased as Nd replaced Sc in the $Nd_xSc_yZr_{1-x-y}O_{2-\delta}$ compounds. These results show that the O-vacancies migrated to more ordered positions upon annealing. The Nd prevented the migration of O-vacancies within the material, which prevented the formation of β-phase Sc-Zr-O. This is consistent with several other studies of RE-doped Sc-ZrO_2 systems which showed that the anion mobility decreased as the dopant cation size increased [215–217]. From these results it can be concluded that Sc-doped zirconia is not appropriate for IMF applications.

5.4 Conclusions

The thermal stability and local and long-range structures in a series of $Nd_xSc_yZr_{1-x-y}O_{2-\delta}$ materials have been characterized using a number of techniques. The powder XRD results showed that neither the $Nd_xZr_{1-x}O_{2-\delta}$ nor the $Sc_yZr_{1-y}O_{2-\delta}$ materials were stable when annealed at T $\geq$ 1100 °C. This indicates that the ternary materials are not suitable for IMF applications. The addition of a small amount of Sc to the system (y = 0.05) greatly reduced the amount of monoclinic

and tetragonal ZrO_2 that was formed upon annealing while the addition of slightly more Sc (y = 0.10) completely stabilized the cubic structure. The fluorite structure was only stable at high temperatures when x+y $>$ 0.15. The EDS data indicates that Sc stabilizes the cubic structure by maintaining a sufficient concentration of 3+ cations in the system when Nd segregates in the materials upon annealing. The fluorite structure of the $Sc_yZr_{1-y}O_{2-\delta}$ materials was also not stable at high temperatures, and a β-phase Sc-Zr-O oxide was formed when these materials were annealed. However, the addition of Nd to the system prevented this transformation. The XANES results indicated that the local coordination environments around the Sc and Nd metal centres were mostly independent of changes in composition and thermal treatment. This indicates that the local structures in $Nd_xSc_yZr_{1-x-y}O_{2-\delta}$ materials with x+y $>$ 0.15 are stable at high temperatures. The Zr K-edge EXAFS results indicated that the Zr CN decreased as Nd replaced Sc in the materials and that changes in the Zr CN decreased with increasing Nd content upon annealing.

A mechanism by which the fluorite structure is stabilized in the quaternary $Nd_xSc_yZr_{1-x-y}O_{2-\delta}$ materials was proposed from these results. The addition of Sc limits the effect of Nd migration upon annealing, likely by ensuring that an adequate number of O-vacancies remain in the fluorite system. This results in the stabilization of the fluorite structure upon high-temperature annealing. Conversely, the addition of Nd prevents the formation of an ordered β-phase by limiting O-vacancy migration within the fluorite phase. The results presented here indicate that both Nd and Sc are required to stabilize the fluorite structure in $Nd_xSc_yZr_{1-x-y}O_{2-\delta}$ materials at temperatures up to 1400 °C.

Chapter 6

CONCLUSIONS

6.1 Summary and Significance

Nuclear energy can be used to produce large quantities of electricity while producing minimal carbon emissions. The nuclear fuel cycle is complex, and involves the use of a wide variety of different materials. Given the high safety standards of the nuclear industry, it is necessary to fully understand all properties of the materials involved in the nuclear fuel cycle to ensure continued safe operations and to mitigate the environmental impacts of nuclear energy. To this end, this thesis has presented a comprehensive characterization of the fundamental properties of several materials associated with the nuclear fuel cycle. X-ray absorption spectroscopy (XAS) was used to determine the structure and behaviour of these materials on an atomic scale. XAS was used because it can provide information about the local bonding structures around a metal centre [142]. Further, XAS is also an element specific technique, and can be used to distinguish the structures around different metal ions in a chemically complex mixture [142]. The XAS characterizations were complemented by studying the materials using techniques that probe the long-range crystal structure and microscopic structures of the material. To this end, powder XRD was used to determine the behavior of the long-range crystal structures of the materials studied while SEM and μ-XRF were used to understand how the microscopic structures of the materials behaved. This knowledge can be used to provide an experimental basis for calculations used to predict material behaviours under extreme conditions (i.e., irradiation in a reactor) and over long time scales (i.e., thousands of years).

6.1.1 The Speciation of Mo Content in TMF Tailings

The mining of uranium can result in negative environmental consequences, and it is important to ensure that the environmental impacts of the mining activities are properly mitigated. This was the focus of Chapter 2, which explored methods to speciate Mo-bearing materials deposited in the JEB TMF. The JEB TMF is operated by AREVA Resources Canada, and is located at the McClean Lake Milling Site in Northern Saskatchewan [40]. The TMF was designed to store the mill tailings and other waste products in order to control and prevent the release of elements of concern into the surrounding environment. Elements of concern, which include As, Ni, Mo, U, Se, and Ra, are co-mineralized with uranium in the ore body, and are liberated into mobile phases during the milling process [40]. Ultimately, over the very long term the geochemical control of these elements of concern will rely on controlling the equilibria between these elements and the surrounding mineralogy [40]. However, these systems are far from equilibrium when materials are first placed in the TMF, and the reactions can occur over very long time periods (i.e., years or decades). It is incumbent upon AREVA to ensure that the appropriate mineralogical sinks are forming within the TMF, and it is necessary to understand how these reactions are evolving over time.

The mineral powellite ($CaMoO_4$), which is insoluble in the conditions present in the JEB TMF, is expected to control the concentration of Mo over the long-term [75]. However, the formation of powellite within the JEB TMF had not been experimentally confirmed previously. In Chapter 2, a series of element specific and non-element specific techniques were used in an attempt to speciate the Mo present in the JEB TMF. The study showed that only Mo K-edge XANES was able to determine the Mo species present in the tailings samples. Non-element specific techniques, such as powder XRD and Laue diffraction, were not effective because of the chemically complex nature of the tailings and the low concentration of Mo in the tailings samples. Using principal component analysis, in addition to linear combination fitting, the Mo K-edge XANES spectra from the mine tailings provided a quantitative determination of the Mo speciation in the JEB TMF. This study was the first to definitively show that powellite is present in the JEB TMF.

The research provided a basis for further study of the Mo speciation within the JEB TMF. The chemistry of the JEB TMF is always evolving over time due to the nature of the slow reactions and equilibria processes occurring with the TMF. Therefore, AREVA conducts sampling campaigns every five years to follow and track these changes in the chemistry. Building upon the methods outlined in Chapter 2, Blanchard et al. successfully completed a quantitative analysis of the Mo speciation in a large set of tailings samples collected during the 2013 sampling campaign [218]. These results confirmed that powellite is present in the TMF. Further, these results showed that concentrations of other Mo-bearing species present in the TMF, such as ferrimolybdite ($Fe_2(MoO_4)_3$) and molybdate adsorbed on ferrihydrite ($Fe(OH)_3$-MoO_4), were diminishing over time concurrent with the formation of powellite. The work of Blanchard et al. was therefore able to provide verification of the models predicating the behavior of Mo in the JEB TMF, and the study presented in Chapter 2 along with the study by Blanchard et al. has provided the groundwork for analysis of the Mo-speciation in the JEB TMF [218].

6.1.2 Impact of Synthetic Method and Annealing Temperature on the Fluorite Structure of Nd-YSZ Materials

The use of IMFs has been proposed to efficiently "burn up", or transmutate, existing TRU stockpiles using both currently available commercial nuclear reactors and future Generation IV reactors [37, 60]. TRU species are largely responsible for the long-term radioactivity and heat loads generated by spent nuclear fuel, and removing these inventories would greatly improve the efficiencies of the deep geological repositories proposed for the disposal of spent nuclear fuel [63]. However, before a material can be used in nuclear fuel applications, it must be extensively characterized to ensure that it will behave in a safe manner both inside the reactor and after use in the reactor. Cubic zirconia has been proposed for use in IMF applications due to its chemical durability, but the fluorite structure of cubic zirconia must be stabilized at room temperatures by doping aliovalent cation such as Y^{3+} into the system. Chapters 3 and 4 present an initial assessment of the applicability of yttria-stabilized zirconia (YSZ) materials for IMF applications by studying a

number of Nd-substituted YSZ materials. (Nd was used as a surrogate for Am.)

In Chapter 3, the thermal stability of a number of $Nd_xY_yZr_{1-x-y}O_{2-\delta}$ materials synthesized using a ceramic method was studied. The materials were synthesized using a standard ceramic method at 1500 °C, and then subsequently annealed at high temperatures. The as-synthesized and annealed materials were characterized using powder XRD, SEM, EDS and Zr K-, Y K-, and Nd L_3-edge XAS. The results showed that the fluorite phase was initially formed for all $Nd_xY_yZr_{1-x-y}O_{2-\delta}$ materials with $x + y \geq 0.25$. The fluorite phase was not stable when the ternary $Nd_xZr_{1-x}O_{2-\delta}$ materials were annealed at 1400 °C, and monoclinic and tetragonal zirconia phases were formed upon annealing. However, the fluorite structure was stable upon annealing at 1400 °C for materials with $y \geq 0.05$. This chapter proposed that the segregation of Nd in the annealed materials resulted in areas where the dopant concentration was not high enough to support the fluorite structure. The addition of Y, which did not segregate upon annealing, ensured that the average dopant concentration was high enough to stabilize the fluorite structure throughout the material despite the spatial variations in the Nd^{3+} concentration. This study provided fundamental insights into the behavior of $Nd_xY_yZr_{1-x-y}O_{2-\delta}$ materials at high temperatures. This information can be used in fuel models when licensing these materials for use as a nuclear fuel.

Chapter 4 extended this analysis of the $Nd_xY_yZr_{1-x-y}O_{2-\delta}$ system to explore the effect of synthetic method on the properties of these materials. Ceramic methods are both expensive at an industrial scale and produce dust that is an inhalation hazard for workers [196]. A solution-based approach could be more easily automated, reducing the risk of radiation exposure to workers and could also reduce the fuel production costs. In Chapter 4, a co-precipitation method was used to synthesize a series of $Nd_xY_{0.25-x}Zr_{0.75}O_{1.88}$ materials, and the thermal stability of these materials was characterized. Cubic $Nd_xY_{0.25-x}Zr_{0.75}O_{1.88}$ materials were formed by calcining the precipitate formed from the co-precipitation method at 800 °C, and these "as-synthesized" materials were then annealed at 1400 °C and 1500 °C. Similar to Chapter 3, the as-synthesized and annealed materials were characterized by powder XRD, SEM, Wavelength dispersive spectroscopy (WDS), and Zr K-, Y K-, and Nd L_3-edge XAS. These results showed that the fluorite phase was the

only phase present in the as-synthesized materials made by the low-temperature co-precipitation method. However, the materials made by the co-precipitation method were significantly less crystalline than the materials made by ceramic method at 1500 °C. The materials made by the co-precipitation method also behaved differently from the materials made by the ceramic method, and were less stable when annealed at 1400 °C. Notably, the $Nd_{0.05}Y_{0.20}Zr_{0.75}O_{1.88}$ material made by the co-precipitation method was observed to partially decompose into lower symmetry zirconia phases, whereas the fluorite structure was observed to be stable when $Nd_{0.05}Y_{0.20}Zr_{0.75}O_{1.88}$ made by the ceramic method was annealed at 1400 °C. This could indicate that the reaction kinetics are slower in materials made by the ceramic method, and that these materials may decompose to lower symmetry phases upon extended annealing at 1400 °C. The XAS and powder XRD results indicated that the long-range disorder within the materials made by co-precipitation originates from disorder between metal-oxygen polyhedra, rather than within metal-oxygen polyhedra. The results presented in this chapter showed that $Nd_xY_{0.25-x}Zr_{0.75}O_{1.88}$ compounds with $x \leq 0.15$ made by a co-precipitation method could be suitable IMF candidates. Further, the reduced annealing times required to produce these materials could lead to a significant opportunity to reduce the cost of producing IMF fuels.

6.1.3 On the Effect of Different Cations to Stabilize the Fluorite Structure in Doped Cubic Zirconia Materials

While yttria-stabilized zirconia has been widely explored for use in IMF applications, it has a low thermal conductivity which limits its performance as a nuclear fuel. It is therefore of interest to explore other stabilized-zirconia materials which may have a higher thermal conductivity. Chapter 5 presents an investigation of the structure and thermal stability of $Nd_xSc_yZr_{1-x-y}O_{2-\delta}$ materials. Sc^{3+} was chosen as the stabilizing dopant because it has a low atomic number, and therefore the thermal conductivity of Sc-stabilized zirconia (ScSZ) materials should be higher than the thermal conductivity of YSZ materials [124]. Further, ScSZ material properties are relatively well-known, as ScSZ materials have been investigated for use in solid-oxide fuel cell applications [107, 125–

127]. In the study presented in Chapter 5, $Nd_xSc_yZr_{1-x-y}O_{2-\delta}$ materials were prepared using a co-precipitation method and annealed at 1100 °C and 1400 °C. The as-synthesized and annealed materials were characterized using powder XRD, SEM, EDS, and Zr K-, Sc K-, and Nd L_3-edge XAS spectroscopy.

This study was the first of its kind to explore the properties of ScSZ materials containing high concentrations (i.e., $>$1 at. %) of rare-earth element dopants. The fluorite structure of the $Nd_xSc_yZr_{1-x-y}O_{2-\delta}$ materials was only stable at high temperature when x + y $>$ 0.15. Further, the powder XRD results showed that the fluorite structure was not stable when the ternary $Nd_xZr_{1-x}O_{2-\delta}$ and the $Sc_yZr_{1-y}O_{2-\delta}$ materials were stable when annealed at 1400 °C, and a mixture of monoclinic, tetragonal, and cubic ZrO_2 was formed when $Nd_xZr_{1-x}O_{2-\delta}$ was annealed at 1400 °C. A rhombohedral β-phase Sc-Zr-O material, in which the oxygen anion vacancies are ordered, was formed when the $Sc_yZr_{1-y}O_{2-\delta}$ materials were annealed at 1400 °C. The powder XRD results showed that the fluorite structure was only stable in $Nd_xSc_yZr_{1-x-y}O_{2-\delta}$ materials annealed at 1400 °C when x $\geq$ 0.05 and y $\geq$ 0.10.

6.2 Future Work

The research presented in this thesis has enriched the scientific community's knowledge of several materials related to the nuclear fuel cycle. This thesis has presented a comprehensive understanding of the thermal stability of YSZ and ScSZ IMF materials. However, the properties of these materials under other conditions relevant to in-reactor and post-reactor service remain under studied, and represent an avenue for future research. Given the need for comprehensive understanding of nuclear fuel materials properties, two major studies are proposed to further explore the characteristics and behaviour of YSZ and ScSZ materials under extreme conditions.

Nuclear fuel materials will be exposed to extreme radiation doses during both in-reactor and post-reactor service, and it is necessary to understand how these materials will be affected by exposure to these high radiation fields [32, 92, 139, 219, 220]. The only way to fully understand the

effects of high radiation fields on fuel materials is to actually irradiate it in a reactor using specific test loops. However, these experiments require long times, require the use of limited reactor facilities, and are generally very expensive. Therefore, it is of value to gather an initial understanding of how these materials will behave in-reactor by simulating this exposure to radiation damage. One method to simulate radiation damage is to bombard the material with a beam of high-energy particles [48, 49, 88, 141, 221, 222]. Here, it is proposed to study the effect of radiation damage in Nd-doped YSZ and ScSZ materials by bombarding these materials with highly energetic particles. In this study a series of $Nd_xY_yZr_{1-x-y}O_{2-\delta}$ and $Nd_xSc_yZr_{1-x-y}O_{2-\delta}$ materials would be synthesized and the powder materials would be pressed and sintered into pellets. These pellets would then be irradiated with a high energy (i.e., on the order of MeV) Au^- ion beam, which would be used to simulate the effects of fission product decay. The use of Au^- ions is preferable as it simulates the impact of the daughter product recoil that occurs during a decay process [48, 49]. The materials would be irradiated at several different doses to determine their resistance to radiation damage. The surfaces of the pellets would then be studied using a technique known as Glancing-Angle XANES (GA-XANES). In a GA-XANES experiment, the sample is placed in the X-ray beam with a very small incident angle [48, 223]. The penetration depth of the X-rays increases with increasing incident angle, and by collecting XANES spectra at different the incident angles the structure of the irradiated materials at different depths from the surface can be investigated. Previous experiments by our group have suggested that Zr K-edge and Y K-edges are not suitable for GA-XANES experiments, as the high energy of these edges reduces the number of depths that can be probed using a conventional GA-XANES set-up. It will therefore be necessary to collect GA-XANES spectra at the lower-energy Zr L_3- and Y L_3-edges. Sc K-edge GA-XANES spectra from the $Nd_xSc_yZr_{1-x-y}O_{2-\delta}$ materials could also be collected. It may also be possible to collect GA-EXAFS spectra from the irradiated pellets as well, given sufficient beamtime, and this would provide first-of-its-kind insight into how the local bonding structures around the metal centres in radiation-damaged substituted zirconia materials. The results from this study will provide a good indication about how resistant the Nd-YSZ and Nd-ScSZ materials are to radiation damage. Ad-

ditionally, by irradiating and collecting spectra from a number of different material compositions, significant insights into any connections between composition and resistance to radiation damage can be gained. This will provide a necessary base of knowledge when considering YSZ and ScSZ materials for in-situ irradiation studies.

When studying materials for IMF applications, one of the considerations that is often ill-considered is how the fuel will react to the presence of the fission products created in-reactor. It is of interest to understand how these fission products will be incorporated into the IMF materials, and how the fission products will behave when exposed to a number of different conditions. Similar to the problem of irradiation mentioned above, the only exact way to understand how these fission products will affect the fuel material is through irradiation in a test reactor. However, irradiation will produce highly radioactive fission products, and the presence of these fission products makes characterization of the post-irradiated fuel difficult given the extreme safety hazards and special handling requirements. This hurdle can be overcome when studying traditional UO_2 or MOX fuels by producing so-called SIMFUEL [78, 224, 225]. SIMFUEL is simulated high-burn up fuel, and this material attempts to replicate the chemical state and chemical composition of irradiated fuel by incorporating a number of non-radioactive fission product nuclides [78, 224, 225]. Here, it is proposed to create a similar effect by incorporating the non-radioactive fission products of an Am-based IMF fuel into the Nd-YSZ and Nd-ScSZ materials. In this experiment, powdered metallic fission product materials would be mixed in proportion to their fission product yields with as-synthesized Nd-YSZ and Nd-ScSZ powders. The materials would then be heated in a slightly reducing atmosphere at high temperatures. Once synthesized, the long-range structures of the SIMFUEL Nd-YSZ and Nd-ScSZ materials would then be characterized using powder XRD, SEM, EDS. Local structures could also be characterized using XAS. In addition to the typical Zr K-edge, Y K-edge, and Sc K-edge XAS spectra, it would be of value to collect XAS spectra from the major fission-product K- and L_3-edges. For example, the behaviour of Mo in these SIMFUEL Nd-YSZ and Nd-ScSZ materials could be of particular interest, given the poorly characterized behaviour of Mo in UO_2 fuels. The results of this study would provide first-of-its-kind insight into

the behaviour of fission products within IMF materials. If successful, this study would provide an understanding of what happens to the structures of the IMF materials at an atomic level, and would provide an understanding of the local structures around the fission products in these materials.

The work presented in this thesis has contributed to the knowledge and understanding of materials related to the nuclear fuel cycle. Mill tailings produced during the processing of uranium ore were studied in order ensure that the procedures in processes used to mitigate the environmental impact of uranium ore mining were effective. The structures and thermal stability of materials proposed for use as inert matrix fuels were also studied. Given the high safety standards of the nuclear industry, it is important to have a comprehensive understanding of material properties. The research presented here contributes to this understanding, allowing for better modelling of material behaviours. Finally, two projects aimed at increasing the knowledge base regarding Nd-YSZ and Nd-ScSZ materials were proposed. These investigations will provide a better understanding of the materials associated with the nuclear fuel cycle. This will ensure that nuclear power remains a safe an effective option for generating electricity while producing minimal carbon emissions, and will allow for the sustainable growth and development throughout the world.

THE END

REFERENCES

[1] Michal, R. *Nuclear News* **2001**, *44*, 28–29.

[2] Hoffert, M. I.; Caldeira, K.; Benford, G.; Criswell, D. R.; Green, C.; Herzog, H.; Jain, A. K.; Kheshgi, H. S.; Lackner, K. S.; Lewis, J. S.; Lightfoot, H. D.; Manheimer, W.; Mankins, J. C.; Mauel, M. E.; Perkins, L. J.; Schlesinger, M. E.; Volk, T.; Wigley, T. M. L. *Science* **2002**, *298*, 981–987.

[3] National Oceanic and Atmospheric Administration; *ESRL Global Monitoring Division - Global Greenhouse Gas Reference Network*; Online; Accessed 23 January 2016. `http://www.esrl.noaa.gov/gmd/ccgg/trends/`.

[4] IPCC *Climate Change 2013 - The Physical Science Basis*; Cambridge University Press: Cambridge, 2014; Chapter Climate Change 2013 Synthesis Report Summary Chapter for Policymakers, pp 1–30.

[5] Parmesan, C.; Yohe, G. *Nature* **2003**, *421*, 37–42.

[6] Karl, T.; Trenberth, K. *Science* **2003**, *302*, 1719–1723.

[7] Parry, M.; Rosenzweig, C.; Iglesias, A.; Livermore, M.; Fischer, G. *Global Environmental Change* **2004**, *14*, 53–67.

[8] Kharecha, P. A.; Hansen, J. E. *Environmental Science and Technology* **2013**, *47*, 4889–4895.

[9] Hoffert, M.; Caldeira, K.; Jain, A. K.; Haites, E.; Harvey, L.; Potter, S.; Schlesinger, M.; Schneider, S.; Watts, R.; Wigley, T.; Wuebbles, D. *Nature* **1998**, *395*, 881–884.

[10] Lenzen, M. *Energy Conversion and Management* **2008**, *49*, 2178–2199.

[11] Sovacool, B. K. *Energy Policy* **2008**, *36*, 2950–2963.

[12] O'Neill, B. C. *Science* **2002**, *296*, 1971–1972.

[13] Wigley, T. M. L.; Richels, R.; Edmonds, J. A. *Nature* **1996**, *379*, 240–243.

[14] IEA *World Energy Outlook 2014*; IEA: Paris, 2014.

[15] Asif, M.; Muneer, T. *Renewable and Sustainable Energy Review* **2007**, *11*, 1388–1413.

[16] Bruneton, P. In *Economic Minerals of Saskatchewan*; Lorsong, J.; Wilson, M., Eds.; Saskatchewan Geological Society: Regina, SK, 1987; pp 99–119.

[17] Ewing, R. C. *Applied Geochemistry* **1997**, *12*, 549–565.

[18] Mudd, G. M.; Diesendorf, M. *Environmental Science and Technology* **2008**, *42*, 2624–30.

[19] Mudd, G. M.; Diesendorf, M. In *2nd International Conference on Sustainable Engineering and Science*; Auckland, New Zealand; pp 1–10.

[20] OECD/NEA *Trends in the Nuclear Fuel Cycle: Economic, Environmental, and Social Aspects*; Nuclear Development; OECD Publishing: Paris, 2001.

[21] Long, J. C.; Ewing, R. C. *Annual Review of Earth and Planetary Sciences* **2004**, *32*, 363–401.

[22] Donald, I. W.; Metcalfe, B. L.; Taylor, R. N. J. *Journal of Material Science* **1997**, *32*, 5851–5887.

[23] Chapman, N.; Hooper, A. *Proceeding of the Geological Association* **2012**, *123*, 46–63.

[24] Rempe, N. T. *Progress in Nuclear Energy* **2007**, *49*, 365–374.

[25] IAEA; *Estimation of Global Inventories of Radioactive Waste and Other Radioactive Materials*; Tech. Rep. IAEA-TECDOC-1591; International Atomic Energy Agency; 2007.

[26] Blissett, R. S.; Rowson, N. A. *Fuel* **2012**, *97*, 1–23.

[27] Allen, T.; Busby, J.; Meyer, M.; Petti, D. *Mater. Today* **2010**, *13*, 14–23.

[28] Waldrop, M. M. *Nature* **2012**, *492*, 26–29.

[29] Kessler, G. *Sustainable and Safe Nuclear Fission Energy*; Power Systems; Springer Berlin Heidelberg: Berlin, Heidelberg, 2012.

[30] United States Nuclear Regulatory Commission; *The Pressurized Water Reactor*; Online; Accessed 2 Feb 2016. `http://www.nrc.gov/reading-rm/basic-ref/students/animated-pwr.html`.

[31] Abe, T.; Asakura, K. *Comprehensive Nuclear Materials*; Konings, R. J. M., Ed.; Elsevier, 2012; Vol. 2, Chapter 2.15 - Uranium Oxide and MOX Production, pp 393–422.

[32] Ewing, R. *Mineralogical Magazine* **2011**, *75*, 2359–2377.

[33] Peters, M. T.; Ewing, R. C. *Journal of Nuclear Materials* **2007**, *362*, 395–401.

[34] Ewing, R. C. *Elements* **2006**, *2*, 331–334.

[35] Kazimi, M.; Moniz, E. J.; Forsberg, C. *The Future of the Nuclear Fuel Cycle*; Massachusettes Institute of Technology, 2011; Chapter 1: Overview, Conclusions, and Recommendations, pp 1–17.

[36] Bunn, M.; Fetter, S.; P, H. J.; van der Zwann, B.; *The Economics of Reprocessing vs. Direct Disposal of Spent Nuclear Fuel*; Tech. Rep. DE-FG26-99FT4028; Belfer Center for Science and International Affairs; Harvard University, Cambridge; 2003.

[37] Salvatores, M. *Nuclear Engineering and Design* **2005**, *235*, 805–816.

[38] Gras, J.-M.; Quang, R. D.; Masson, H.; Lieven, T.; Ferry, C.; Poinssot, C.; Debes, M.; Delbecq, J.-M. *Journal of Nuclear Materials* **2007**, *362*, 383–394.

[39] Edwards, C. R.; Oliver, A. J. *JOM* **2000**, *52*, 12–20.

[40] Rowson, J.; Schmid, B.; *Tailings Optimization and Validation Program*; Tech. Rep.; AREVA Resources Canada Inc.; Saskatoon, SK; 2011.

[41] Taylor, T. B. *Annual Review of Nuclear Science* **1975**, *25*, 407–421.

[42] Dreicer, M.; Tort, V.; H., M.; *Nuclear Fuel Cycle: Implentation in France*; Tech. Rep. Contract No. CCE/ARMINES JOU2-CT92-0236; Commission of the European Communities in the Framework of the ExternE Project; 1995.

[43] Lauf, R. *Introduction to Radioactive Minerals*; Schiffer Publishing: Atglen, 2008.

[44] Verrall, R.; He, Z.; Mouris, J. *Journal of Nuclear Materials* **2005**, *344*, 240–245.

[45] Olander, D. *Journal of Nuclear Materials* **2009**, *389*, 1–22.

[46] *Actinide and fission product partitioning and transmutation*; Nuclear Energy Agency/Organisation for Economic Co-operation and Development: Mito, Japan, 2010.

[47] Johnson Jr., A.; *Behavior of Spent Nuclear Fuel in Water Pool Storage*; Tech. Rep. BNWL-2256; Pacific Northwest Laboratories; 1977.

[48] Aluri, E. R.; Grosvenor, A. P. *Journal of Alloys and Compounds* **2014**, *616*, 516–526.

[49] Aluri, E. R.; Grosvenor, A. P. *Physical Chemistry Chemical Physics* **2013**, *15*, 10477–10486.

[50] Bevard, B. B.; Wagner, J. C.; Parks, C. V.; Aissa, M.; *Review of Information for Spent Nuclear Fuel Burnup Confirmation*; Tech. Rep. NUREG/CR-6998; United States Nuclear Regulatory Comission; 2009.

[51] Rondinella, V. V.; Wiss, T. *Materials Today* **2010**, *13*, 24–32.

[52] Widder, S. *Journal of Renewable and Sustainable Energy* **2010**, *2*, 062801.

[53] Martin, J. E. *Physics for Radiation Protection*; Wiley-VCH Verlag GmbH & Co. KGaA: Weinheim, Germany, 2013.

[54] Lumpkin, G. R. *Elements* **2006**, *2*, 365–372.

[55] Salvatores, M.; Palmiotti, G. *Progress in Particle and Nuclear Physics* **2011**, *66*, 144–166.

[56] Prítrský, J.; Nečas, V. *Progress in Nuclear Energy* **2012**, *54*, 36–40.

[57] Garrick, B. J.; Kaplan, S. *Risk Analysis* **1999**, *19*, 903–13.

[58] Baisden, P. A.; Choppin, G. R. *Radiochemistry and Nuclear Chemistry*; Nagy, S., Ed.; Encyclopedia of Life Support Systems, 2007; Chapter 11: Nuclear Waste Management and the Nuclear Fuel Cycle.

[59] Degueldre, C.; Paratte, J. *Journal of Nuclear Materials* **1999**, *274*, 1–6.

[60] Degueldre, C. *Journal of Alloys and Compounds* **2007**, *444-445*, 36–41.

[61] Ledergerber, G.; Degueldre, C.; Heimgartner, P.; Pouchon, M.; Kasemeyer, U. *Progress in Nuclear Energy* **2001**, *38*, 301–308.

[62] Oversby, V. M.; McPheeters, C. C.; Degueldre, C.; Paratte, J. M. *Journal of Nuclear Materials* **1997**, *245*, 17–26.

[63] Ottensmeyer, P. *Proceedings of the 35th Annual Canadian Nuclear Society Conference*; Canadian Nuclear Society: Saint John, NB, 2015; Chapter Productive Elimination of Nuclear Waste (PENW): A complementary boon for CANDUs and the Canadian Nuclear Industry.

[64] Evans, R. D. *American Journal of Public Health and the Nation's Health* **1933**, *23*, 1017–1023.

[65] Reed, B. C. *Physics in Perspective* **2014**, *16*, 461–479.

[66] World Nuclear Association; *Uranium in Canada*; Online; Accessed 23 January 2016. `http://www.world-nuclear.org/info/country-profiles/countries-a-f/canada--uranium/`.

[67] Philippe, S.; Lancelot, J. R.; Clauer, N.; Pacquet, A. *Canadian Journal of Earth Sciences* **1993**, *30*, 720–730.

[68] Raffensperger, J. P.; Garven, G. *American Journal of Science* **1995**, *295*, 639–696.

[69] Van Wagoner, J.; Posamentier, H. W.; Mitchum, R. M.; Vail, P. R.; Sarg, J.; Loutit, T. S.; Hardenbol, J. *Sea-Level Changes*; Wilgus, C.; Hastings, B.; H., P.; J., V. W.; C.A., R., Eds.; Society for Sedimentary Geology, 1988; Vol. 42, Chapter An Overiew of the Fundamentals of Sequence Stratigraphy and Key Definitions, pp 39–45.

[70] *The Merriam-Webster Dictionary*; Merriam-Webster Mass Market, 2004.

[71] Langmuir, D.; Mahoney, J.; MacDonald, A.; Rowson, J. *Geochimica et Cosmochimica Acta* **1999**, *63*, 3379–3394.

[72] Langmuir, D.; Mahoney, J.; Rowson, J. *Geochimica et Cosmochimica Acta* **2006**, *70*, 2942–2956.

[73] Mahoney, J.; Langmuir, D.; Gosselin, N.; Rowson, J. *Applied Geochemistry* **2005**, *20*, 947–959.

[74] Mahoney, J.; Slaughter, M.; Langmuir, D.; Rowson, J. *Applied Geochemistry* **2007**, *22*, 2758–2776.

[75] Mahoney, J.; *Review of the Molybdenum Geochemistry in the JEB TMF*; Tech. Rep.; AREVA Resources Canada; 2010.

[76] Walker, C.; Staicu, D.; Sheindlin, M.; Papaioannou, D.; Goll, W.; Sontheimer, F. *Journal of Nuclear Materials* **2006**, *350*, 19–39.

[77] Yin, Q.; Savrasov, S. Y. *Physical Review Letters* **2008**, *100*, 225504.

[78] Lucuta, P. G.; Matzke, H.; Verrall, R. A. *Journal of Nuclear Materials* **1995**, *223*, 51–60.

[79] Williamson, R. L.; Hales, J. D.; Novascone, S. R.; Tonks, M. R.; Gaston, D. R.; Permann, C. J.; Andrs, D.; Martineau, R. C. *Journal of Nuclear Materials* **2012**, *423*, 149–163.

[80] Olander, D.; Soo Kim, Y.; Wang, W.-E.; Yagnik, S. K. *Journal of Nuclear Materials* **1999**, *270*, 11–20.

[81] Corcoran, E.; Lewis, B.; Thompson, W.; Mouris, J.; He, Z. *Journal of Nuclear Materials* **2011**, *414*, 73–82.

[82] Mathur, J. N.; Murali, M. S.; Nash, K. L. *Solvent Extraction and Ion Exchange* **2001**, *19*, 357–390.

[83] Zabunoğlu, O. H.; Özdemir, L. *Annuals of Nuclear Energy* **2005**, *32*, 151–162.

[84] Irish, E. R.; Reas, W. H.; *The PUREX Process - A Solvent Extraction Reprocessing Method for Irradiated Uranium*; Tech. Rep. HW-49483A; Hanford Atomic Products Operation; Richland, WA; 1977.

[85] Laidler, J.; Battles, J.; Miller, W.; Ackerman, J.; Carls, E. *Progress in Nuclear Energy* **1997**, *31*, 131–140.

[86] McPheeters, C.; Pierce, R.; Mulcahey, T. *Progress in Nuclear Energy* **1997**, *31*, 175–186.

[87] Inoue, T.; Kock, L. *Nuclear Engineering and Technology* **2008**, *40*, 183–191.

[88] Degueldre, C.; Pouchon, M.; Döbeli, M.; Sickafus, K.; Hojou, K.; Ledergerber, G.; Abolhassani-Dadras, S. *Journal of Nuclear Materials* **2001**, *289*, 115–121.

[89] Lombardi, C.; Mazzola, A. *Annuals of Nuclear Energy* **1996**, *23*, 1117–1126.

[90] González-Romero, E. *Nuclear Engineering and Design* **2011**, *241*, 3436–3444.

[91] Wang, H. *Journal of Crystal Growth* **2001**, *226*, 261–266.

[92] Wang, L. M.; Wang, S. X.; Ewing, R. C. *Philosophical Magazine Letters* **2000**, *80*, 341–347.

[93] Momma, K.; Izumi, F. *Journal of Applied Crystallography* **2008**, *41*, 653–658.

[94] Miller, S. P.; Dunlap, B. I.; Fleischer, A. S. *Solid State Ionics* **2012**, *227*, 66–72.

[95] Schneider, E.; Deinert, M.; Herring, S.; Cady, K. *Journal of Nuclear Materials* **2007**, *361*, 41–51.

[96] Degueldre, C.; Hellwig, C. *Journal of Nuclear Materials* **2003**, *320*, 96–105.

[97] Holliday, K.; Hartmann, T.; Poineau, F.; Rory Kennedy, J.; Czerwinski, K. *Journal of Nuclear Materials* **2009**, *393*, 224–229.

[98] Kamel, N.; Aït-Amar, H.; Taouinet, M.; Benazzouz, C.; Kamel, Z.; Fodil-Cherif, H.; Telmoune, S.; Slimani, R.; Zahri, A.; Sahel, D. *Progress in Nuclear Energy* **2006**, *48*, 70–84.

[99] Pöml, P.; Konings, R. J. M.; Somers, J.; Wiss, T.; de Haas, G. J. L. M.; Klaassen, F. C. *Comprehensive Nuclear Materials*; Konings, R. J. M., Ed.; Elsevier, 2012; Vol. 3, Chapter 3.09 - Inert Matrix Fuels, pp 237–256.

[100] Walter, M.; Nästren, C.; Somers, J.; Jardin, R.; Denecke, M. A.; Brendebach, B. *Journal of Solid State Chemistry* **2007**, *180*, 3130–3135.

[101] Belin, R. C.; Martin, P. M.; Valenza, P. J.; Scheinost, A. C. *Inorganic Chemistry* **2009**, *48*, 5376–81.

[102] Bocanegra-Bernal, M. H.; Díaz de la Torre, S. *Journal of Material Science* **2002**, *37*, 4947–4971.

[103] Zhang, F.; Chupas, P. J.; Lui, S. L. A.; Hanson, J. C.; Caliebe, W. A.; Lee, P. L.; Chan, S.-W. *Chemistry of Materials* **2007**, *19*, 3118–3126.

[104] Lemonnier, S.; Grandjean, S.; Robisson, A.-C.; Jolivet, J.-P. *Dalton Transactions* **2010**, *39*, 2254–62.

[105] Li, P.; Chen, I.-W.; Penner-Hahn, J. E. *Physical Review B* **1993**, *48*, 10063–10073.

[106] Wang, C.; Zinkevich, M.; Aldinger, F. *Pure and Applied Chemistry* **2007**, *79*, 1731–1753.

[107] Huang, H.; Hsieh, C.-H.; Kim, N.; Stebbins, J.; Prinz, F. *Solid State Ionics* **2008**, *179*, 1442–1445.

[108] Badwal, S. P. S.; Ciacchi, F. T.; Milosevic, D. *Solid State Ionics* **2000**, *136-137*, 91–99.

[109] Shibata, N.; Katamura, J.; Kuwabara, A.; Ikuhara, Y.; Sakuma, T. *Materials Science and Engineering A* **2001**, *312*, 90–98.

[110] Zavodinsky, V. G.; Chibisov, A. N. *Physics of the Solid State* **2006**, *48*, 363–368.

[111] Garvie, R. C.; Hannink, R. H.; Pascoe, R. T. *Nature* **1975**, *258*, 703–704.

[112] Hannink, R. H. J.; Kelly, P. M.; Muddle, B. C. *Journal of the American Ceramic Society* **2000**, *83*, 461–487.

[113] Nesaraj, A. S. *J. Scientific and Industrial Research* **2010**, *69*, 169–176.

[114] Petitjean, J. E.; Kearsey, R. M.; Huang, X. *Surface and Coatings Technology* **2010**, *205*, 1843–1849.

[115] Chow, C. K.; Khartabil, H. F. *Nuclear Engineering and Technology* **2007**, *40*, 139–146.

[116] Pouchon, M.; Degueldre, C.; Tissot, P. *Thermochimica Acta* **1998**, *323*, 109–121.

[117] Arima, T.; Tokura, Y.; Torrance, J. *Phys. Rev. B* **1993**, *48*, 17006–17009.

[118] Ronchi, C.; Ottaviani, J.; Degueldre, C.; Calabrese, R. *Journal of Nuclear Materials* **2003**, *320*, 54–65.

[119] Guo, X. *Physica Status Solidi* **2000**, *177*, 191–201.

[120] Villarreal, R.; Spall, D.; *Selection of Actinide Chemical Analogues for WIPP Tests*; Tech. Rep. LA-13500-MS; Los Alamos National Laboratory; 1995.

[121] Shannon, R. D. *Acta Crystallographica A* **1976**, *32*, 751–767.

[122] Seaborg, G. T. *Radiochimica Acta* **1993**, *61*, 115–122.

[123] Restani, R.; Martin, M.; Kivel, N.; Gavillet, D. *Journal of Nuclear Materials* **2009**, *385*, 435–442.

[124] Keyes, R. W. *Physical Review* **1959**, *115*, 564–567.

[125] Angeles-Rosas, M.; Camacho-López, M. A.; Ruiz-Trejo, E. *Solid State Ionics* **2010**, *181*, 1349–1354.

[126] Haering, C.; Roosen, A.; Schichl, H.; Schnoller, M. *Solid State Ionics* **2005**, *176*, 261–268.

[127] Yamamoto, O.; Arati, Y.; Takeda, Y.; Imanishi, N.; Mizutani, Y.; Kawai, M.; Nakamura, Y. *Solid State Ionics* **1995**, *79*, 137–142.

[128] OECD/NEA *The Safety of the Nuclear Fuel Cycle*, 3rd ed.; OECD Publishing: Paris, 2005; Chapter The Nuclear Fuel Cycle.

[129] Devanathan, R.; Gao, F.; Sun, X.; *Challenges in Modeling the Degradations of Ceramic Waste Forms*; Tech. Rep. PNNL-20738; Pacific Northwest National Laboratory; 2011.

[130] Rogers, K. A. *Progress in Nuclear Energy* **2009**, *51*, 281–289.

[131] Santos, B. G.; Nesbitt, H. W.; Noël, J. J.; Shoesmith, D. W. *Electrochim. Acta* **2004**, *49*, 1863–1873.

[132] Santos, B. G.; Noël, J. J.; Shoesmith, D. W. *Electrochim. Acta* **2006**, *51*, 4157–4166.

[133] Santos, B. G.; Noël, J. J.; Shoesmith, D. W. *J. Nucl. Mater.* **2006**, *350*, 320–331.

[134] Read, J.; *APM Conceptual Design and Cost Estimate Update Deep Geological Repository Design Report Sedimentary Rock Environment Copper Used Fuel Container*; Tech. Rep. SLN Report No. 020606-6200-REPT-0001; SNC-:Lavalin Nuclear Inc.; 2011.

[135] Trachenko, K. *J. Phys. Condens. Matter* **2004**, *16*, R1491–R1515.

[136] Caurant, D.; Majérus, O.; Fadel, E.; Quintas, a.; Gervais, C.; Charpentier, T.; Neuville, D. *Journal of Nuclear Materials* **2010**, *396*, 94–101.

[137] Short, R. J.; Hand, R. J.; Hyatt, N. C.; Möbus, G. *J. Nucl. Mater.* **2005**, *340*, 179–186.

[138] Lumpkin, G. R.; Pruneda, M.; Rios, S.; Smith, K. L.; Trachenko, K.; Whittle, K. R.; Zaluzec, N. J. *J. Solid State Chem.* **2007**, *180*, 1512–1518.

[139] Lumpkin, G.; Ewing, R. *Phys. Chem. Miner.* **1988**, *16*, 2–20.

[140] Digeos, A. A.; Valdez, J. A.; Sickafus, K. E.; Atiq, S.; Grimes, W.; Boccaccini, A. R. *J. Mater. Sci.* **2003**, *38*, 1597–1604.

[141] Ewing, R. C.; Weber, W. J.; Lian, J. *J. Appl. Phys.* **2004**, *95*, 5949–5971.

[142] Hayes, J. R.; Investigations of the Effect of Transition Metal Substitution on the Pre-edge of X-ray Absorption Near-Edge Spectra; M.sc. thesis; University of Saskatchewan; 2012.

[143] Chen, N.; Jiang, D.; Cutler, J.; Kotzer, T.; Jia, Y.; Demopoulos, G.; Rowson, J. *Geochim. Cosmochim. Acta* **2009**, *73*, 3260–3276.

[144] Essilfie-Dughan, J.; Pickering, I. J.; Hendry, M. J.; George, G. N.; Kotzer, T. *Environmental Science and Technology* **2011**, *45*, 455–60.

[145] Achary, S. N.; Patwe, S. J.; Mathews, M. D.; Tyagi, A. K. *Journal of Physics and Chemistry of Solids* **2006**, *67*, 774–781.

[146] Sleight, A. W.; Chamberland, B. L.; Weiher, J. F. *Inorganic Chemistry* **1968**, *7*, 1094–1098.

[147] Otsuka, K.; Wang, Y.; Yamanaka, I.; Morikawa, A. *Journal of the Chemical Society, Faraday Transactions* **1993**, *89*, 4225–4230.

[148] Michel, F. M.; Ehm, L.; Liu, G.; Han, W. Q.; Antao, S. M.; Chupas, P. J.; Lee, P. L.; Knorr, K.; Eulert, H.; Kim, J.; Grey, C. P.; Celestian, A. J.; Gillow, J.; Schoonen, M. A. A.; Strongin, D. R.; Parise, J. B. *Chem. Mater.* **2007**, *19*, 1489–1496.

[149] Kashiwabara, T.; Takahashi, Y.; Tanimizu, M. *Geochemical Journal* **2009**, *43*, e31–e36.

[150] Kraus, W.; Nolze, G. *Journal of Applied Crystallography* **1996**, *29*, 301–303.

[151] Tamura, N.; MacDowell, A. A.; Spolenak, R.; Valek, B. C.; Bravman, J. C.; Brown, W. L.; Celestre, R. S.; Padmore, H. A.; Batterman, B. W.; Patal, J. R. *Journal of Synchrotron Radiation* **2003**, *10*, 137–143.

[152] Webb, S. M. *AIP Conference Proceedings* **2011**, *1365*, 196–199.

[153] Jiang, D. T.; Chen, N.; Zhang, L.; Malgorzata, G.; Wright, G. *AIP Conference Proceedings* **2007**, *882*, 893.

[154] Thompson, A.; Attwood, D.; Gullikson, E.; Howells, M.; Kim, K. J.; Kirz, J.; Kortright, J.; Lindau, I.; Pianetta, P.; Robinson, A.; Scofield, J.; Underwood, J.; Vaughn, D.; Williams, G.; Winick, H. *X-ray Data Booklet*; Lawrence Berkeley National Laboratory: Berkeley, 2009.

[155] Ravel, B.; Newville, M. *Journal of Synchrotron Radiation* **2005**, *12*, 537–41.

[156] Pecharsky, V. K.; Zavalij, P. Y. *Fundamentals of Powder Diffraction and Structural Characterization of Materials*, 2nd ed.; Springer US: Boston, MA, 2009.

[157] Smith, D. K. *Defect and Microstructure Analysis*; Snyder, R. L.; Fiala, J.; Bunge, H. J., Eds.; Oxford University Press: Oxford, 1999; Chapter Crystallite statistics and accuracy in powder diffraction intensity measurements, pp 333–345.

[158] Rindby, A.; Engström, P.; Janssens, K. *Journal of Synchrotron Radiation* **1997**, *4*, 228–35.

[159] Gaultois, M. W.; Grosvenor, A. P. *Journal of Physical Chemistry C* **2010**, *114*, 19822–19829.

[160] Farges, F.; Siewert, R.; Brown, G. E.; Guesdon, A.; Morin, G. *The Canadian Mineralogist* **2006**, *44*, 731–753.

[161] Karppinen, M.; Fukuoka, A.; Niinistö, L.; Yamauchi, H. *Superconductor Science and Technology* **1996**, *9*, 121–135.

[162] Atkins, P.; Overton, T.; Rourke, J.; Weller, M.; Armstrong, F. *Inorganic Chemistry*, 4th ed.; Oxford University Press: Oxford, 2006.

[163] Fernandez-Garcia, M.; Marquez Alvarez, C.; Haller, G. L. *Journal of Physical Chemistry* **1995**, *99*, 12565–12569.

[164] Malinowski, E. R. *Factor Analysis in Chemistry*, 3rd ed.; John Wiley & Sons: New York, 2002.

[165] Malinowski, E. R. *Analytical Chemistry* **1977**, *49*, 606–612.

[166] Frey, R.; *Personal Communication*; AREVA Resources Canada, 2013.

[167] Herrero-Martín, J.; García, J.; Subías, G.; Blasco, J.; Sánchez, M. C. *Journal of Physics: Condensed Matter* **2004**, *16*, 6877–6890.

[168] Rehr, J. J.; Albers, R. C. *Reviews of Modern Physics* **2000**, *72*, 621–654.

[169] Huguenin, F.; Ticianelli, E. A.; Torresi, R. M. *Electrochimica Acta* **2002**, *47*, 3179–3186.

[170] Rodriguez, J. a.; Hanson, J. C.; Chaturvedi, S.; Maiti, A.; Brito, J. L. *Journal of Chemical Physics* **2000**, *112*, 935.

[171] Brito, J. L.; Barbosa, A. L. *Journal of Catalysis* **1997**, *171*, 467–475.

[172] Mazzocchia, C.; Aboumrad, C.; Diagne, C.; Tempesti, E.; Herrmann, J. M.; Thomas, G. *Catalysis Letters* **1991**, *10*, 181–192.

[173] *PANalytical HighScore Plus Version 3.0.4*; PANalytical BV: Almelo, The Netherlands, 2011.

[174] Jaffe, J.; Bachorz, R.; Gutowski, M. *Physical Review B* **2005**, *72*, 144107.

[175] Igawa, N.; Ishii, Y. *Journal of the American Ceramic Society* **2001**, *84*, 1169–1171.

[176] Bondars, B.; Heidemane, G.; Grabis, J.; Laschke, K.; Boysen, H.; Schneider, J.; Frey, F. *Journal of Material Science* **1995**, *30*, 1621–1625.

[177] Heald, S. M.; Brewe, D. L.; Stern, E. A.; Kim, K. H.; Brown, F. C.; Jiang, D. T.; Crozier, E. D.; Gordon, R. A. *Journal of Synchrotron Radiation* **1999**, *6*, 347–9.

[178] Newville, M. *Fundamentals of XAFS*, 1st ed.; University of Chicago: Chicago, 2004.

[179] Rehr, J.; Albers, R. *Physical Review B* **1990**, *41*, 8139–8149.

[180] Li, P.; Chen, I.-W.; Penner-Hahn, J. E. *Physical Review B* **1993**, *48*, 10074–10081.

[181] Hu, Y. F.; Coulthard, I.; Chevrier, D.; Wright, G.; Igarashi, R.; Sitnikov, A. *AIP Conference Proceedings* **2010**, *1234*, 343–346.

[182] Denton, A.; Ashcroft, N. *Physical Review A* **1991**, *43*, 3161–3164.

[183] Mountjoy, G.; Pickup, D. M.; Anderson, R.; Wallidge, G. W.; Holland, M. A.; Newport, R. J.; Smith, M. E. *Physical Chemistry Chemical Physics* **2000**, *2*, 2455–2460.

[184] Mountjoy, G.; Holland, M. A.; Wallidge, G. W.; Gunawidjaja, P.; Smith, M. E.; Pickup, D. M.; Newport, R. J. *Journal of Physical Chemistry B* **2003**, *107*, 7557–7566.

[185] Villella, P.; Conradson, S.; Espinosa-Faller, F.; Foltyn, S.; Sickafus, K.; Valdez, J.; Deguel-dre, C. *Physical Review B* **2001**, *64*, 104101.

[186] Catlow, C. R. A.; Chadwick, A. V.; Greaves, G. N.; Moroney, L. M. *Journal of the American Ceramic Society* **1986**, *69*, 272–277.

[187] Gómez, A.; Villanueva, R.; Vie, D.; Murcia-Mascaros, S.; Martínez, E.; Beltrán, A.; Sapiña, F.; Vicent, M.; Sánchez, E. *Journal of Solid State Chemistry* **2013**, *197*, 120–127.

[188] Li, P.; Chen, I.-W.; Penner-Hahn, J. E. *Physical Review B* **1993**, *48*, 10082–10089.

[189] Blanchard, P. E. R.; Liu, S.; Kennedy, B. J.; Ling, C. D.; Zhang, Z.; Avdeev, M.; Cowie, B. C. C.; Thomsen, L.; Jang, L.-Y. *Dalton Transactions* **2013**, *42*, 14875–82.

[190] Blanchard, P. E. R.; Clements, R.; Kennedy, B. J.; Ling, C. D.; Reynolds, E.; Avdeev, M.; Stampfl, A. P. J.; Zhang, Z.; Jang, L.-Y. *Inorganic Chemistry* **2012**, *51*, 13237–44.

[191] Artini, C.; Pani, M.; Lausi, A.; Masini, R.; Costa, G. A. *Inorganic Chemistry* **2014**, *53*, 10140–9.

[192] Zinkevich, M. *Progress in Materials Science* **2007**, *52*, 597–647.

[193] Wu, Z.; Benfatto, M.; Natoli, C. *Physical Review B* **1998**, *57*, 10336–10339.

[194] Fabrichnaya, O.; Savinykh, G.; Schreiber, G.; Seifert, H. J. *Journal of Phase Equilibria and Diffusion* **2011**, *32*, 284–297.

[195] Sarsfield, B. A.; Davidovich, M.; Desikan, S.; Fakes, M.; Futernik, S.; Hilden, J. L.; Tan, J. S.; Yin, S.; Young, G.; Vakkalagadda, B.; Volk, K. *Advances in X-ray Science* **2006**, *49*, 322–327.

[196] Vaidya, V. N. *J. Sol-Gel Sci. Technol.* **2008**, *46*, 369–381.

[197] Arachi, Y. *Solid State Ionics* **2004**, *175*, 119–121.

[198] Suárez, G.; Garrido, L. B.; Aglietti, E. F. *Materials Chemistry and Physics* **2008**, *110*, 370–375.

[199] Song, X.; Lu, J.; Zhang, T.; Ma, J. *Journal of the American Ceramic Society* **2011**, *94*, 1053–1059.

[200] Fujimori, H.; Yashima, M.; Kakihana, M.; Yoshimura, M. *Journal of the American Ceramic Society* **1998**, *81*, 2885–2893.

[201] Schelling, P. K.; Phillpot, S. R.; Wolf, D. *Journal of the American Ceramic Society* **2001**, *84*, 1609–1619.

[202] Walker, J. D. S.; Grosvenor, A. P. *Inorganic Chemistry* **2013**, *52*, 8612–8620.

[203] Wu, B.; Zinkevich, M.; Aldinger, F.; Wen, D.; Chen, L. *Journal of Solid State Chemistry* **2007**, *180*, 3280–3287.

[204] Fujimori, H.; Yashima, M.; Kakihana, M.; Yoshimura, M. *Journal of Applied Physics* **2002**, *91*, 6493–6498.

[205] Sakuma, T.; Suto, H. *Journal of Materials Science* **1986**, *21*, 4359–4365.

[206] Zhang, J.; Wang, Y.; Valdez, J.; Tang, M.; Won, J.; Sickafus, K. *Nuclear Instruments and Methods Phyical Research Section B* **2012**, *272*, 244–248.

[207] Zacate, M. O.; Minervini, L.; Bradfield, D. J.; Grimes, R. W.; Sickafus, K. E. *Solid State Ionics* **2000**, *128*, 243–254.

[208] Kim, N.; Hsieh, C.-H.; Stebbins, J. F. *Chemistry of Materials* **2006**, *18*, 3855–3859.

[209] Bogicevic, A.; Wolverton, C. *Physical Review B* **2003**, *67*, 024106.

[210] Oberti, R.; Quartieri, S.; Dalconi, M. C.; Boscherini, F.; Iezzi, G.; Boiocchi, M.; Eeckhout, S. G. *American Mineralogist* **2006**, *91*, 1230–1239.

[211] Lindqvist-Reis, P.; Persson, I.; Sandström, M. *Dalton Transactions* **2006**, 3868–3878.

[212] Li, P.; Chen, I.-W.; Penner-Hahn, J. E.; Tien, T.-Y. *Journal of the American Ceramic Society* **1991**, *74*, 958–967.

[213] Yamamoto, T. *X-Ray Spectrometry* **2008**, *37*, 572–584.

[214] Allred, A. L. *J. Inorg. Nucl. Chem.* **1961**, *17*, 215–221.

[215] Omar, S.; Bonanos, N. *Journal of Material Science* **2010**, *45*, 6406–6410.

[216] Yamamura, H. *Solid State Ionics* **1998**, *107*, 185–189.

[217] Yamamura, H.; Matsusita, T.; Nishino, H.; Kakinuma, K. *Journal of Materials Science: Materials in Electronics* **2002**, *13*, 57–61.

[218] Blanchard, P. E. R.; Hayes, J. R.; Grosvenor, A. P.; Rowson, J.; Hughes, K.; Brown, C. *Environmental Science and Technology* **2015**, *49*, 6504–6509.

[219] Lian, J.; Wang, L. M.; Ewing, R. C.; Yudintsev, S. V.; Stefanovsky, S. V. *Journal of Applied Physics* **2005**, *97*, 113536.

[220] Weber, W. J.; Ewing, R. C.; Catlow, C. R. A.; Diaz de la Rubia, T.; Hobbs, L. W.; Kinoshita, C.; Matzke, H.; Motta, A. T.; Nastasi, M.; Salje, E. K. H.; Vance, E. R.; Zinkle, S. J. *Journal of Materials Research* **1998**, *13*, 1434–1484.

[221] Wang, L.; Wang, S.; Zhu, S.; Ewing, R. *Journal of Nuclear Materials* **2001**, *289*, 122–127.

[222] Davoisne, C.; Stennett, M.; Hyatt, N.; Peng, N.; Jeynes, C.; Lee, W. *Journal of Nuclear Materials* **2011**, *415*, 67–73.

[223] Aluri, E. R.; Grosvenor, A. P. *RSC Advances* **2015**, *5*, 80939–80949.

[224] Higgs, J.; Lewis, B.; Thompson, W.; He, Z. *Journal of Nuclear Materials* **2007**, *366*, 99–128.

[225] Lucuta, P.; Verrall, R.; Matzke, H.; Palmer, B. *Journal of Nuclear Materials* **1991**, *178*, 48–60.

Appendix A

Supporting Tables and Figures for Chapter 2[1]

[1]Reproduced in part with permission from J.R. Hayes, A.P Grosvenor, J. Rowson, K. Hughes, R.A. Frey, J. Reid *Environmental Society and Technology* (2014) 48, 4460-4467. DOI: 10.1021/es404980x. Copyright 2014 American Chemical Society.

Table A.1: Concentration of selected elements in the JEB-TMF tailings samples as determined by ICP-MS

Bore-hole		**Central (TMF08-01)**			**Periphery (TMF08-03**		
Sample		**SA-04**	**SA-09**	**SA-19**	**SA-02**	**SA-08**	**SA-16**
Sample Elevation (mASL)[a]		411	398	366	411	397	370
Analyte	**Units**						
Al	μg/g	50100	51500	82600	82500	76000	95000
Sb	μg/g	0.2	<0.2	0.6	0.2	<0.2	0.4
As	μg/g	227	433	7000	5100	5700	5600
Ba	μg/g	46	150	270	150	110	330
Be	μg/g	2.3	4.1	7	4.0	4.2	8.1
B	μg/g	100	140	240	430	290	450
Cd	μg/g	<0.1	<0.1	0.2	<0.1	<0.1	0.2
Cr	μg/g	4.6	28	33	15	26	25
Co	μg/g	5.7	8.2	110	23	30	82
Cu	μg/g	5.1	18	260	34	30	170
Fe	μg/g	7700	10100	13700	11200	10400	21000
Pb	μg/g	41	478	889	409	134	2200
Mn	μg/g	40	76	300	120	160	460
Mo	**μg/g**	**20**	**92**	**97**	**143**	**185**	**409**
Ni	μg/g	194	311	4200	3100	3700	3500
Se	μg/g	0.5	5.7	30	7.0	5.5	22
Ag	μg/g	0.1	1	6	1.5	1.2	6.0
Sr	μg/g	180	170	280	380	420	370
Tl	μg/g	0.2	0.3	0.8	0.5	0.5	1.4
Sb	μg/g	0.2	0.3	0.7	0.6	0.7	1.0
Ti	μg/g	120	210	170	400	280	470
U	μg/g	40	219	649	208	554	504
V	μg/g	262	570	745	628	781	1000
Zn	μg/g	9.8	23	54	44	12	64

[a]Meters above sea level

Table A.2: Results of Laue diffraction fitting for TMF08-01 SA19

Image[a]	**Number of Peaks Indexed[b]**						
	Powellite	**Quartz**	**Illite-Smectite**	**Chlorite**	**Gypsum**	**Kamiokite**	**β-$FeMoO_4$**
1	47	82	55	49	40	58	160
5	47	62	45	44	47	58	167
8	49	264	48	48	60	69	169
10	55	59	57	48	49	50	168

[a]Numbering refers to where on the sample the diffraction pattern was collected. Please refer to Figure S8 for image locations.

[b]A larger numbers of peaks indexed usually indicates a higher quality fit.

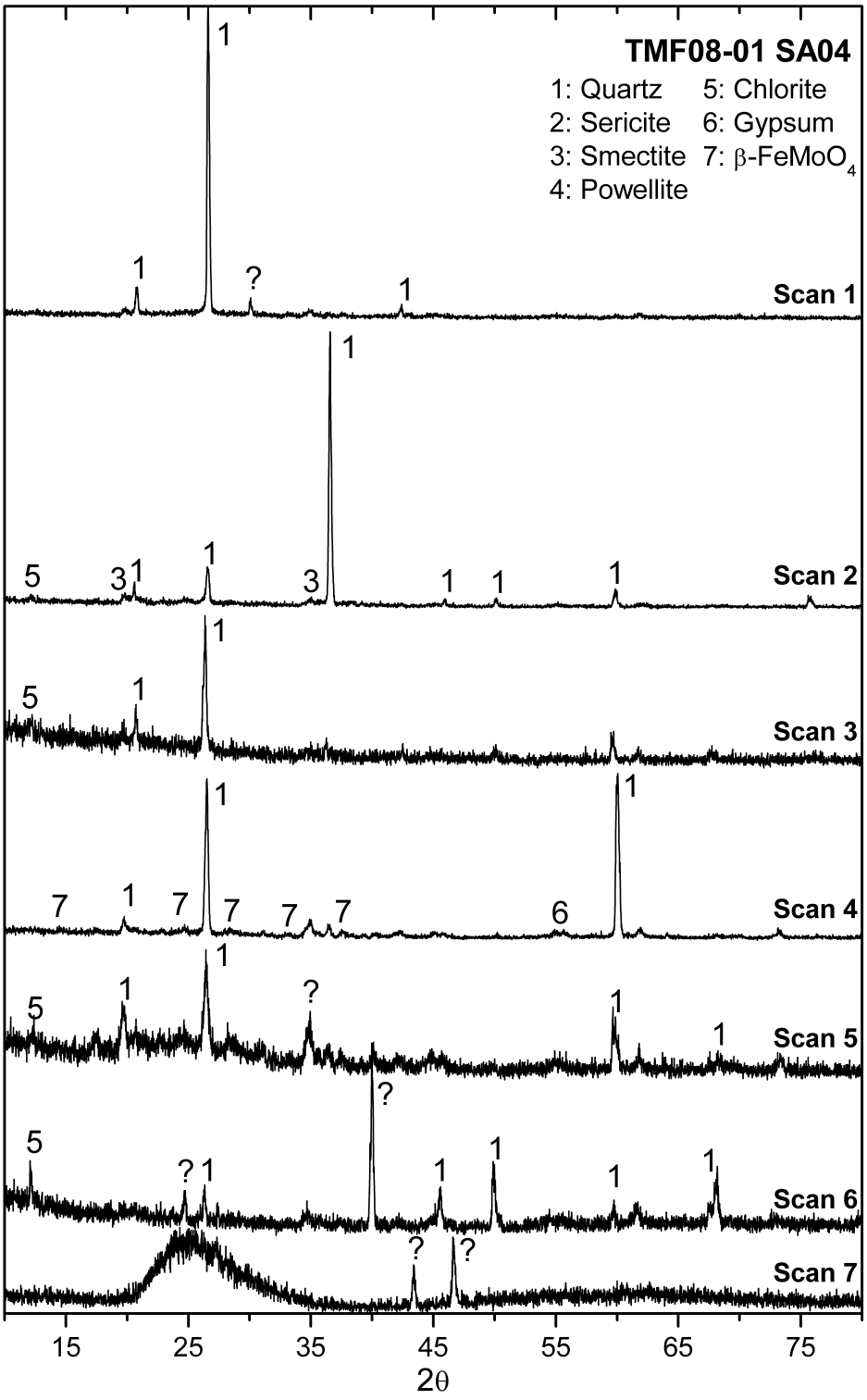

Figure A.1: The μXRD results from the TMF08-01 SA04 sample are presented. Possible evidence of a β-$FeMoO_4$ phase was observed in Scan 4. Peaks that could not be identified are labelled with a "?".

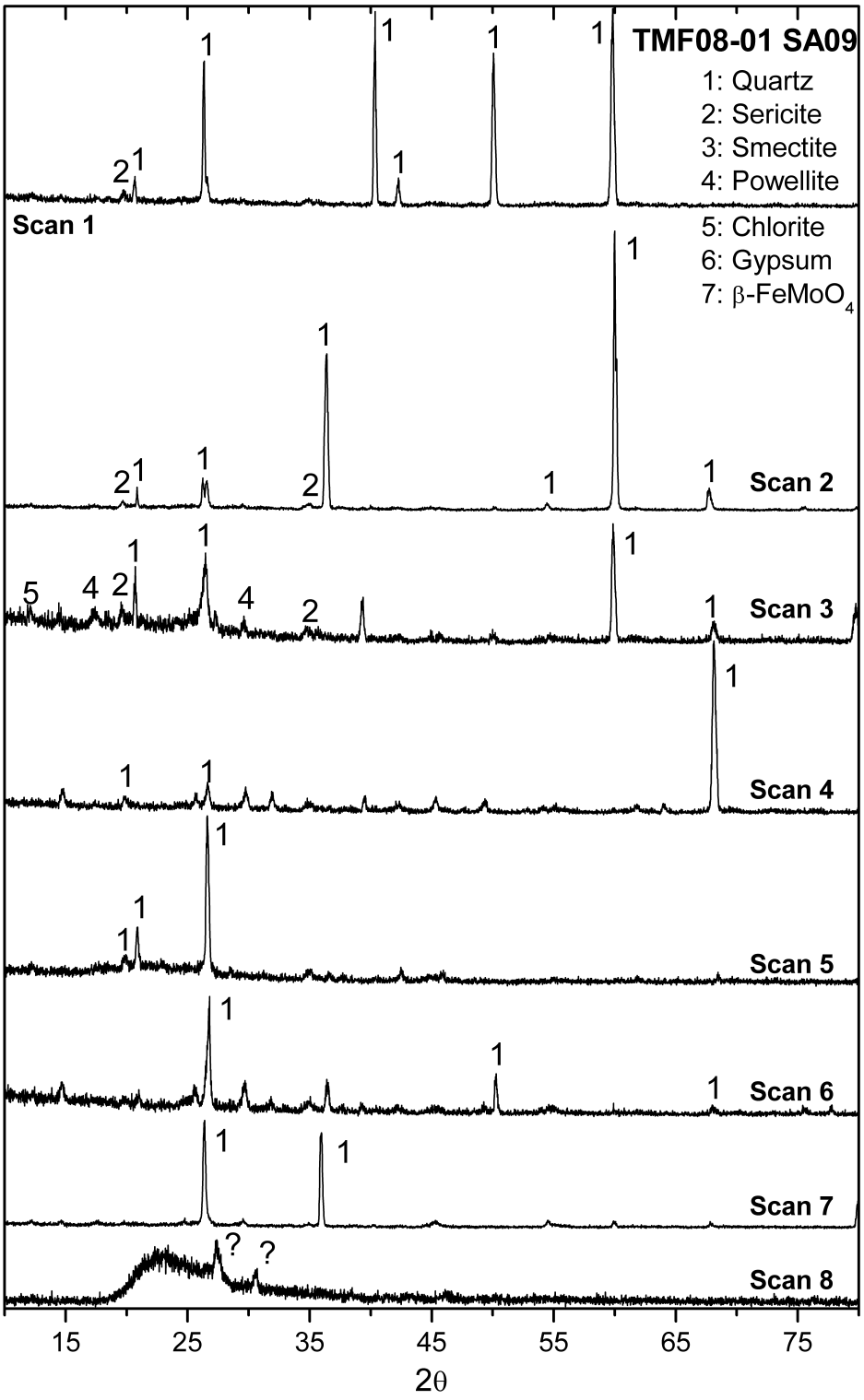

Figure A.2: The μXRD results from the TMF08-01 SA09 sample are presented. Peaks associated with the powellite phase were observed in Scan 3. Peaks that could not be identified are labelled with a "?".

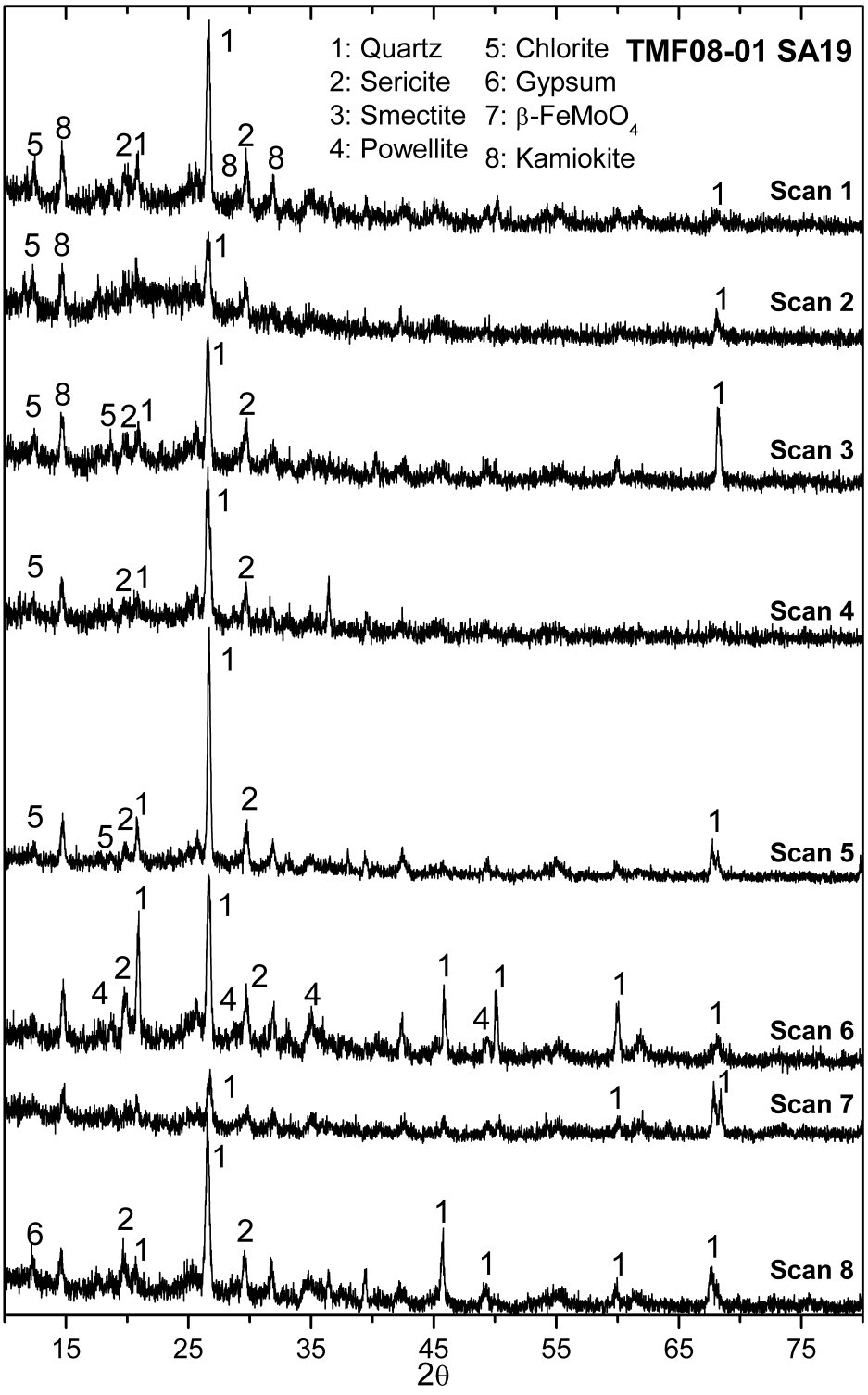

Figure A.3: The μXRD results from the TMF08-01 SA19 sample are presented. Possible peaks from a kamiokite phase were observed in Scans 1-3.

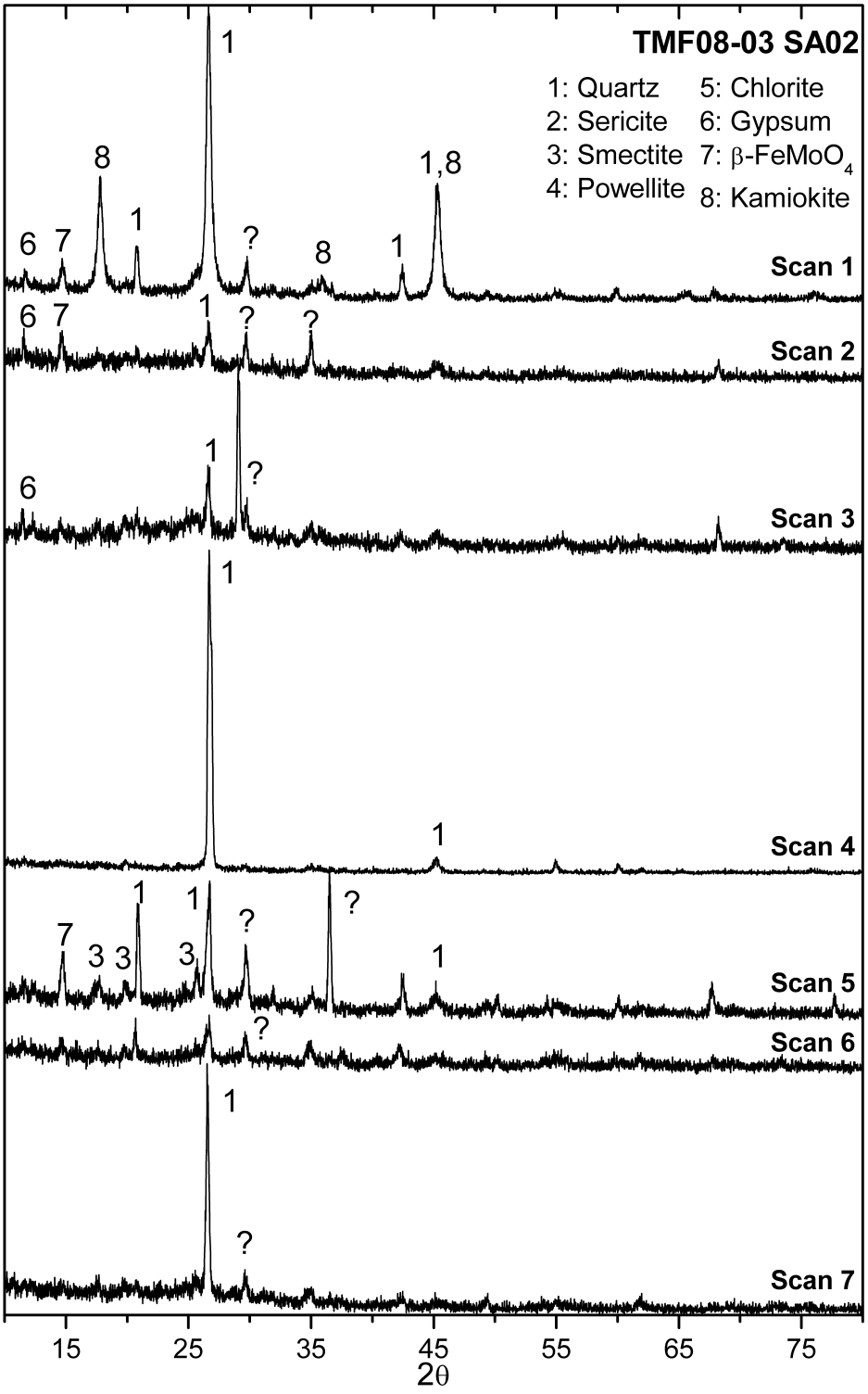

Figure A.4: The μXRD results from the TMF08-03 SA02 sample are presented. Possible evidence of a β-FeMoO4 phase was observed in Scans 1, 2, and 5. Peaks that could not be identified are labelled with a "?".

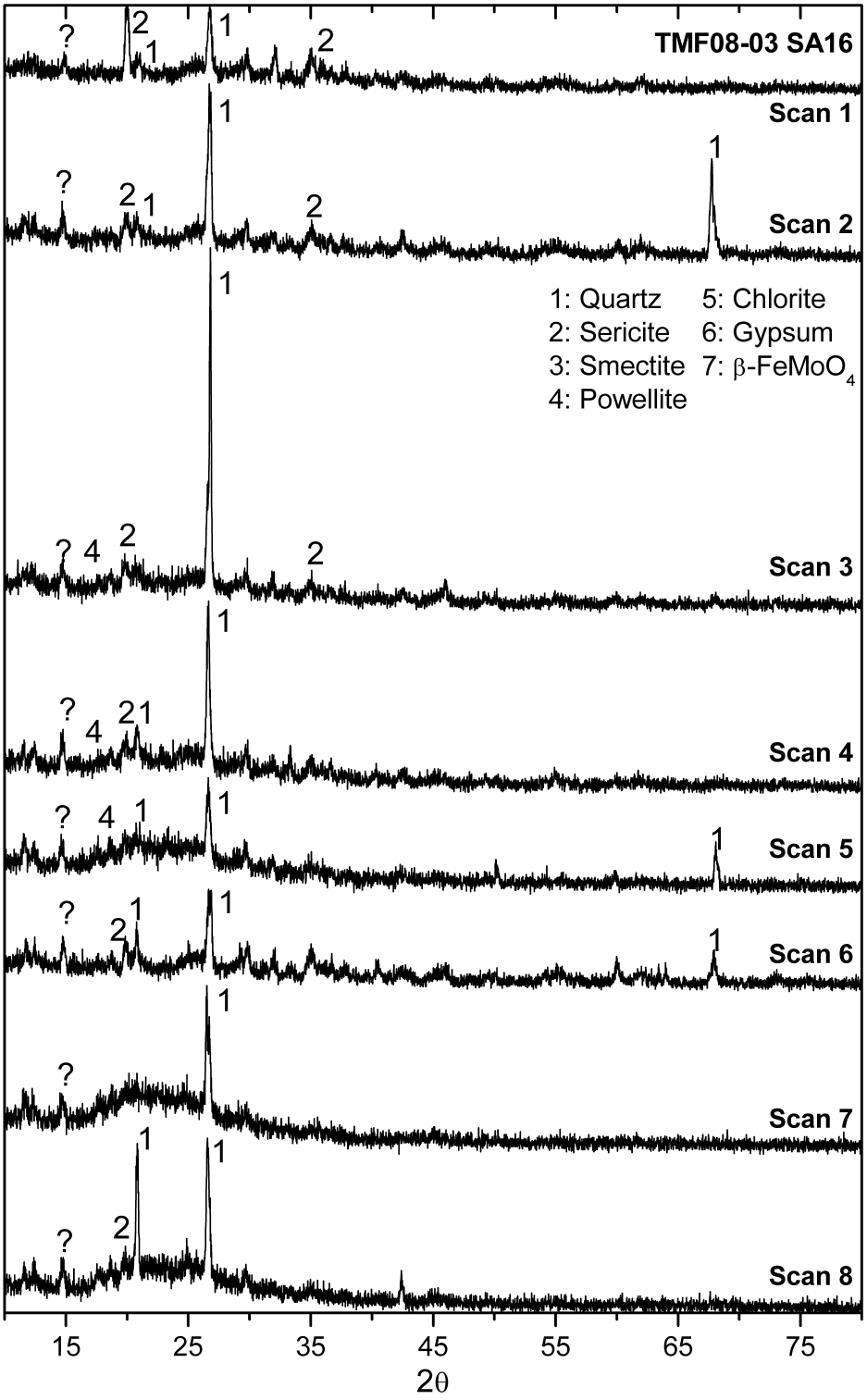

Figure A.5: The μ-XRD results from the TMF08-03 SA16 sample are presented. Peaks associated with the powellite phase were observed in Scans 3-5. Peaks that could not be identified are labelled with a "?".

Table A.3: Results of Laue diffraction fitting for TMF08-03 SA16

Image[a]	Number of Peaks Indexed[b]						
	Powellite	**Quartz**	**Illite-Smectite**	**Chlorite**	**Gypsum**	**Kamiokite**	**β-$FeMoO_4$**
1	92	14	89	82	81	86	314
6	66	86	65	75	71	75	243
7	86	104	78	86	93	108	308
8	77	92	72	78	68	76	253

[a]Numbering refers to where on the sample the diffraction pattern was collected. Please refer to Figure S8 for image locations.
[b]A larger numbers of peaks indexed usually indicates a higher quality fit.

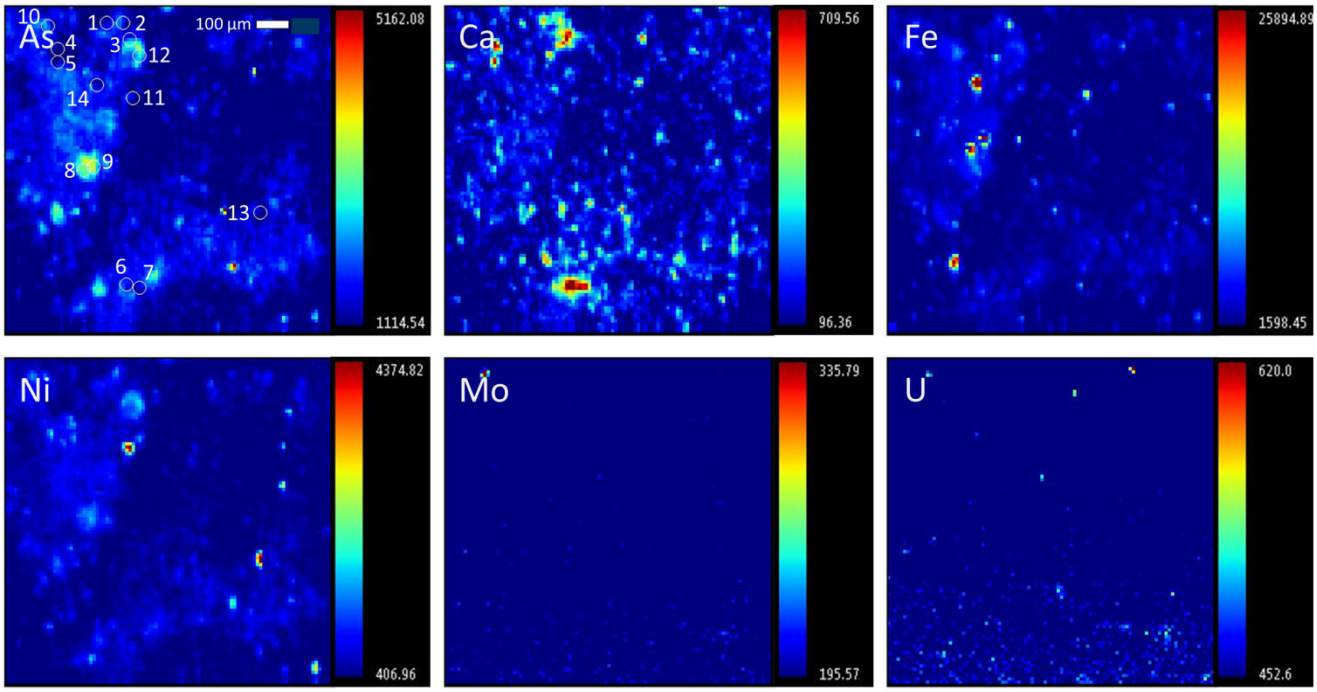

Figure A.6: Fluorescence maps collected from the TMF08-01 SA19 sample. The spots where Laue diffraction patterns were collected are labelled according to their Scan number in the As map. No fluorescence signals from Mo or U were observed.

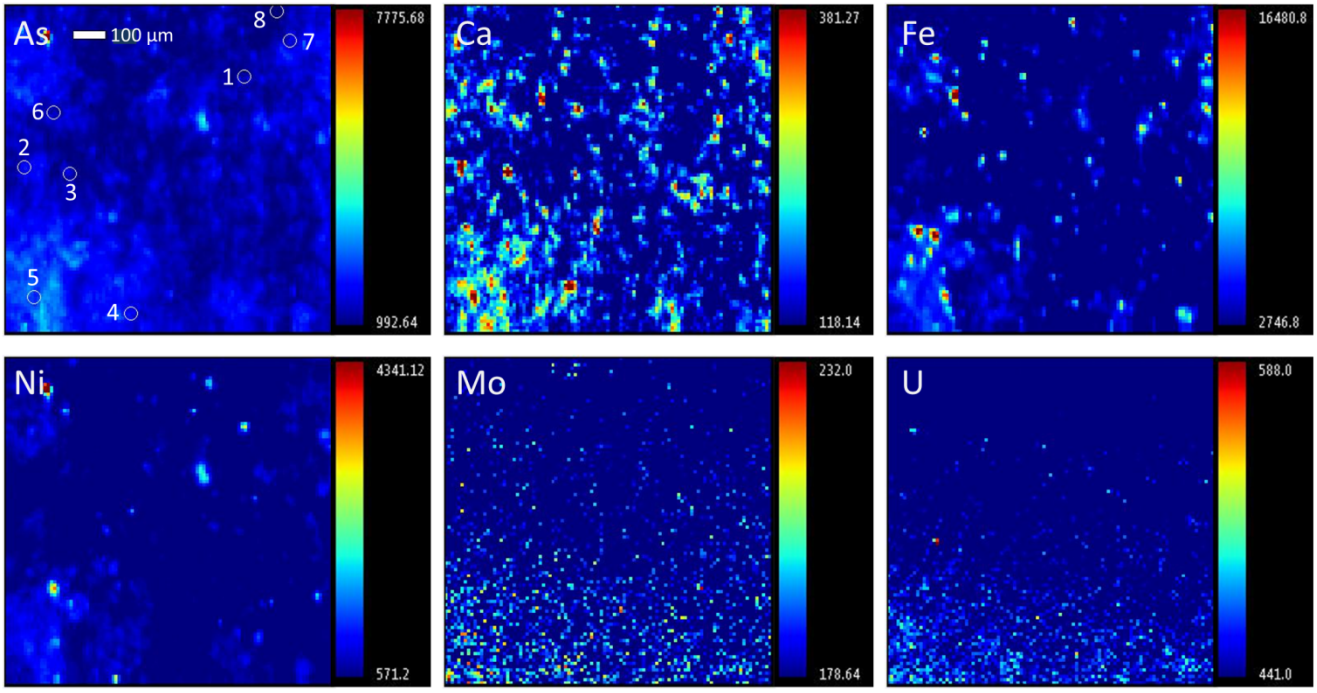

Figure A.7: Fluorescence maps collected from the TMF08-03 SA16 sample. The spots where Laue diffraction patterns were collected are labelled according to their Scan number in the As map. No fluorescence signals from Mo or U were observed.

Appendix B

Supporting Tables and Figures for Chapter 3[1]

[1]Reprinted in part from *Journal of Alloys and Compounds,* 635, J.R. Hayes, A.P. Grosvenor, M. Saoudi "An Investigation of the Thermal Stability of $Nd_xY_yZr_{1-x-y}O_{2-\delta}$ Inert Matrix Fuel Materials," 245-255, 2015, DOI: 10.1016/j.jallcom.2015.02.022 with permission from Elsevier.

Table B.1: Powder XRD Refinement Results

	As synthesized	Annealed 600 °C	Annealed 900°C	Annealed 1400 °C
$Nd_{0.25}Zr_{0.75}O_{1.88}$				
R_{wp}[a]	7.14	8.58	7.19	9.00
Unit Cell (Å)	5.2089(7)	5.2088(1)	5.2094(1)	5.2060(1)
Wt. Fraction	100% Cubic	98.8% Cubic 1.2% Monoclinic	100% Cubic	84.5 % Cubic 11.3% Monoclinic 4.2% Tetragonal
$Nd_{0.20}Y_{0.05}Zr_{0.75}O_{1.88}$				
R_{wp}[a]	7.05	7.39	6.76	12.29
Unit Cell (Å)	5.1977(6)	5.19674(7)	5.19668(7)	5.1932(1)
Wt. Fraction	100% Cubic	100% Cubic	100% Cubic	100% Cubic
$Nd_{0.05}Y_{0.20}Zr_{0.75}O_{1.88}$				
R_{wp}[a]	8.66	7.76	9.16	12.74
Unit Cell (Å)	5.1658(6)	5.16481(6)	5.15401(9)	5.1639(1)
Wt. Fraction	100% Cubic	97.7% Cubic 2.3% Tetragonal	100% Cubic	100% Cubic
$Y_{0.25}Zr_{0.75}O_{1.88}$				
R_{wp}[a]	7.41	7.91	7.99	9.38
Unit Cell (Å)	5.1555(7)	5.15437(9)	5.15417(8)	5.1494(1)
Wt. Fraction	98.3% Cubic 1.7% Monoclinic	100% Cubic	100% Cubic	100% Cubic
$Nd_{0.10}Y_{0.10}Zr_{0.80}O_{1.90}$				
R_{wp}[a]	8.45	7.44	8.45	11.75
Unit Cell (Å)	5.16897(6)	5.1683(6)	5.16802(7)	5.1677(2)
Wt. Fraction	100% Cubic	100% Cubic	100% Cubic	100% Cubic
$Nd_{0.25}Y_{0.05}Zr_{0.70}O_{1.85}$				
R_{wp}[a]	7.21	7.13	8.09	14.16
Unit Cell (Å)	5.2119(1)	5.2167(1)	5.2167(1)	5.2155(3)
Wt. Fraction	100% Cubic	100% Cubic	100% Cubic	100% Cubic
$Nd_{0.15}Y_{0.15}Zr_{0.70}O_{1.85}$				
R_{wp}[a]	11.35	7.86	7.94	9.74
Unit Cell (Å)	5.1942(1)	5.19366(7)	5.19328(7)	5.1915(2)
Wt. Fraction	100% Cubic	100% Cubic	100% Cubic	100% Cubic
$Nd_{0.05}Y_{0.25}Zr_{0.70}O_{1.85}$				
R_{wp}[a]	7.23	7.70	7.55	10.10
Unit Cell (Å)	5.17491(9)	5.1741(1)	5.16366(6)	5.1719(1)
Wt. Fraction	100% Cubic	100% Cubic	100% Cubic	100% Cubic

[a] $R_{wp} = \sum w_i(y_{io} - y_{ic})^2 / \sum w_i y_{io}$; w_i = ith comp. wt. fraction; y_{ic} = calculated intensity; y_{io} = diffraction pattern intensity.

Table B.2: Summary of Zr K-edge EXAFS Results

	As synthesized			Annealed 600 °C			Annealed 900 °C			Annealed 1400 °C		
	$Y_{0.25}Zr_{0.75}O_{1.88}$											
	S_o^2 =0.92(9), ΔE =-4(1) eV			S_o^2 =0.92(9), ΔE =-4(1) eV			S_o^2 =0.92(9), ΔE =-4(1) eV			S_o^2 =0.91(9), ΔE =-5(1) eV		
	R_{fit}= 0.022			R_{fit}= 0.021			R_{fit}= 0.025			R_{fit}= 0.023		
	CN	R(Å)	σ^2	CN	R(Å)	σ^2	CN	R(Å)	σ^2	CN	R(Å)	σ^2
Zr-O	7	2.16(1)	0.007(2)	7	2.16(1)	0.007(1)	7	2.16(1)	0.007(1)	7	2.16(1)	0.007(2)
Zr-Zr/Y	12	3.57(1)	0.011(1)	12	3.569(9)	0.011(1)	12	3.57(1)	0.011(1)	12	3.572(9)	0.010(1)
Zr-O2	22	4.32(6)	0.031(2)	22	4.39(7)	0.03(1)	22	4.31(7)	0.03(1)	22	4.31(6)	0.03(1)
	$Nd_{0.05}Y_{0.20}Zr_{0.75}O_{1.88}$											
	S_o^2 =0.91(8), ΔE =-4(1) eV			S_o^2 =0.92(9), ΔE =-3.8(9) eV			S_o^2 =0.91(8), ΔE =-1.9(9) eV			S_o^2 =0.91(8), ΔE =-2.5(9) eV		
	R_{fit}= 0.023			R_{fit}= 0.014			R_{fit}= 0.017			R_{fit}= 0.015		
	CN	R(Å)	σ^2	CN	R(Å)	σ^2	CN	R(Å)	σ^2	CN	R(Å)	σ^2
Zr-O	7	2.16(1)	0.007(2)	7	2.152(1)	0.007(1)	7	2.15(1)	0.007(1)	7	2.15(1)	0.007(1)
Zr-Zr/Y	12	3.57(1)	0.011(1)	11	3.559(9)	0.011(1)	11	3.56(1)	0.010(1)	11	3.56(1)	0.010(1)
Zr-Nd	0	N/A	N/A	1	3.89(5)	0.007(5)	1	3.86(7)	0.007(7)	1	3.89(7)	0.007(7)
Zr-O2	22	4.35(5)	0.03(1)	22	4.32(7)	0.03(1)	22	4.29(7)	0.03(1)	22	4.32(7)	0.03(1)
	$Nd_{0.05}Y_{0.20}Zr_{0.75}O_{1.88}$											
	S_o^2 =0.85(9), ΔE =-4(1) eV			S_o^2 =0.88(9), ΔE =-4(1) eV			S_o^2 =0.86(9), ΔE =-4(1) eV			S_o^2 =0.85(9), ΔE =-3(1) eV		
	R_{fit}= 0.024			R_{fit}= 0.025			R_{fit}= 0.025			R_{fit}= 0.023		
	CN	R(Å)	σ^2	CN	R(Å)	σ^2	CN	R(Å)	σ^2	CN	R(Å)	σ^2
Zr-O	7	2.16(1)	0.007(1)	7	2.16(1)	0.008(1)	7	2.16(1)	0.007(2)	7	2.16(1)	0.007(2)
Zr-Zr/Y	10.8	3.57(1)	0.011(1)	10.8	3.58(1)	0.011(1)	10.8	3.58(1)	0.011(1)	10.8	3.58(1)	0.011(1)
Zr-Nd	1.2	3.83(8)	0.008(8)	1.2	3.83(9)	0.009(9)	1.2	3.9(1)	0.01(1)	1.2	3.83(9)	0.008(9)
Zr-O2	22	4.37(1)	0.03(1)	22	4.37(7)	0.03(2)	22	4.38(6)	0.03(1)	22	4.38(6)	0.03(1)

	$Nd_{0.15}Y_{0.15}Zr_{0.70}O_{1.85}$						$Nd_{0.25}Y_{0.05}Zr_{0.70}O_{1.85}$					
	As synthesized			Annealed 1400 °C			As Synthesized			Annealed 1400 °C		
	S_o^2 =0.88(9), ΔE =-4(1) eV			S_o^2 =0.90(8), ΔE =-3(1) eV			S_o^2 =0.9(1), ΔE =-4(1) eV			S_o^2 =0.88(9), ΔE =-4(1) eV		
	R_{fit}= 0.026			R_{fit}= 0.026			R_{fit}= 0.037			R_{fit}= 0.028		
	CN	R(Å)	σ^2	CN	R(Å)	σ^2	CN	R(Å)	σ^2	CN	R(Å)	σ^2
Zr-O	7	2.16(1)	0.007(1)	7	2.16(1)	0.007(2)	7	2.15(1)	0.007(1)	7	2.16(1)	0.007(1)
Zr-Zr/Y	10.5	3.56(1)	0.011(1)	10.5	3.56(1)	0.012(1)	9	3.55(1)	0.011(2)	9	3.55(1)	0.011(2)
Zr-Nd	1.5	3.9(1)	0.01(1)	1.5	3.8(1)	0.01(2)	3	3.75(5)	0.013(7)	3	3.77(6)	0.014(9)
Zr-O2	22	4.39(7)	0.04(2)	22	4.36(7)	0.04(2)	22	4.40(6)	0.04(2)	22	4.40(6)	0.04(2)

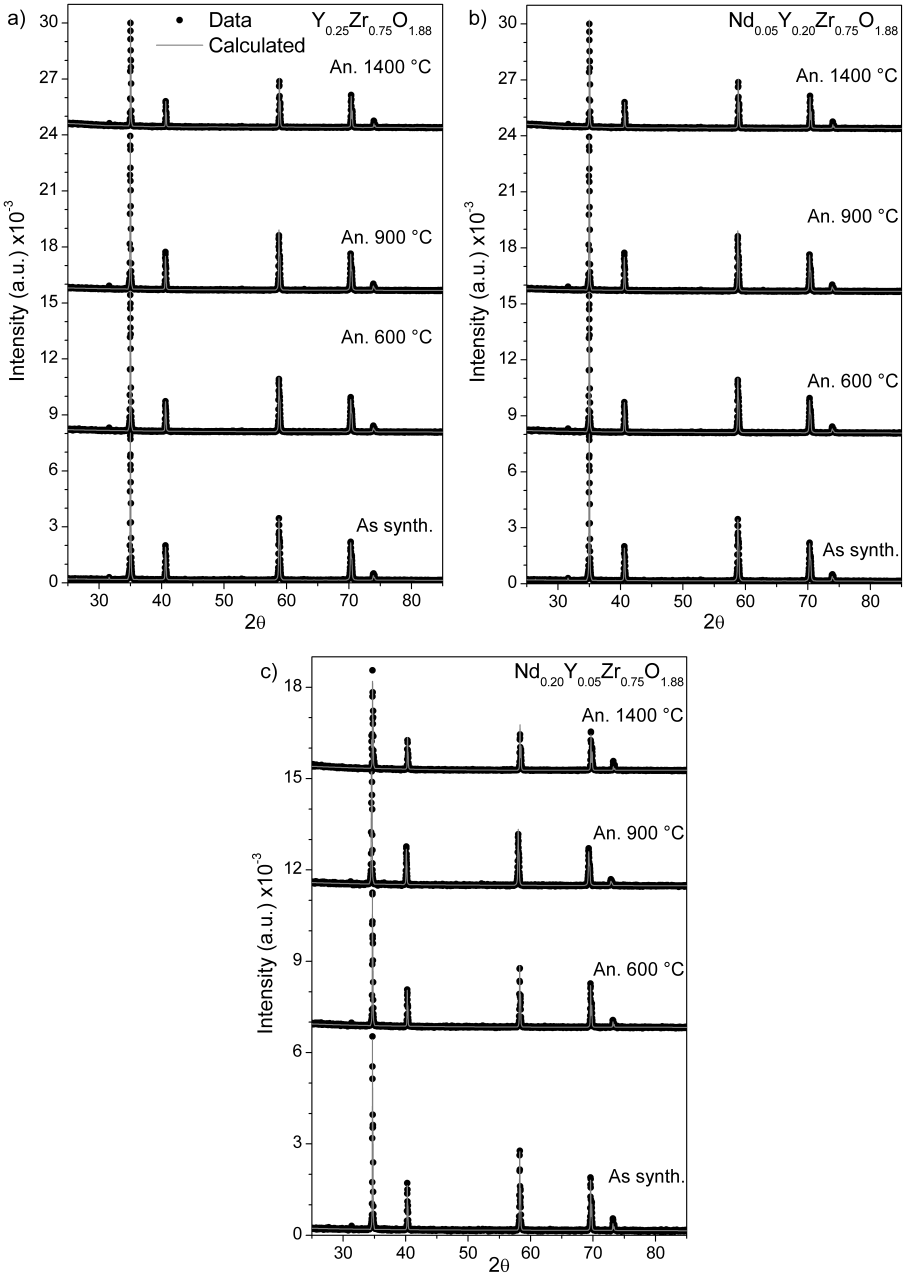

Figure B.1: Powder XRD patterns from the synthesized and annealed (a) $Y_{0.25}Zr_{0.75}O_{1.88}$, (b) $Nd_{0.05}Y_{0.25}Zr_{0.75}O_{1.88}$, and (c) $Nd_{0.20}Y_{0.05}Zr_{0.75}O_{1.88}$ materials. The XRD pattern collected from $Nd_{0.20}Y_{0.05}Zr_{0.75}O_{1.88}$ annealed at 1400 °C was collected using a Cu source, while the other patterns were collected using a Co source. The data collected using a Cu source was shifted to allow for better comparison to the data collected using the Co source.

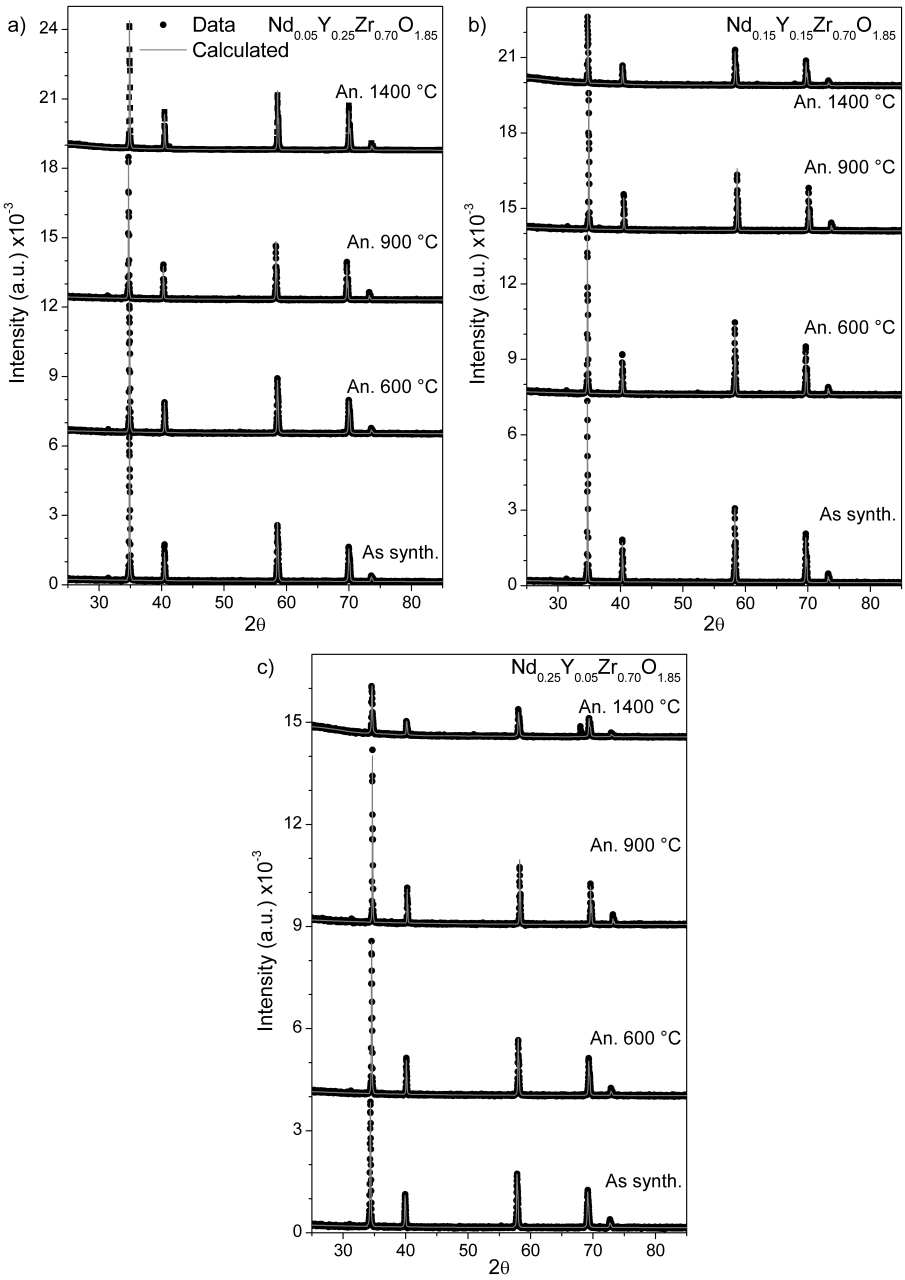

Figure B.2: Powder XRD patterns from the synthesized and annealed (a) $Nd_{0.05}Y_{0.25}Zr_{0.70}O_{1.85}$, (b) $Nd_{0.15}Y_{0.15}Zr_{0.70}O_{1.85}$, and (c) $Nd_{0.25}Y_{0.05}Zr_{0.70}O_{1.85}$ materials. The XRD pattern collected from materials annealed at 1400 °C were collected using a Cu source, while the other patterns were collected using a Co source. The data collected using a Cu source was shifted to allow for better comparison to the data collected using the Co source).

Table B.3: Summary of Y K-edge EXAFS Results

$Nd_{0.05}Y_{0.20}Zr_{0.75}O_{1.88}$	As synthesized S_o^2 =0.9(1), ΔE =-3(1) eV R_{fit}= 0.023			Annealed 900 °C S_o^2 =0.9(1), ΔE =-3(1) eV R_{fit}= 0.027			Annealed 1400 °C S_o^2 =0.82(9), ΔE =-2.9(9) eV R_{fit}= 0.021		
	CN	R(Å)	σ^2	CN	R(Å)	σ^2	CN	R(Å)	σ^2
Y-O	8	2.33(1)	0.008(2)	8	2.33(1)	0.008(1)	8	2.33(1)	0.007(2)
Y-Zr/Y	10	3.67(1)	0.005(2)	10	3.67(1)	0.005(1)	10	3.65(1)	0.005(2)
Y-Nd	2	3.40(2)	0.002(2)	2	3.40(2)	0.001(1)	2	3.39(2)	0.001(2)
Y-O2	22	4.38(6)	0.02(1)	22	4.38(7)	0.03(1)	22	4.36(6)	0.021(9)

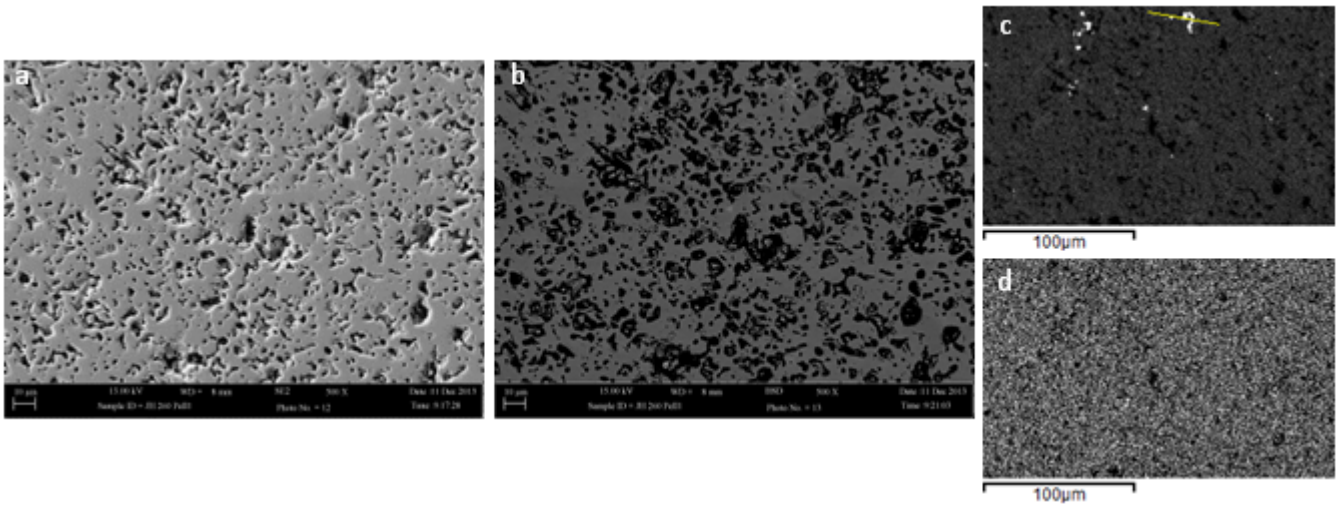

Figure B.3: The (a) SE and (b) BSE scanning electron micrographs and (c) Nd and (d) Zr EDS maps of the surface of the as-synthesized $Nd_{0.10}Y_{0.10}Zr_{0.80}O_{1.90}$ pellet are presented.

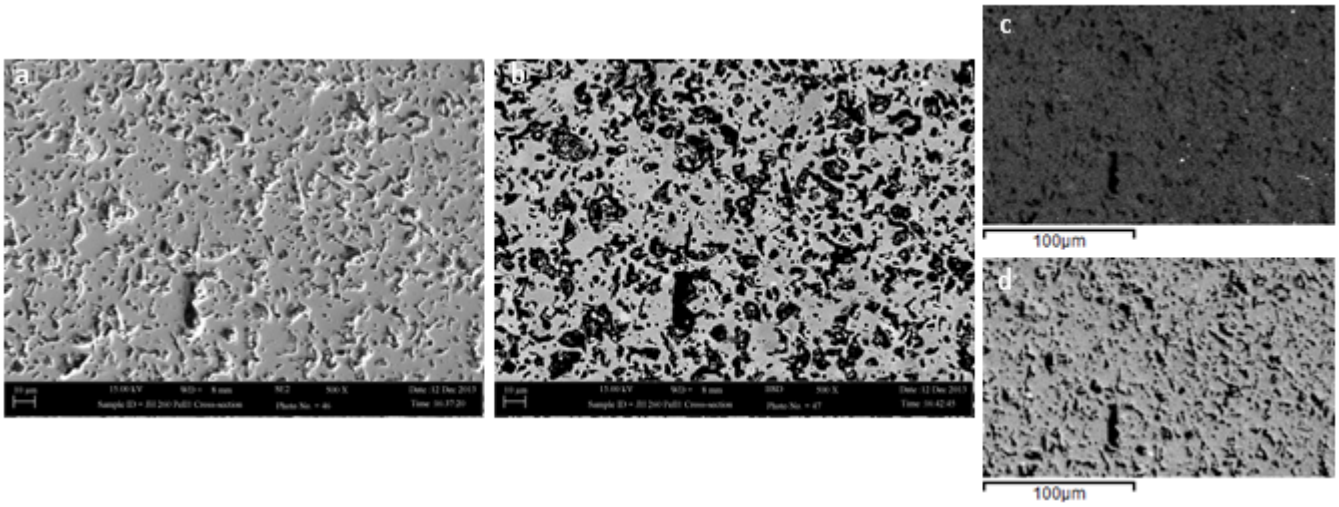

Figure B.4: The (a) SE and (b) BSE scanning electron micrographs and (c) Nd and (d) Zr EDS maps of the cross-section of the as-synthesized $Nd_{0.10}Y_{0.10}Zr_{0.80}O_{1.90}$ pellet are presented.

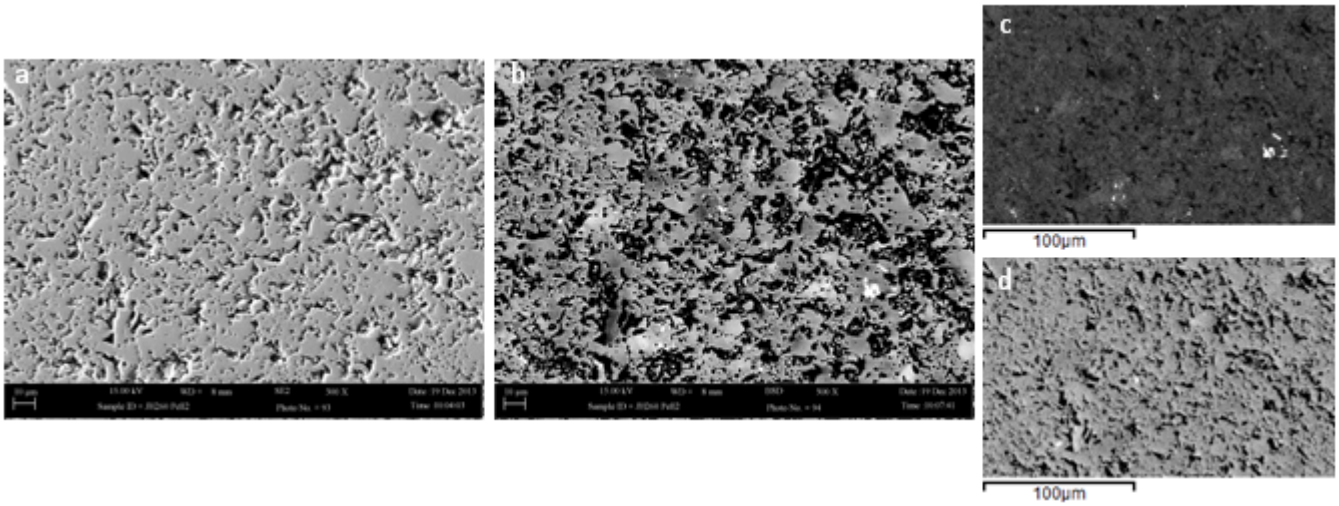

Figure B.5: The (a) SE and (b) BSE scanning electron micrographs and (c) Nd and (d) Zr EDS maps of the $Nd_{0.10}Y_{0.10}Zr_{0.80}O_{1.90}$ material annealed at 1400 °C are presented.

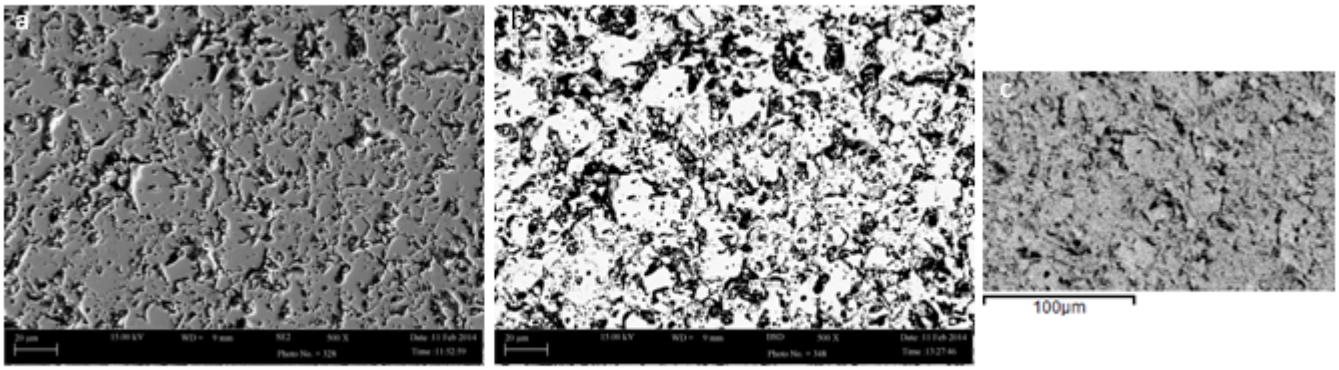

Figure B.6: The (a) SE and (b) BSE scanning electron micrographs and (c) Zr EDS maps of the as synthesized $Y_{0.25}Zr_{0.75}O_{1.88}$ material are presented.

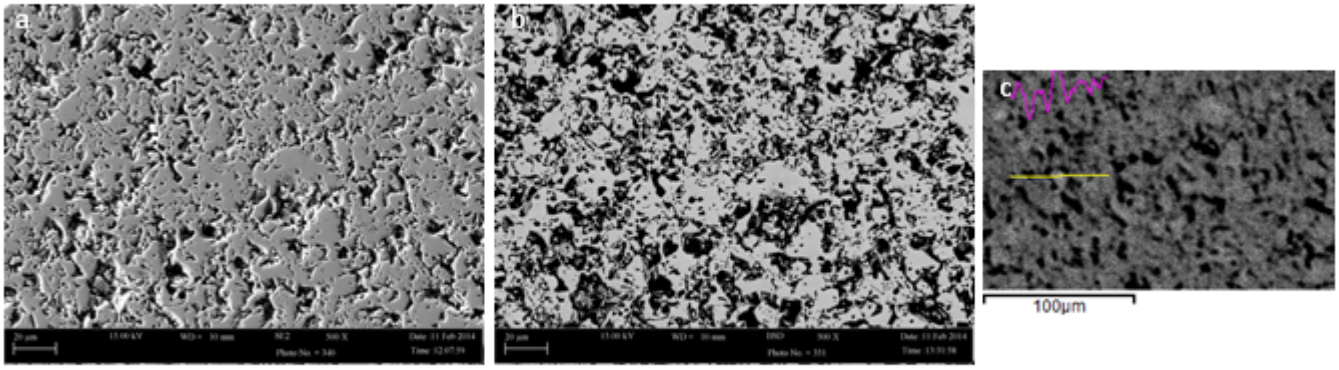

Figure B.7: The (a) SE and (b) BSE scanning electron micrographs and (c) Zr EDS maps of the $Y_{0.25}Zr_{0.75}O_{1.88}$ material annealed at 1400 °C are presented.

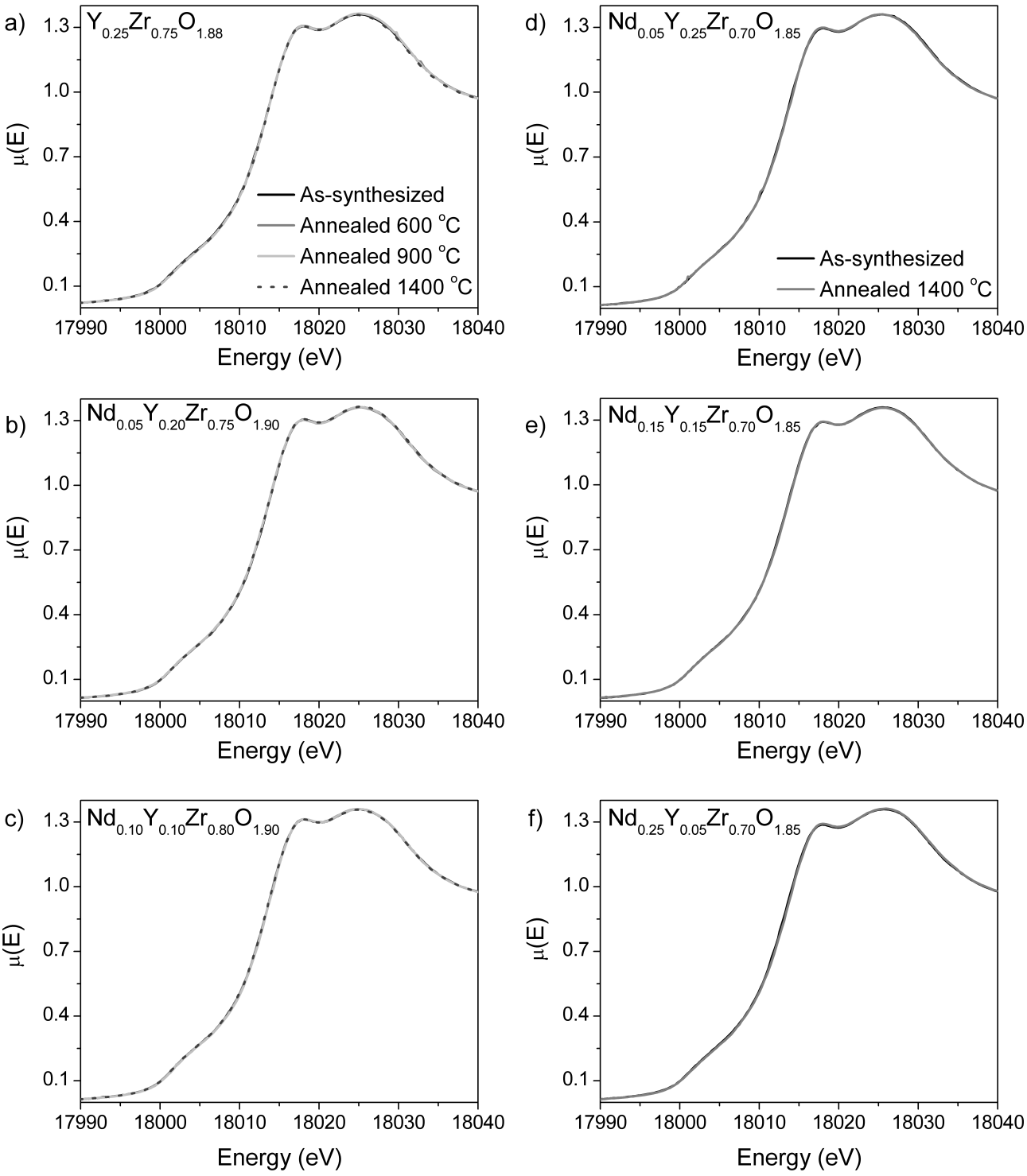

Figure B.8: The Zr K-edge XANES spectra from as-synthesized and annealed (a) $Y_{0.25}Zr_{0.75}O_{1.88}$, (b) $Nd_{0.05}Y_{0.25}Zr_{0.75}O_{1.88}$, (c) $Nd_{0.10}Y_{0.10}Zr_{0.80}O_{1.90}$, (d) $Nd_{0.05}Y_{0.25}Zr_{0.70}O_{1.85}$, (e) $Nd_{0.15}Y_{0.15}Zr_{0.70}O_{1.85}$, and (f) $Nd_{0.25}Y_{0.05}Zr_{0.70}O_{1.85}$ materials are presented.

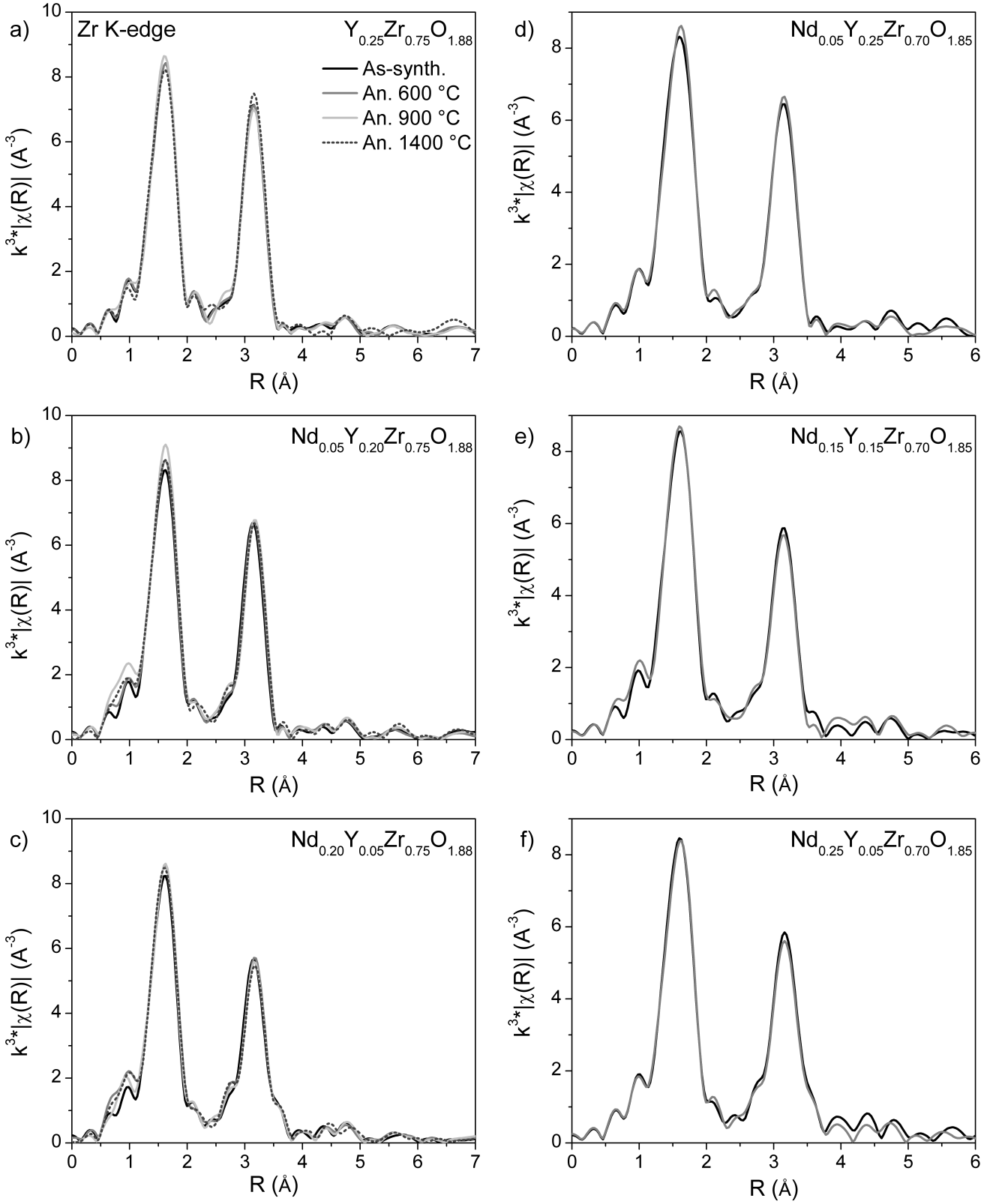

Figure B.9: The Zr K-edge EXAFS spectra from as-synthesized and annealed (a) $Y_{0.25}Zr_{0.75}O_{1.88}$, (b) $Nd_{0.05}Y_{0.20}Zr_{0.75}O_{1.88}$, (c) $Nd_{0.20}Y_{0.05}Zr_{0.75}O_{1.88}$, (d) $Nd_{0.05}Y_{0.25}Zr_{0.70}O_{1.85}$, (e) $Nd_{0.15}Y_{0.15}Zr_{0.70}O_{1.85}$, and (f) $Nd_{0.25}Y_{0.05}Zr_{0.70}O_{1.85}$ materials are presented.

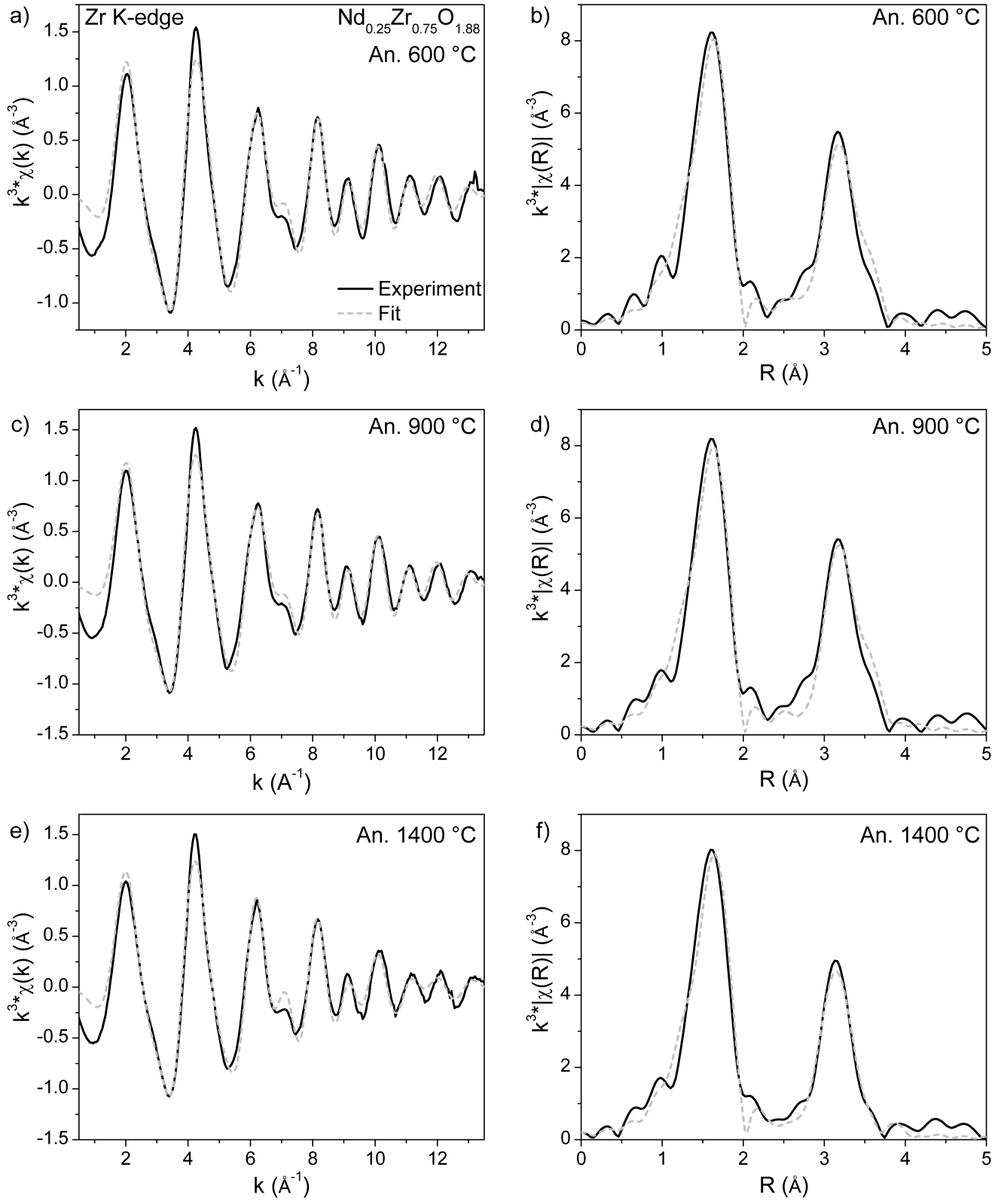

Figure B.10: The fits of the Zr K-edge EXAFS spectra from $Nd_{0.25}Zr_{0.75}O_{1.88}$ materials annealed at (a,b) 600 °C, (c,d) 900 °C, and (e,f) 1400 °C are plotted in (a,c,e) k-space and R-space (b,d,f).

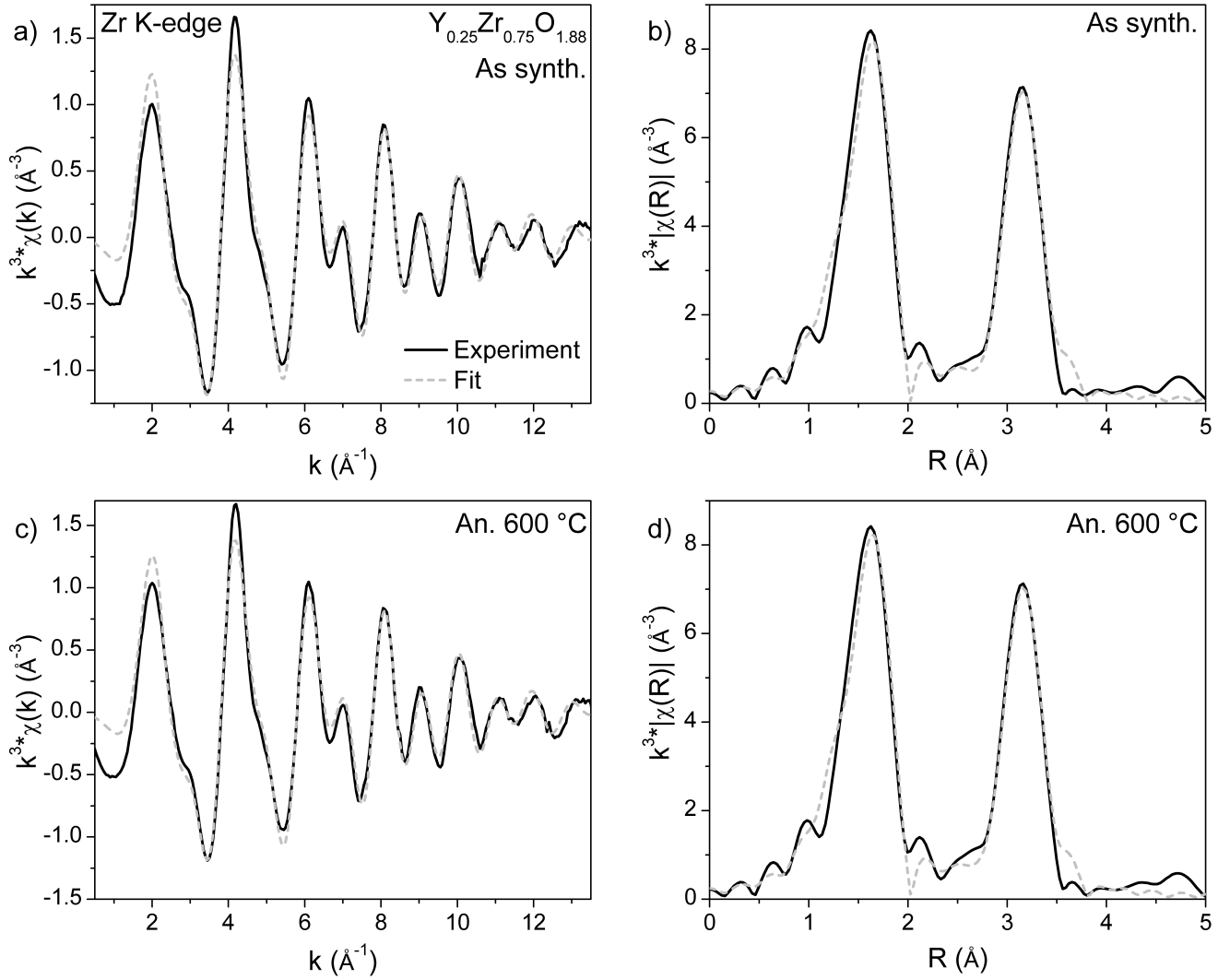

Figure B.11: The fits of the Zr K-edge EXAFS spectra from as-synthesized (a,b) $Y_{0.25}Zr_{0.75}O_{1.88}$ and (c,d) $Y_{0.25}Zr_{0.75}O_{1.88}$ annealed at 600 °C in (a,c) k-space and R-space (b,d).

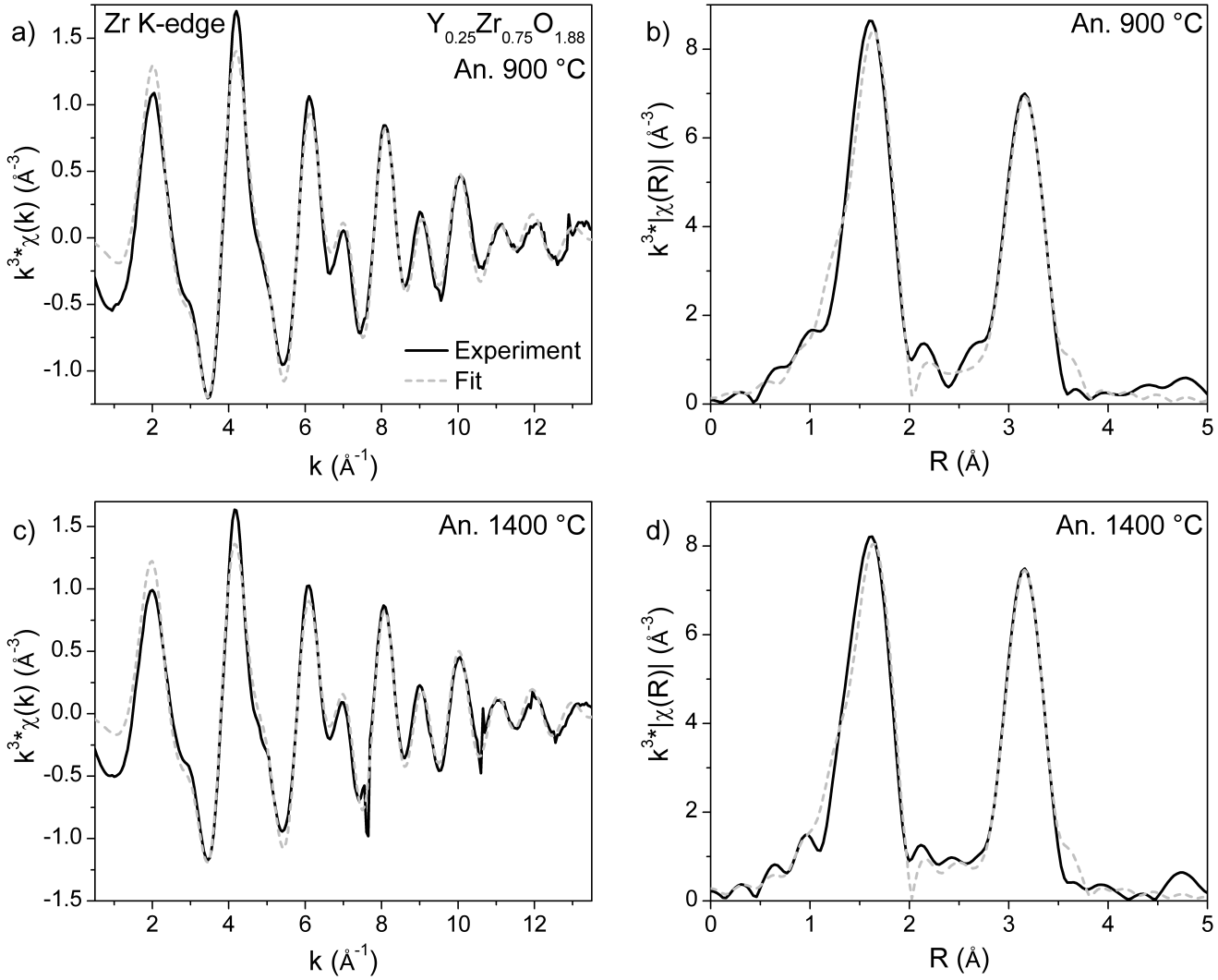

Figure B.12: The fits of the Zr K-edge EXAFS spectra from (a,b) $Y_{0.25}Zr_{0.75}O_{1.88}$ annealed at 900 °C and (c,d) $Y_{0.25}Zr_{0.75}O_{1.88}$ annealed at 1400 °C in (a,c) k-space and R-space (b,d).

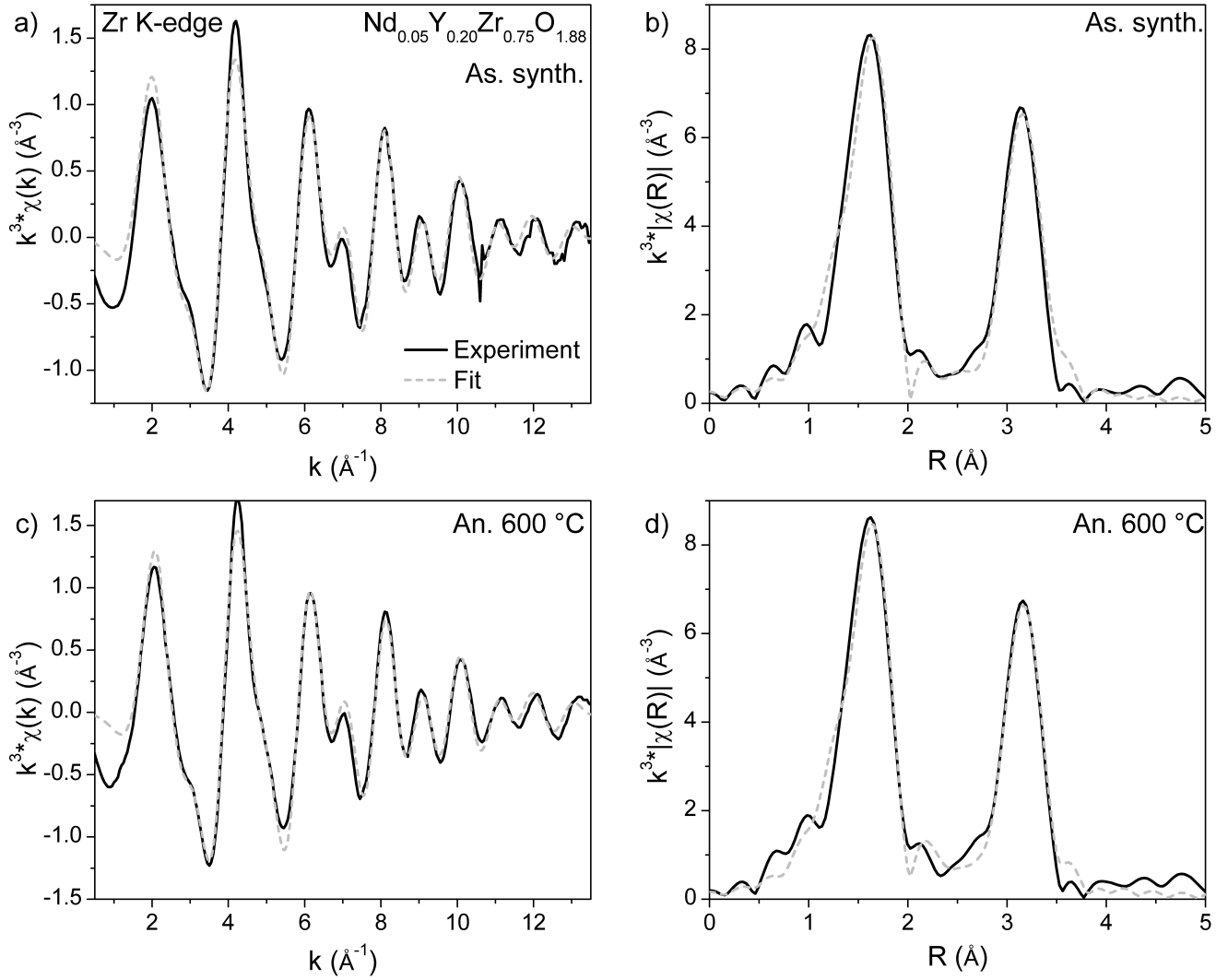

Figure B.13: The fits of the Zr K-edge EXAFS spectra from as-synthesized (a,b) $Nd_{0.05}Y_{0.20}Zr_{0.75}O_{1.88}$ and (c,d) $Nd_{0.05}Y_{0.20}Zr_{0.75}O_{1.88}$ annealed at 600 °C in (a,c) k-space and R-space (b,d).

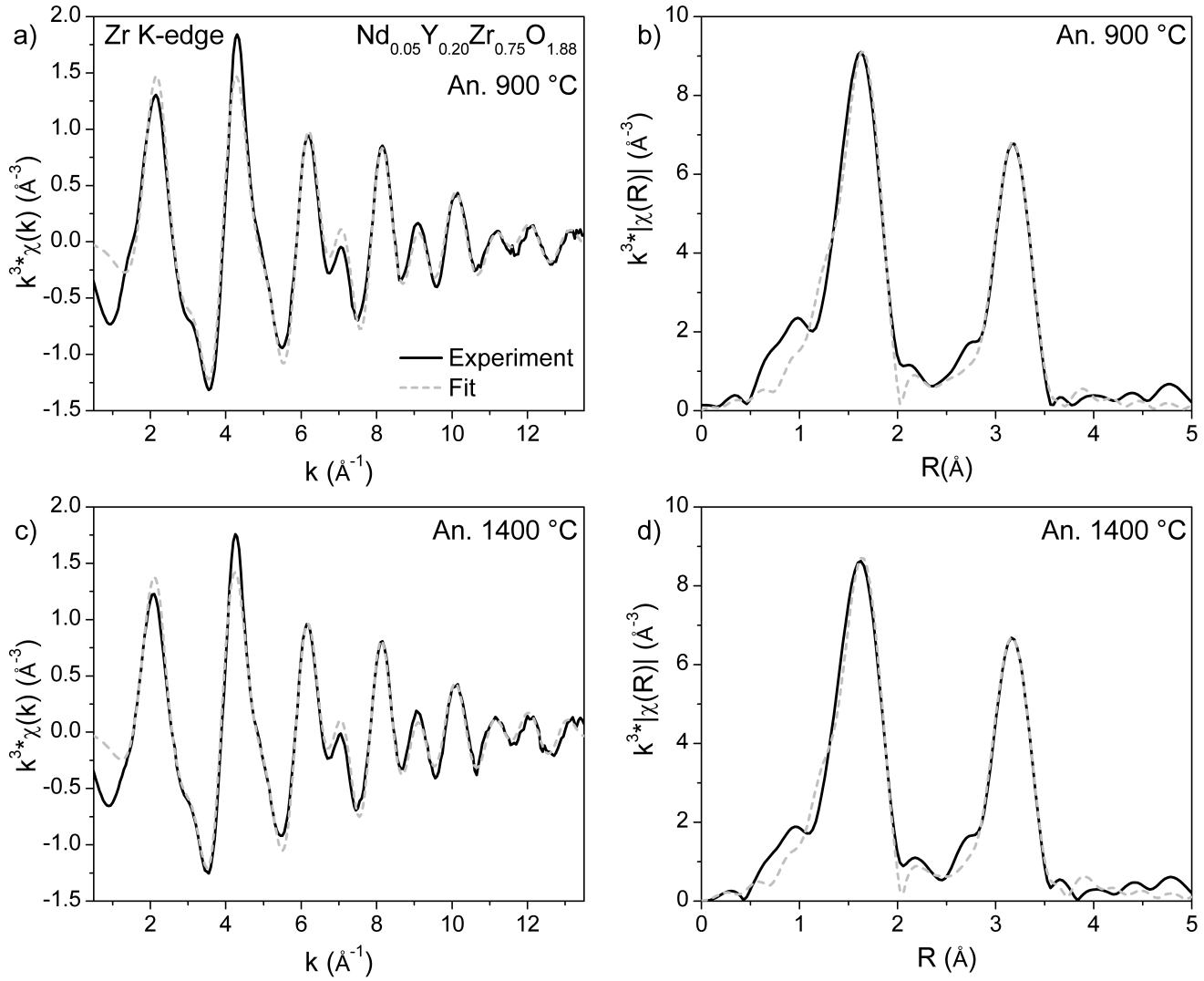

Figure B.14: The fits of the Zr K-edge EXAFS spectra from (a,b) $Nd_{0.05}Y_{0.20}Zr_{0.75}O_{1.88}$ annealed at 900 °C and (c,d) $Nd_{0.05}Y_{0.20}Zr_{0.75}O_{1.88}$ annealed at 1400 °C in (a,c) k-space and R-space (b,d).

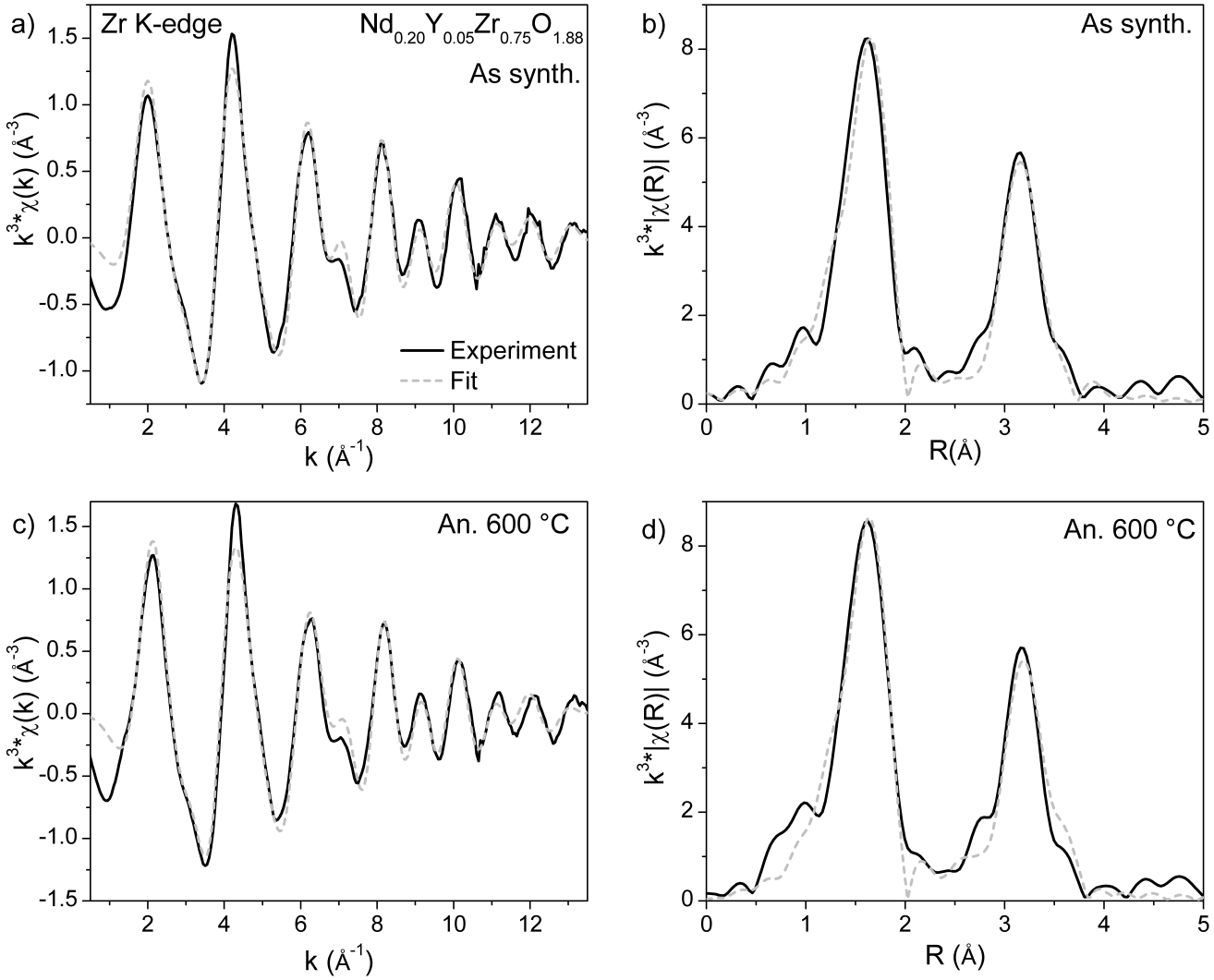

Figure B.15: The fits of the Zr K-edge EXAFS spectra from as-synthesized (a,b) $Nd_{0.20}Y_{0.05}Zr_{0.75}O_{1.88}$ and (c,d) $Nd_{0.20}Y_{0.05}Zr_{0.75}O_{1.88}$ annealed at 600 °C in (a,c) k-space and R-space (b,d).

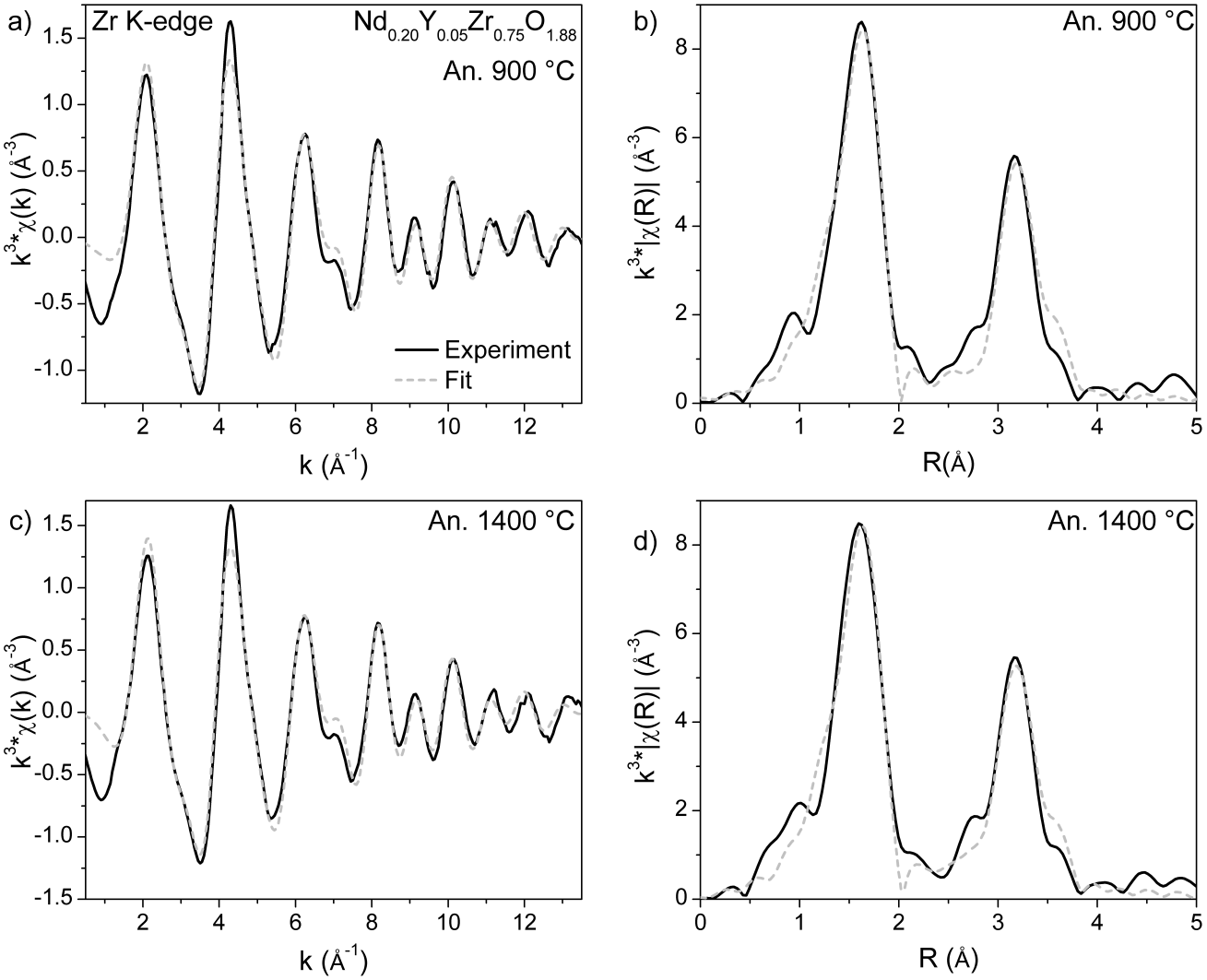

Figure B.16: The fits of the Zr K-edge EXAFS spectra from (a,b) $Nd_{0.20}Y_{0.05}Zr_{0.75}O_{1.88}$ annealed at 900 °C and (c,d) $Nd_{0.20}Y_{0.05}Zr_{0.75}O_{1.88}$ annealed at 1400 °C in (a,c) k-space and R-space (b,d).

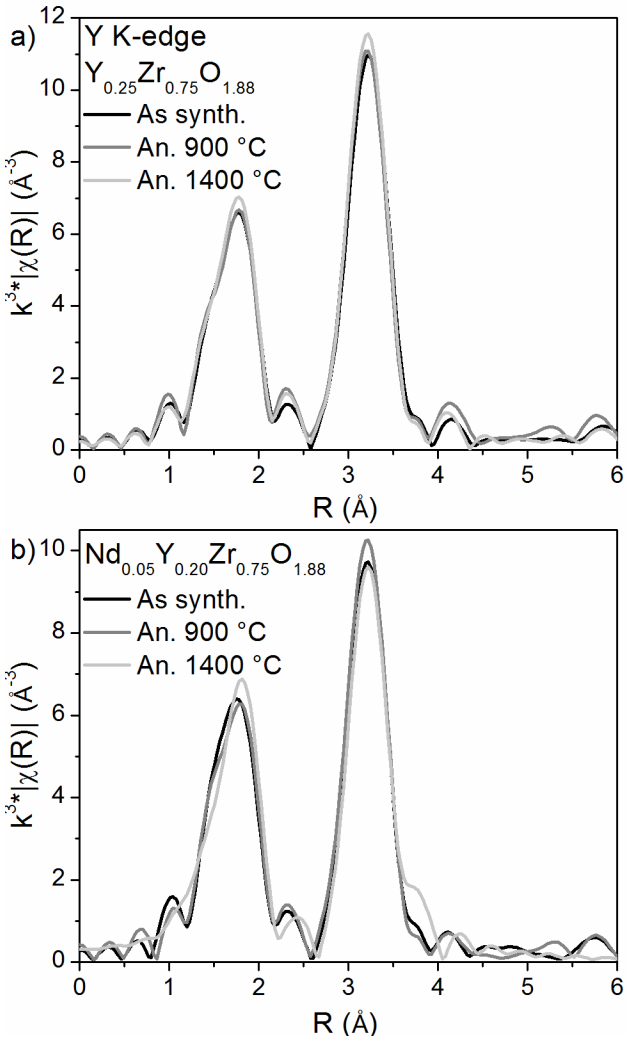

Figure B.17: The magnitude of the Fourier Transform of the Y K-edge EXAFS spectra from the as-synthesized and annealed (a) $Y_{0.25}Zr_{0.75}O_{1.88}$, and (b) $Nd_{0.05}Y_{0.20}Zr_{0.75}O_{1.88}$ materials

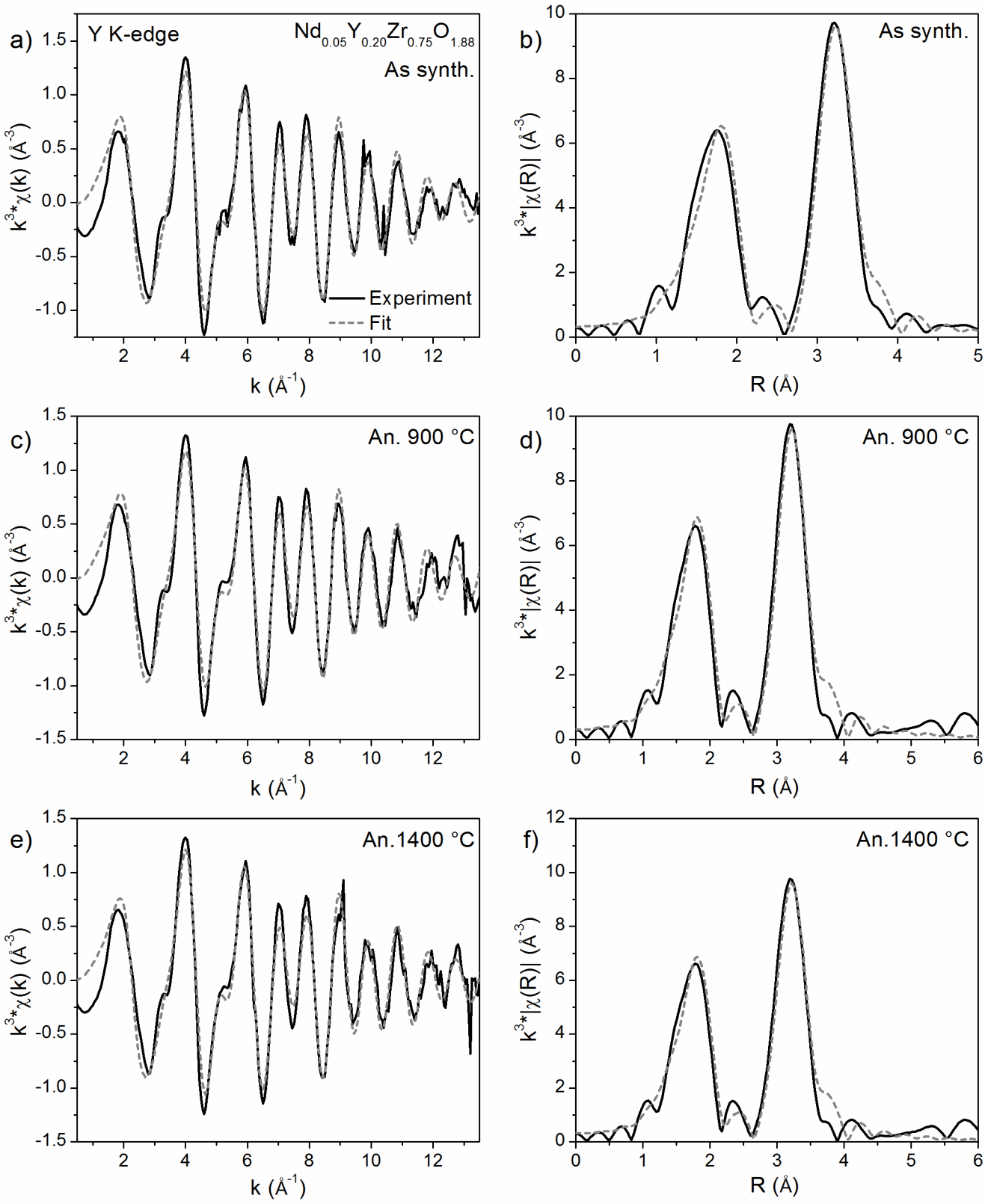

Figure B.18: The fits of the Y K-edge EXAFS spectra from (a,b) as-synthesized $Nd_{0.05}Y_{0.20}Zr_{0.75}O_{1.88}$ material, $Nd_{0.05}Y_{0.20}Zr_{0.75}O_{1.88}$ annealed at (c,d) 900 °C, and (e,f) 1400 °C are plotted in (a,c,e) k-space and R-space (b,d,f).

Appendix C

Supporting Tables and Figures for Chapter 4[1]

[1] A version of this paper has been accepted by the *Canadian Journal of Chemistry* for publication as an article by J.R. Hayes and A.P. Grosvenor.

Table C.1: Zr K-edge EXAFS Fit Results

$Y_{0.25}Zr_{0.75}O_{1.88}$									
	As synthesized			Annealed 1400 °C			Annealed 1500 °C		
	S_o^2 = 0.91(7), ΔE = -3.6(8)			S_o^2 = 0.93(8), ΔE = -4.0(9)			S_o^2 = 0.93(8), ΔE = -3.7(9)		
	R_{fit} = 0.0212			R_{fit} = 0.0237			R_{fit} = 0.0218		
	CN	R (Å)	σ^2	CN	R (Å)	σ^2	CN	R (Å)	σ^2
Zr - O	7	2.16(1)	0.008(1)	7	2.16(1)	0.008(2)	7	2.16(1)	0.007(2)
Zr - Zr/Y	12	3.57(1)	0.012(1)	10.2	3.571(9)	0.010(1)	10.2	3.572(9)	0.010(1)
Zr - O2	24	4.34(5)	0.04(1)	24	4.31(6)	0.03(1)	24	4.32(5)	0.03(1)

$Nd_{0.05}Y_{0.20}Zr_{0.75}O_{1.88}$									
	As synthesized			Annealed 1400 °C			Annealed 1500 °C		
	S_o^2 = 1.1(1), ΔE = -5(2)			S_o^2 = 0.88(9), ΔE = -3.8(9)			S_o^2 = 1.04(9), ΔE = -5(1)		
	R_{fit} = 0.0215			R_{fit} = 0.0224			R_{fit} = 0.0129		
	CN	R (Å)	σ^2	CN	R (Å)	σ^2	CN	R (Å)	σ^2
Zr - O	7	2.16(1)	0.010(2)	7	2.16(1)	0.007(2)	7	2.16(1)	0.009(1)
Zr - Zr/Y	11.4	3.58(1)	0.014(1)	11.4	3.58(1)	0.011(1)	11	3.70(5)	0.008(6)
Zr - Nd	0.6	3.70(5)	0.005(5)	0.6	3.44(2)	0.04(4)	1	3.576(9)	0.011(1)
Zr - O2	24	4.22(7)	0.031(8)	24	4.33(5)	0.03(1)	24	4.23(5)	0.025(6)

$Nd_{0.10}Y_{0.15}Zr_{0.75}O_{1.88}$									
	As synthesized			Annealed 1400 °C			Annealed 1500 °C		
	S_o^2 = 0.84(8), ΔE = -3.4(9)			S_o^2 = 0.88(9), ΔE = -3.6(9)			S_o^2 = 0.87(8), ΔE = -3.6(9)		
	R_{fit} = 0.0246			R_{fit} = 0.0256			R_{fit} = 0.0217		
	CN	R (Å)	σ^2	CN	R (Å)	σ^2	CN	R (Å)	σ^2
Zr - O	7	2.16(1)	0.007(2)	7	2.16(1)	0.007(2)	7	2.162(9)	0.007(2)
Zr - Zr/Y	10.8	3.59(2)	0.011(2)	10.8	3.58(1)	0.010(1)	10	3.58(1)	0.009(1)
Zr - Nd	1.2	3.348(7)	0.007(6)	1.2	3.348(9)	0.02(3)	2	3.348(6)	0.03(3)
Zr - O2	24	4.34(6)	0.03(1)	24	4.33(5)	0.026(9)	24	4.33(5)	0.026(8)

$Nd_{0.25}Zr_{0.75}O_{1.88}$									
	As synthesized			Annealed 1400 °C			Annealed 1500 °C		
	S_o^2 = 0.84(8), ΔE = -3.4(9)			S_o^2 = 0.88(9), ΔE = -3.6(9)			S_o^2 = 0.87(8), ΔE = -3.6(9)		
	R_{fit} = 0.0246			R_{fit} = 0.0256			R_{fit} = 0.0217		
	CN	R (Å)	σ^2	CN	R (Å)	σ^2	CN	R (Å)	σ^2
Zr - O	7	2.16(1)	0.008(2)	7	2.16(1)	0.007(2)	7	2.16(1)	0.007(2)
Zr - Zr/Y	9	3.58(2)	0.013(2)	9	3.54(1)	0.011(1)	9	3.55(1)	0.011(1)
Zr - Nd	3	3.77(8)	0.02(1)	3	3.366(9)	0.04(4)	3	3.36(1)	0.04(4)
Zr - O2	24	4.38(6)	0.04(2)	24	4.39(5)	0.04(1)	24	4.40(5)	0.03(1)

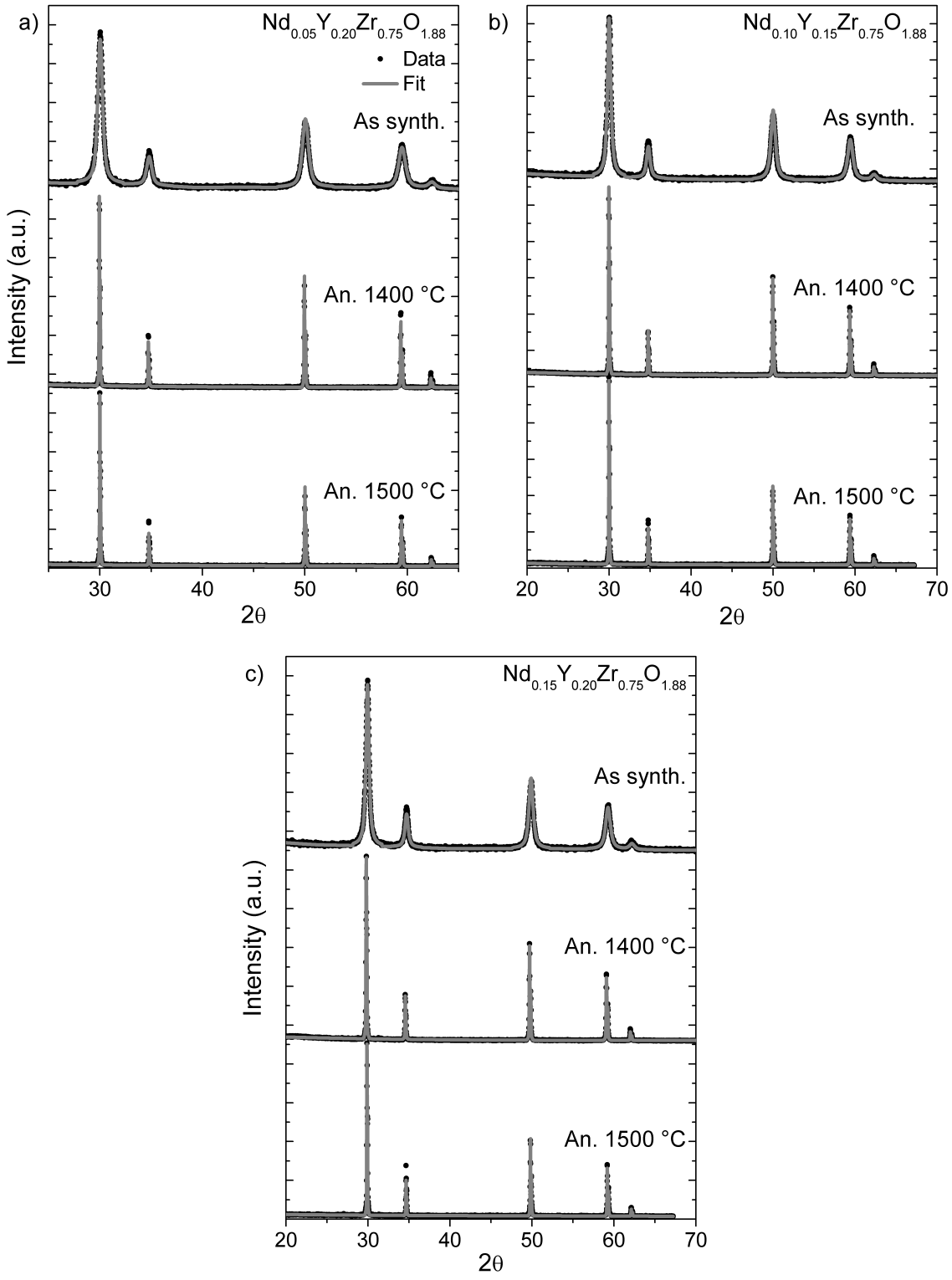

Figure C.1: Powder XRD patterns from the as-synthesized and high-temperature annealed (a) $Nd_{0.05}Y_{0.20}Zr_{0.75}O_{1.88}$, (b) $Nd_{0.10}Y_{0.15}Zr_{0.75}O_{1.88}$, and (c) $Nd_{0.15}Y_{0.10}Zr_{0.75}O_{1.88}$ materials made by the co-precipitation method.

Table C.2: Y K-edge EXAFS Fit Results

$Y_{0.25}Zr_{0.75}O_{1.88}$									
	As synthesized			Annealed 1400 °C			Annealed 1500 °C		
	S_o^2 = 0.8(1), ΔE = -4(2)			S_o^2 = 1.0(1), ΔE = -4(2)			S_o^2 = 0.9(2), ΔE = -5(2)		
	R_{fit} = 0.047			R_{fit} = 0.046			R_{fit} = 0.046		
	CN	R (Å)	σ^2	CN	R (Å)	σ^2	CN	R (Å)	σ^2
Zr - O	8	2.32(2)	0.009(3)	8	2.32(2)	0.010(4)	8	2.32(1)	0.010(4)
Zr - Zr/Y	12	3.63(1)	0.009(1)	12	3.63(1)	0.008(1)	12	3.63(1)	0.007(1)
Zr - O2	24	4.6(1)	0.05(4)	24	4.7(3)	0.06(6)	24	4.7(3)	0.06(6)
$Nd_{0.10}Y_{0.15}Zr_{0.75}O_{1.88}$									
	As synthesized			Annealed 1400 °C			Annealed 1500 °C		
	S_o^2 = 0.8(1), ΔE = -4(2)			S_o^2 = 0.9(1), ΔE = -4(1)			S_o^2 = 0.9(1), ΔE = -4(1)		
	R_{fit} = 0.025			R_{fit} = 0.022			R_{fit} = 0.025		
	CN	R (Å)	σ^2	CN	R (Å)	σ^2	CN	R (Å)	σ^2
Zr - O	8	2.33(2)	0.008(2)	8	2.32(2)	0.008(2)	8	2.32(2)	0.008(3)
Zr - Zr/Y	10.8	3.65(1)	0.007(2)	10	3.65(1)	0.005(2)	10.8	3.65(1)	0.006(2)
Zr - Nd	1.2	3.40(3)	0.000(3)	2	3.39(2)	0.002(2)	1.2	3.39(3)	0.000(3)
Zr - O2	24	4.6(1)	0.05(3)	24	4.74(3)	0.08(7)	24	4.7(2)	0.06(5)

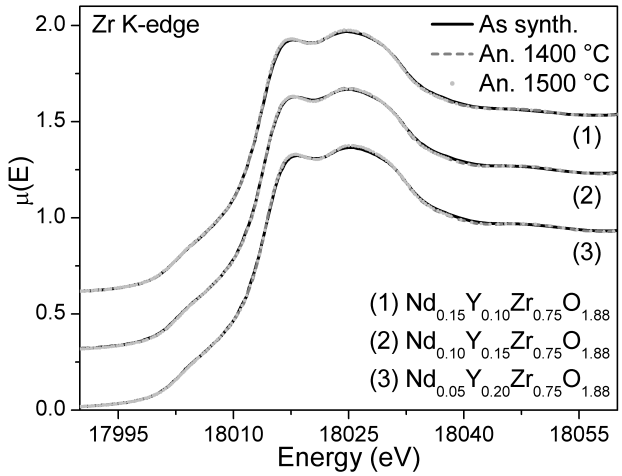

Figure C.2: The Zr K-edge XANES spectra from the as-synthesized and high-temperature annealed $Nd_xY_{0.25-x}Zr_{0.75}O_{1.88}$ materials made by a co-precipitation method are compared.

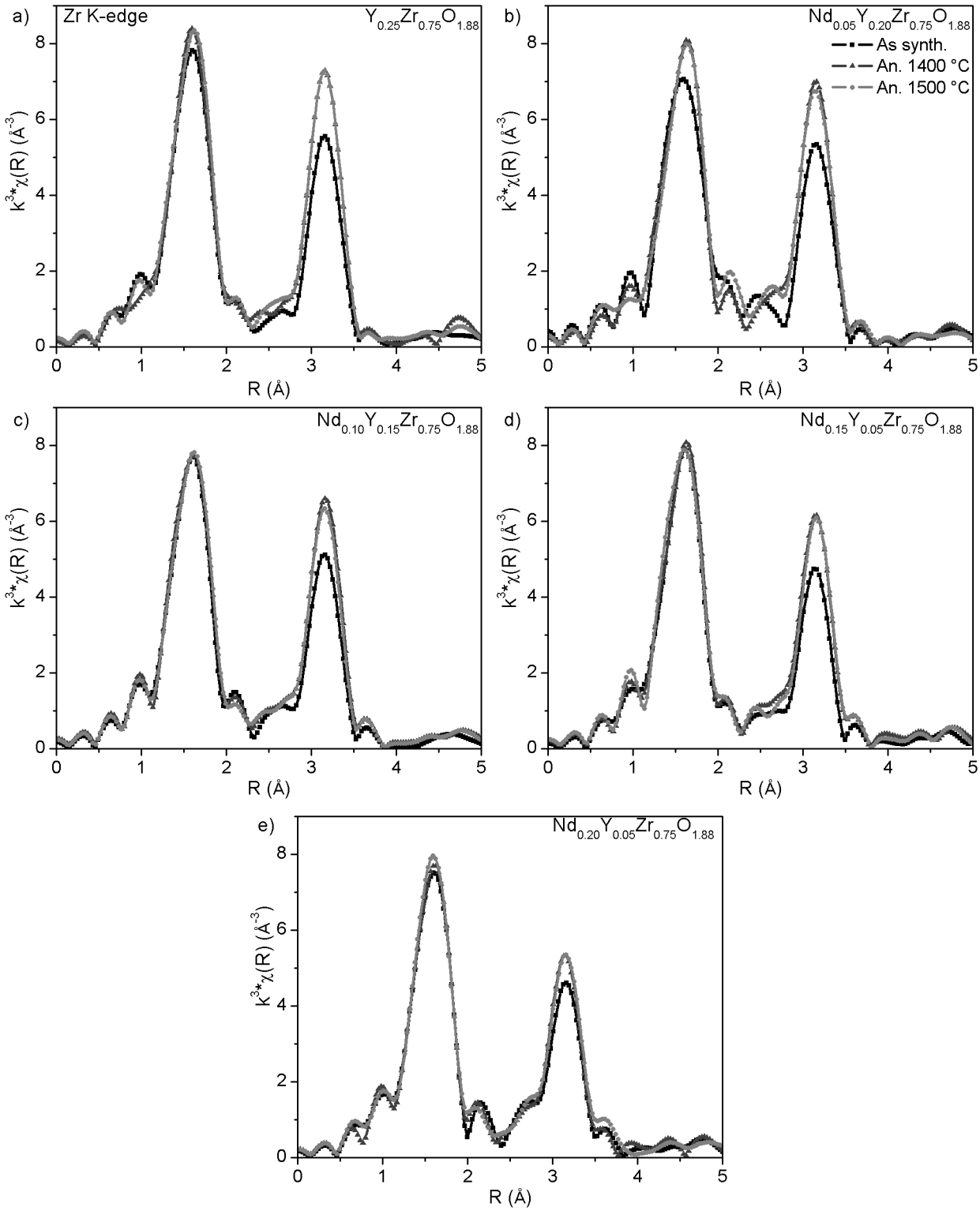

Figure C.3: The spectra Zr K-edge EXAFS spectra from as-synthesized and high-temperature annealed (a) $Y_{0.25}Zr_{0.75}O_{1.88}$, (b) $Nd_{0.20}Y_{0.05}Zr_{0.75}O_{1.88}$, (c) $Nd_{0.10}Y_{0.15}Zr_{0.75}O_{1.88}$, (d) $Nd_{0.15}Y_{0.05}Zr_{0.75}O_{1.88}$, and (e) $Nd_{0.20}Y_{0.05}Zr_{0.75}O_{1.88}$ materials made by the co-precipitation synthetic method.

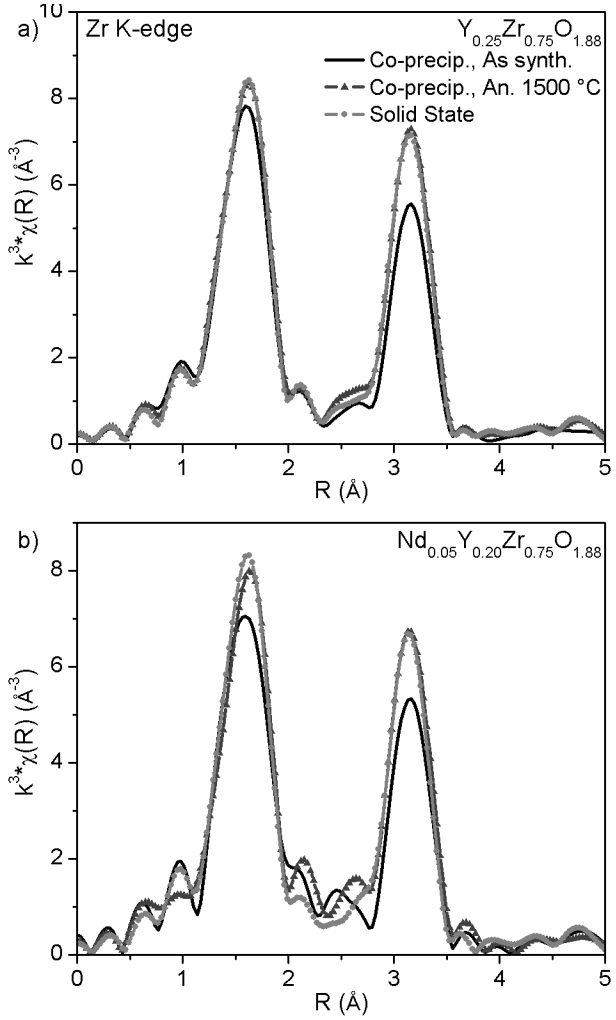

Figure C.4: The Fourier-transformed Zr K-edge EXAFS spectra from (a) $Y_{0.25}Zr_{0.75}O_{1.88}$ and (b) $Nd_{0.05}Y_{0.20}Zr_{0.75}O_{1.88}$ materials made by the co-precipitation and ceramic synthetic routes are compared.

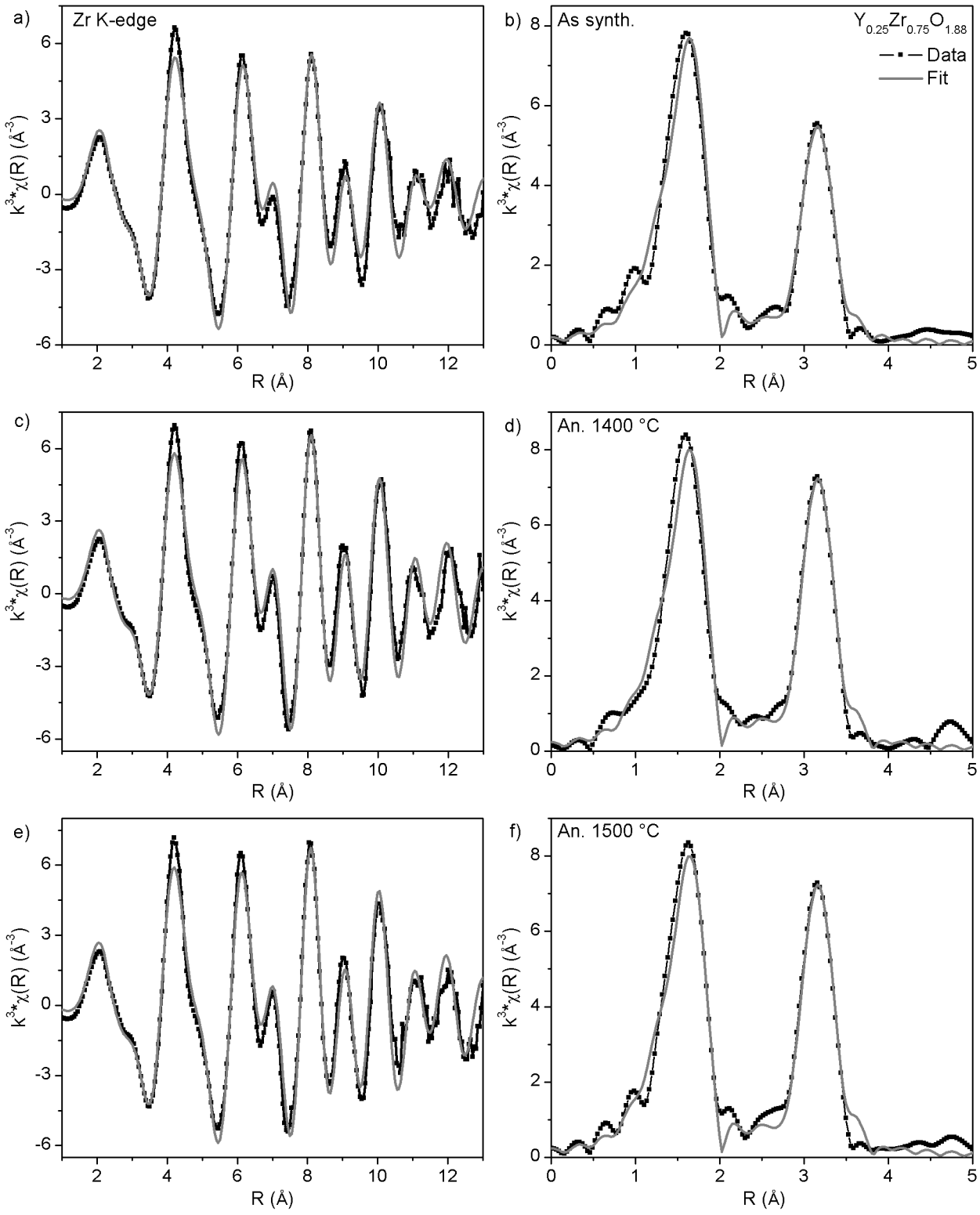

Figure C.5: The fits of the Zr K-edge EXAFS spectra from (a,b) as-synthesized $Y_{0.25}Zr_{0.75}O_{1.88}$ material, $Y_{0.25}Zr_{0.75}O_{1.88}$ annealed at (c,d) 1400 °C, and (e,f) 1500 °C are plotted in (a,c,e) R-space and k-space (b,d,f).

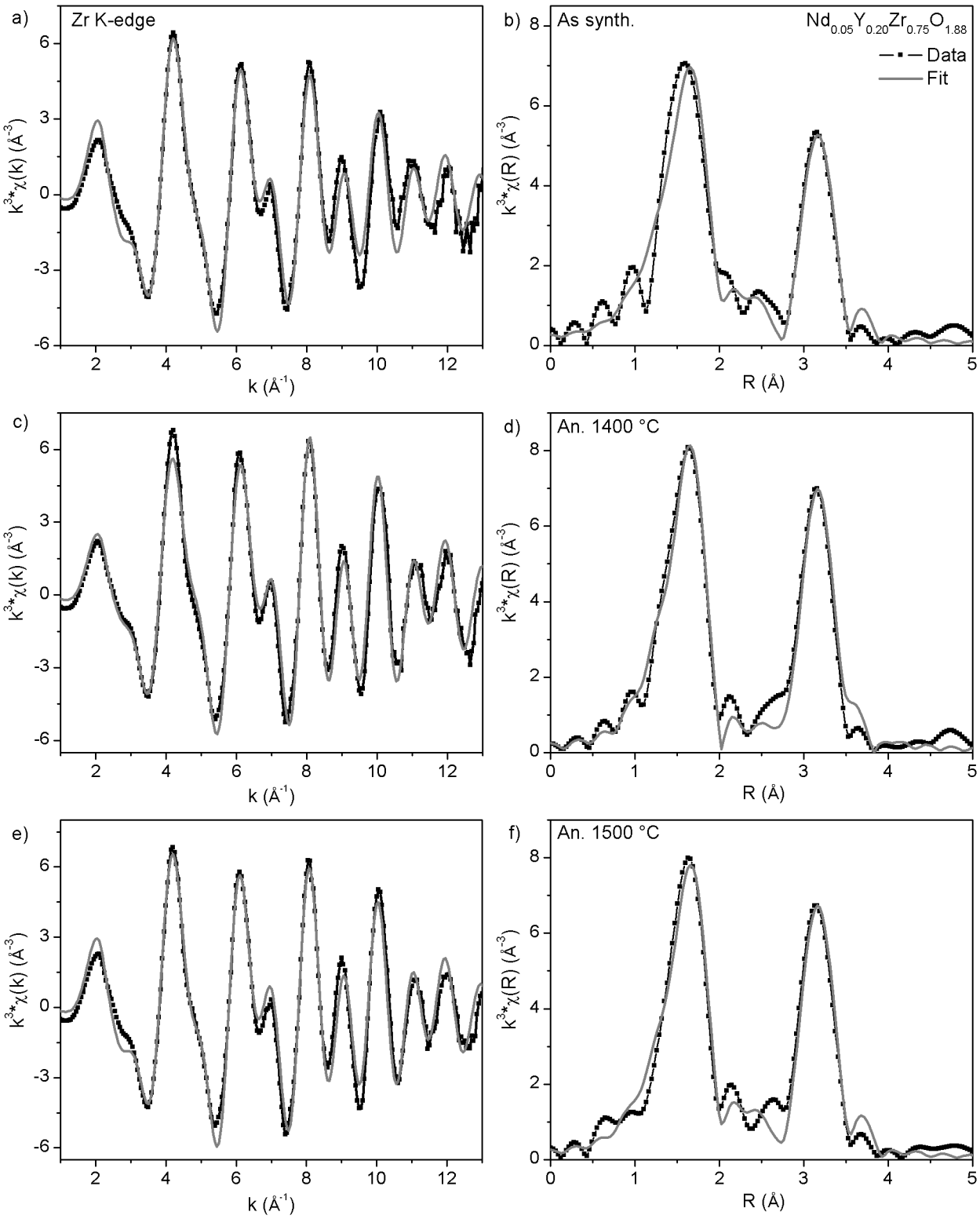

Figure C.6: The fits of the Zr K-edge EXAFS spectra from (a,b) as-synthesized $Nd_{0.05}Y_{0.20}Zr_{0.75}O_{1.88}$ material, $Nd_{0.05}Y_{0.20}Zr_{0.75}O_{1.88}$ annealed at (c,d) 1400 °C, and (e,f) 1500 °C are plotted in (a,c,e) R-space and k-space (b,d,f).

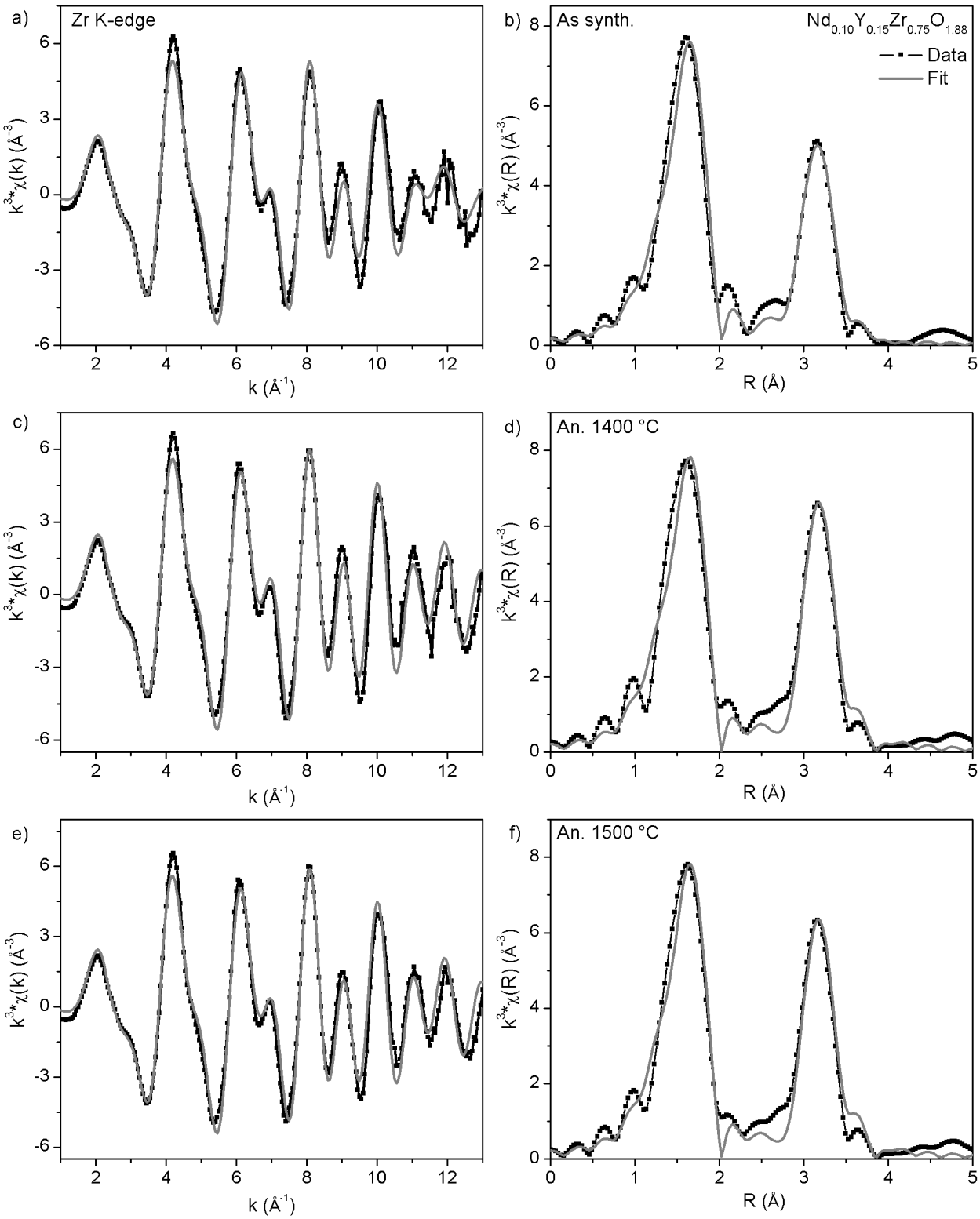

Figure C.7: The fits of the Zr K-edge EXAFS spectra from (a,b) as-synthesized $Nd_{0.10}Y_{0.15}Zr_{0.75}O_{1.88}$ material, $Nd_{0.10}Y_{0.15}Zr_{0.75}O_{1.88}$ annealed at (c,d) 1400 °C, and (e,f) 1500 °C are plotted in (a,c,e) R-space and k-space (b,d,f).

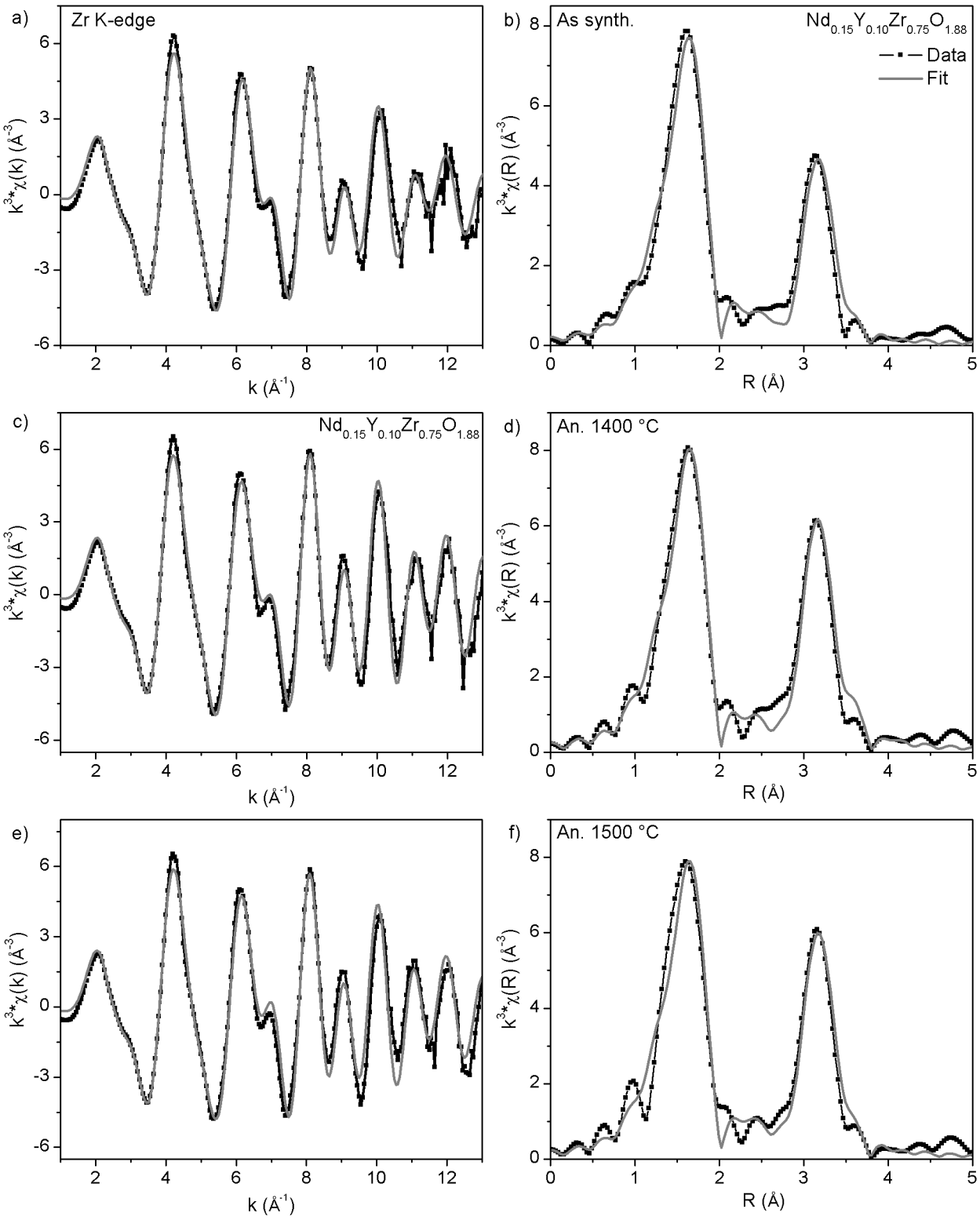

Figure C.8: The fits of the Zr K-edge EXAFS spectra from (a,b) as-synthesized $Nd_{0.15}Y_{0.10}Zr_{0.75}O_{1.88}$ material, $Nd_{0.15}Y_{0.10}Zr_{0.75}O_{1.88}$ annealed at (c,d) 1400 °C, and (e,f) 1500 °C are plotted in (a,c,e) R-space and k-space (b,d,f).

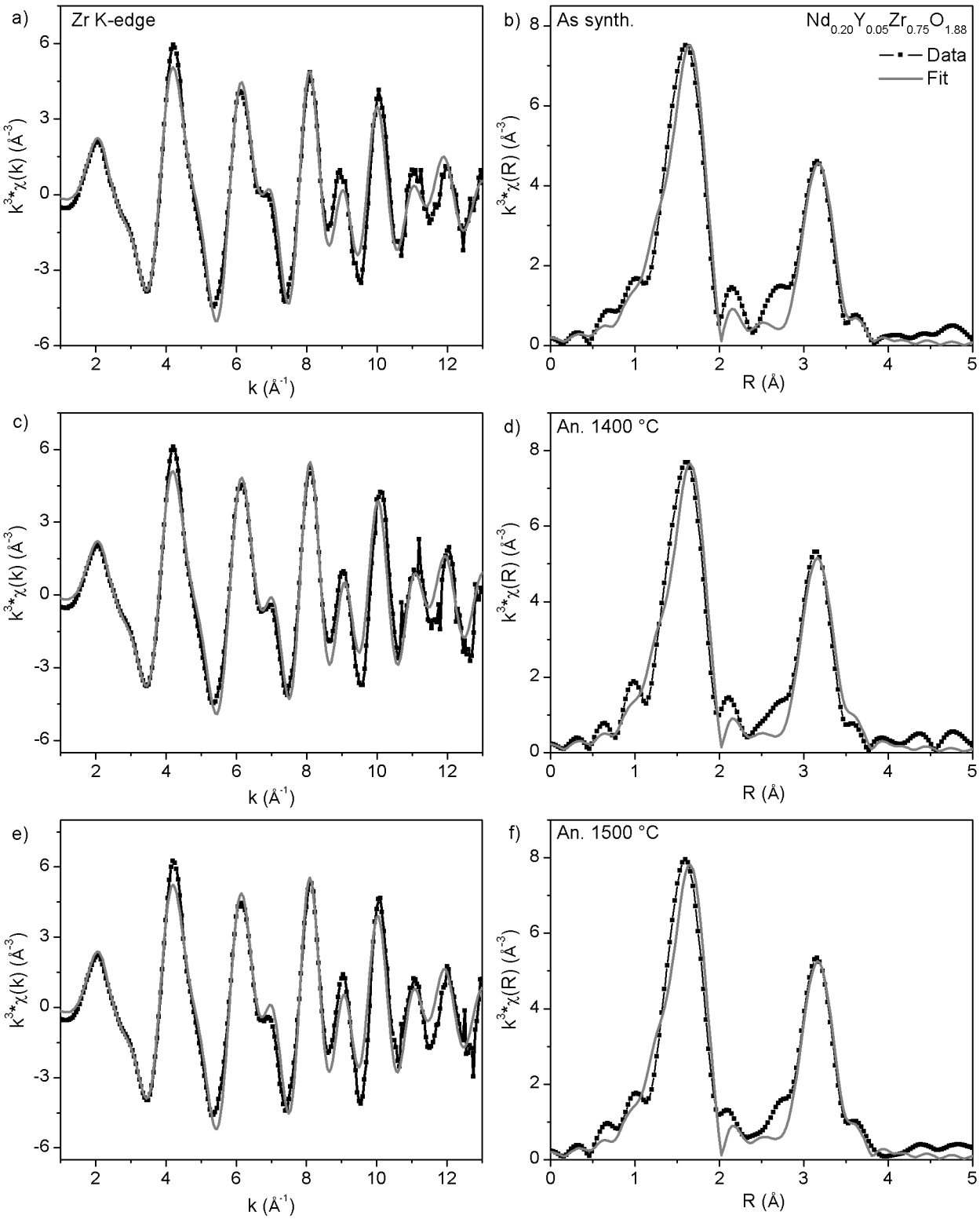

Figure C.9: The fits of the Zr K-edge EXAFS spectra from (a,b) as-synthesized $Nd_{0.20}Y_{0.05}Zr_{0.75}O_{1.88}$ material, $Nd_{0.20}Y_{0.05}Zr_{0.75}O_{1.88}$ annealed at (c,d) 1400 °C, and (e,f) 1500 °C are plotted in (a,c,e) R-space and k-space (b,d,f).

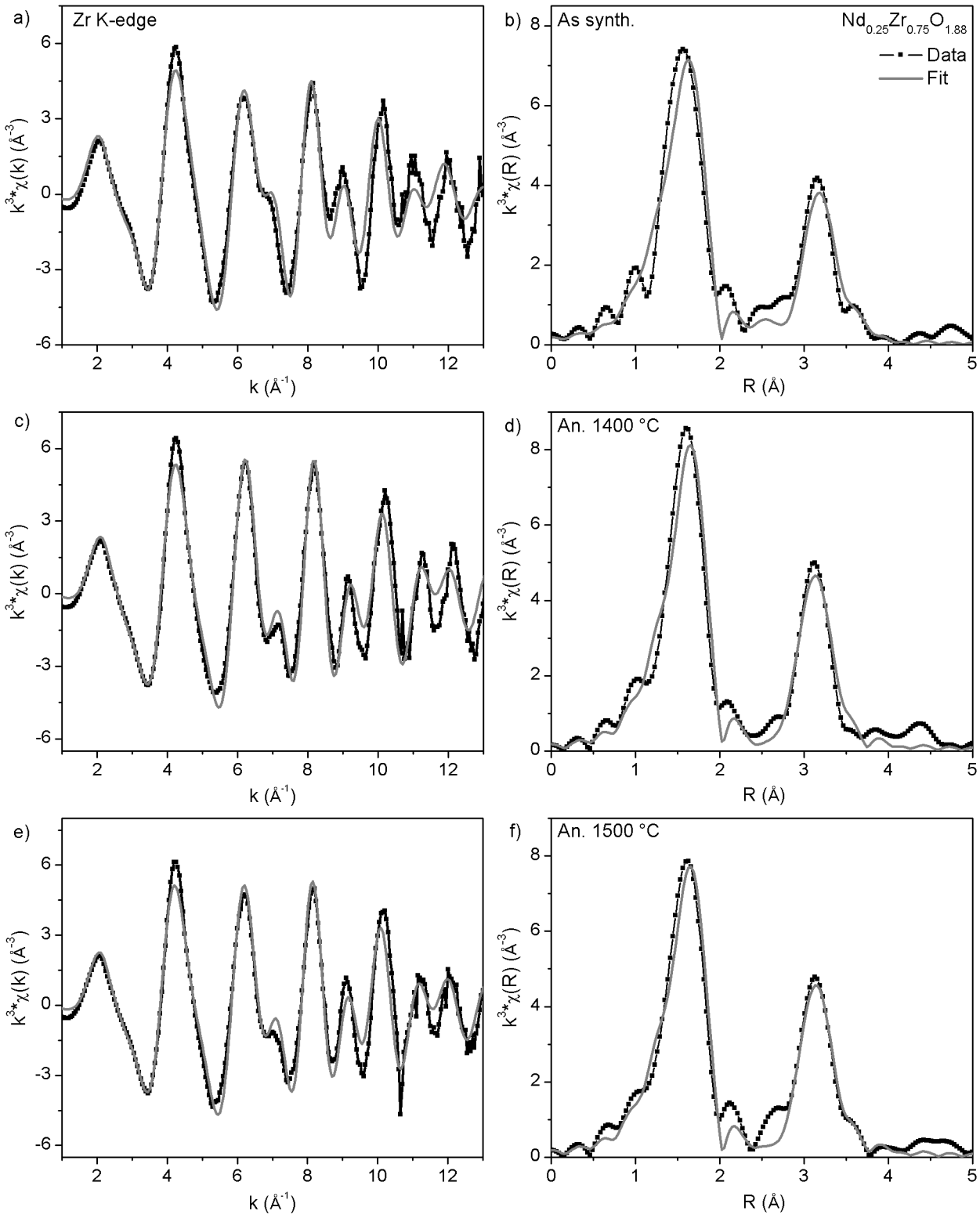

Figure C.10: The fits of the Zr K-edge EXAFS spectra from (a,b) as-synthesized $Nd_{0.25}Zr_{0.75}O_{1.88}$ material, $Nd_{0.25}Zr_{0.75}O_{1.88}$ annealed at (c,d) 1400 °C, and (e,f) 1500 °C are plotted in (a,c,e) R-space and k-space (b,d,f).

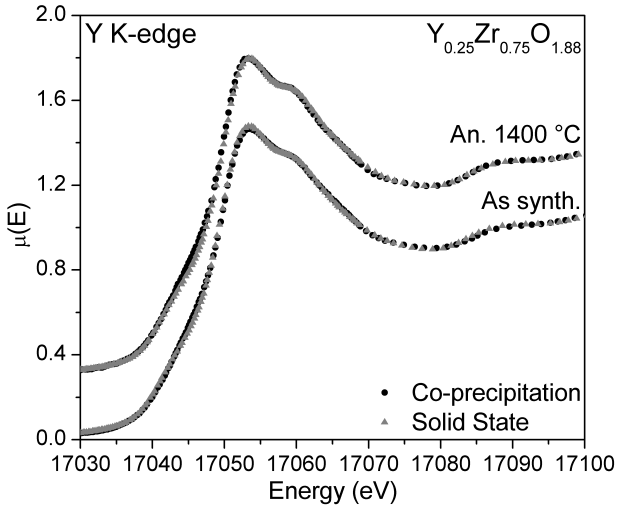

Figure C.11: Y K-edge XANES spectra from $Y_{0.25}Zr_{0.75}O_{1.88}$ as-synthesized materials and materials annealed at high temperature made by the co-precipitation and ceramic synthetic routes are compared.

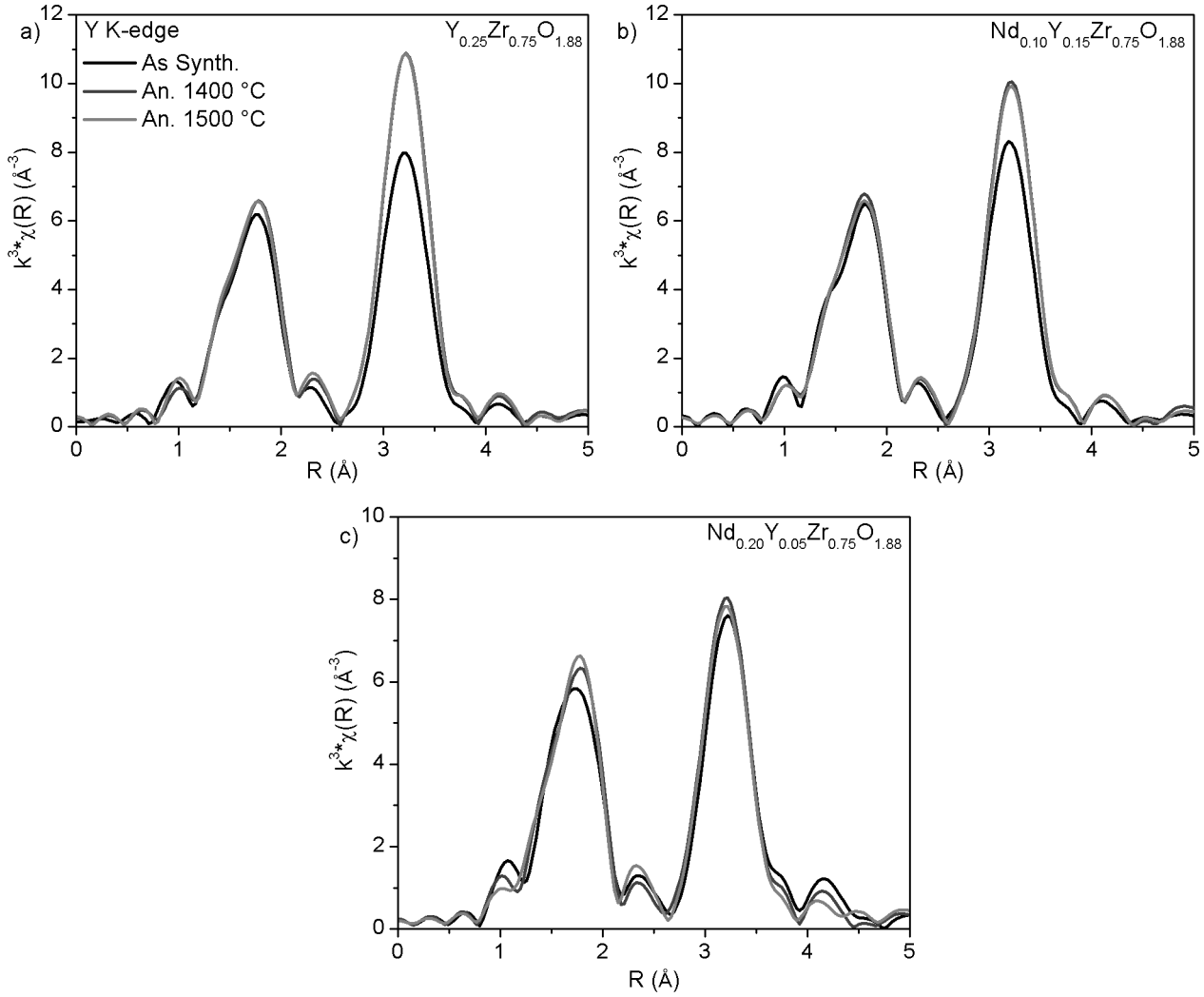

Figure C.12: Y K-edge EXAFS spectra from (a) $Y_{0.25}Zr_{0.75}O_{1.88}$, (b) $Nd_{0.10}Y_{0.15}Zr_{0.75}O_{1.88}$ and (c) $Nd_{0.20}Y_{0.05}Zr_{0.75}O_{1.88}$ as-synthesized materials and materials annealed at high temperature are compared.

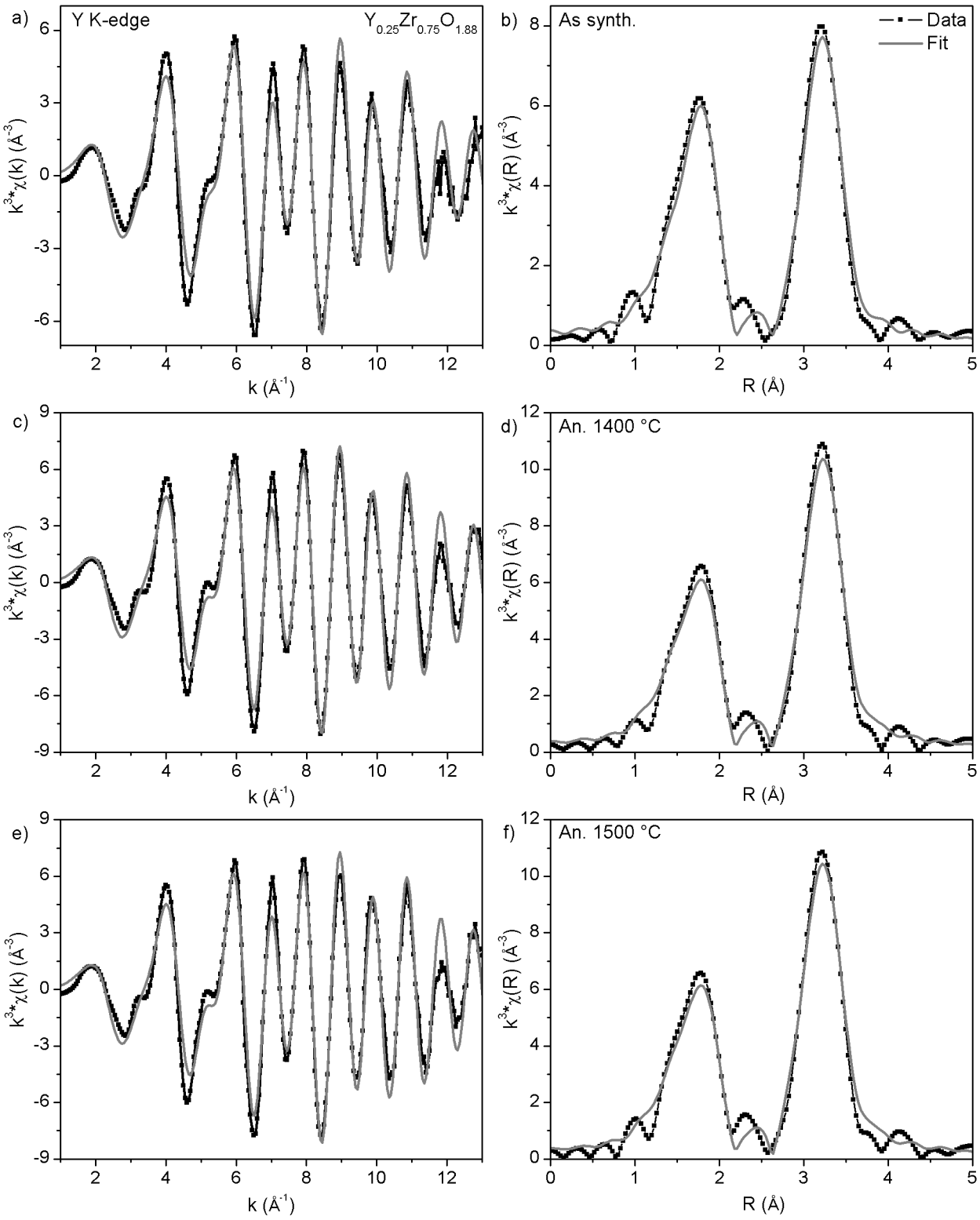

Figure C.13: The fits of the Y K-edge EXAFS spectra from (a,b) as-synthesized $Y_{0.25}Zr_{0.75}O_{1.88}$ material, $Y_{0.25}Zr_{0.75}O_{1.88}$ annealed at (c,d) 1400 °C, and (e,f) 1500 °C are plotted in (a,c,e) R-space and k-space (b,d,f).

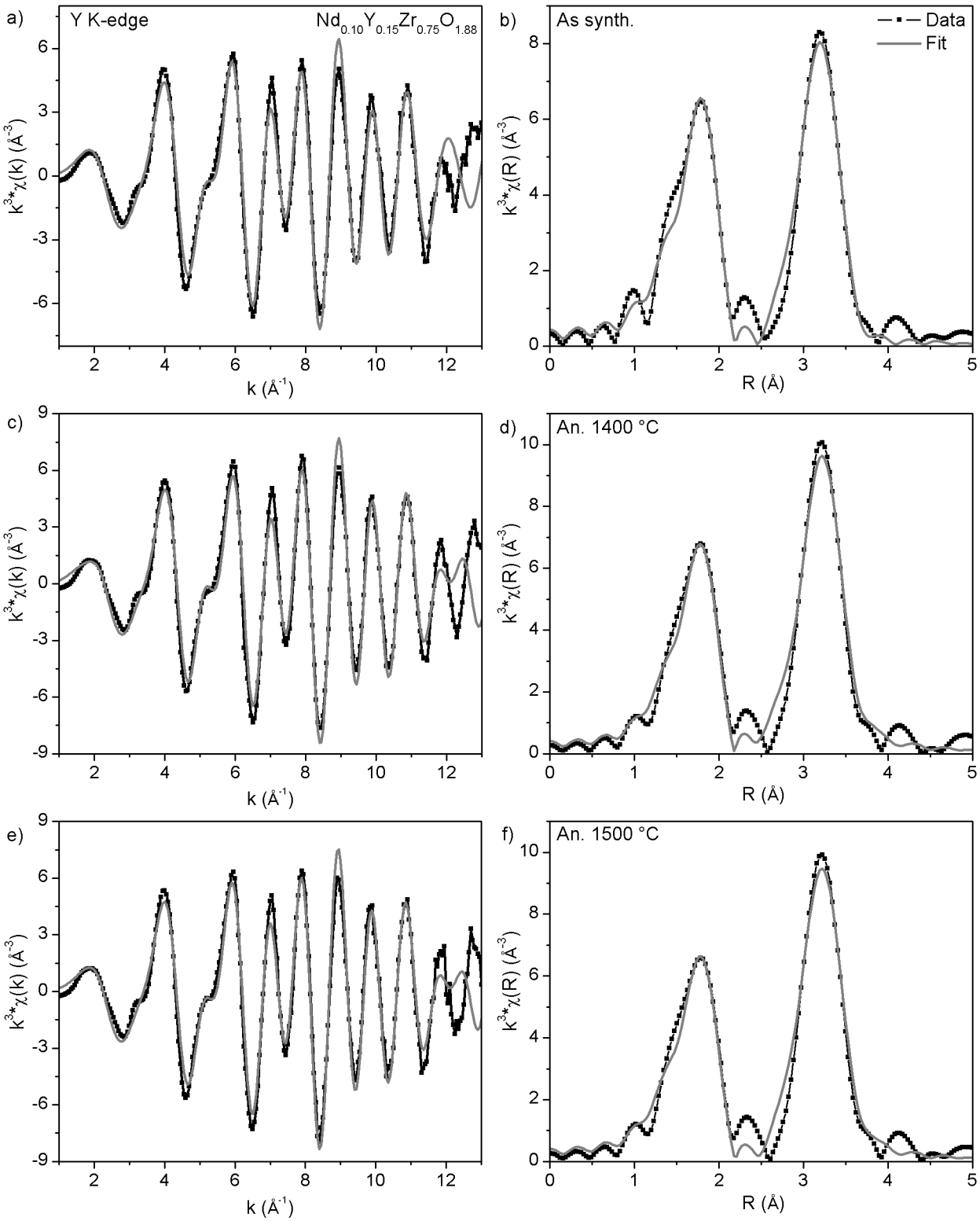

Figure C.14: The fits of the Y K-edge EXAFS spectra from (a,b) as-synthesized $Nd_{0.10}Y_{0.15}Zr_{0.75}O_{1.88}$ material, $Nd_{0.10}Y_{0.15}Zr_{0.75}O_{1.88}$ annealed at (c,d) 1400 °C, and (e,f) 1500 °C are plotted in (a,c,e) R-space and k-space (b,d,f).

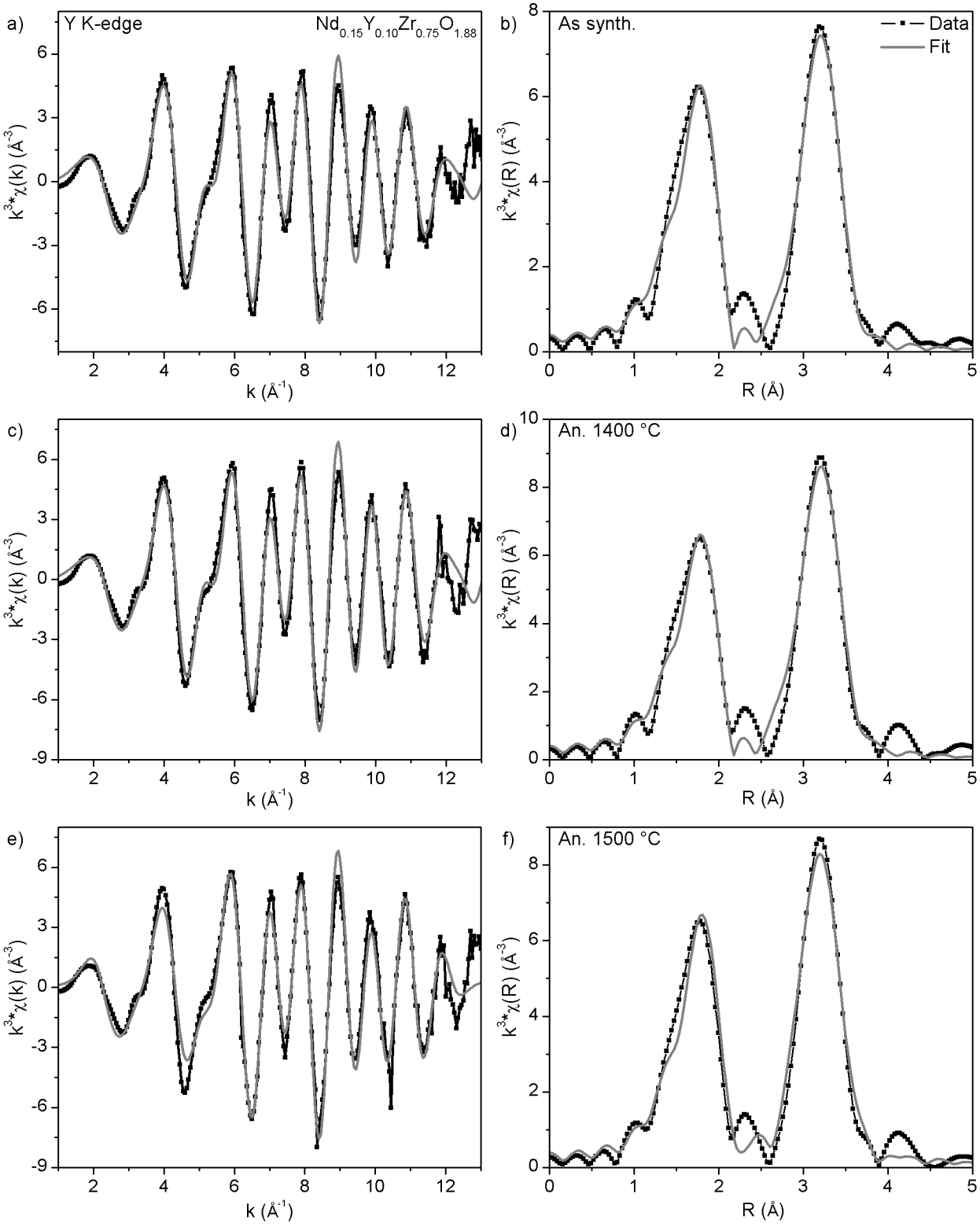

Figure C.15: The fits of the Y K-edge EXAFS spectra from (a,b) as-synthesized $Nd_{0.15}Y_{0.10}Zr_{0.75}O_{1.88}$ material, $Nd_{0.15}Y_{0.10}Zr_{0.75}O_{1.88}$ annealed at (c,d) 1400 °C, and (e,f) 1500 °C are plotted in (a,c,e) R-space and k-space (b,d,f).

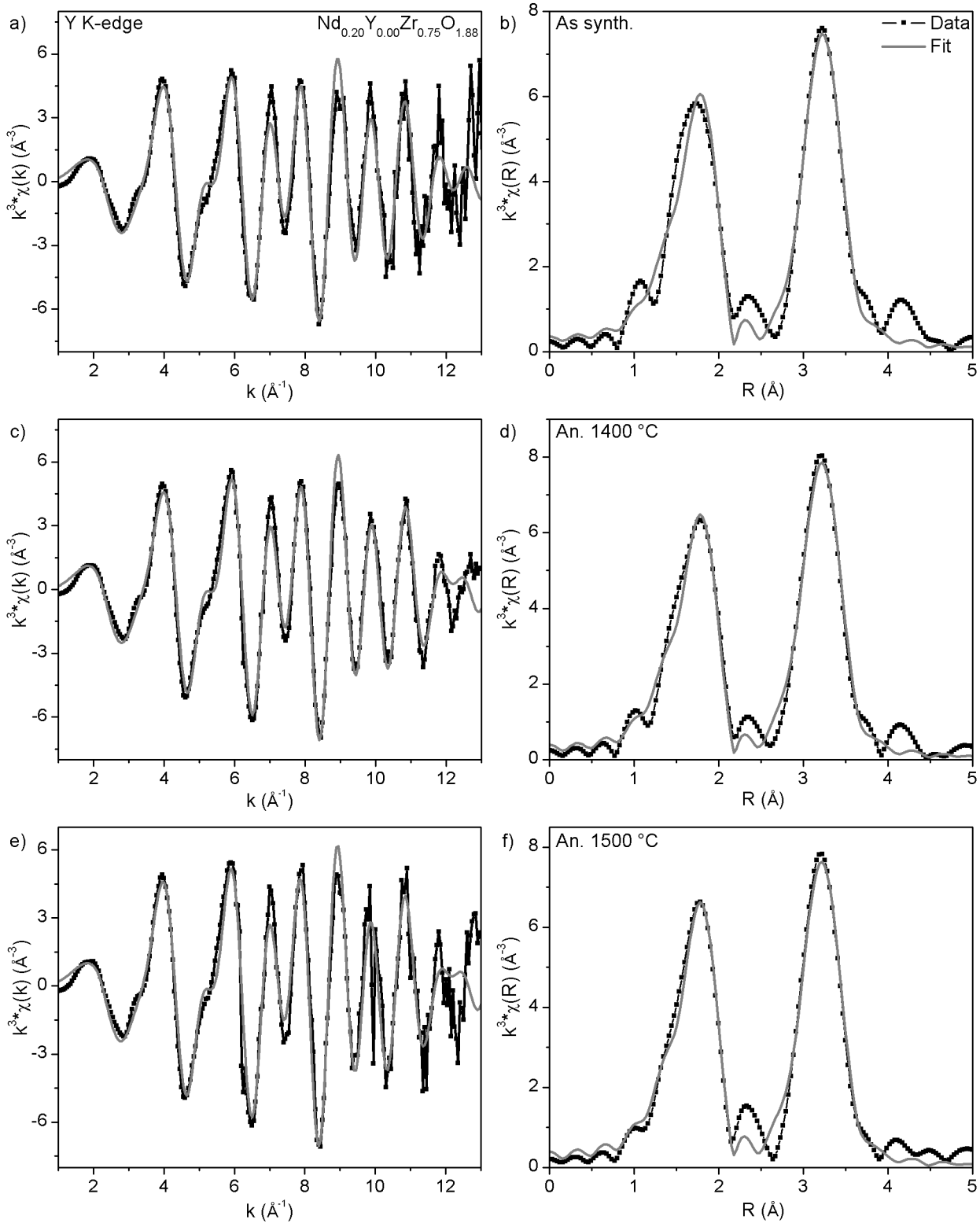

Figure C.16: The fits of the Y K-edge EXAFS spectra from (a,b) as-synthesized $Nd_{0.20}Y_{0.05}Zr_{0.75}O_{1.88}$ material, $Nd_{0.20}Y_{0.05}Zr_{0.75}O_{1.88}$ annealed at (c,d) 1400 °C, and (e,f) 1500 °C are plotted in (a,c,e) R-space and k-space (b,d,f).

Appendix D

Supporting Tables and Figures for Chapter 5[1]

[1]Reproduced in part with permission from J.R. Hayes, A.P. Grosvenor, M. Saoudi *Inorganic Chemistry*, (2016), 55, 1032-1043, DOI: 10.1021/acs.inorgchem.5b01886. Copyright 2015 American Chemical Society.

Table D.1: XRD Parameters Determined from Rietveld Refinement

	As Synthesized	Annealed 1100 °C	Annealed 1400 °C
$Nd_{0.10}Sc_{0.05}Zr_{0.85}O_{1.92}$			
R_{wp}	8.95	10.74	8.01
Unit Cell (Å)	5.1076(3)	5.1123(4)	5.1093(3)
Wt. Fraction	100% Cubic	29.8% Cubic	45.9% Cubic
		65.6% Tetragonal	54.1% Tetragonal
		4.6% Monoclinic	
$Nd_{0.05}Sc_{0.10}Zr_{0.85}O_{1.92}$			
R_{wp}	9.17	8.17	8.89
Unit Cell (Å)	5.12947(3)	5.1390(7)	5.1454(2)
Wt. Fraction	100% Cubic	47.5% Cubic	59.2% Cubic
		52.5% Tetragonal	6.4% Tetragonal
			34.5% Monoclinic
$Nd_{0.05}Sc_{0.15}Zr_{0.80}O_{1.90}$			
R_{wp}	8.35	8.93	9.55
Unit Cell (Å)	5.1010(3)	5.1042(1)	5.10570(6)
Wt. Fraction	100% Cubic	100% Cubic	100% Cubic
$Nd_{0.10}Sc_{0.10}Zr_{0.80}O_{1.90}$			
R_{wp}	8.57	9.36	9.83
Unit Cell (Å)	5.1182(3)	5.1225(3)	5.12407(6)
Wt. Fraction	100% Cubic	100% Cubic	100% Cubic
$Nd_{0.15}Sc_{0.05}Zr_{0.80}O_{1.90}$			
R_{wp}	9.91	8.21	8.52
Unit Cell (Å)	5.1376(3)	5.1538(5)	5.1478(1)
Wt. Fraction	100% Cubic	66.2% Cubic	56.3% Cubic
		33.8% Tetragonal	16.1% Tetragonal
			27.5% Monoclinic
$Nd_{0.05}Sc_{0.25}Zr_{0.70}O_{1.85}$			
R_{wp}	8.60	10.41	9.07
Unit Cell (Å)	5.0784(6)	5.0865(1)	5.08554(6)
Wt. Fraction	100% Cubic	100% Cubic	100% Cubic
$Nd_{0.10}Sc_{0.20}Zr_{0.70}O_{1.85}$			
R_{wp}	8.10	9.86	9.46
Unit Cell (Å)	5.0994(6)	5.1049(1)	5.10204(2)
Wt. Fraction	100% Cubic	100% Cubic	100% Cubic
$Nd_{0.15}Sc_{0.15}Zr_{0.70}O_{1.85}$			
R_{wp}	8.02	8.79	8.87
Unit Cell (Å)	5.1280(5)	5.1329(2)	5.12908(9)
Wt. Fraction	100% Cubic	100% Cubic	100% Cubic

Table D.2: Structural parameters determine from EXAFS fits

$Nd_{0.25}Zr_{0.75}O_{1.88}$						
	As synthesized			Annealed 1400 °C		
	S_o^2 =0.92(9), ΔE =-4(1) eV			S_o^2 =0.95(7), ΔE =-3.0(8) eV		
	R_{fit}= 0.026			R_{fit}= 0.024		
	CN	R(Å)	σ^2	CN	R(Å)	σ^2
Zr-O	7	2.15(1)	0.009(2)	7	2.166(9)	0.009(2)
Zr-Zr	9	3.59(1)	0.013(2)	9	3.54(1)	0.012(1)
Zr-Nd	3	3.26(7)	0.03(2)	3	3.36(8)	0.03(2)
Zr-O2	22	4.3(1)	0.06(2)	22	4.38(5)	0.04(1)

$Nd_{0.05}Sc_{0.20}Zr_{0.75}O_{1.88}$						
	As synthesized			Annealed 1400 °C		
	S_o^2 =0.92(9), ΔE =-4(1) eV			S_o^2 =0.92(9), ΔE =-4(1) eV		
	R_{fit}= 0.022			R_{fit}= 0.021		
	CN	R(Å)	σ^2	CN	R(Å)	σ^2
Zr-O	7	2.15(1)	0.10(2)	7	2.155(9)	0.008(1)
Zr-Zr	9	3.55(2)	0.012(2)	9	3.54(1)	0.011(1)
Zr-Sc	2.5	3.56(4)	0.009(6)	3	3.55(5)	0.014(8)
Zr-Nd	0.5	3.93(5)	0.004(5)	0	N/A	N/A
Zr-O2	N/A	N/A	N/A	22	4.27(6)	0.03(1)

$Nd_{0.15}Sc_{0.05}Zr_{0.80}O_{1.90}$						
	As synthesized			Annealed 1400 °C		
	S_o^2 =0.92(9), ΔE =-4(1) eV			S_o^2 =0.92(9), ΔE =-4(1) eV		
	R_{fit}= 0.022			R_{fit}= 0.021		
	CN	R(Å)	σ^2	CN	R(Å)	σ^2
Zr-O	7	2.15(1)	0.009(2)	7	2.14(1)	0.010(2)
Zr-Zr	9.6	3.60(3)	0.010(2)	9.6	3.63(1)	0.008(1)
Zr-Sc	1.2	3.57(8)	0.00(1)	2.4	3.7(2)	0.03(3)
Zr-Nd	1.2	3.96(7)	0.006(8)	0	N/A	N/A
Zr-O2	22	4.34(7)	0.03(1)	22	4.24(9)	0.03(1)

Table D.3: More structural parameters determine from EXAFS fits

$Nd_{0.15}Sc_{0.10}Zr_{0.75}O_{1.88}$									
	As synthesized			Annealed 1100 °C			Annealed 1400 °C		
	S_o^2 =0.93(9), ΔE =-2.8(9) eV			S_o^2 =0.93(8), ΔE =-2.7(9) eV			S_o^2 =0.94(7), ΔE =-1.7(7) eV		
	R_{fit}= 0.014			R_{fit}= 0.014			R_{fit}= 0.014		
	CN	R(Å)	σ^2	CN	R(Å)	σ^2	CN	R(Å)	σ^2
Zr-O	7	2.14(1)	0.009(2)	7	2.153(9)	0.008(1)	7	2.160(8)	0.008(1)
Zr-Zr	9	3.57(2)	0.009(3)	9	3.59(2)	0.012(2)	9	3.58(2)	0.012(2)
Zr-Sc	2	3.58(4)	0.002(6)	1.2	3.36(5)	0.006(4)	1.8	3.52(4)	0.005(6)
Zr-Nd	1	3.61(5)	0.005(4)	1.8	3.52(5)	0.007(7)	1.2	3.36(3)	0.004(3)
Zr-O2	22	4.30(7)	0.04(1)	22	4.27(6)	0.032(9)	22	4.30(5)	0.030(8)
$Nd_{0.05}Sc_{0.25}Zr_{0.70}O_{1.85}$									
	As synthesized			Annealed 1100 °C			Annealed 1400 °C		
	S_o^2 =0.88(9), ΔE =-3(1) eV			S_o^2 =0.9(1), ΔE =-4(1) eV			S_o^2 =0.9(1), ΔE =-4(1) eV		
	R_{fit}= 0.023			R_{fit}= 0.024			R_{fit}= 0.029		
	CN	R(Å)	σ^2	CN	R(Å)	σ^2	CN	R(Å)	σ^2
Zr-O	7	2.16(1)	0.008(2)	7	2.16(1)	0.007(2)	7	2.16(1)	0.007(2)
Zr-Zr	8.4	3.56(2)	0.009(3)	8.4	3.56(2)	0.008(3)	8.4	3.57(3)	0.010(4)
Zr-Sc	3	3.60(4)	0.008(8)	3	3.60(5)	0.006(9)	3	3.63(5)	-0.004(4)
Zr-Nd	0.6	3.59(4)	0.001(3)	0.6	3.59(4)	0.001(4)	0.6	3.73(1)	0.02(2)
Zr-O2	22	4.34(6)	0.03(1)	22	4.33(6)	0.03(1)	22	4.30(9)	0.03(1)
$Nd_{0.10}Sc_{0.20}Zr_{0.70}O_{1.85}$									
	As synthesized			Annealed 1100 °C			Annealed 1400 °C		
	S_o^2 =0.9(1), ΔE =-4(1) eV			S_o^2 =0.9(1), ΔE =-4(1) eV			S_o^2 =0.9(1), ΔE =-4(1) eV		
	R_{fit}= 0.027			R_{fit}= 0.020			R_{fit}= 0.029		
	CN	R(Å)	σ^2	CN	R(Å)	σ^2	CN	R(Å)	σ^2
Zr-O	7	2.16(1)	0.008(2)	7	2.16(1)	0.007(2)	7	2.16(1)	0.007(2)
Zr-Zr	8.4	3.58(4)	0.014(6)	8.4	3.54(2)	0.010(2)	8.4	3.55(2)	0.009(3)
Zr-Sc	0.6	3.64(5)	-0.003(4)	2.4	3.54(5)	0.007(8)	3	3.57(5)	0.008(9)
Zr-Nd	3	3.73(8)	0.01(1)	1.2	3.91(5)	0.006(5)	0.6	3.91(5)	0.001(5)
Zr-O2	22	4.30(8)	0.03(1)	22	4.33(5)	0.02(1)	22	4.35(5)	0.03(1)
$Nd_{0.15}Sc_{0.15}Zr_{0.70}O_{1.85}$									
	As synthesized			Annealed 1100 °C			Annealed 1400 °C		
	S_o^2 =0.9(1), ΔE =-4(1) eV			S_o^2 =0.9(1), ΔE =-4(1) eV			S_o^2 =0.9(1), ΔE =-4(1) eV		
	R_{fit}= 0.026			R_{fit}= 0.022			R_{fit}= 0.022		
	CN	R(Å)	σ^2	CN	R(Å)	σ^2	CN	R(Å)	σ^2
Zr-O	7	2.16(1)	0.008(2)	7	2.16(1)	0.007(2)	7	2.16(1)	0.008(2)
Zr-Zr	8.4	3.55(3)	0.010(4)	8.4	3.55(2)	0.009(2)	8.4	3.54(2)	0.009(3)
Zr-Sc	1.8	3.56(6)	0.004(1)	2.4	3.92(4)	0.006(7)	1.8	3.54(5)	0.004(8)
Zr-Nd	1.8	3.94(6)	0.008(7)	1.2	3.55(5)	0.004(5)	1.8	3.92(5)	0.006(5)
Zr-O2	22	4.38(6)	0.03(2)	22	4.36(4)	0.02(1)	22	4.36(5)	0.02(1)

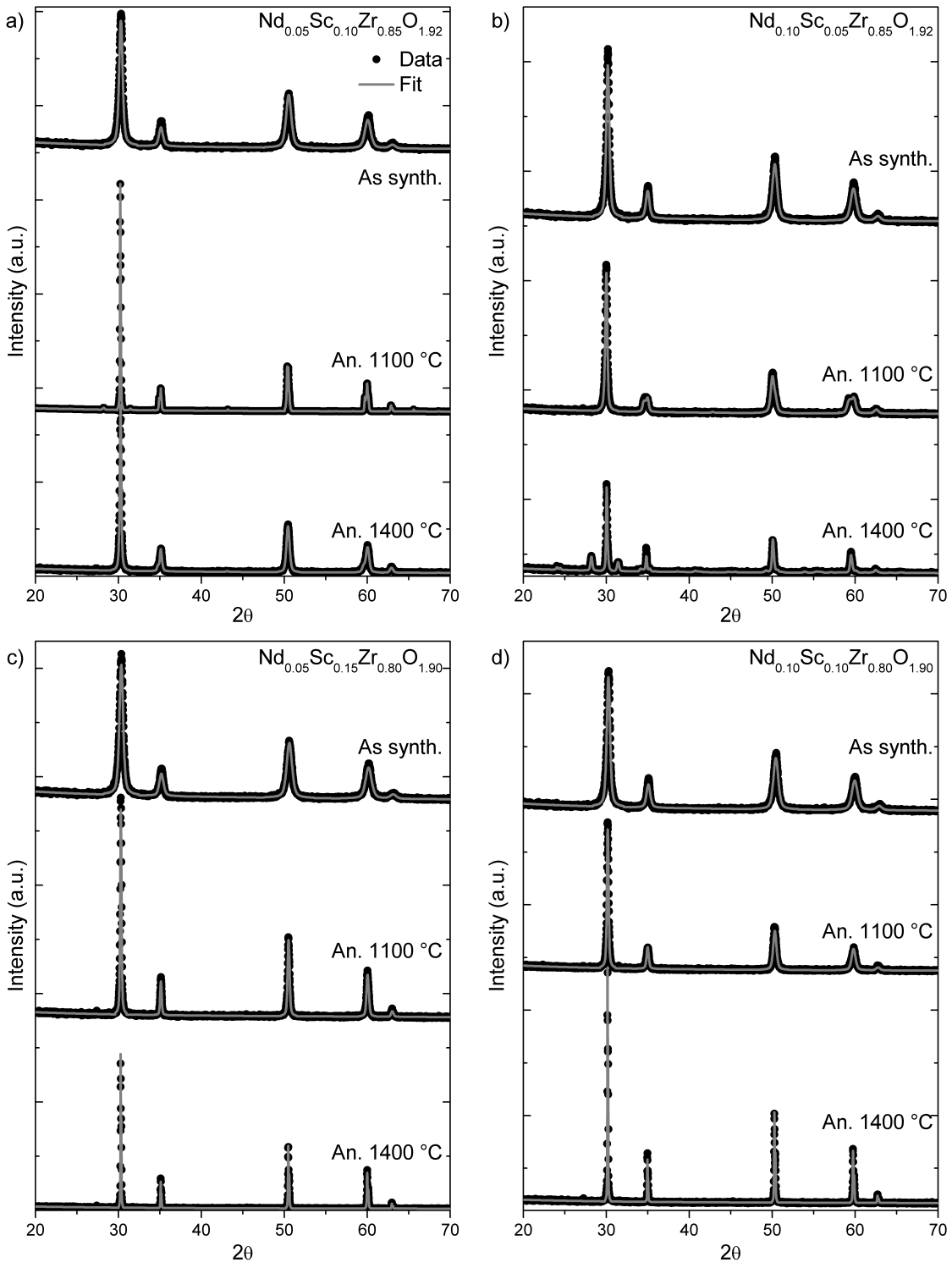

Figure D.1: Powder XRD patterns from the synthesized and high-temperature annealed (a) $Nd_{0.05}Sc_{0.10}Zr_{0.85}O_{1.92}$, (b) $Nd_{0.10}Sc_{0.05}Zr_{0.85}O_{1.92}$, and (c) $Nd_{0.05}Sc_{0.15}Zr_{0.80}O_{1.90}$ (d) $Nd_{0.10}Sc_{0.10}Zr_{0.80}O_{1.90}$ materials. A small, unidentified peak at ∼27.4° was observed in several of the patterns. The XRD patterns collected from the as-synthesized materials were collected using a Cu source, while the other patterns were collected using a Co source. The patterns collected using a Cu source were shifted to allow for better comparison to the data collected using the Co source.

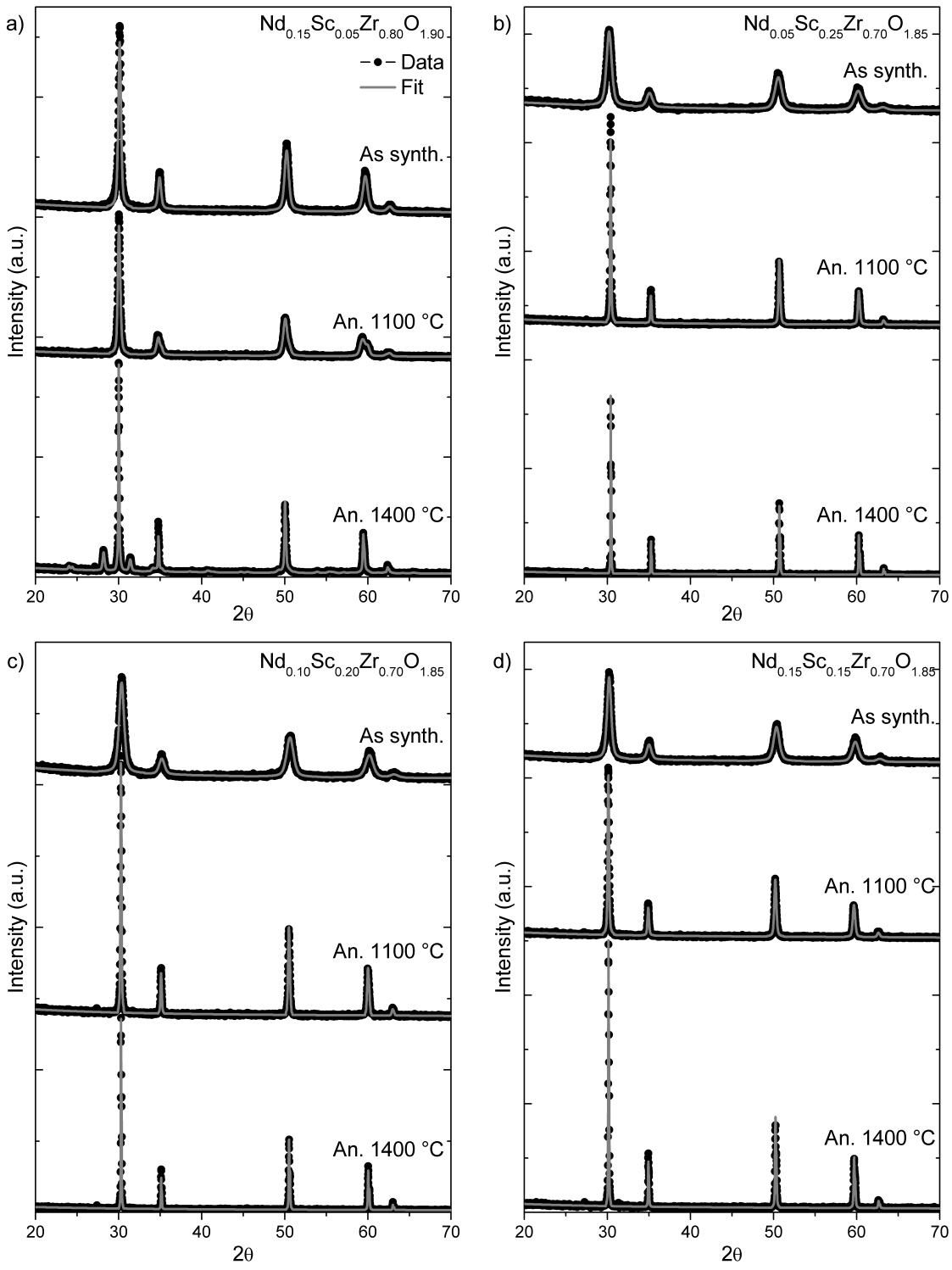

Figure D.2: Powder XRD patterns from the synthesized and high-temperature annealed (a) $Nd_{0.15}Sc_{0.05}Zr_{0.80}O_{1.90}$, (b) $Nd_{0.05}Sc_{0.25}Zr_{0.70}O_{1.85}$, and (c) $Nd_{0.10}Sc_{0.20}Zr_{0.70}O_{1.85}$ (d) $Nd_{0.15}Sc_{0.15}Zr_{0.70}O_{1.85}$ materials. A small, unidentified peak at $\sim$27.4° was observed in several of the patterns. The XRD patterns collected from the as-synthesized materials were collected using a Cu source, while the other patterns were collected using a Co source. The patterns collected using a Cu source were shifted to allow for better comparison to the data collected using the Co source.

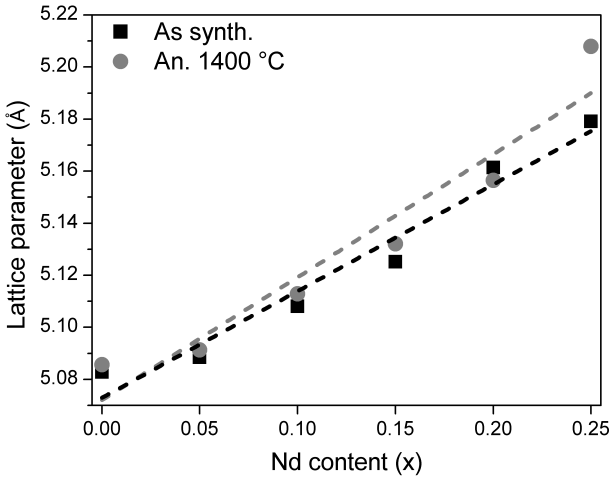

Figure D.3: Lattice parameters of the $Nd_xSc_{0.25-x}Zr_{0.75}O_{1.88}$ determined by Rietveld analysis are plotted as a function of x. (The error bars are smaller than the symbol size.) The plots show that the lattice parameters vary from Vegard's law, most notably in the case of the end members. The linear best fits from both the as-synthesized and annealed materials are also presented.

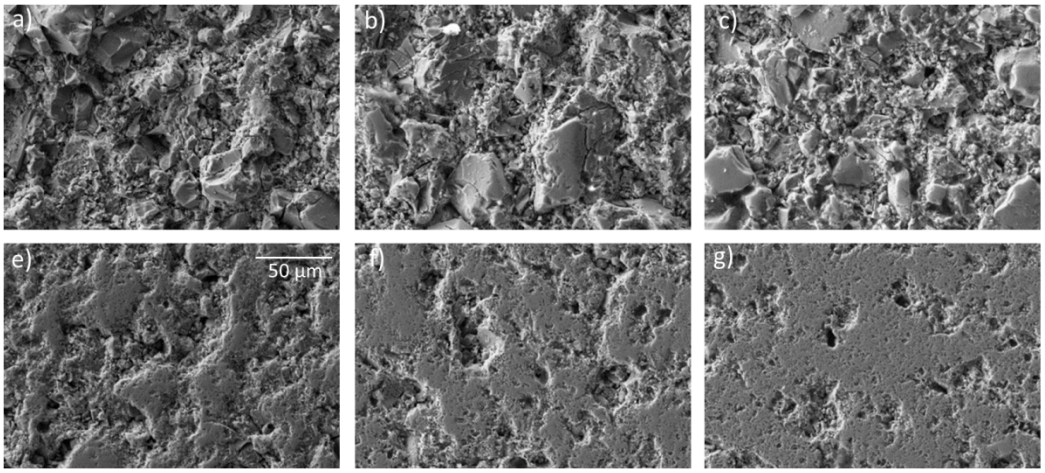

Figure D.4: SE micrographs from as-synthesized (a) $Nd_{0.15}Sc_{0.05}Zr_{0.80}O_{1.90}$, (b) $Nd_{0.10}Sc_{0.10}Zr_{0.80}O_{1.90}$, (c) $Nd_{0.05}Sc_{0.15}Zr_{0.80}O_{1.90}$ pellets and the (d) $Nd_{0.15}Sc_{0.05}Zr_{0.80}O_{1.90}$, (e) $Nd_{0.15}Sc_{0.05}Zr_{0.80}O_{1.90}$, and (f) $Nd_{0.15}Sc_{0.05}Zr_{0.80}O_{1.90}$ pellets annealed at 1400 °C.

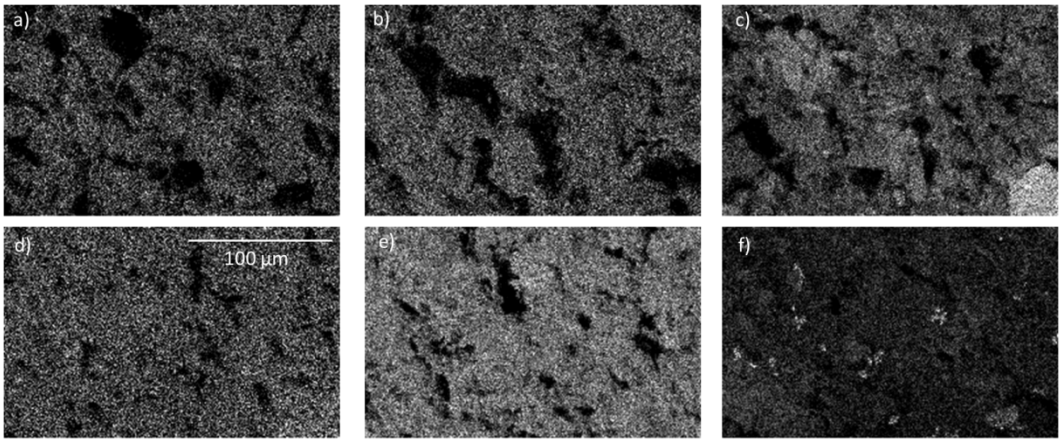

Figure D.5: Nd L_α EDS maps from as-synthesized (a) $Nd_{0.15}Sc_{0.05}Zr_{0.80}O_{1.90}$, (b) $Nd_{0.10}Sc_{0.10}Zr_{0.80}O_{1.90}$, (c) $Nd_{0.05}Sc_{0.15}Zr_{0.80}O_{1.90}$ pellets and the (d) $Nd_{0.15}Sc_{0.05}Zr_{0.80}O_{1.90}$, (e) $Nd_{0.15}Sc_{0.05}Zr_{0.80}O_{1.90}$, and (f) $Nd_{0.15}Sc_{0.05}Zr_{0.80}O_{1.90}$ pellets annealed at 1400 °C.

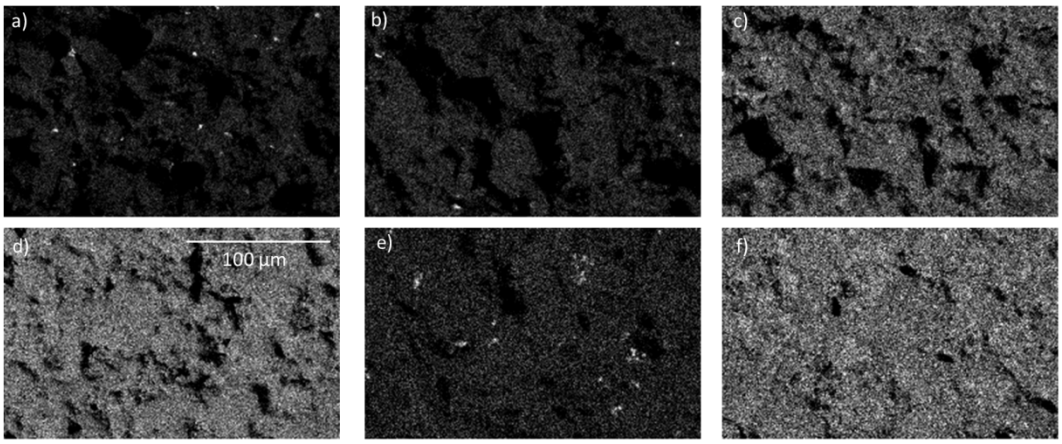

Figure D.6: Sc K_α EDS maps from as-synthesized (a) $Nd_{0.15}Sc_{0.05}Zr_{0.80}O_{1.90}$, (b) $Nd_{0.10}Sc_{0.10}Zr_{0.80}O_{1.90}$, (c) $Nd_{0.05}Sc_{0.15}Zr_{0.80}O_{1.90}$ pellets and the (d) $Nd_{0.15}Sc_{0.05}Zr_{0.80}O_{1.90}$, (e) $Nd_{0.15}Sc_{0.05}Zr_{0.80}O_{1.90}$, and (f) $Nd_{0.15}Sc_{0.05}Zr_{0.80}O_{1.90}$ pellets annealed at 1400 °C.

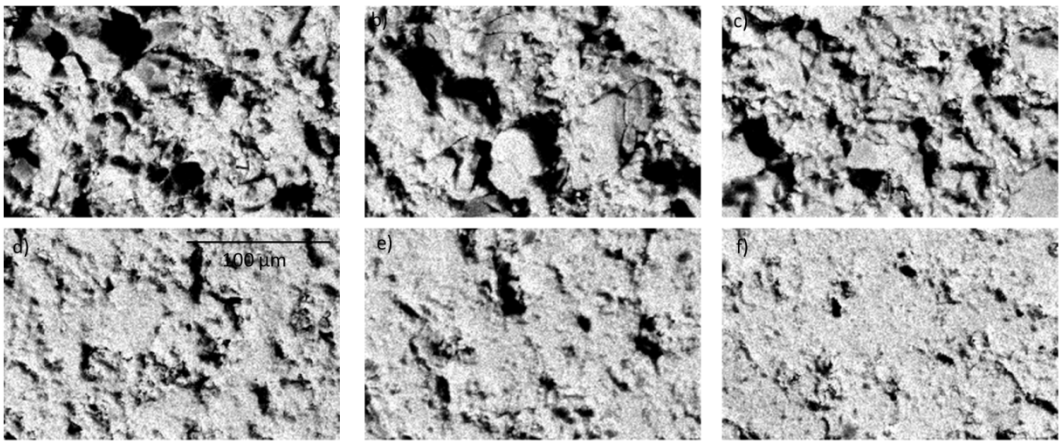

Figure D.7: Zr K_α EDS maps from as-synthesized (a) $Nd_{0.15}Sc_{0.05}Zr_{0.80}O_{1.90}$, (b) $Nd_{0.10}Sc_{0.10}Zr_{0.80}O_{1.90}$, (c) $Nd_{0.05}Sc_{0.15}Zr_{0.80}O_{1.90}$ pellets and the (d) $Nd_{0.15}Sc_{0.05}Zr_{0.80}O_{1.90}$, (e) $Nd_{0.15}Sc_{0.05}Zr_{0.80}O_{1.90}$, and (f) $Nd_{0.15}Sc_{0.05}Zr_{0.80}O_{1.90}$ pellets annealed at 1400 °C.

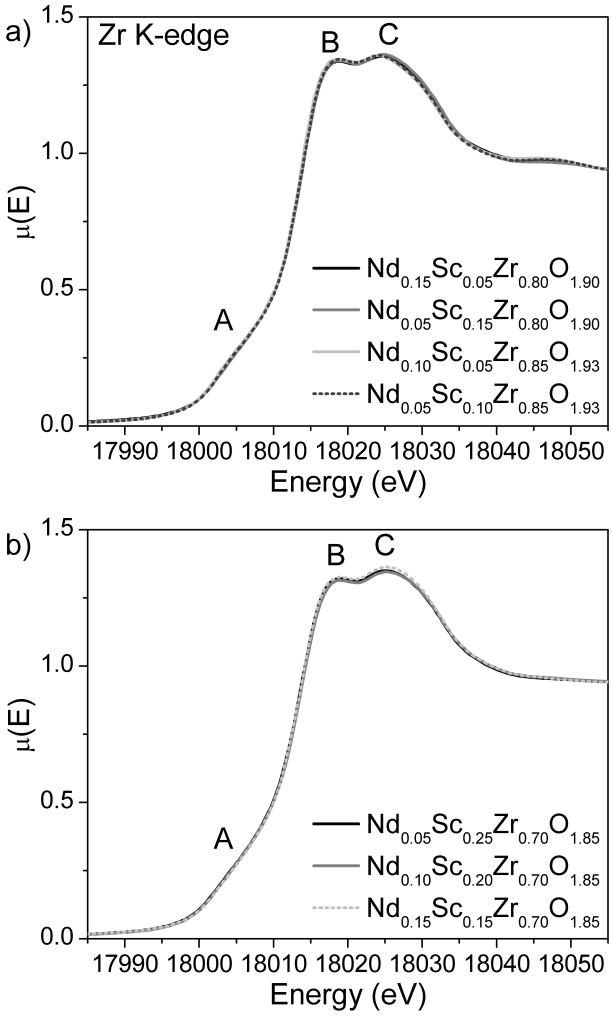

Figure D.8: Zr K-edge XANES spectra from the as-synthesized $Nd_xSc_yZr_{1-x-y}O_{2-\delta}$ materials are presented.

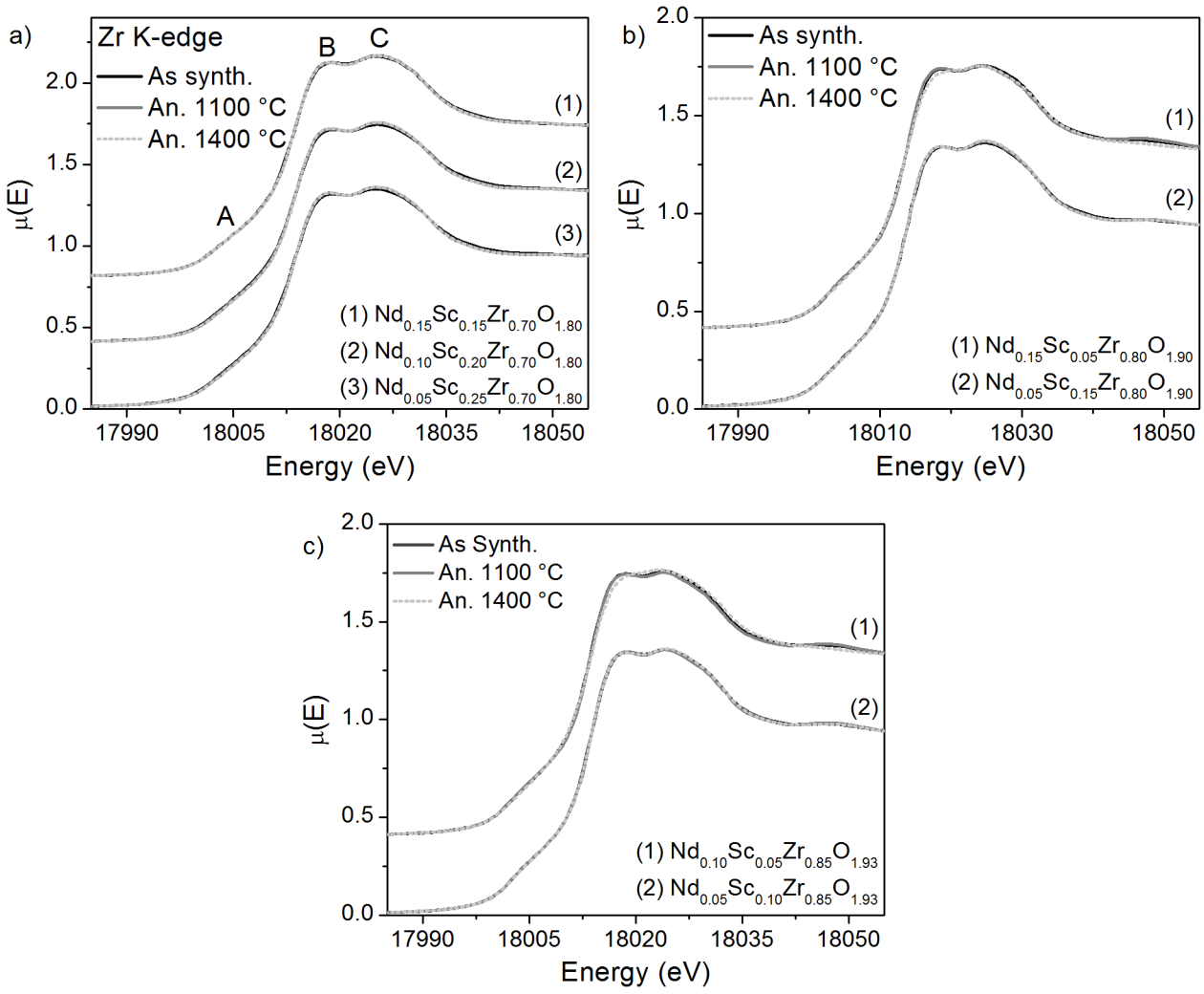

Figure D.9: The Zr K-edge XANES spectra from the as-synthesized and annealed $Nd_xSc_yZr_{1-x-y}O_{2-\delta}$ materials.

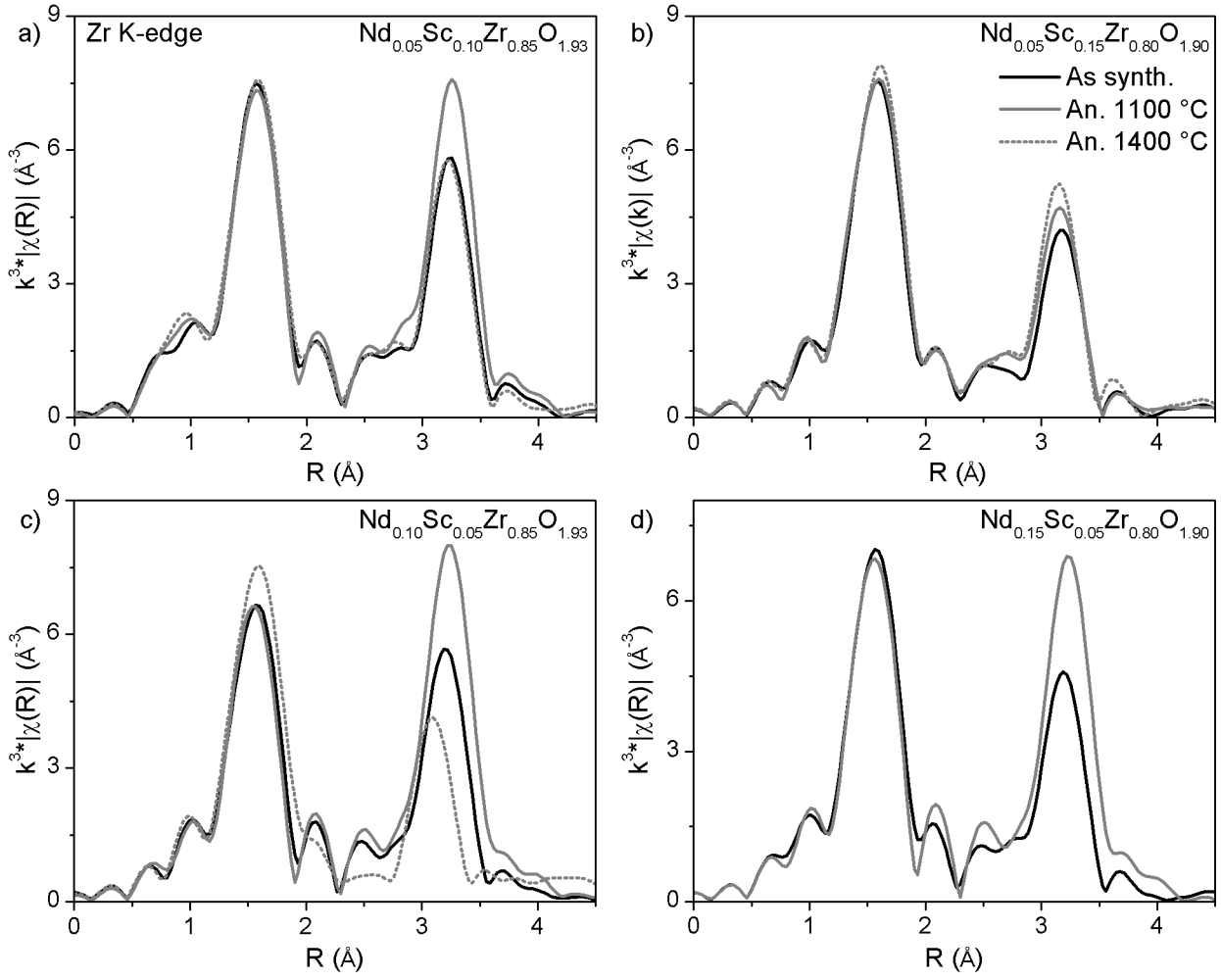

Figure D.10: The Zr K-edge EXAFS spectra from the as-synthesized and annealed $Nd_xSc_yZr_{1-x-y}O_{2-\delta}$ compounds.

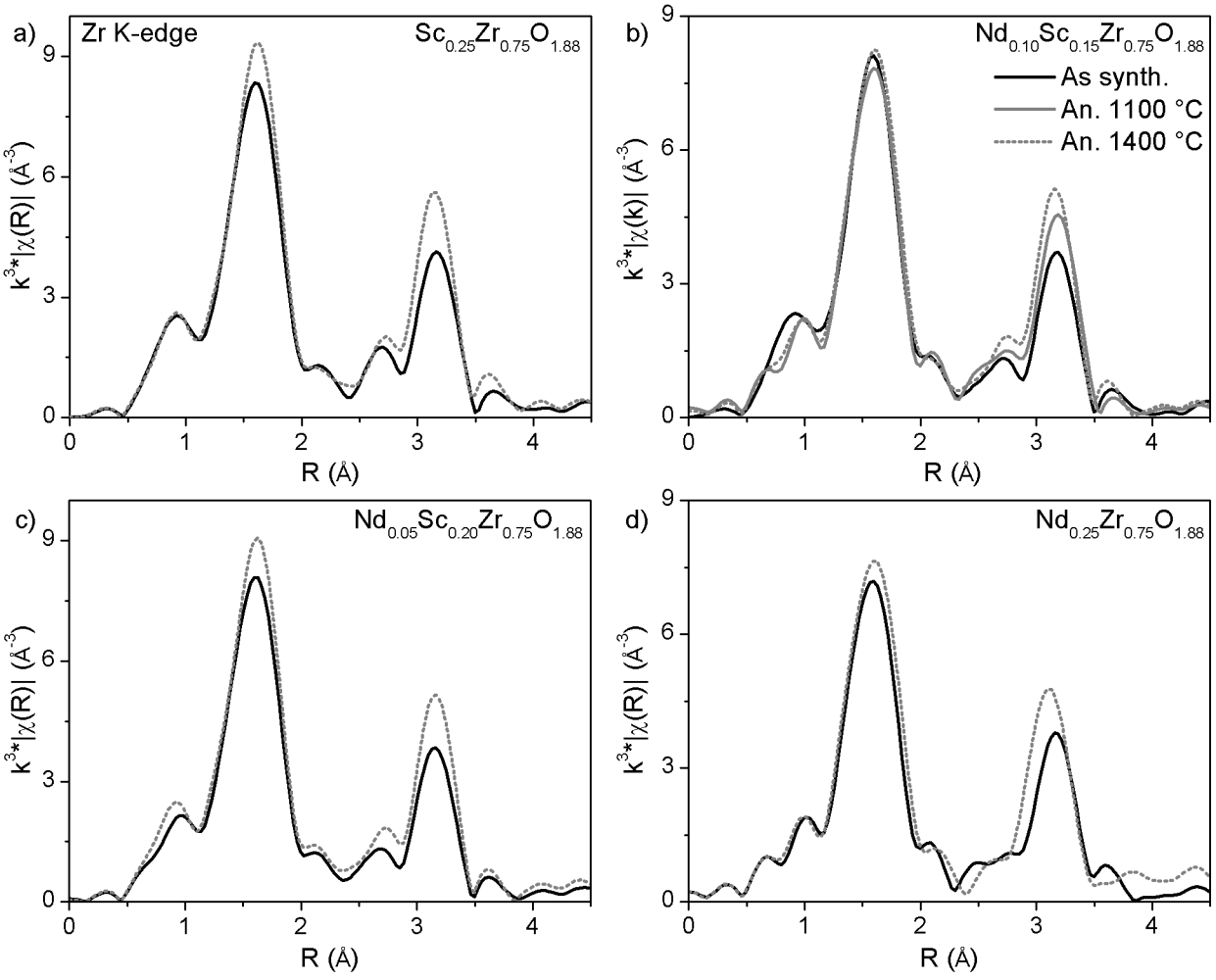

Figure D.11: The Zr K-edge EXAFS spectra from the as-synthesized and annealed $Nd_xSc_yZr_{1-x-y}O_{2-\delta}$ compounds.

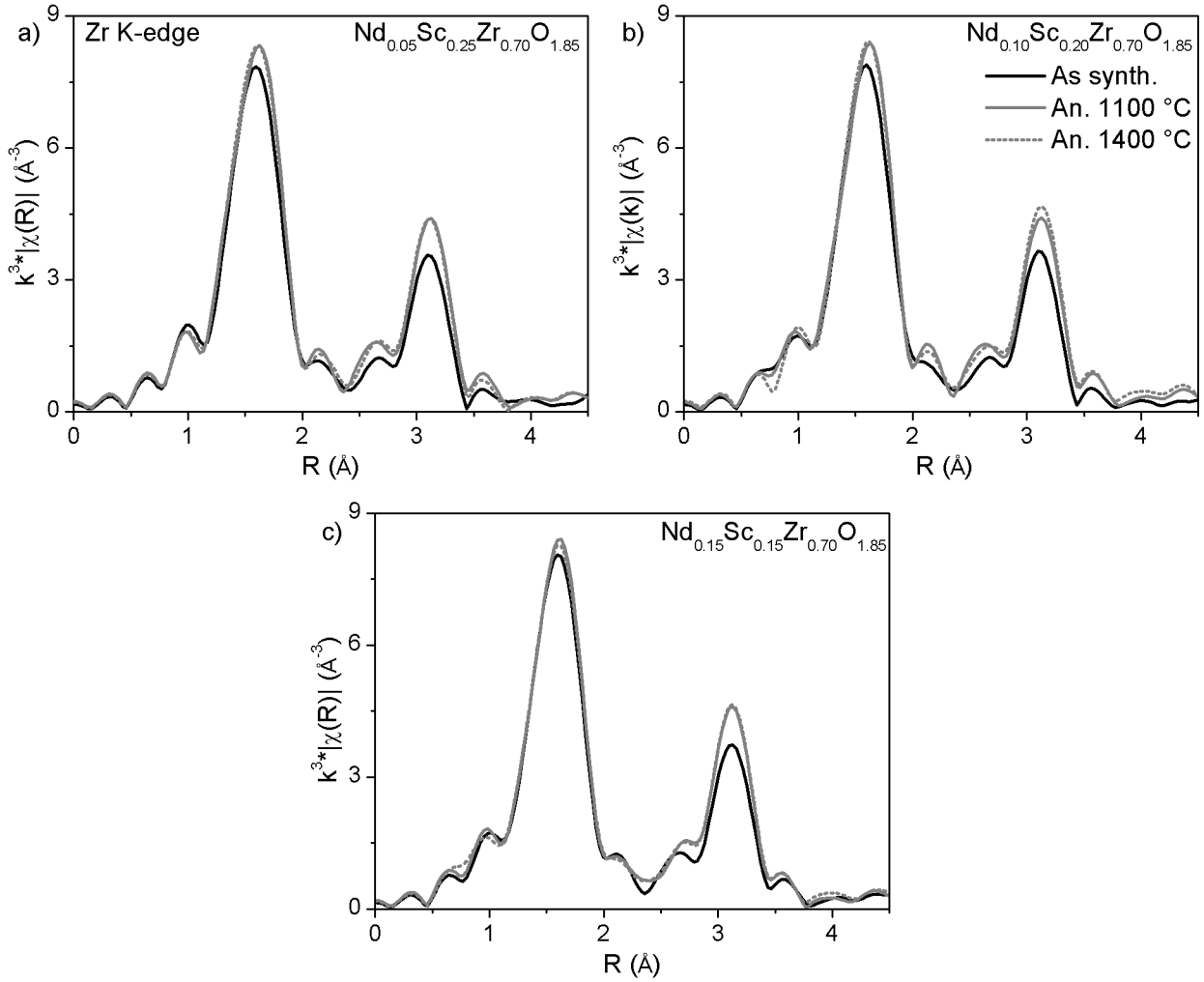

Figure D.12: The Zr K-edge EXAFS spectra from the as-synthesized and annealed $Nd_xSc_yZr_{1-x-y}O_{2-\delta}$ compounds.

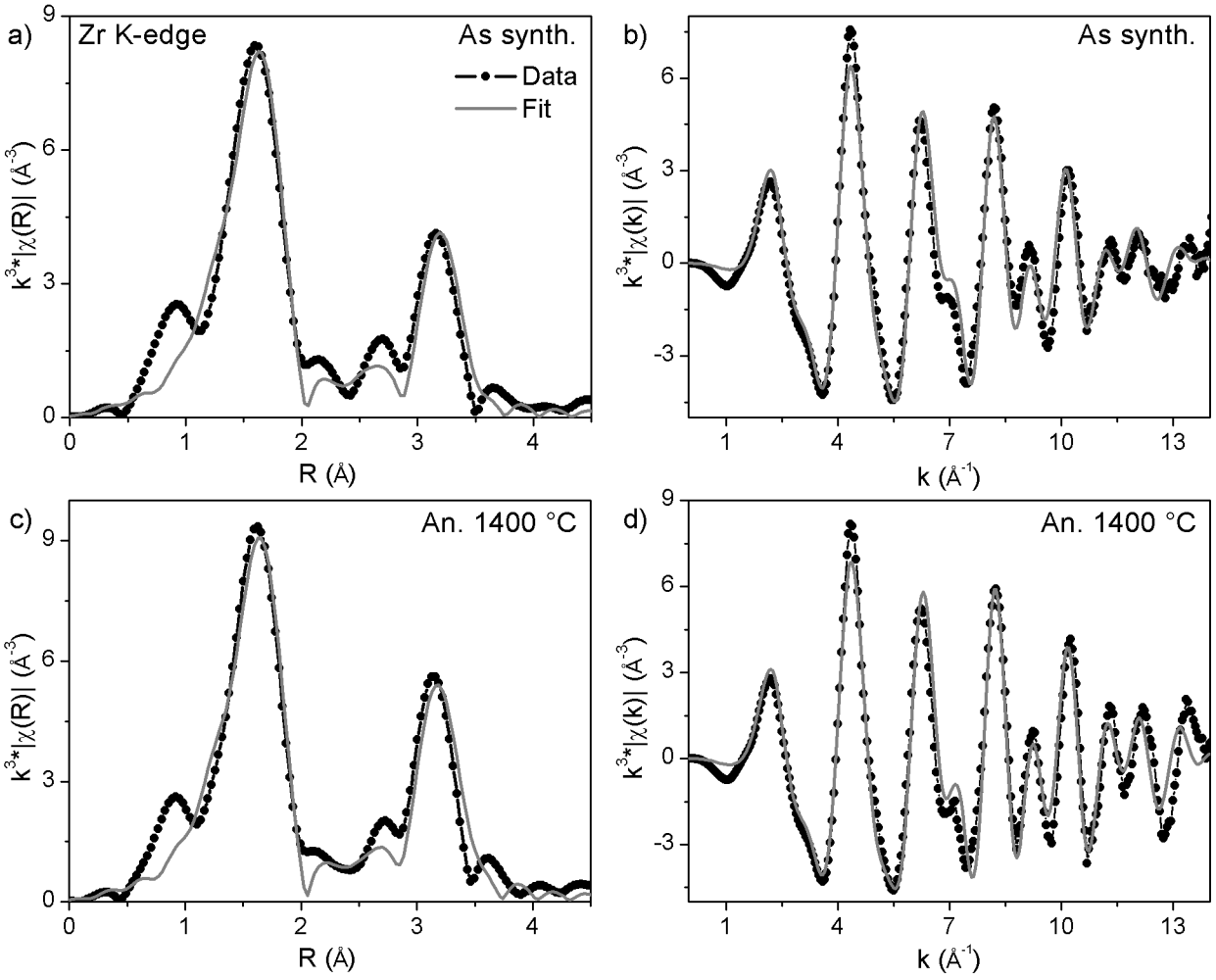

Figure D.13: The fits of the Zr K-edge EXAFS spectra from as-synthesized (a,b) $Sc_{0.25}Zr_{0.75}O_{1.88}$ and (c,d) $Sc_{0.25}Zr_{0.75}O_{1.88}$ annealed at 600 °C in (a,c) R-space and k-space (b,d).

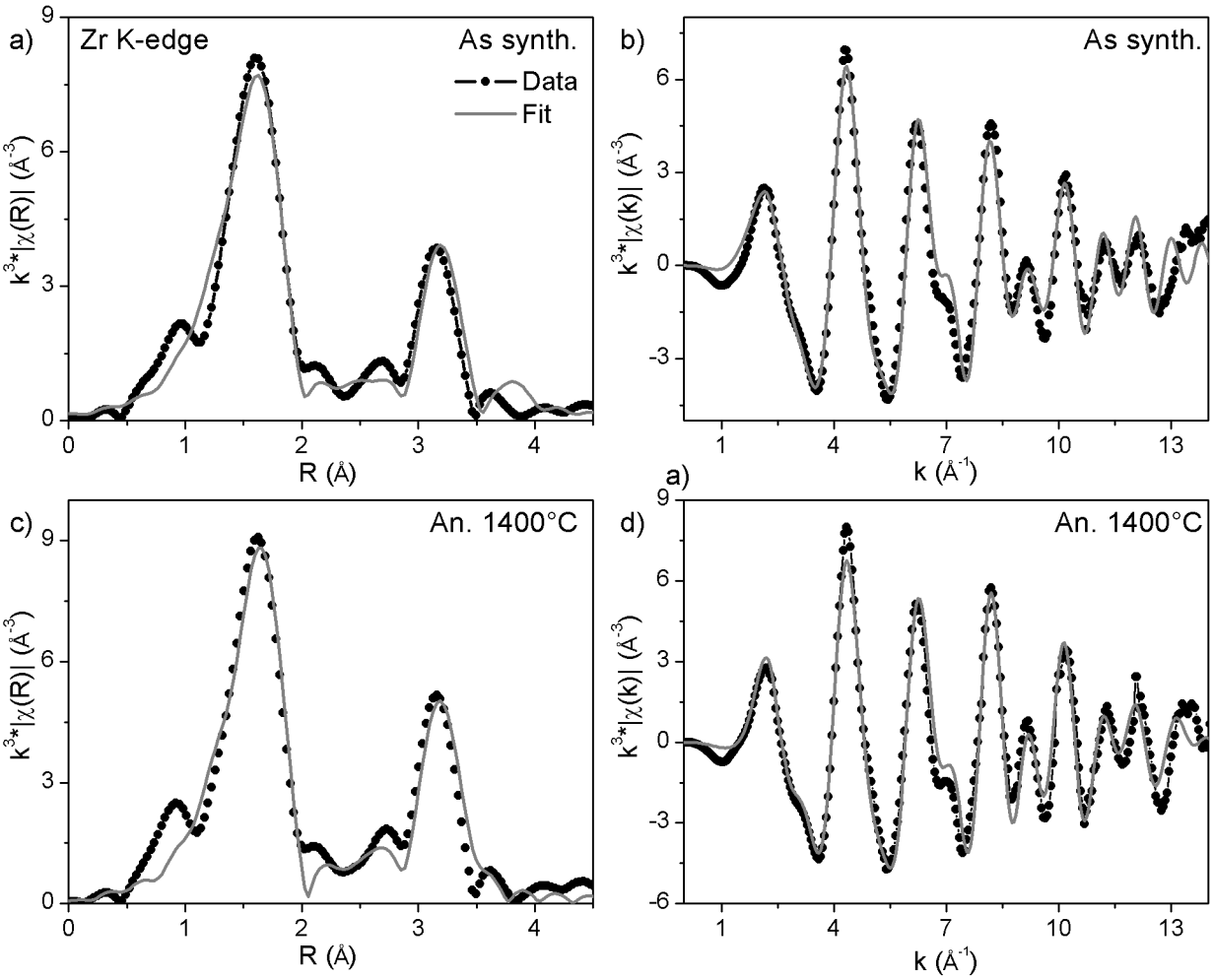

Figure D.14: The fits of the Zr K-edge EXAFS spectra from as-synthesized (a,b) $Nd_{0.05}Sc_{0.20}Zr_{0.75}O_{1.88}$ and (c,d) $Nd_{0.05}Sc_{0.20}Zr_{0.75}O_{1.88}$ annealed at 600 °C in (a,c) R-space and k-space (b,d).

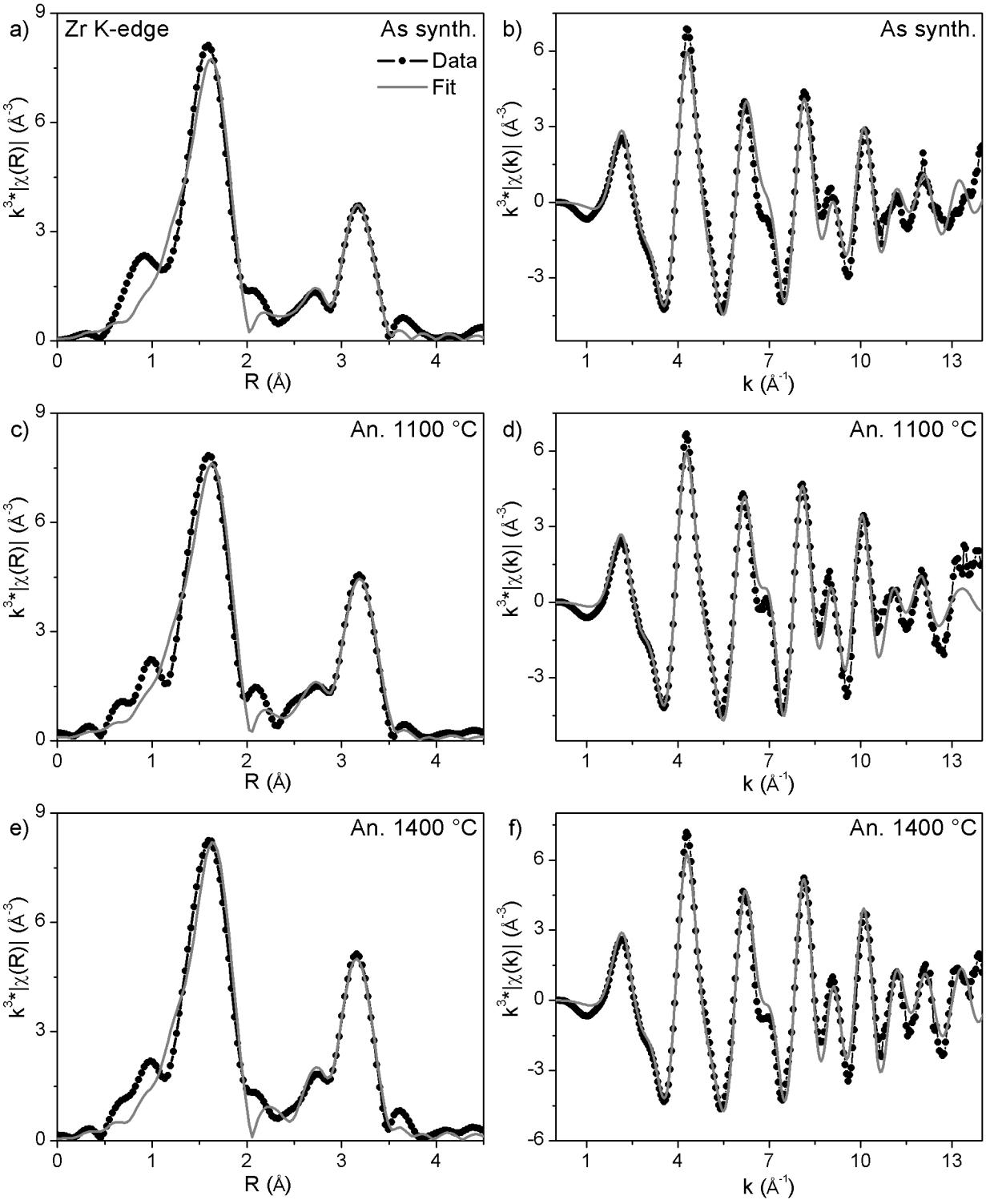

Figure D.15: The fits of the Zr K-edge EXAFS spectra from (a,b) as-synthesized $Nd_{0.15}Sc_{0.10}Zr_{0.75}O_{1.88}$ material, $Nd_{0.15}Sc_{0.10}Zr_{0.75}O_{1.88}$ annealed at (c,d) 1100 °C, and (e,f) 1400 °C are plotted in (a,c,e) R-space and k-space (b,d,f).

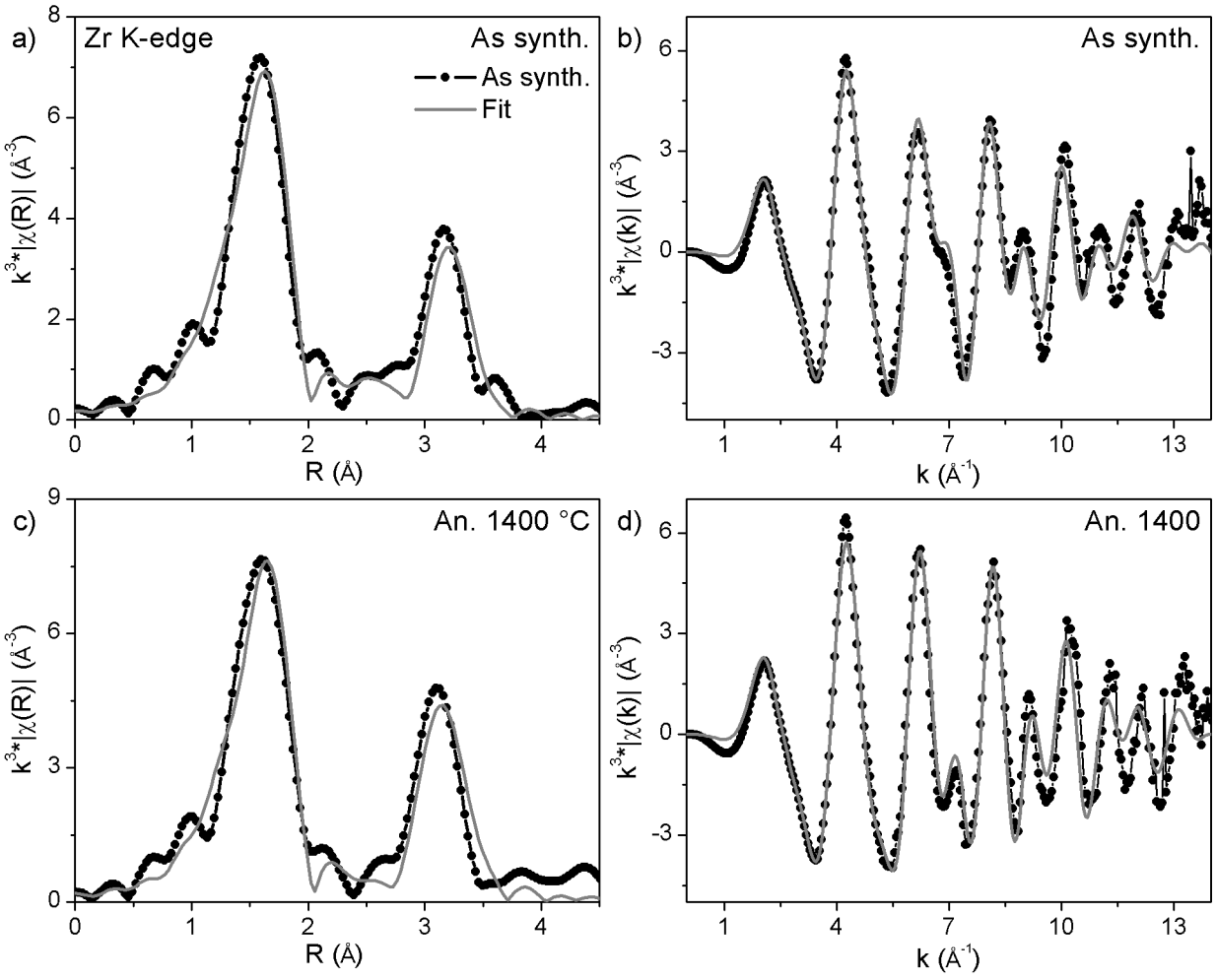

Figure D.16: The fits of the Zr K-edge EXAFS spectra from as-synthesized (a,b) $Nd_{0.25}Zr_{0.75}O_{1.88}$ and (c,d) $Nd_{0.25}Zr_{0.75}O_{1.88}$ annealed at 600 °C in (a,c) R-space and k-space (b,d).

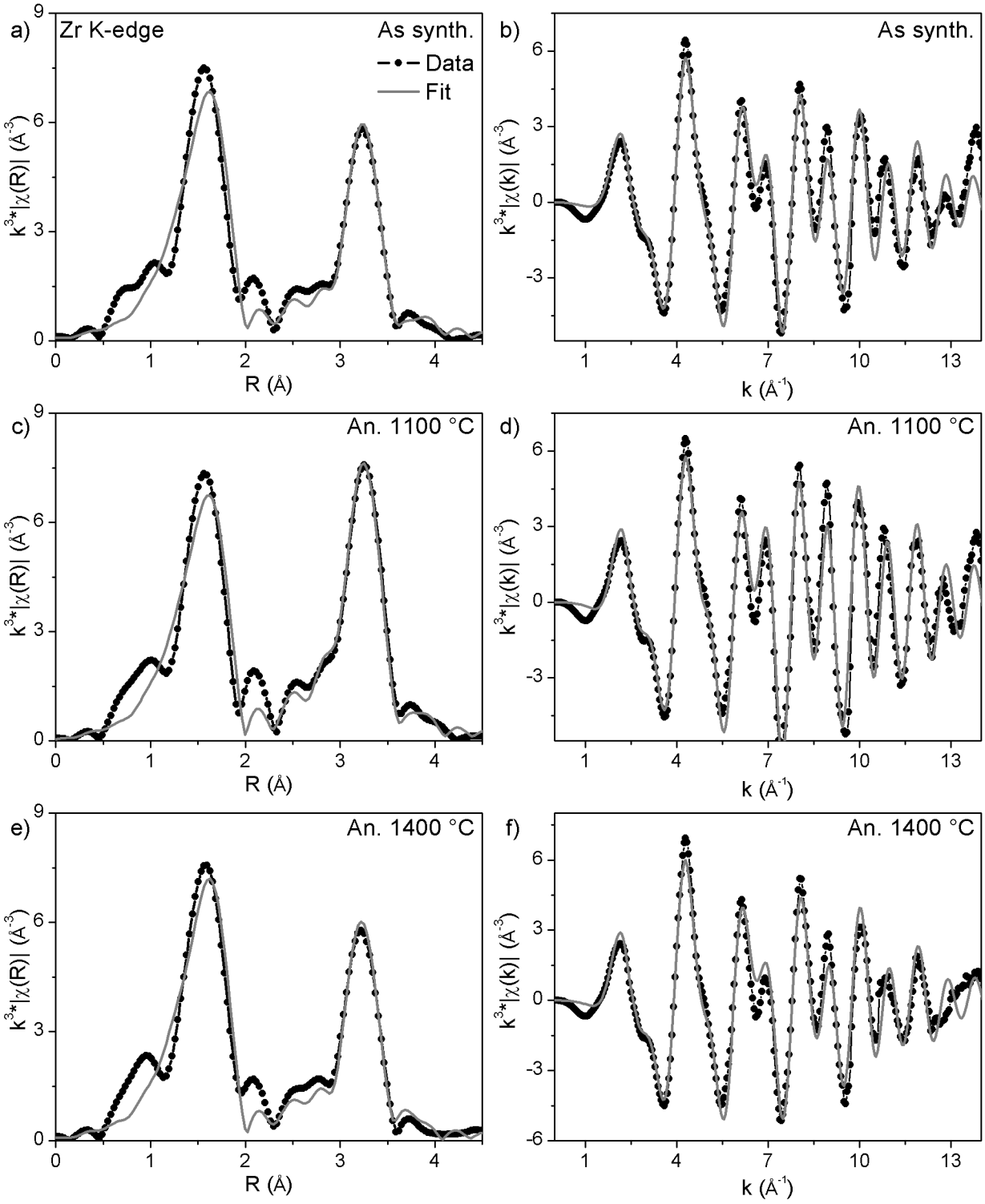

Figure D.17: The fits of the Zr K-edge EXAFS spectra from (a,b) as-synthesized $Nd_{0.05}Sc_{0.10}Zr_{0.85}O_{1.92}$ material, $Nd_{0.05}Sc_{0.10}Zr_{0.85}O_{1.92}$ annealed at (c,d) 1100 °C, and (e,f) 1400 °C are plotted in (a,c,e) R-space and k-space (b,d,f).

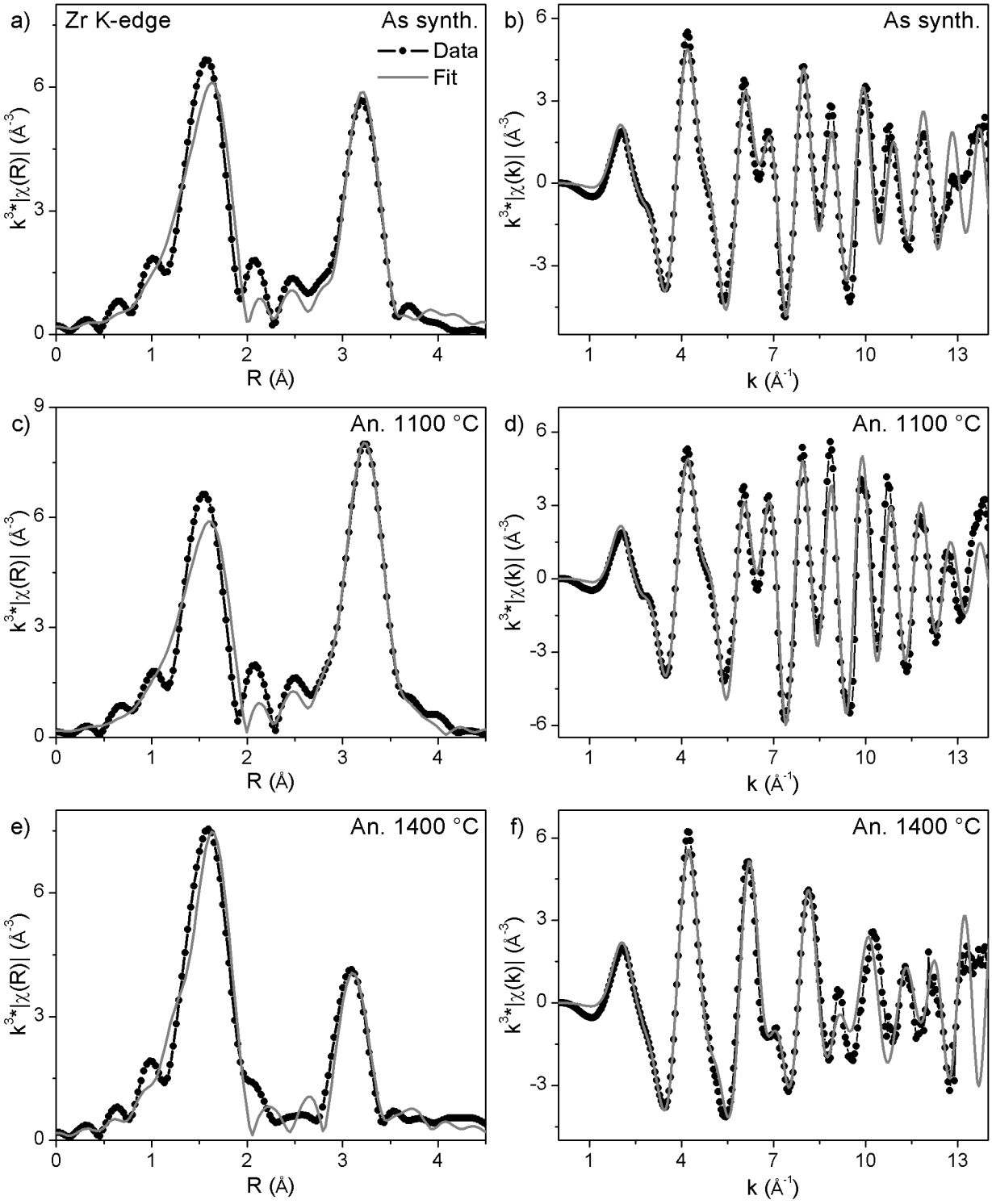

Figure D.18: The fits of the Zr K-edge EXAFS spectra from (a,b) as-synthesized $Nd_{0.10}Sc_{0.05}Zr_{0.85}O_{1.92}$ material, $Nd_{0.10}Sc_{0.05}Zr_{0.85}O_{1.92}$ annealed at (c,d) 1100 °C, and (e,f) 1400 °C are plotted in (a,c,e) R-space and k-space (b,d,f).

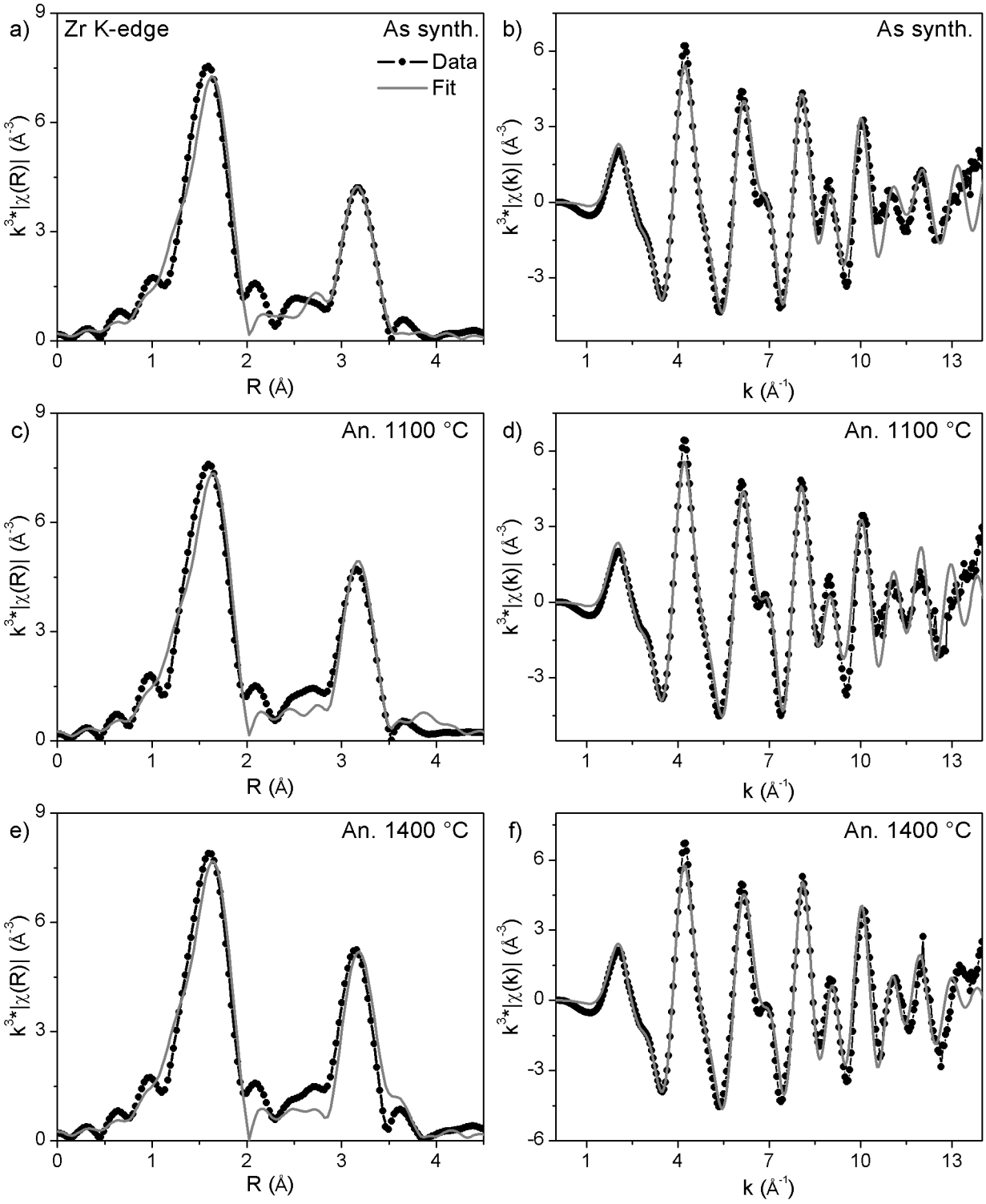

Figure D.19: The fits of the Zr K-edge EXAFS spectra from (a,b) as-synthesized $Nd_{0.05}Sc_{0.15}Zr_{0.80}O_{1.90}$ material, $Nd_{0.05}Sc_{0.15}Zr_{0.80}O_{1.90}$ annealed at (c,d) 1100 °C, and (e,f) 1400 °C are plotted in (a,c,e) R-space and k-space (b,d,f).

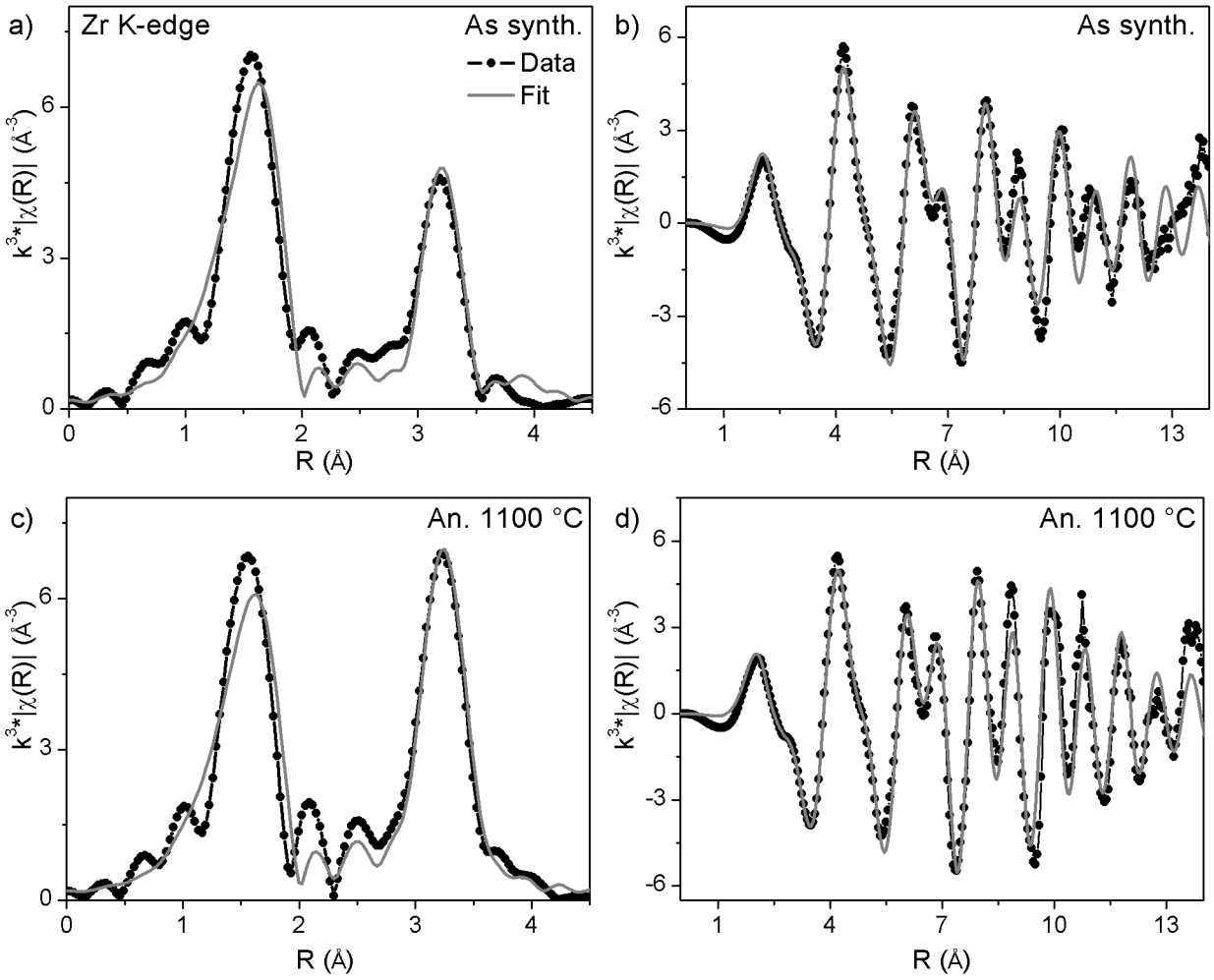

Figure D.20: The fits of the Zr K-edge EXAFS spectra from as-synthesized (a,b) $Nd_{0.20}Sc_{0.05}Zr_{0.80}O_{1.90}$ and (c,d) $Nd_{0.20}Sc_{0.05}Zr_{0.80}O_{1.90}$ annealed at 600 °C in (a,c) R-space and k-space (b,d).

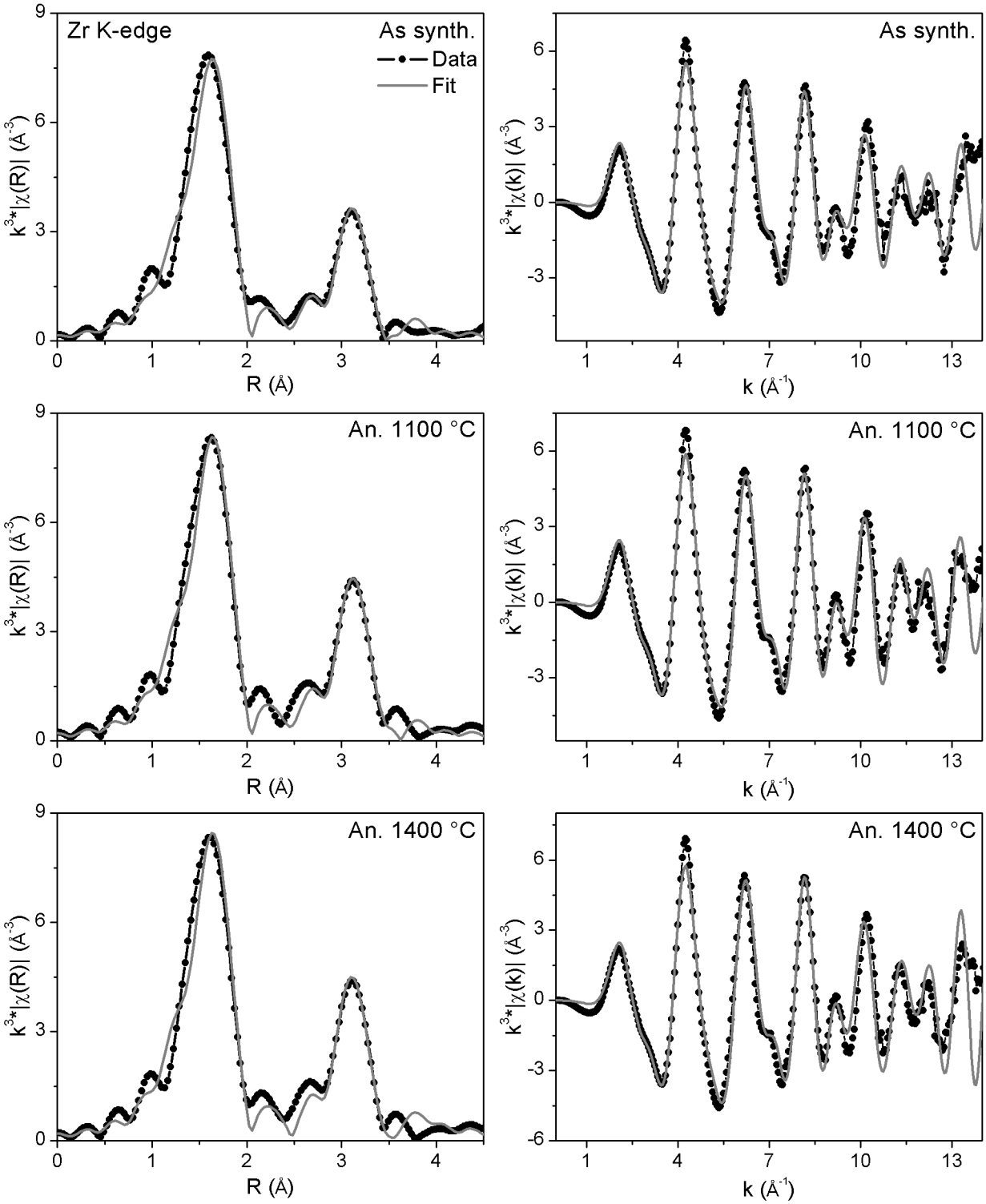

Figure D.21: The fits of the Zr K-edge EXAFS spectra from (a,b) as-synthesized $Nd_{0.05}Sc_{0.25}Zr_{0.70}O_{1.85}$ material, $Nd_{0.05}Sc_{0.25}Zr_{0.75}O_{1.85}$ annealed at (c,d) 1100 °C, and (e,f) 1400 °C are plotted in (a,c,e) R-space and k-space (b,d,f).

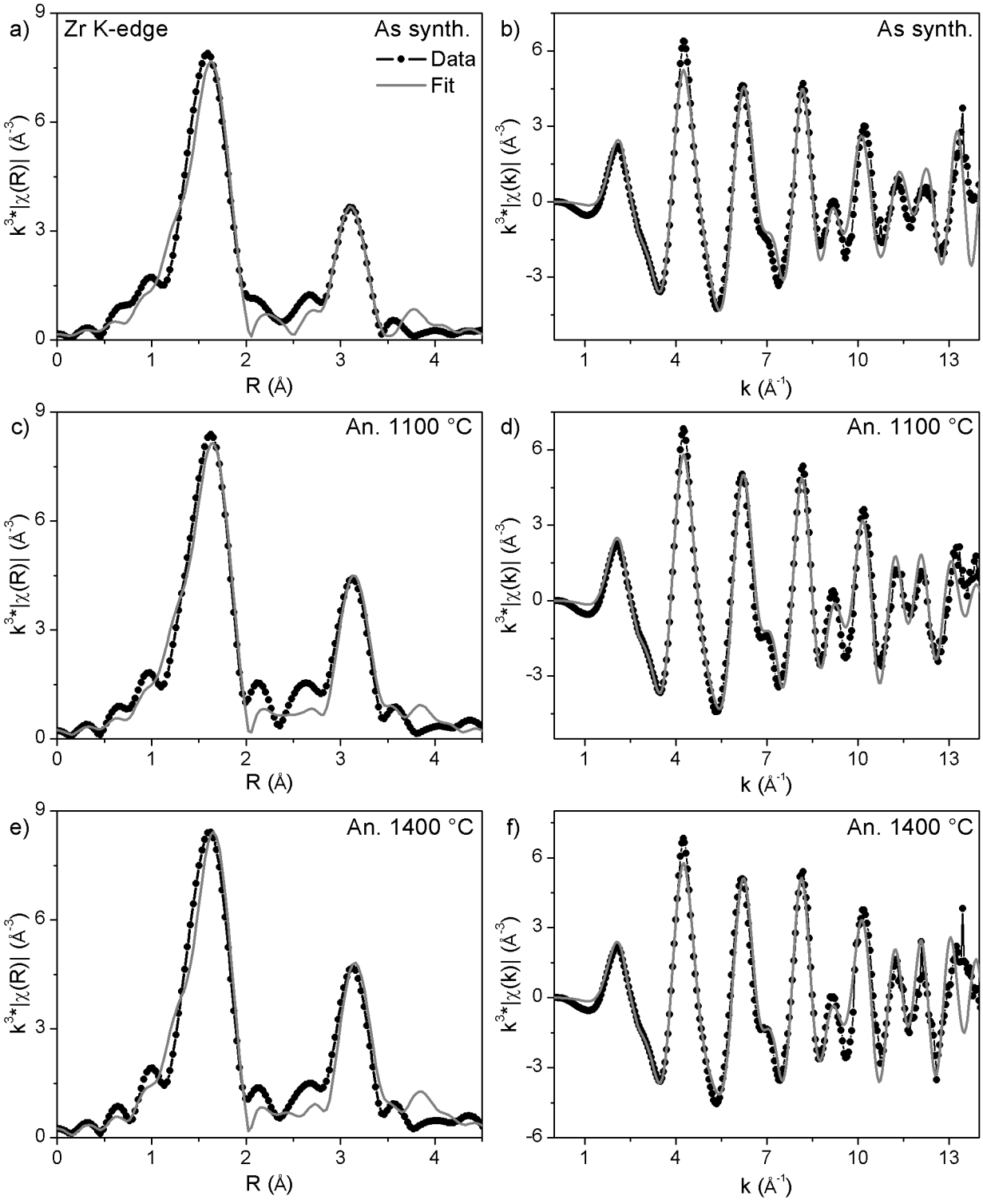

Figure D.22: The fits of the Zr K-edge EXAFS spectra from (a,b) as-synthesized $Nd_{0.10}Sc_{0.20}Zr_{0.70}O_{1.85}$ material, $Nd_{0.10}Sc_{0.20}Zr_{0.70}O_{1.85}$ annealed at (c,d) 1100 °C, and (e,f) 1400 °C are plotted in (a,c,e) R-space and k-space (b,d,f).

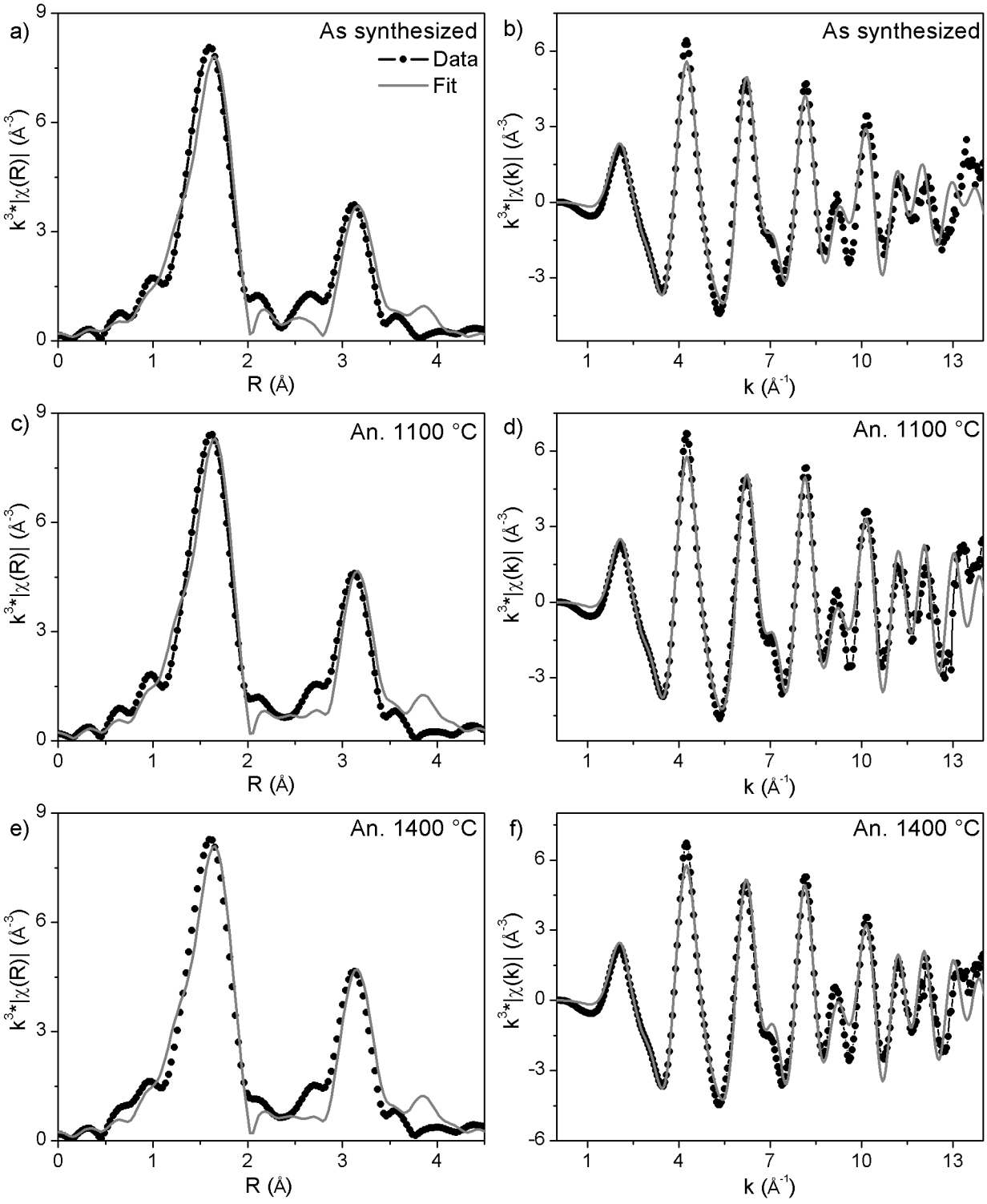

Figure D.23: The fits of the Zr K-edge EXAFS spectra from (a,b) as-synthesized $Nd_{0.15}Sc_{0.15}Zr_{0.70}O_{1.85}$ material, $Nd_{0.15}Sc_{0.15}Zr_{0.70}O_{1.85}$ annealed at (c,d) 1100 °C, and (e,f) 1400 °C are plotted in (a,c,e) R-space and k-space (b,d,f).

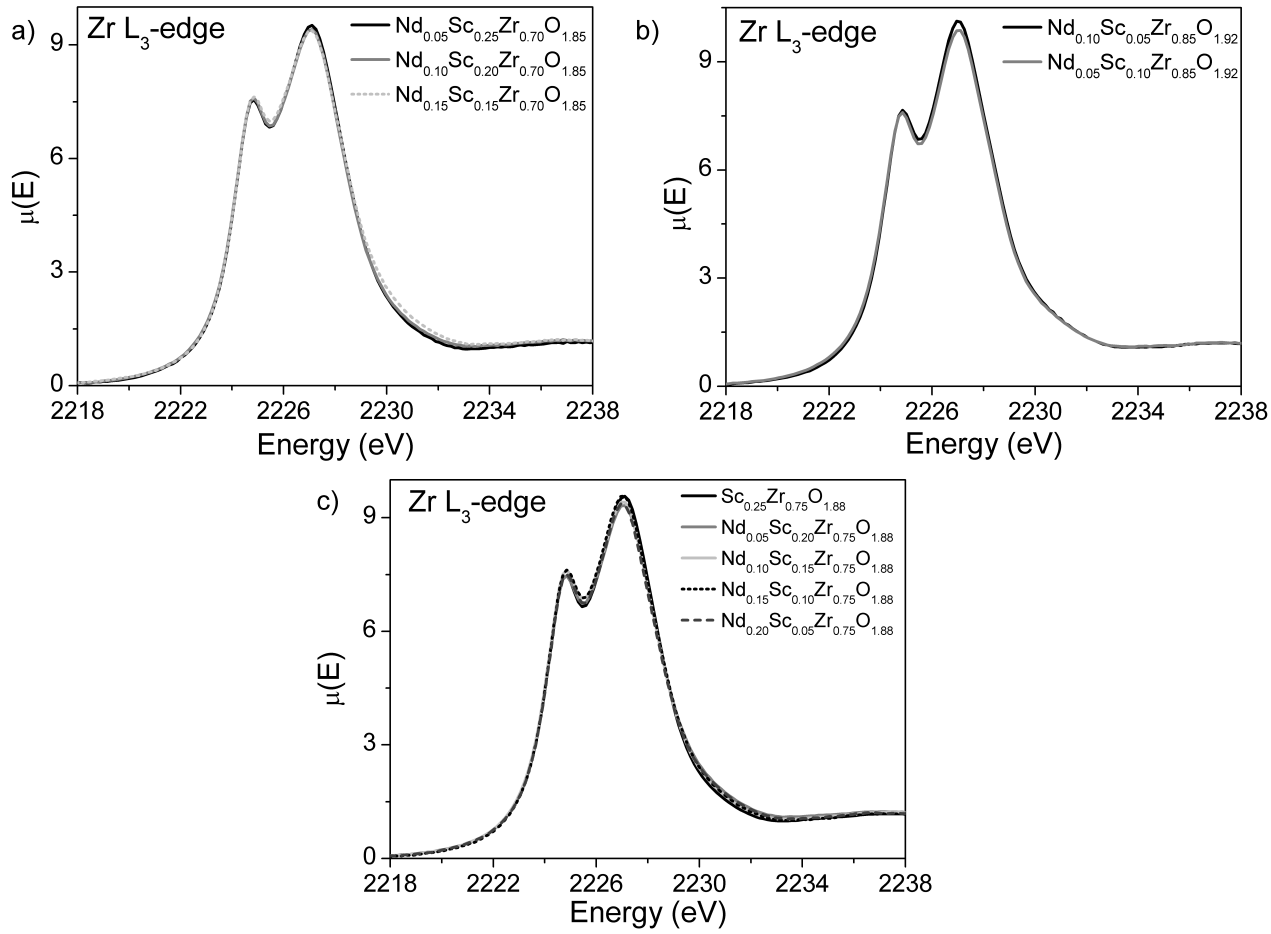

Figure D.24: The Zr L_3-edge spectra from (a) $Nd_xSc_{0.30-x}Zr_{0.70}O_{1.85}$, (b) $Nd_xSc_{0.15-x}O_{1.92}$, and (c) $Nd_xSc_{0.25-x}Zr_{0.75}O_{1.88}$ materials are compared.